University of Southampton Research Repository
ePrints Soton

http://eprints.soton.ac.uk

UNIVERSITY OF SOUTHAMPTON

FACULTY OF ENGINEERING AND THE ENVIRONMENT

THE PREPARATION AND CHARACTERISATION OF AUXETIC FOAMS FOR THE APPLICATION OF TRAUMA ATTENUATING BACKINGS

by
Richard Critchley

A thesis submitted in partial fulfilment of
the requirements for the degree of

Doctor of Philosophy

February 2015

UNIVERSITY OF SOUTHAMPTON

ABSTRACT

FACULTY OF ENGINEERING AND THE ENVIRONMENT

NATIONAL CENTRE FOR ADVANCED TRIBOLOGY AT SOUTHAMPTON RESEARCH GROUP

Doctor of Philosophy

THE PREPARATION AND CHARACTERISATION OF AUXETIC FOAMS FOR THE APPLICATION OF TRAUMA ATTENUATING BACKINGS

Richard Andrew Critchley

Blunt body trauma, due to a heavy impact or blow, has the potential to cause catastrophic injury in a broad range of professions and workplace environments. At particular risk are those who work in areas such as the military, the engineering and construction industries, contact sports (such as American football or rugby) or indeed any other area where an individual has the potential to come into physical contact with other moving objects. Unlike other occupations, the primary cause of blunt trauma in the military is associated with high impact kinetic energies transferred onto the body through the deformation and displacement of body armour.

To date, the effects of behind armour blunt trauma (BABT) are counteracted by materials known as Trauma Attenuating Backings (TABs), which have the ability to dissipate and redistributed the impact energy. Unlike currently available TABs that utilise conventional materials, this thesis explores the feasibility of reducing the effects of BABT through the employment of auxetic foams. In contrast to conventional materials, auxetics exhibit a negative Poisson's ratio when subjected to both tensile and compressive loading, whilst also exhibiting a range of enhanced mechanical properties.

Utilising the well-established three-step auxetic foam fabrication process, the influence of fabrication parameters with key focus on Poisson's ratio and energy absorption have been explored. Auxetic foams were produced for a number of fabrication parameter combinations, where heating time and volumetric compression ratio were identified to be co-dependent in determining Poisson's ratio and energy absorption behaviour. While many individual samples demonstrated a negative Poisson's ratio with enhanced energy absorption, due to the presence of defective and/or damaged cellular structures throughout the foam structures, large variability and little sample repeatability were shown to exist between samples produced from the same combination of fabrication parameters.

A novel 3D printing approach was then developed to produce two types of repeatable pliable polymeric foam structures (re-entrant and honeycomb, auxetic and conventional, respectively) where the majority of geometric features have a dimensional error between 0.5% - 5.0% and exhibited negative Poisson's ratios under both tensile and compressive loading.

Interestingly under direct impact conditions (7.2J of impact energy under freefall) no discernible difference regarding energy absorption was shown between the auxetic and conventional systems. However, when considered with respect to the peak force, the auxetic systems exhibited a lower overall mean peak force by a factor of two. Whilst the auxetic system significantly reduced the transmitted peak force but maintained similar energy absorption when compared to the conventional system, it was difficult to surmise whether or

not the auxetic system performed better than the conventional system. However, with respect to the quasi-static testing (where the auxetics exhibited a greater energy absorption per unit volume due to both systems having an approximately same relative density), for a like-for-like weight basis the auxetic foams absorb more energy than their conventional counterparts due to their structure and not just because of the increase in relative density that the classic auxetic fabrication process instils.

Therefore, it may be concluded that auxetics are potentially suitable for the application as a trauma attenuating backing material as they demonstrated that they satisfy the two key requirements that TAB materials must possess: the ability to absorb energy and reduce the transferable force. However, due to a current lack of understanding on the effects governing BABT, particularly in the area of mechanical and biophysical interactions that take place, it is important that more rigorous testing is undertaken to explore other effects, including pressure wave propagation, ergonomics and replicating in-field conditions before committing auxetic foams to a TAB application.

Contents

List of Figures

List of tables

List of Accompanying Materials

Appendix 4A: Calculating Poisson's ratio from raw data

Appendix 4B: Thermocouple graphs

Appendix 5A: Calculating energy absorption from raw data

List of Publications and Conferences

Publications:

A review of the manufacture, mechanical properties and potential applications of auxetic foams. – Richard Critchley, Ilaria Corni, Julian A. Wharton, Frank C. Walsh, Robert J. K. Wood, Keith R. Stokes - *physica status solidi (b), Volume 250, Issue 10, pages 1963–1982, October 2013, DOI: 10.1002/pssb.201248550*

The Preparation of Auxetic Foams by Three-Dimensional Printing and Their Characteristics - Richard Critchley, Ilaria Corni, Julian A. Wharton, Frank C. Walsh, Robert J. K. Wood, Keith R. Stokes - *Advanced Engineering Materials, Volume 15, Issue 10, pages 980–985, October 2013, DOI: 10.1002/adem.201300030*

Conferences:

Tribo UK, 22 – 23 April 2010, Imperial College London - *Impact and erosion resistant coatings –double auto expanding polymer foam and hybrid CVD/PVD laminated hierarchical multi-layered approaches.*
Auxetics 2010, July, Malta – *Delegate*

JARPD Poster event on 24th March, 2011 at Porton Down – *x2 posters entitled: High strain materials for body armour inspired from nature*

Auxetic Technologies in Healthcare Application, April 2012, London – *Delegate*

CDE Armour and Protection STC - 15 May 2012, Edgbaston, Birmingham – *Delegate*
Auxetics 2012, September, Bolton - *Fabrication of novel auxetic microstructure through the application of 3D printing and finite element technologies*

Armour Appreciation Conference 28th – 30th January 2014- *Delegate*

Academic Thesis: Declaration of Authorship

I, Richard Andrew Critchley

declare that this thesis and the work presented in it are my own and has been generated by me as the result of my own original research.

……………………………………………………………………………………………

……………..…………………………………………………………….…………………

……………………………………………………

 I confirm that:

1. This work was done wholly or mainly while in candidature for a research degree at this University;

2. Where any part of this thesis has previously been submitted for a degree or any other qualification at this University or any other institution, this has been clearly stated;

3. Where I have consulted the published work of others, this is always clearly attributed;

4. Where I have quoted from the work of others, the source is always given. With the exception of such quotations, this thesis is entirely my own work;

5. I have acknowledged all main sources of help;

6. Where the thesis is based on work done by myself jointly with others, I have made clear exactly what was done by others and what I have contributed myself;

7. Parts of this work have been published as described in the list of publications.

Signed:

…………………………………………………………………………………………………

……………………….

Date:

    …………………………………………………………………………………

…………………………………

Acknowledgements

I would like to take the opportunity to thank the many individuals who without, this work would not be possible.

Firstly I would to say a special thank you to my supervisors Dr Julian Wharton, Professor Frank Walsh, Professor Robert Wood and Professor Keith Stokes for their knowledge, support, input and encouragement throughout this project. I would also like to thank the many post docs that have offered their continued assistance, especially Dr Ilaria Corni, Dr Nicola Symonds, and Dr Terry Harvey.

My appreciation and thanks also goes to the many technical staff at the University of Southampton. A particular thanks goes to the Electronics and Computer Science technical support staff (Ken Frampton, Tony Gardner, Mark Long and Eric Webb) and Steve Pilcher. My appreciation also goes to the many academic staff that has provided support and assistance, with a particular mention to Dr Richard Boardman, Dr Mark Mavrogordato Dr Dmitry Grinev at mu-VIS .

I would also like to thank my many friends and colleagues at the University of Southampton, who have not only made the experience an enjoyable one, but for also providing both valuable advice and emotional support. While it is not possible to name everyone, I would like to especially thank, Daniel Bull, Faye Gillard, Nick Alderman, Liam Goodes, Danny Sutton and Martin Evans.

I would also like to thank my family for their continued support throughout this work, and to them I dedicate this work.

Nomenclature:

AFIT	Air Force Institute of Technology
AM	Additive Manufacturing
ARDS	Adult Respiratory Distress Syndrom
BABT	Behind Armour Blunt Trauma
BFS	Backface Signature
BL	Ballistic Limit
CAD	Computer Aided Design
CT	Computed Tomography
DEA	Differential Evolutionary Algorithm
DIC	Digital Image Correlation
DVC	Digital Volume Correlation
EBM	Electron Beam Melting
FEA	Finite Element Analysis
FFT	Fast Fourier Transform
FSP	Fragment Simulating Projectile
GA	Genetic Algorithm
HEL	Hugoniot Elastic Limit
HPPE	High Performance Polyethylene
HOSDB	Home Office Scientific Development Branch
MIMIC	Micromoulding in Capillaries
MTM	Microtransfer Moulding
NIJ	National Institute of Justice
NILECJ	National Institute of Law Enforcement and Criminal Justice
PBFS	Perforation and Backface Signature
PPI	Pores Per Inch
P-Wave	Primary Wave
SEM	Scanning Electronic Microscope
SMP	Shape Memory Polymer
TAB	Trauma Attenuating Backing
VCR	Volumetric Compression Ratio

υ – Poisson's ratio

a - Radius of a circular localised pressure / m

a_n – Narrow radius of a circular localised pressure / m

a_w – Wide radius of a circular localised pressure / m

E - Young's modulus / Pa

E^* - Young's modulus of the foam / Pa

E_impact - Impact energy / J

E_s - Young's modulus of cell wall material / Pa

E_sample – Energy absorbed by a sample / J

E_unit - Energy absorption per unit volume / Jm^{-3}

F – Force / N

F_{in} – Indentation Force / N

G - Shear modulus / Pa

h – Cell height / m

H – Mat thickness / m

K - Bulk modulus / Pa

k_n - Normal stiffness / Nm^{-1}

k_s – Shear stiffness / Nm^{-1}

L – Cell length / m

m – Ball bearing mass / kg

N – Number of cycles

P – Localised pressure / Pa

P^* - Density of a foam / kgm^{-3}

P_s – Density of a cell wall material / kgm^{-3}

R - Circular crack radius / m

r – Loading levels

r_h – Radius of a crater height / m

r_l – Radius of a craters length / m

r_w – Radius of a crater width / m

T – Surface tension / Nm^{-1}

u – Maximum displacement / m

U_max - Maximum displacement (cyclic) / m

U_r – Displacement at a given loading level 'r' / m

V_actual - Measured volumes of the sample after conversion / m^{-3}

VCR_actual - Measured volumetric compression ratio

V_crater – Crater volume / m^3

$VCR_{imposed}$ - Imposed volume compression ratio

V_f – Final Volume / m^3

V_{mould} - Internal volume of the moulds / m^{-3}

V_o – Original Volume / m^3

V_p - P-wave velocity / ms^{-1}

W – Energy dissipated per unit volume / Jm^{-3}

w – Indentation depth / m

ε – Strain

ε_f – Strain upon failure

ε_{length} – Sample strain (length axis)

ε_{max} – Maximum strain

ε_{min} – Minimum strain

ε_{width} – Sample strain (width axis)

λ – Stiffness / Nm^{-1}

σ – Stress / Pa

Chapter 1: Introduction

Ever since firearms appeared on the battlefield, military commanders have endeavoured to protect soldiers from the threats of these weapons through personal protection in the form of body armour. Currently there are numerous different effective body armour systems in existence throughout the world, many of which are specific to a single country or region. For example, the UK uses Osprey body armour [1], whereas the United States army employs the improved outer tactical vest [2]. Although today's armour systems provide excellent protection against most threats, with the ever increasing bullet energies, coupled with a desire among armour designers to increase mobility, reduce weight and keep costing reasonable [3, 4] there are often trade-offs between the following properties:

- Lightweight;
- Flexible;
- Low cost;
- Effective in preventing projectile penetration;
- Capable of dissipating impact energies from reaching the body.

One of the greatest problems currently associated with these trade-offs is the increased risk of behind armour blunt trauma (BABT). BABT is an emerging problem that is directly caused by the transfer of high impact kinetic energies (up to 33% of the projectile impact energy [5]) onto the torso, through the deformation and displacement of the armour materials (the resulting acceleration can damage the thoracic wall and underlying organs [6]). While displacement and deformation are key within modern body armour systems in dissipating the high energy of a projectile, the non-penetrating injury caused by these mechanisms can be as deadly as full penetration [3, 4].

Interestingly, BABT has been reported to occur in two distinct phases, known as the twin peaks phenomena (Figure 1.1) [4, 7]. In general, the first peak is a high amplitude, short duration pressure pulse (the magnitude of this peak is dependent on the armour-projectile combination, as well as the distance between impact and measurement region) which results from the deformed armour impacting the torso. The second peak, which can occur up to 800 μs after the first one, is lower in amplitude, but longer in duration, and is the direct resultant of the torso re-impacting the armour, having been accelerated away from the armour during the initial impact [4].
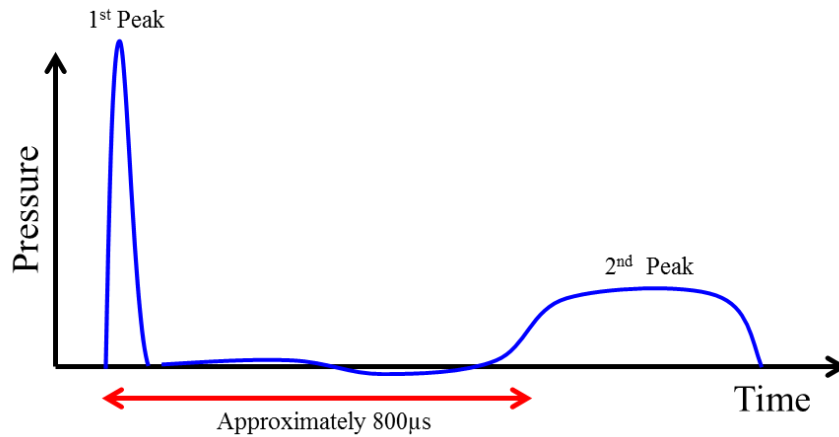
Figure 1.1: Schematic representation of the twin peak phenomena, adapted from [4]**.**

Currently, the effects of BABT are counteracted by materials known as Trauma Attenuating Backings (TABS), which when placed between the armour and the body have been shown to reduce the peak pressures in the thorax by up to 91%, by decreasing deflection of the body wall through absorption, dissipation and redistribution of energy transferred from the armour [3, 6]. In a further attempt to reduce the threat of BABT, current body armour is restricted to a backface signature of 44 mm (along with other performance requirements in order to be considered safe), as set out within the National Institute of Justice body armour standards (NIJ) [8]). An example of the pass requirements for a Type IV heavy plate armour system is shown in Table 1.1 and the subsequent test parameters.

Table 1.1: Table outlining the performance requirements of Type IV body armour.

Hits per panel at 0° angle	Maximum backface depth	Hits per panel at 30° or 45° angle
1 to 6	44 mm	0

- **Bullet type:** .30 Calibre M2 AP
- **Bullet mass**: 10.8 g
- **Impact velocity**: 878 m s^{-1}
- **Shots per panel**: 1 – 6
- **Total number of armour panels**: 4 to 24
- **Total number of shots fired**: 24

In light of these requirements the Joint Grant Scheme – EPSRC Impact and erosion resistant coatings (EP/G042195/1) 'High Strain' programme aimed to limit the current trade-offs through the development of a bio-inspired hard and tough lightweight body armour coatings (external) coupled with a novel porous airbag system to minimise behind armour blunt trauma, through a combination of elastic response and plastic deformation. These systems

2

will further be required to be considered with respect to atmospheric and marine induced corrosion, and good wear performance in order to survive the harsh military operational environments, in which they will be operating. The programme was structured into two sub-projects, with one concentrating on the tough hard outer coatings, whilst the other on systems to enhance BABT reduction. Specifically, the work conducted within the research reported here concerns the BABT.

Unlike other BABT reduction systems that are now commercially available, this project endeavours to reduce or ideally remove the effects of BABT through the application of negative Poisson's ratio materials known as auxetics [9]. These materials are porous in nature, and have demonstrated the mechanical property enhancements in Table 1.2 and will be employed in the novel application of 'smart airbags' where they will be situated at the rear of the sandwich structure, behind the outer ballistic protection.

Table 1.2: Known mechanical properties enhanced within auxetic foams

Auxetic enhanced mechanical properties	References
Shear resistance	[10-15]
Hardness	[10, 12, 13, 16-21]
Toughness	[10, 12-14, 22, 23]
Stiffness	[22, 24]
Acoustics	[10, 14, 16, 25, 26]

1.2   Aims and Objectives:

The following section outlines the thesis aims and objectives for the auxetic materials aspect of this work, followed by a graphical representation (Figure 1.2).

1.2.1   Aim:

To reduce the effects of behind armour blunt trauma through the employment of negative Poisson's ratio materials as trauma attenuating backings.

1.2.2   Objectives:

- To provide an overview of the current requirements of armour systems, testing methodologies, and the materials currently used. Injuries induced from wearing armour will also be explored, with a specific focus on BABT.

- To critically assess the auxetic field with particular emphasis to the auxetic foams, concluding in identifying studies required for assessing auxetic foams as potential trauma attenuating backings. Key areas to explore include the

fabrication method, the known influences of different parameters (temperature, heating time, cell shape and size and volumetric compression ratio), microstructural models, mechanical properties and potential applications.

- To evaluate the current methodology and fabrication parameters detailed by the literature to ascertain the optimal fabrication parameters for producing an auxetic foam. Key assessment criteria will include: maximum and minimum achievable Poisson's ratio, and the overall repeatability of producing a negative Poisson's ratio. Study will also be undertaken with regard to assessing the individual influence that the fabrication parameters have upon sample fabrication, through the employment of heat transfer modelling and computed tomography.

- To evaluate the mechanical performance of auxetic foams fabricated through the current fabrication methodology with primary focus on backface signature profiles and energy absorption. Key assessment criteria will include maximum and minimum measureable energy absorption and backface signatures, and repeatability of mechanical performance. Comparisons will be made against the base conventional foams from which the auxetics are produced, as well as assessed against the established behind armour blunt trauma energies and armour configurations.

- To implement and assess a novel fabrication methodology of polymeric auxetic foams utilising 3D additive manufacturing, where a preliminary study will first identify the limitations and capabilities of additive manufacturing, including its ability to produce repeatable auxetic foams. Comparisons between classic and 3D printed auxetic foams will be then undertaken by using digital volume correlation coupled with computed tomography. Finally the mechanical performance of 3D auxetic foams will be assessed with a key focus on backface signatures profiles and energy absorption under compressive loading, high mass, low velocity and low mass, high velocity impacts, before being assessed against trauma attenuating backing application.

1.3 Thesis Structure:

The following provides a summary of each distinct chapter of this thesis, where two distinct strands of experimental work entitled classical auxetic fabrication and 3D printed fabrication were investigated.

- **Literature review** - A detailed overview of the current requirements of armour systems, testing methodologies, and the materials currently used followed by an overall assessment of the current techniques and studies that have been undertaken with respect to auxetic foams, concluding with areas to be researched for the application of auxetic foams as materials in the reduction of BABT.

- **Methodology** – Techniques and equipment used in the novel experimental testing and analysis of auxetic samples along with justification as suggested within the conclusions of the literature review.

- **Classical fabrication methodology:**
  - **Experimental (Poisson's ratio)** – Presentation and discussion of the data obtained through the testing of the Poisson's ratio of auxetic foams produced utilising the classic fabrication process. Relationships and trends between fabrication parameters and experimental data are additionally discussed, with heat and volumetric studies providing further insight in to behaviour.

  - **Experimental (Crater depth and energy absorption)** – Presentation and discussions of the data obtained for crater depth and energy absorption utilising a novel drop tower and Roma plastilina clay experimental setup. Relationships and trends between fabrication parameters and experimental data additionally discussed.

- **3D Printing fabrication methodology:**
  - **Experimental (3D printing preliminary study)** – Exploration, presentation and discussion of the feasibility of utilising additive manufacturing methods (3D printing) for producing novel polymer auxetic foams. Areas of focus include geometric dimensional repeatability, microstructural damage (optical and electron microscopy and computed tomography) and Poisson's ratio.

  - **Experimental (3D printing main study)** – Presentation and discussions of the data obtained through testing auxetic and conventional 3D printed polymer foams. Area of focus include

Poisson's ratio, microstructural displacement under quasi-static loading, crater depth and energy absorption. Relationships and trends are discussed.

- **Conclusions and future work** – Overall conclusions drawn from both the experimental and microstructural analysis, indicating the pros and cons of the current auxetic foam fabrication method for use as a material for reducing the BABT.
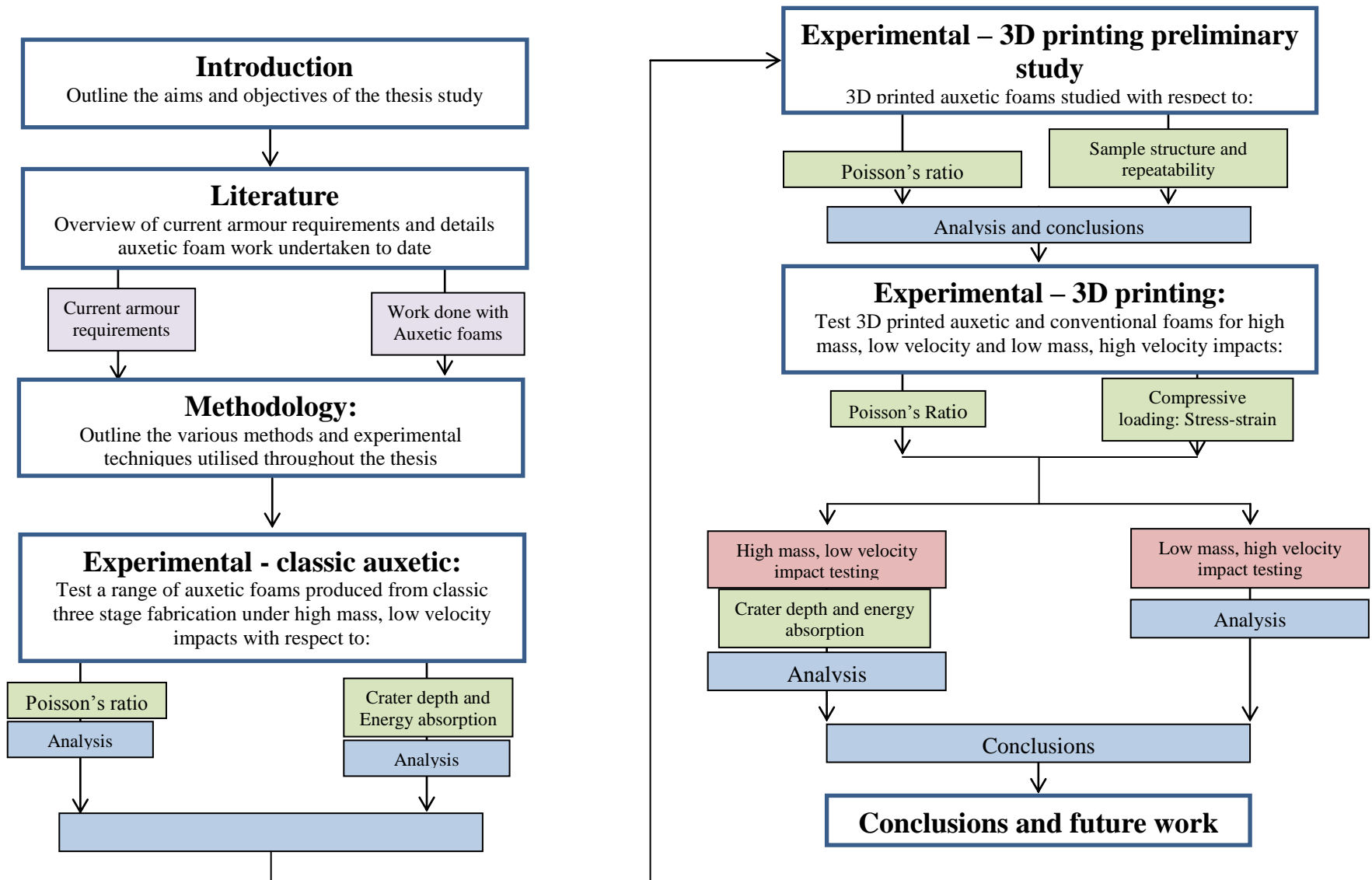
Figure 1.2: Flow chart detailing the stages of the thesis from literature to future work.

Chapter 2: Literature review

2.1 Body Armour:

Personal protection in the form of body armour has been used throughout history in military scenarios ever since the Roman era [27]. While modifications over time saw armour performance improve, it was not until the medieval times (A.D. 400 to ca. 1500) that full body protection (a knight's suit of armour) was adopted [27, 28]. Eventually, with the development of firearms, these armour systems were rendered obsolete [29] and it was not until a series of inventions in 1861 that saw the introduction of thin steel plates enclosed in military jacket materials to protect against sabre attacks, bullets and fragmentation [7]. Interestingly, the decision to use protective armour was a personal choice and depended on a number of factors including cost[1] ($5-$7)[2], weight (2 kg), and appearance (too unmanly) [7]. The use of protective vests ceased after the American Civil War and did not reappear in earnest until 100 years later, when the Korean War coupled with the development of Kevlar provided the catalyst needed to provide a resurgence of modern scientific study into ways to counter ballistic projectiles [3] [29].

In recent times, although the materials and threats have become more advanced, the primary function of body armour still remains the same, i.e., to impede weapon and projectile penetration into the human body and to diffuse the impact energy [27]. In law-enforcement and military environments, energy is typically delivered by impacts from non-penetrating projectiles or blows, blast waves from explosions, and penetrating missiles [30]. In order to overcome these threats, a number of modern personal protection systems have been created, each designed to defeat against specific threats. The ballistic helmet for example provides head protection against low energy bullets, fragments and environmental risks (such as 'bumps'). Alternatively body armour can provide torso protection against fragmentation, low energy and high energy projectiles. Other protective systems also include: Explosive Ordnance Disposal suits (also known as bomb-disposal suits) which protect against blast threats; stab proof vests which defends against knife slashes and stabbings; and hand held armour systems such as ballistic shields, which protect against low energy projectiles. Current body armour systems have a basic mass of typically 7.1 kg (a total of 15 percent of typical maximum load carriage) but can be as high as 15.1 kg (31 percent of maximum load carriage) [7]. There are two main types of personal body armour in service; soft flexible

---

[1] The cost in the 1860's.
[2] Approximately £3-£4 based upon dollar to sterling conversion rate on 03/11/14.

armours and ceramic based rigid hard armours [3]. Soft armour vests are designed to protect against shrapnel resulting from explosions and against low-velocity, low-energy bullets (e.g., 9 mm), and are often deployed in situations where weight limitations are an issue [31]. Hard armour (also known as hybrid armour [32]) incorporates hard-plate inserts made of ceramic composite materials in soft armour vests to defeat high velocity threats such as 7.62 mm and 12.7 mm rifle bullets. For both armour systems, projectiles are defeated by trading momentum and energy for bullet fragmentation and armour deformation. This deformation includes: direct deformation for soft armour systems and deformation with fracture in hard armour systems [7]. These deformations have the potential to deform and transfer energy to the underlying thoracic body wall, which can ultimately cause serious injury or death. This non-penetrating impact injury is termed behind-armour blunt trauma (BABT) [3, 30]. To limit the effects of BABT the energy transferred from armours may be absorbed, dissipated or redistributed using materials placed between the armour system and the body. These materials are termed Trauma Attenuating Backings (TABs) [3, 33, 34].

To date, body armour has been proven to be an effective shield against small arms fire and is well-documented to have saved lives, without exacerbating injury. However, with the increase in high-energy weapons, their effectiveness has come into question and in light of this armour testing has become more rigorous with explicit goals of ensuring that body armour meets survivability standards [35, 36]. The aim of this section is to provide an overview of the current requirements of armour systems, testing methodologies, and the materials currently used. Injuries induced from wearing armour will also be explored, with a specific focus on BABT. A critical overview of auxetic foams, and their processing methods, deformation mechanisms and applications is also provided. The mechanical properties and the possible applications of auxetic foams are also reviewed.

2.1.1 Armour Materials:

Throughout history, many different materials have been utilised for personal protection, with new materials being explored and utilised as advancements are made. For much of human history, personal protection was constructed from organic materials such as animal hides, cloth and wood [37]. Leather armour is considered by many to be the most successful of these early natural armours, and is commonly thought of as the first step in a long development of stronger, better armours [37]. Organic armour dominated personal protection until the capacity to work with metals was developed. Initially, numerous small metal plates would be fastened onto organic backings such as cloth or leather, to form 'scale armour', until further developments would evolve the armour into a stronger, more mobile variation named 'lamellar armour'. Examples of this armour can be seen among the Roman armies [37].

At the same time as the lamellar armour, metal only 'plate armour' was also developed and was initially employed by the Greeks and was later adopted by the Romans. Initially, this armour was fabricated from bronze, and would cover the torso region, and possibly the wrists or shins. Upon adoption by the Romans the plate materials changed to iron. By the 14th century, plate armour had developed into a powerful full suit comprised of steel. 'Chain mail armour' was also introduced around this period, and comprised of thousands of chain links. Similar to plate armour, this armour was produced from various metals throughout history including copper, bronze, brass, iron and steel [37]. However, once firearms become common place on the battlefield, all previous armours and materials become obsolete.

It was not until the 1960s when the United States witnessed a dramatic rise in law enforcement fatalities, that the National Institute of Law Enforcement and Criminal Justice (NILECJ) – a predecessor of the National Institute of Justice (NIJ) - initiated a research programme to investigate the development of a lightweight body armour that could defeat ballistic threats that on-duty police could wear full time [38]. Of all the materials tested by the NIJ, the most significant was DuPont's Kevlar® ballistic fabric, which was originally developed to replace steel belting in vehicle tires. Suspecting that this new material might have potential to greatly improve personal armour, a piece of Kevlar® was folded over a couple of times, and shot at it, only for the bullets not to penetrate [38].

To date, Kevlar still remains a vital material in the development of body armour, and is now categorised as a ballistic fibre / fabric. Other materials used in modern body armour include hard ceramics and laminated composites [27].

2.1.2 Ballistic fibres and fabrics:

Ballistic fibres are typically natural or synthetic fibres with low densities, high strength, high modulus, and high energy absorption capabilities [27, 31]. Currently, there are a number of ballistic fibres available on the market including: glass, high performance polyethylene (HPPE) (Spectra, Dyneema), aramid (Twaron, Kevlar) and poly (p-phenylene-2,6-benzobisoxazole) (PBO) fibres (Zylon) [31].

Through the process of bundling and weaving, ballistic fibres can be manufactured into ballistic yarns and ballistic fabrics. Most ballistic fabrics comprise of a two-dimensional (2D) plain weave pattern that are produced by interlacing warp and weft yarns in two orthogonal directions [39]. Whilst a comprehensive understanding of all the mechanisms that occur during a ballistic impact into these fabrics are currently unknown, through experimental observations and modelling the following are deemed to influence performance:

- the material properties of the yarns [40];
- the fabric structure [40];
- the projectile geometry and velocity [41, 42];
- the interaction of multiple plies [43];
- the far-field boundary conditions [44];
- Friction:
  - Yarn-Yarn [45-47];
  - Fabric-projectile friction [46].

2.1.2.1 Material Properties:

The material properties of ballistic fibres are a key component in its ability to absorb energy as they determine the maximum load conditions a fabric can experience before failure. When a projectile strikes a ballistic fabric, the yarns in direct contact with the projectile (defined as principal yarns) experience a sharp increase in stress (the magnitude of which is related to the impact velocity). If the impact velocity is greater than the 'critical velocity' (the velocity at which yarns rupture instantly [48], the stress increase causes the fabric yarns to fail causing localised damage [49]. Alternatively, if the impact velocity is lower than the 'critical velocity' the stress increase is insufficient to break the yarn fibres, causing a transverse deflection to be produced while also generating longitudinal strain waves that propagate the impact kinetic energy at the speed of sound along the yarn towards the fabric edges [6, 49-51].

As the transverse deflection proceeds (causing the fibres to stretch), orthogonal yarns (yarns that intersect the principal yarns) are then pulled out of their original fabric plane by the principle yarns, causing the orthogonal yarns to deform and develop strain waves comparable to those observed in the principle yarns. This behaviour continues to repeat until either the transverse deflection exceeds its breaking strain or all kinetic energy has been absorbed [6, 49, 50, 52].

It can therefore be seen that fibre straining is the primary mechanism of energy absorption in ballistic fabrics. Furthermore, a direct correlation between energy absorption and the amount of yarns damaged has been reported by Lee *et al.* [51]. The merits of utilising fibres with high-tensile strengths and large failure strains allow for greater resistance to the stresses and transverse deflections induced by the ballistic projectile.

Other important material properties of ballistic fibres are the Young's modulus and density. Roylance and Wang [53] found that ballistic fabrics possessing a high modulus, E, and low density, ρ, (and thus high wave velocity) rapidly propagate stresses and strain waves more quickly to neighbouring fibres and layers. Thus, the energy is distributed over a wider area, through engaging more material in the ballistic event, whilst preventing large strains developing at the impact point. This behaviour was further confirmed by Field and Sun [54], where transverse wave speeds of various fibres, Kevlar fabrics and spectra laminates were impacted with steel balls at velocities up to 1000 m s^{-1} and captured utilising high speed camera technologies.

Prosser *et al.* [55] showed that although each of these material properties (tensile strength, modulus, fibre density and strain to failure) of the yarn play an important role in ballistic performance, no one property individually is in sole control. Furthermore, the authors support this notion by remarking that if ballistic performance were based exclusively on yarn toughness, then Nylon would be a better performer than Kevlar (which it is not). However, Nylon with a strength two-thirds that of high-strength polypropylene was found to be the better performer [56].

2.1.2.1.1 Fabric Structure:

A fabric's performance is not determined by its material properties alone, but through the structural response that is created through the combination of material properties and fabric pattern [57]. Typically most ballistic fabrics utilise either plain or basket weaves patterns (although other patterns have also been studied [42]), and should possess a cover factor from 0.6 to 0.95 for ballistic applications [58]. The cover factor (density of the weave) is

determined from the width and pitch of the warp and weft yarns and gives an indication of the percentage of gross area covered by the fabric. In the case that the cover factor is greater than 0.95, typically the yarns are degraded by the weaving process. Alternatively, if the cover factor is below 0.6 the fabric pattern may be too loose.

Loose fabrics, along with unbalanced weaves, are highly undesirable as they not only reduce ballistic performance but also become more susceptible to having a projectile 'wedge through' the fabric mesh (Figure 2.1). 'Wedge through' behaviour has been reported numerous times [49, 51, 55, 59-61], with evidence of its occurrence, including: fabric perforation hole smaller than the diameter of the projectile [49], a number of broken yarns is less than the number of yarns engaged by the projectile [51] and yarn space enlargement (also known as a 'trap door') [51, 55, 60, 62, 63].
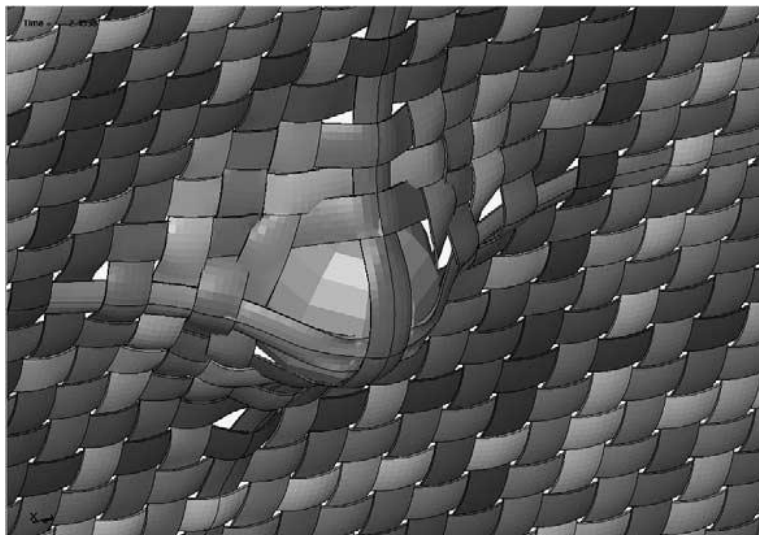
Figure 2.1: Depiction of wedge through behaviour associated with fabric impact [42]**.**

Yarn crimp is another structural property reported to influence ballistic performance [58]. Crimp is the waviness of the yarns, caused by their interlacing woven structure (Figure 2.2). Traditionally within a plain weave structure, the degree of crimp is unbalanced, with the warp yarns typically more crimped than the weft. It has been reasoned [58], that because the weft yarns possess less crimp, they would fail before the warp yarns, because the warp yarns need more time to de-crimp before elongating to failure. To circumvent this occurrence, weft yarns possessing larger elongation to failure were proposed. When these hybridised weave patterns were tested against those comprised entirely from Kevlar in both 6 and 12 ply layups, the hybrid patterns exhibited a greater V50. V50 or V_{50} is the velocity at which a given bullet type is expected to perforate an armour fifty percent of the time [8].

Crimped Fibre
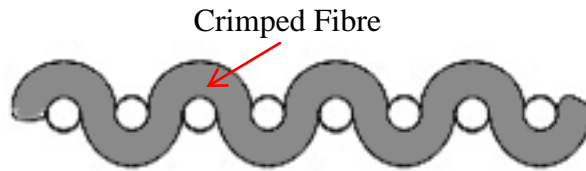
Figure 2.2: Diagram shown yarn crimp in fibre orientation of 0 ° / 90 °. Adapted from [64]**.**

Yarn crossovers within the fabric pattern have also been investigated to ascertain its influence upon the energy dissipation and absorption properties of the ballistic fabric. Interestingly, there appears to be some debate regarding the influence of yarn cross-over. Freeston and Claus [65] conclude that longitudinal strain wave transmission and reflection at the yarn crossover do not significantly affect the propagation of strain waves away from the impact point during a ballistic event. These remarks contradict the findings from a numerical study by Ting *et al.* [66] in which transverse yarn interactions were found to significantly influence the results from ballistic response models. As such this topic requires further study.

2.1.2.1.2   Plies:

To date, no body armour system consists of a single ply layer, instead most armour systems comprise of 15 plies or more. Cunniff [67] investigated the through thickness decoupling response of multi-ply armour systems, where it was reported that during an impact event the first few plies of the armour behave as if unbacked by the remaining plies. Furthermore, when the impact velocity was sufficiently high the armour was dominated by an inelastic behaviour. These observations led Cunniff to propose utilising hybrid armour systems, that replace the strike face materials with those that are cheaper, but exhibit similar inelastic properties, while potentially improving other armour properties such as stiffness.

An example of a hybrid amour system was reported by Larsson and Svenson [68], in which hybridised compliant armour systems using various combinations of carbon, Dyneema and PBO were investigated against ballistic performance using 5.46 mm Fragment Simulating Projectile (FSP) rounds. It was found that when approximately 50% of the impact face of the panels was replaced by carbon fibre, the ballistic limits of the panels were essentially the same as panels containing 100% Dyneema or PBO. However, when only carbon fibre was used on the impact surface, the ballistic limits were shown to improve by 25%.

Descriptions of how multiple ply compliant composite laminates react during ballistic impact have also been widely discussed within the published literature [61, 69, 70]. Iremonger and Went [69] postulated that when a projectile initially impacts an armour panel,

15

it generates a compressive wave that propagates through the thickness of the laminate that reflects off the rear surface as a tensile wave, which may cause delamination. The ballistic geometry was also shown to influence the ballistic response, as the sharp edges of chisel-pointed FSP rounds sheared through the Nylon armour panel fibres, while the oblique faces stretched the fibres until they fail in tension. Similar work has been reported by Lee *et al.* [61], in which they studied the failure of Spectra fibre reinforced composites impacted by 0.22 calibre FSPs rounds. Following plug formation, shown in Figure 2.3, sequential delamination was noted, along with fibre pull-out and fibre tensile failure in the back layers of the laminate. Lateral movement of fibres were observed in unidirectional cross-ply laminates, but not in fabric laminates [61]. Scott [70] also reported evidence of fibre stretching in compliant laminates following penetration even in the first few layers.
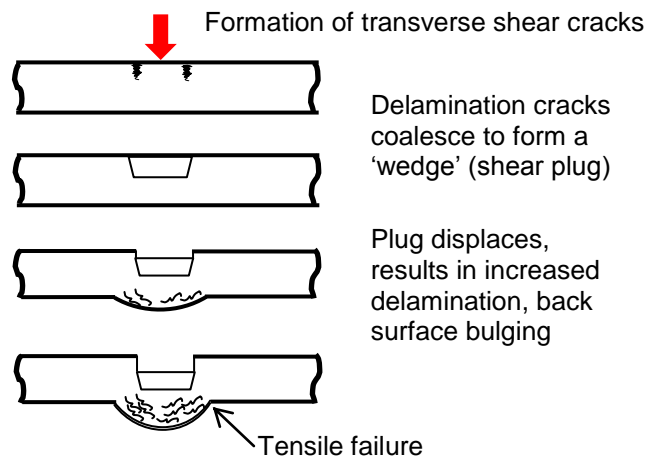
Figure 2.3: Shear plug formation. Adapted from [70].

2.1.2.1.3   Friction:

Friction is a key component influencing the ballistic performance of a fabric, both directly and indirectly. While yarn straining and pull-out have been shown to be directly responsible for absorbing energy during a non-perforating impact event [6, 49, 50, 52], there is evidence that the frictional interactions between the projectile and the yarns, and yarn-yarn interaction may also influence how much energy is absorbed during an impact. Lee *et al.* [51] reported that through restricting a yarn's ability to move laterally from the projectile during impact (through the use of small amounts of resin) the amount of energy absorbed by the fabric increased due to the projectile requiring to engage and break more yarns. Interestingly, by introducing a restricting agent such as a resin matrix, it was also possible to reduce the likelihood of a phenomenon known as Yarn space enlargement. Yarn space enlargement (also known as a 'trap door') is an indicator of 'wedge through' (as previously discussed)

behaviour that is caused not only as a function of fabric structure, but also yarn mobility and projectile geometry [55, 60].

The role of yarn friction on ballistic performance was also studied by Briscoe and Motamedi [71] using Kevlar 29 and Kevlar 49 in three states of yarn-yarn lubrication ('as received', Soxhlet extracted (scoured) and coated with a 5% solution of polydimethysiloxane (PDMS)) were investigated. It was found that generally, the velocity required to perforate a fabric increased with decreasing levels of lubrication, or more specifically, more energy is absorbed in fabrics with greater yarn-yarn friction. Through this finding it was concluded by the authors that through modest changes in yarn-yarn and inter-yarn friction it is possible to induce changes to the ballistic performance of a fabric.

2.1.2.1.4 Projectiles:

A ballistic fabric's performance is not only affected by its own properties but also by the projectiles encountered. Within the available published literature there are two primary aspects of a projectile reported that influences a fabric's ballistic performance: projectile geometry and impact velocity. Projectile geometry has been reported to be a deterministic factor in influencing a projectile's ability to perforate a ballistic fabric. In studies where a limited number of plies (1 to 4) of Kevlar 49 and Armos fabrics were impacted, pointed projectiles have been reported to reduce ballistic fabric performance as they wedge through the fabric, and did not decelerate as quickly as blunt projectiles [59, 72].

In a similar study by Tan *et al.* [6] where single plies of plain weave Twaron CT 716 fabric was impacted by four different projectile types (flat, ogival, hemispherical, and conical headed), projectile geometry was shown to influence the V50 behaviour of the fabric. For the lowest V50 of 58 m s^{-1} and 76 m s^{-1} reported (conical and ogival projectiles, respectively), fabric perforation occurred through wedge through behaviour. Alternatively, the flat head projectile sheared the yarns across the thickness, resulting in a V50 of 100 ms^{-1}, while the hemispherical projectile had the highest V50 of 159 ms^{-1}.

Similarly, Prosser *et al.* [55] reported that the cutting action of a projectile possessing sharp edges was a prime mode of penetration of fabric layers in experiments conducted on multiple layers of Nylon or Spectrashield panels. In panels consisting of 20 layers of fabric, the first few layers were punched out in the shape of the leading surface of the projectile [55]. The effect of projectile geometry can be decreased by increasing the number of plies [55, 59, 73].

Projectiles travelling at a high velocity can also penetrate fabric targets by shearing yarns, rather than extending them to failure [52, 55, 61, 73-77]. Shim *et al.* [49] explored the differences between high and low-velocity impacts through impacting Twaron fabric with steel spheres. It was found that when a high velocity projectile impacted the fabric target, damage was localised with the yarns failing before any significant transverse deflection occurred. Alternatively, during low velocity impact, the transverse deflection of the fabric occurred, without the yarns failing during the initial stress. Similar descriptions have also been reported by Tan *et al.* [6].

In addition to inducing yarn failure through shear, high velocity impact has been reported to cause small amount of fibre melt damage to various materials including Kevlar, ultrahigh-molecular weight polyethylene (UHMWPE), (PBO) and Dyneema [75-77]. Such heat degradation of fibres have been observed since the 1950s, when it was reported that filaments were damaged by softening, melting, decomposition, burning and fibrillation during ballistic impact testing of nylon panels [78]. Other reported melt damage include: fibre fusion, bridging, contraction, along with crystallinity changes in UHMWPE filaments [55, 77, 79, 80].

The source of the heat increase induced through high velocity impact was explored in [55] where an infrared camera was focused on the rear surface of nylon ballistic panels, where temperatures as high as 76.6°C were recorded just after panel perforation by 0.22 calibre circular cylinder projectiles. Through the employment of finite element and finite difference analysis by Prevorsek *et al.* [79] the heat generation and temperature rise were shown to be caused by friction, and only has a minimal effect on the ballistic performance of UHMWPE ballistic fabrics. This conclusion is supported by [60, 81] where UHMWPE panels were heated to 110°C, only a 5 % reduction in ballistic performance was recorded when impacted.

2.1.3 Ceramics:

Whilst textile armour is appropriate for dealing with ballistic threats as high as those detailed in the test conditions of Type IIIA armour systems of the NIJ 0101 standard, it is unlikely that it will defeat a high velocity round fired from almost any range except the most extreme. To counter the threats of high velocity rounds, it is therefore necessary to utilise hard strike face plates that perform two functions [30]:

- They distort, fracture and break up projectiles through their high hardness (used to deflect and deform the projectile) and toughness properties (toughness determines the amount of energy that can be absorbed during the deformation of the projectile before fractures or failure occurs) [27, 30];
- They distribute the impact load over a greater area of the backing material [27, 30].

Strike plates are generally low density, high-hardness, brittle materials (often ceramics) that usually possess high compressive strengths, low fracture toughness and low tensile strength upon damage [82]. Currently a range of materials are used as strike plates including aluminium oxide (Al_2O_3; also known as alumina), boron carbide (B_4C), titanium diboride (TiB_2), and silicon carbide (SiC) and its variants such as SiC–B (silicon carbon boride) and SiC–N (silicon carbon nitride) [82]. The following section discusses the types of ceramic armour available, their failure mechanisms and the influence of various material properties upon ballistic resistive performance.

2.1.3.1 Failure Mechanisms:

Thin ceramic strike plates are composite structures comprising of a front ceramic tile bonded to either a ductile metal or a fabric-based backing plate via a thin adhesive layer. Following initial projectile impact onto the strike panel surface, a high-amplitude stress wave is generated that propagates into the ceramic panel ahead of the projectile [32]. Initially, these stress waves are compressive and travel at the speed of sound in the ceramic. However, due to a mechanical impedance mismatch between the ceramic and backing plate, when the stress waves reach the ceramic / backing interface, they are partially transmitted into the backing plate and partially reflected back through the ceramic as tensile waves.

This leads to a crack zone developing at the rear surface of the ceramic tile that ascends towards the impact surface, causing ceramic fracture at any location where the dynamic tensile yield strength is exceeded in an upwards tapering shape, to form a fracture conoid (Figure 2.4). Typically, full formation of a fracture conoid in ceramics occurs in the order of a few microseconds [83], with the angle of the fracture conoid (usually 65°) dependent on factors such as dynamic loading.

Furthermore, during fracture conoid formation, the impact projectile is unable to penetrate the ceramic tile until the fracture conoid fully propagates and extends to the frontal surface of the ceramic and the projectile. The time duration of this non-penetration event is termed "*dwell*" [84].

For a short projectile (low aspect ratio) or an impact velocity below the ballistic limit of the ceramic armour panel, the dwell period can be long enough to cause a build-up of stress that may exceed the yield strength of the projectile. This leads to the projectile plastically deforming, which, in turn, prolongs the time needed for upward propagation of the damage zone to the free surface, thereby limiting the projectile's ability to penetrate the ceramic armour panel. This non-penetration phenomenon of complete erosion of a projectile is termed interface defeat [85].

Alternatively, if the same projectile is axially long enough (high aspect ratio), the projectile impart its kinetic energy over the same impact area for a longer duration. In this scenario a thicker ceramic layer is required to defeat the projectile [85]. A thick ceramic will continue shatter as a result of continuous penetration by the long projectile, which may exert a compressive stress exceeding the compressive strength of the ceramic. A common technique to contain the debris from scattering is to confine the comminuted ceramic in a metallic ring or cover. Containment of the ceramic also brings additional benefits such as increased time to total failure and enhanced ability to erode the projectile [86, 87].

Alternatively, complete failure (or perforation) of the ceramic tile arises when the fracture conoid fully expands onto the impact surface, and the damaged area becomes comparable to the cross section of the projectile. Failure depends on the velocity and length of the projectile, and can be predicted through studying a materials response and failure under impact loading, examples of which are provided in [88, 89].

Should complete penetration of the ceramic panel arise, the backing plate will deflect and comminuted ceramic forced out of the impact area, will migrate into the newly created volume (Figure 2.4). However, should the load become too focused over a small area, the backing material will fail by either plug shearing or bending for a thin plate or by cratering if the backing is semi-infinite [32]. The extent of the backing plate damage can be controlled by modifying the backing material [27].
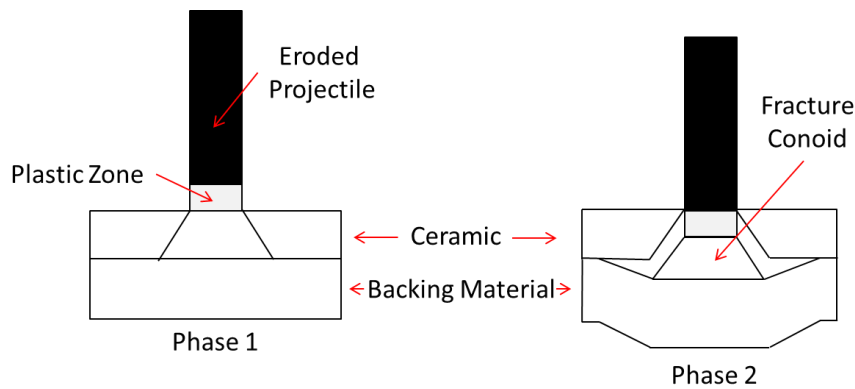
Figure 2.4: Failure mechanisms in a ceramic tile adapted from [32].

2.1.3.1.1 Material properties:

Within the literature, the ballistic performance of ceramic armour panels has been reported to be influenced by various material properties. One important material property is its fracture toughness, which is defined as a material's ability to resist fracture in the presence of cracks and it is an important factor in determining an armour panel's impact response. For armour panels it is desirable to have large fracture toughness as more energy can be absorbed at the point of impact, compared to those with low fracture toughness due to its ability to undergo ductile failure [27]. Another method of improving the ballistic performance of armour panels is through material hardness. Woodward *et al.* [90] noted that if the ceramic is of sufficient hardness to blunt or otherwise destroy the projectile tip at the point of impact, the ability of the projectile to penetrate the armour panel is significantly reduced or diminished all together. Whilst Reijer *et al.* [91] supports the assertion that the hardness of the ceramic should be greater than that of the penetrator, they also state that any further increase above this value is superfluous.

Compressive strength is an additional property that assists in the fracture, deformation or deflection of a projectile, and is reported to provide an armour panel's initial resistance to penetration [92]. If the compressive strength of the armour panel exceeds that of a relatively short ratio projectile, then the projectile will be defeated. However, if the projectile is longer in design, although it may become damaged at the point of impact, an intact rear portion of projectile may continue to advance and penetrate the armour panel [32]. High shear strength is also advantageous in defeating a projectile, as it has been reported to be the material property responsible for decelerating a projectile. Shear strength is a volume effect and to utilise this property, the thickness of the armour panel must be sufficiently large compared to the projectile dimensions. If the armour panel thickness dimensions compared to the radius of the loading area of the projectile is too small, failure can occur from in-plane stresses without ever exercising the shear strength of the material [93]. An armour panel's

performance is also influenced by its Hugoniot Elastic Limit (HEL). HEL is defined as the yield stress of a material under uniaxial dynamic loading, and is important, as materials that are dynamically loaded above its HEL, can exhibit a significant loss of yield strength [94, 95]. HEL values of 1.5 and 1.0 for B_4C and SiC were determined when normalised against high density (99.9%) Al_2O_3 [27]. It was noted, however, that due to compressive strength of the ceramics being determined in a quasi-static manner, it does not necessarily describe the high strain-rate behaviour exhibited by the ceramic material under ballistic impact [32]. Wilkins considered that bulk, shear and Young's modulus are also important parameters for armour panels as they are responsible for a ceramic's resistance to deformation when defeating a projectile [93]. Density is additionally considered as an important property of ceramic armour panels, as low density materials allow the thicker ceramics to be used without a substantial weight penalty [93].

2.1.4   Armour testing and requirements:

Today, more than 80 manufacturers worldwide produce body armour, and estimates suggest that the annual turnover of business generated from this in the United States alone is in excess of $200 million [38]. The majority of this business originates from law enforcement and the military [38]. Although not mandatory, almost all of these manufacturers participate in the National Institute of Justice 0101 voluntary compliance testing program (NIJ 0101), (now in its sixth revision NIJ 0101.06 [8]), which has now gained worldwide acceptance as the benchmark to judge the effectiveness of any given body armour system [38, 96]. Many of the requirements and testing procedures set out by the NIJ 0101 standard can be traced back to the work undertaken between the 1960s and 1970s [38], which led to the initial development and evaluation of modern, concealable, soft body armour, specifically designed for daily use by law enforcement [38, 97].

Historically body armour has generally been developed by and for the military, followed by adaption to civilian use. As the threats faced by the military and law enforcement are different, the NIJ 0101 standard outlines performance requirements and test methodologies for the ballistic resistance of personal body armour based on increasing levels of threat. Currently there are five types of armour specified in the standard, with three pertaining to soft armour without hard plate inserts, and two pertaining to hard armour with hard plate inserts [8, 29].

2.1.4.1 Testing:

To achieve NIJ certification, armour designs are required to pass a compliance test comprising of two parts: perforation and backface signature (PBFS) tests and ballistic limit

(BL) tests. For each of these tests, specific testing variables, performance requirements and shot requirements are outlined that are specific to the armour types being tested. For example if the armour to be tested is categorised as Type IIA through to IIIA (soft armour) by the manufacturer, the compliance test group requires 28 complete armours to be tested against two bullet threats. Hard armour is only required to be tested against one bullet threat with compliance test group consisting of 14 complete armours.

Within Type IIA through to IIIA compliance test groups, an armour design is also required to be tested in two different sizes (larger sizes and smaller sizes) where both sizes are determined by the manufacturer, by matching the sizing of their largest and smallest manufactured armour designs, against those outlined in Appendix C of [8].

For each test threat, the manufacturer is required to provide 3 smaller sized and 11 larger sized test samples, from which 1 smaller size and 3 larger sized armours are randomly selected and subjected to a conditioning protocol. This conditioning protocol is armour type specific and is used to provide some insight into the armour's ability to maintain ballistic performance after being exposed to conditions including: heat, moisture, and mechanical wear. The protocol does not predict the service life of the armour, nor does it simulate an exact period of time in the deployment. The details of this protocol procedure for each armour type are as follows:

2.1.4.1.1   Soft armour conditioning protocol:

1. On procurement of a compliance test group, all samples are stored in a controlled laboratory environment at a temperature of 25°C ± 10°C with a relative humidity of 20 % to 50 % for a minimum period of 24 h prior to testing.

2. The conditioning test group is placed into a tumbler with a temperature, relative humidity and rotation rate of 65°C ± 2°C, 80% ± 5% and of 5.0 ± 1.0 rpm, respectively. The test is run for a period of 10 days ± 1 h, in which 72,000 ± 1,500 complete rotations must occur.

3. Conditioned samples are then to be returned to the conditions outlined in step 1, before being visually examined (and documented) to ascertain if any changes in physical appearance have occurred from exposure.

4. Armours must remain at step 1 storage conditions for a minimum of 12 h before being transported to another facility or before ballistic testing begins.

2.1.4.1.2 Hard armour / plate inserts conditioning protocol:

1. On procurement of a compliance test group, all samples are stored in a controlled laboratory environment at a temperature of 25°C ± 10°C with a relative humidity of 20 % to 50 % for a minimum period of 24 h prior to testing.

2. The conditioning test group is placed into a thermal chamber with a uniform temperature of 65°C ± 2°C and relative humidity of 80% ± 5%, respectively, for a period of 10 days. On completion of the test, thorough visual examination (and documentation) of the test samples is undertaken to ascertain if any changes in physical appearance have occurred during exposure.

3. The conditioning test group is returned to the thermal chamber and subjected to the thermal test cycle for a period of 24 h. On completion of the test, thorough visual examination (and documentation) of the test samples is undertaken to ascertain if any physical changes in appearance have occurred during exposure.

4. Test samples are drop tested at a perpendicular angle to fixed hard panel from a minimum free fall height of 48 inch (1219.2 mm) attached to a 10.0 lb (4.54 kg) clay backing. The weighted fixture is required to be dropped twice while ensuring that impact occurs at the centre face of armour and not the edges. If the plate is part of a complete armour system arrangement, the plate is required to be backed by the flexible armour it is intended for sale with.

2.1.4.1.3 Perforation and backface signature testing:

An armour system is subjected to the PBFS test to demonstrate its resistance to perforation. Within this test, each test panel must withstand an appropriate number of fair hits, and may not experience any perforations, while maintaining a BFS depth measurement less than 44 mm. To measure perforation, and in turn BFS, a plastically deformation witness media (Roma Plastilina Clay #1) is placed and held in direct contact with the back of the armour. Before each shot, the armour panels and the clay backing must be positioned in this arrangement. The armour is then shot on six separate occasions (or five times if using the smallest armour plate template) at the approximate locations detailed in Figure 2.5. In between each shot, the shot location is examined to determine if it complies with the test requirements. In addition to this, an examination of armour plate or panel, and the backing material is undertaken to ascertain if perforation has occurred. Through these observations, it must then be determined if a shot is a fair hit. For a PBFS shot to be considered a fair hit it must:

- Impact the armour panel at an angle of incidence no greater than ±5° from the intended angle of incidence;
- Be no closer to the edge of the ballistic panel than the minimum shot-to-edge distance;
- Be no closer to a prior hit than the minimum shot-to-shot distance;
- Must meet the impact location requirement found in Figure 2.5;
- The shot velocity must be either:
  - Within ±9.1 m s^{-1} of the specified bullet velocity;
  - Be **less than** the minimum velocity and produce a perforation or an excessive BFS (discussed later);
  - Be **greater than** the maximum velocity and not produce a perforation or an excessive BFS (discussed later).
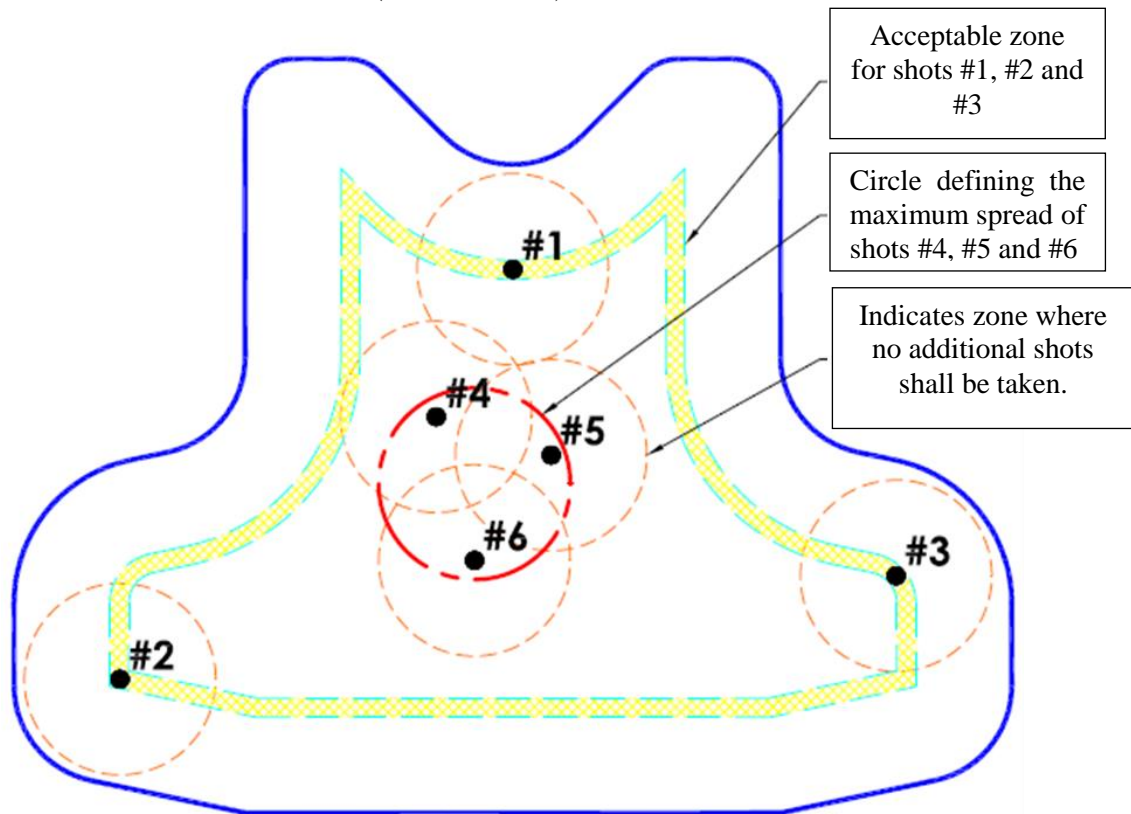
Figure 2.5: General armour panel impact locations as set out in the NIJ standard [8].

If the impact is considered a fair hit, and no perforation has occurred, the BFS depression depth is then recorded using a measuring device capable of ±1 mm or greater accuracy. However, should the depression exceed 40 mm, a second measurements is required to be taken. If the measurement recording is not fully automated or are undertaken manually, a second independent measurement has to be undertaken by another, in order to ensure that the measurements being are recorded are accurate. Alternatively, should the impact be considered not a fair hit, a second attempt shall be made immediately to obtain a fair hit in

the same location and the previous impact. If more than two attempts are required to achieve a fair hit at any of the shot locations, the test series on that panel is then deemed noncompliant, and must be repeated.

2.1.4.1.4 Ballistic limit (BL) determination test:

A ballistic limit test is used to determine the velocity at which a given bullet type is expected to perforate an armour fifty percent of the time, and is typically denoted as the V50 or V_{50} limit value. Within this test, armour test panels are required to be shot by specific bullet threats, a minimum number of times in order to achieve the required penetration results specific to a given armour type. For all BL tests, armour panels are required to be shot at an angle of 0° incidence on twelve occasions or until the maximum number of shots allowed on the panel has been reached. For armours limited to less than twelve shots, the firing sequence continues onto new panels until all twelve shots have been taken. Completion of each twelve shot sequence, requires a new sequence to be undertaken until the total number of shots for a given armour type have been achieved. Throughout this test, no preformation of the armour is permitted, at or below the corresponding maximum PBFS fair hit velocity, while new condition armours require analysis of the BL test data, from which the estimated probability of complete perforation at the corresponding PBFS reference velocity must be less than 5 %. In other words, V50$_{new}$ ≥ V_{ref} new.

2.1.4.2 Requirements:

In addition to the requirements detailed in the NIJ 0101 test standard, as one would expect, the military and law enforcement agencies also have their own specific armour requirements. In the case of military personnel the armour must also be compatible with other equipment that the wearer is carrying [30] while law enforcement requires their armour to be discrete and preferably concealed from open view [38, 97]. Another consideration will be cost [97]. Fortunately, even though the threat levels of law enforcement personnel are considerably less than the military (who rarely face threats greater than .38 calibre, approximately 85% to 90% of the time) [97], the requirements of body armour for both share many common requirements [27].

For example both professions require an armour system that has minimal impact upon the performance of the wearer, but offer sufficient coverage to the most vulnerable areas of the body (vulnerable in this context may with be with respect to maintaining operational effectiveness, saving life or both) [30].

While designers of personal armour systems strive to continue to reduce the weight and thickness of soft armours and armour plates to ease the burden on personnel, these

reductions will likely exacerbate the issue of dissipating the energy in the armour system, due to a greater proportion of the kinetic energy from the retarded projectile being propagated into the body [30]. Body armour must also allow for operational requirements such as weapon carrying, aiming, sitting, crouching, body heat loss etc., while remaining comfortable for long term use. Should any of these not be possible, or if performance excessively degrades, the wearer will have no confidence in the armour, and may not be worn [30].

Body armour requirements can also be situational. In order to increase the protection and survivability rates when engaging high-energy bullets, large ceramic plates are required. However, if the wearer is part of a mobile infantry unit, the carrying of these plates is likely to impede mobility and agility and makes them more vulnerable to sustaining serious physical injury. To counteract this problem, the armour must be designed to save life and one of the major factors that have to be taken into consideration during this process will be the availability of medical facilities. An example of how this was implemented can be seen in the context of the Northern Ireland conflict. Here soldiers were issued with small lightweight plates that covered the heart and primary blood vessels, as wounds to other parts of the body (e.g., lungs), have a low mortality rate with immediate medical care [30]. In addition to preventing wounds through projectile penetration, body armour is also required to reduce or ultimately eradicate non-penetrating injuries to the thorax (termed BABT). Currently, an armour's ability to contain such threats is determined by impacting a soft armour vest over a Roma Plastilina #1 clay backing and measuring the resulting clay deformation as specified in NIJ 0101 standard [8, 29].

2.1.4.3 Behind Armour Blunt Trauma:

BABT constitutes the spectrum of non-penetrating injuries that arise from the backface deformation of personal armour onto the wearer's torso following projectile impact [3, 30]. Historically, BABT has been associated with the defeat of low-energy bullets by flexible tensile armours such as those predominately found in civilian use. However, it is now emerging as a significant military problem, particularly behind rigid armour plates designed to defeat high energy bullets, with its growing prominence being linked to two key factors [3, 30]:

- An increase in bullet energy and calibre used in operational theatre.
- Reduction in weight and thickness of soft textile armour and armour plates by designers in an attempt to limit the burden on military personnel.

While there are many positive reports of body armour wearers only suffering from BABT and making full and uneventful recoveries following a shooting incident, BABT can be lethal [3]. The earliest reported case of lethal BABT is reported by Shepard *et al.* [98], where they describe the case of an US Army sergeant accidently shot at close range with an M-16 round during the Vietnam War. While it is unclear if the sergeant was wearing any rigid body armour, no penetration of his pleural cavity is stated, although massive pulmonary contusions alone were observed post-mortem [3, 98]. It would not, however, be until the late 1970s that BABT would become reported as a clinical entity [30]. At this time, injuries associated with BABT are classified as either direct or indirect, and include, but not limited to, contusions, fractures and haemorrhaging [7], and can occur in both soft and hard armour systems [99]. Direct injuries are those that are localised to the contact area, underlying tissues or areas immediately adjacent to the deformation of the body wall, while indirect injuries occur away from the site of body wall displacement [30, 100].

In an attempt to reduce the severity of BABT, agencies such as the NIJ publish standards that armour manufacturers must demonstrate product compliance, with current standards in the UK and United States stipulating that a maximum backface deformation of armour cannot leave an indentation into Roma Plastilina #1 clay greater than 44 mm [3, 8, 96]. While there are two different recollections of how exactly a maximum deformation of 44 mm became the BABT standard [99], it provides commercial armour developers with the means to assess an armour's ballistic protective performance. The standard fails to accurately represent that formation of BABT is a dynamic event that is caused by energy being transferred into the body through motion of the body wall [3].

While this standard nonetheless offers a first step in reducing BABT, even though much is still unknown about the injury mechanisms of it [7], methodologies to fully prevent BABT must be developed through understanding the biophysical injury principles to the human body and the causes of the resulting pathology [101]. As such, the following provides an overview of the formation mechanisms of BABT and potential methodologies to reduce its effects.

2.1.4.3.1 Formation mechanisms of BABT:
To assess the potential injury effects of BABT and identify the parameters suspected of influencing trauma, it is imperative that techniques are developed that can produce reliable injury data. Currently, there are only three methods of obtaining this data: Cadaver experiments, animal experiments and human epidemiology [7].

Cadaver experiments are those that utilise a cadaver in place of a living human being and tested in a realistic manner. The advantage of this type of experiment is that not only does the cadaver closely match a living human, both anatomically and kinematically, it also allows skeletal and tissue damage to be assessed. The disadvantage of cadavers however is that they do not allow assessment of injuries that require life processes to develop, e.g., commotion cordis, adult respiratory distress syndrome (ARDS), diffuse axonal injury etc.

Animal experiments are those that substitute a living animal in place of a living human and are tested in a realistic manner. The primary advantage of animal testing is that it allows for the assessment of injuries that require life processes to manifest. The principle weakness with animal testing is that animal anatomy offers only a limited correspondence with human anatomy. Furthermore ethical considerations can cause practical difficulties, as there are often protocols that restrict animal involvement to a limited time period (e.g., 2 h). By having time restrictions in place, certain injuries that require hours, days or weeks to develop are difficult to explore. It is possible to extend the time duration of animal involvement if ethically justified.

Unlike cadaver and animal experiments, human epidemiology utilises observations from injuries to humans sustained in field situations. The advantage of human epidemiology studies is that any data obtained often directly applies to the injury being investigated. The disadvantages of epidemiology studies are that there is often only limited information available regarding the causes of the injury, as they do not occur in a controlled environment. Furthermore, the data obtained is always retrospective and limited to systems, technologies and products currently in use (i.e., it cannot be used to inform on unused / future systems, technologies and products).

While each of the above approaches has its own strengths and weaknesses, the most effective studies are those that use as many of these approaches for obtaining injury data. To date various studies have been undertaken in literature regarding BABT testing and findings which have been comprehensively complied and reported by The National Academies in [7]. The following, provides an overview of the formation mechanisms of BABT.

When a projectile impacts on to hard armour, the contact between the bullet and the hard ceramic strike panel, produces a short duration stress wave [102], which propagates through the plate and into the body. This is an extremely fast event with no significant gross motion of the plate or body wall.

The body wall is then subjected to a surface loading from the hard ceramic plate, as it defeats the projectile. This causes a bending load to be applied to the structures within the

body wall (such as the ribs) [3] that have the potential to become fractured as a result of high forces experienced within the body wall. As the body wall deflection increases, local shear is applied to tissues directly underneath the deflection, followed by the generation of shear wave that propagate through the body tissues that cause organ motion.

The loading from the ceramic plate also causes the surface tissues of the body wall to compress, whilst the inner features of the body wall accelerate before reaching a peak velocity. This dynamic motion causes a second stress wave to be generated that propagates into the body [102] and reflect from effectively rigid structures (such as the mediastinum or cranial vault) to result in a complex pressure environment within body compartments, that has the potential to cause local or distant physiological effects [3].

While it can be seen that the formation of BABT is a complex event, with many parameters suspected to influence trauma (including chest wall peak displacement, peak acceleration, peak velocity, peak pressure or a combination of these), the degree to which they play a role in the injury event is somewhat unknown [34]. Nevertheless, it is evident that strategies that minimise the transfer load to the body, delay the moment of impact and absorb the impact energy will potentially reduce trauma. It is necessary that the methods used to reduce trauma must not compromise the armours performance [3].

It has been suggested that mitigation of BABT can be achieved through the employment of TABs. TABs are often specialist low-density materials that sit between the armour and the torso, that attenuate the impact energy through absorption, dissipation and/or redistribution, by allowing energy to be transferred gradually to the thorax through compression in order to initiate motion of the thorax before impact [3, 33, 34]. Unfortunately, as TABs are supplied by armour manufacturers, there is little reported data on specific TABs, due to their proprietary nature.

Whilst the current design methodology for TABs is primarily trial and error [34], NATO is attempting to develop a scientific basis for the design of TABs, however there is little biophysical and pathophysiological information on which to base designs for TABs to counter the very high rates of energy transfer to the body under these circumstances [3]. Interestingly, unlike other aspects of BABT, only a limited number of studies involving TABs are reported in literature.

One of the most comprehensive studies involving TABS is reported by Sondén *et al.* [33]. In this investigation, BABT was studied through three approaches. The first approach

focused on the backface signature impression in ballistic clay with and without the presence of TABs, while approaches two and three investigated various physiological effects on a total of 24 pigs (females and males, ranging in body mass between 45-79 kg), wearing armour with and without TABs.

For each approach, the armour was shot at with 51 7.62 mm bullets travelling with an impact velocity between 799 m s^{-1} and 806 m s^{-1}. The armour used was specially manufactured armour that corresponded to the Mark M/94 Swedish Armed Forces standard that consisted of a ceramic plate, 14 underlying layers of aramid fabric, and three layers of hard woven cotton. The resulting system had an approximate weight of 3.7 kg and a thickness of 25 mm. Alternatively the TABs comprised of a plastic closed cell foam material with a weight of 0.035 kg and thickness of 12 mm. In each of the three studies, the presence of TABs was reported to be highly beneficial. In the study utilising ballistic clay, TABs were observed to reduce the mean clay impression depth from 28 mm (range, 24–31 mm, no TAB present) to 19 mm (range, 17–21 mm, TAB present). The TABs did not change the overall geometry of the clay impressions, as all shots are reported to leave impressions that were shaped similar to a sphere. Alternatively, in the animal testing studies, the presence of TABs was found to not only dramatically decrease the pressure waves transferred into the body, but also significantly reduced the size of pulmonary contusions. Significant transient effects on the brain were still however observed with TAB protection, leading the authors to suggest that "further investigations should be undertaken to try to find the peak pressure level, which does not cause any pathophysiological effects after BABT".

Unlike Sondén et al., Ouellet et al. [34], explored the mechanisms by which TABs could reduce injury severity through numerical modelling. Throughout the study, parameters including compression properties of various polymeric foams and TAB thickness and density were varied, to observe their effect upon various biomechanical parameters including maximum chest wall displacement, peak pressures, velocity and acceleration. Prior to the numerical modelling studies, static and dynamic characterisation of polymeric foams under compression were first undertaken to provide experimental data for the model. Static compression characterisation was undertaken using an Instron machine at 10 mm min^{-1} on specimens of 2,581 mm^2 by 25 mm thick, resulting in a strain rate of 0.007 s^{-1}. Alternatively, dynamic compression characterisation was performed using a Polymeric Compressive Split Hopkinson Bar at strain rates ranging from 483 s^{-1} to 2311 s^{-1}. This range is far below the estimated BABT strain rate (over 6000 s^{-1}).

The model used in the study comprised of polymeric foam of thicknesses 10, 12.5, 15 and 20 mm and of unknown densities, directly modelled on top of a simplified torso, as indicated in Figure 2.6. Loading was applied by a rigid spherical indenter, of radius 50 mm, with a pre-described displacement-time history, representative of the back plane deformation history of the Canadian ceramic plate against a 7.62 mm NATO projectile at 840 m s^{-1} (3200 J). From the parametric study, it was reported that increasing TAB thickness decreases all measured parameters relating to trauma. Furthermore, it was identified that for a specific threat, there was an optimal TAB density that minimises thoracic velocity, peak pressure and acceleration. This optimal density however may depend upon threat faced and TAB thickness considered.
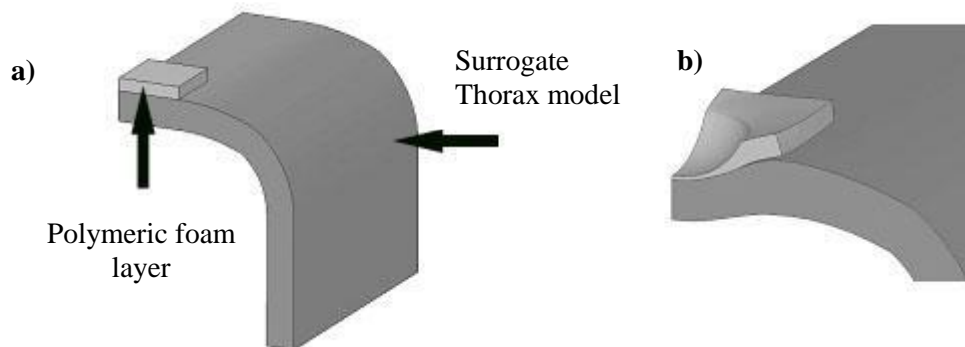
Figure 2.6: Numerical thorax model: **a)** un-deformed and **b)** deformed during impact [34].

2.2 Auxetic foams

Poisson's ratio (υ) is defined as the ratio of transverse contraction to longitudinal expansion in the direction of the stretching force [16]. Conventional materials present a positive Poisson`s ratio and their cross-section becomes larger in compression and smaller in tension (Figure 2.7a) [17]. Thermodynamic considerations of strain energy in the theory of elasticity [103] demonstrate that the Poisson's ratio for a homogeneous solid isotropic material could be between −1 and 0.5 (due to the requirement that for a material to be stable, the stiffness must be positive [104, 105]), thus allowing the existence of materials with a negative Poisson's ratio [16, 106-108]. This class of materials is identified with the term 'auxetics' [9] that derives from the Greek word αὐξητικός (auxetikos) which means 'that tends to increase'. To date auxetics have exhibited a range of Poisson's ratios, as low as −12 in PTFE [109]. Auxetic materials are characterized by a counterintuitive behaviour, which is when tensile load is applied in one direction they expand in another direction, (Figure 2.7b) [22, 24], or more simply they become fatter, laterally, when stretched.
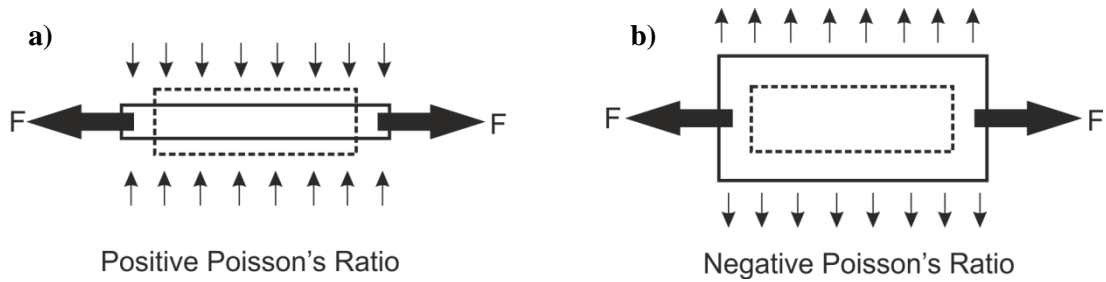
Figure 2.7: Differences between: **a)** a positive and **b)** a negative Poisson's ratio material (adapted from [12]).

To date, auxetic materials have been found throughout nature, *i.e.,* cubic elemental metals, α-cristobalite [110] (high temperature polymorphic mineral), and biological tissues, *i.e.,* cat skin [111] and cow teat skin [112]. These materials demonstrate unique and enhanced mechanical properties and for this reason numerous researches have been carried out to understand the mechanisms that render a material auxetic and to reproduce these mechanisms and properties in man-made materials. To date, a wide range of auxetic materials, such as polymers, metals, ceramics, composites, laminates and fibres [12, 113-115] have been manufactured (see Figure 2.8a) using a particular fabrication process that results in a change of the material structure. A timeline for the discovery and the areas in which man-made and natural auxetic materials are available with their length-scale are reported in Figure 2.8a and Figure 2.8b, respectively. The increased interest in the research and applications of auxetic materials is demonstrated by the increased number of patents filed (Figure 2.9a) and research papers published (Figure 2.9b) since the late 1980s. Auxetic materials can currently be found in commercially available materials such as polytetrafluorethylene (PTFE) and GoreTex [104]; since their discovery by Love [104] organisations including Toyota, Yamaha, Mitsubishi, AlliedSignal Inc, BNFL and the US Office of Naval Research [116] have filed numerous patents. To date, several reviews on auxetic materials have been published dedicating particular attention to known auxetic materials, different types of auxetic microstructures and their applications [12, 114, 117-124].

a) Development and discovery of auxetic materials

b)

Sintered Ceramics
e.g. zirconia

Composites
e.g. carbon fibre
and Kevlar

Biological
e.g. Cat skin and cancellous
bone

Polymeric and metal foams
e.g. polyurethane and copper

Microporous Polymers
e.g. PTFE and UHMWPE

Molecular Auxetics
e.g. iron pyrites,
α-cristobalite polymorph
of crystalline silica, and
arsenic

Honeycombs
e.g. polymer, metal and ceramic

Keyed-Brick Structures
e.g. Magnox reactor
core (graphite)

10^{-10} 10^{-9} 10^{-8} 10^{-7} 10^{-6} 10^{-5} 10^{-4} 10^{-3} 10^{-2} 10^{-1} 10^{0} 10^{1}m

1nm   1μm   1mm   1m

Figure 2.8: a) Timeline for the discovery of natural and man-made auxetic materials, **b)** areas where
auxetic materials have been discovered and their length scale (adapted from [12]).

34
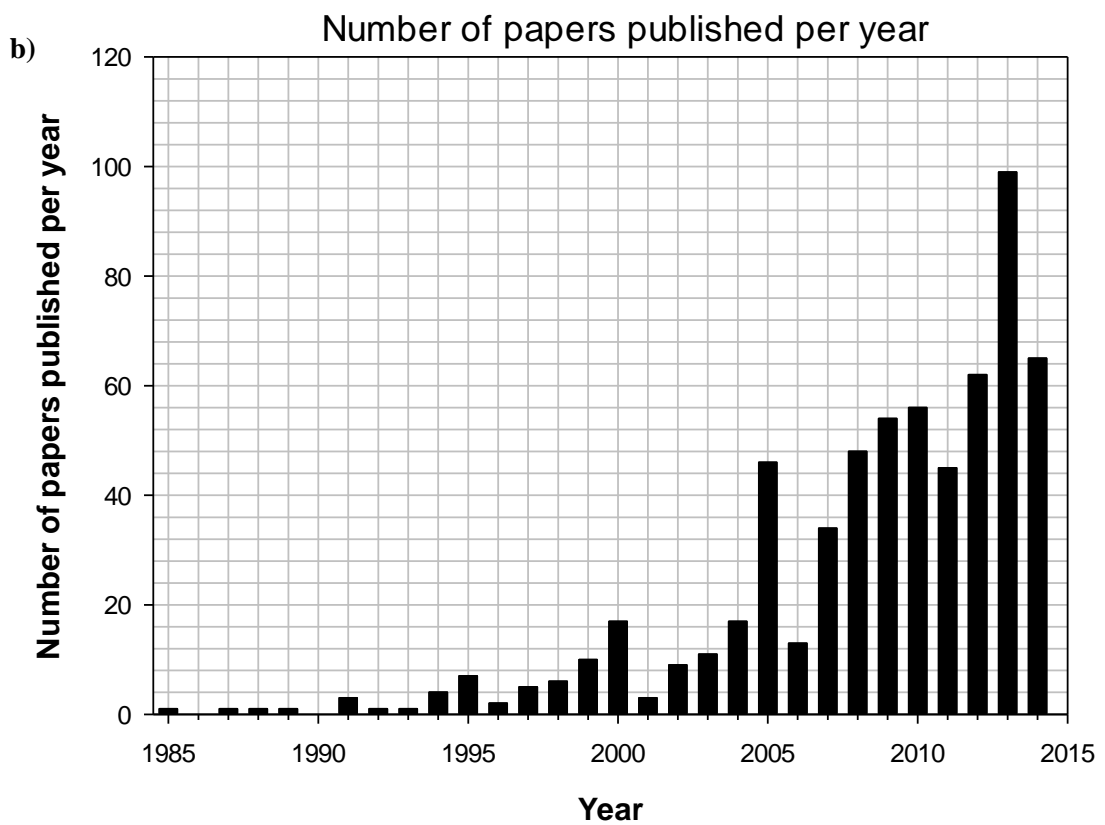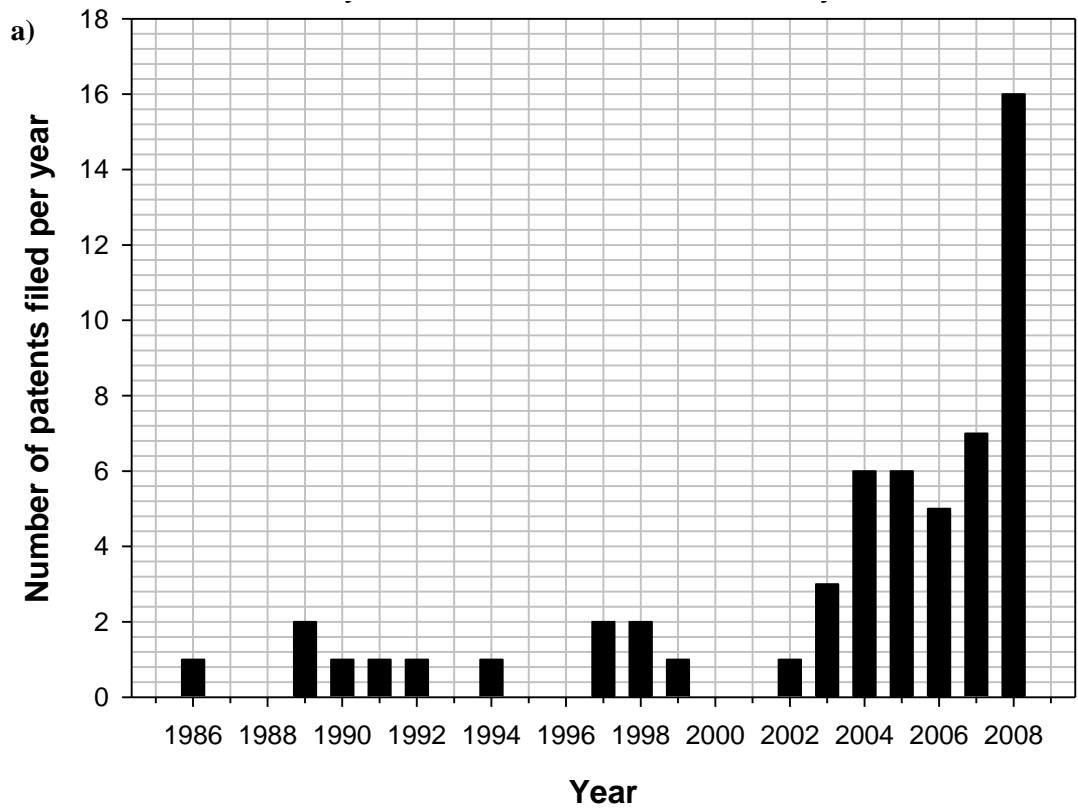
Figure 2.9: **a)** Number of patents filed (information taken from [125] and **b)** number of auxetic papers published since the discovery of the auxetic materials (data obtained from Web of Knowledge searching for 'AUXETIC', data filtered to only include articles (including review papers).

2.2.1 Methods to convert conventional foams into auxetic

The manufacturing of auxetic foams was first reported in 1987 by Lakes [103] (although the concept of auxetic foams was proposed in 1985 by Kolpakov [126]), who suggested two different manufacturing procedures: one for polymeric and one for metallic foams. The remainder of this chapter will only focus on the polymeric aspect of auxetic foams.

2.2.1.1 Methods for the conversions of polymeric foams

For polymeric materials, Lakes [103] started with a conventional thermoplastic open-cell foam and made it auxetic by making the ribs of each cell protrude inward producing a re-entrant structure. This change is achieved in a three-step process in which the open cell foam is tri-axially compressed, heated to a temperature slightly higher than the softening temperature of the material and cooled at room temperature to store potential energy in the compressed ribs [13, 103, 114]. The compression stage of the process changes the shape of the cellular ribs and the heating and cooling stages soften and fix the ribs in a new position.

The main problems that have been identified relate to the auxetic conversion process and in particular the difficulty in making reliable and predictable auxetic materials [127] are: long-term instability with the samples reverting back to their original shape and structure, severe surface creasing, an inability to produce large samples. For example Bianchi *et al.* [107] noticed that following the auxetic conversion, within hours, the samples would naturally attempt to return to their original dimensions. This behaviour was also reported by Scarpa *et al.* [24], who noticed that the final volumetric compression ratio (the change in volume from the sample original dimensions to the new dimensions obtained after the conversion expressed as a ratio) could differ up to 52% from the originally applied value while the sample density was susceptible to a time-dependant change of up to 30% after a week. This behaviour is most likely the result of creep, which occurs as a consequence of the long term exposure to stresses and not sufficient heating times employed during the fabrication process. The surface creasing and wrinkles observed in the more deformable regions of the foam specimen [128] are due to the volumetric compression ratio applied during fabrication [13, 128]. In order to resolve this problem, two solutions have been suggested: lubrication of the mould (the lubricant should not be an oil-derivative or a distilled oil due to their instability at high temperatures and the production of unpleasant smells [13, 18, 108]) and the use of wires or tweezers inside the moulds to pull the foam instead of pushing it [24]. A further solution would be to redesign the moulds so that the tri-axial compression is applied at a uniform rate and no creasing areas form. Another solution has been reported by Chan and Evans in 1997 [13], they attempted to resolve the formation of wrinkles on the sample surface by applying the volumetric compression in several stages in order to produce a more homogeneous auxetic material. Since 1987, this production process has been applied by

numerous researchers [13, 17, 18, 24, 103, 106, 107, 128-135] and a number of modifications have been reported; while each has been altered either to produce differences within the polymeric materials [106, 133] or to optimise the process [13] the overall principle has remained the same, *i.e.,* volumetric compression followed by heating and cooling. These modifications are described in more detail below.

2.2.1.2 Multi-phase auxetic fabrication

Bianchi *et al.* [107] further modified the fabrication process by incorporating a re-conversion back to conventional foam via a *Shape Memory Polymer* (SMP) process followed by a second auxetic conversion. Auxetic materials can be considered as a SMP even if the fabrication process is usually intended as a permanent structural change; in fact it has been observed that the application of an external trigger, such as exposure to a solvent or heat, reverts the auxetic foam back to its conventional state and original dimensions. The re-conversion process is undertaken by heating the unconstrained auxetic samples to a temperature near to the auxetic conversion temperature (200°C) and allowing them to relax. The authors observed that at around 90°C samples began to expand towards their original dimensions, requiring only seconds to regain their initial size; at a temperature of 135°C the auxetic samples completely recovered their original dimensions [107, 130]. The samples that returned to their conventional state had lost the auxetic properties and behaviour resulting in a positive Poisson's ratio; negative Poisson's ratios were achieved again when the samples were re-converted to their auxetic form [107]. A similar study was also reported by Grima *et al.* [136] that re-converted auxetic samples into conventional samples by placing them in acetone, which was followed by air-drying. During acetone exposure the foam re-expanded in all directions. The re-converted samples presented a positive Poisson's ratio and a conventional honeycomb structure.

2.2.1.3 Solvent based auxetic fabrication

More recently Grima *et al.* [136] presented a novel chemo-mechanical process for the fabrication of auxetic foams. Conventional polyurethane samples were mechanically compressed, wrapped in filter paper, placed in acetone for one hour and then air dried. After being removed from the moulds, the samples fabricated with this methodology retained the compressed shape and exhibited auxetic behaviour. When compared to thermo-mechanical fabricated auxetic samples, it was found that both sample types exhibited negative Poisson's ratios of approximately –0.3 and presented highly convoluted auxetic microstructure.

2.2.1.4 Air Force Institute of technology (AFIT) fabrication

An alternative chemical based fabrication process is reported by Lisiecki *et al.* [137]. In this study, a novel fabrication process is proposed that utilises both thermal and chemical processes. Described as a mechanic-chemic-thermal process, this fabrication method is undertaken in four iterations. For each process iteration, the foam sample to be converted is subjected to the following: the conventional polyurethane is tri-axially compressed (by up to 15% volumetric compression) in a specially designed mould (drilled moulds, composed of two identical U-shaped parts), and then exposed to a solvent (in this case acetone) for 30 minutes. The sample is then dried for either 2 h at 55°C or 16 h at 21°C, before repeating the compression and exposure stages until the final iteration of solvent exposure is complete. On completion of the final solvent exposure, the sample is then dried for 1.5 h at 55°C before being subjected to a stabilisation process. During stabilisation, the compressed foam is softened in a compressed state for 20 minutes at 180°C, before being manually stretched, and subjected to a final heating stage of 120°C for 1 h. Interestingly, following fabrication, samples were found to be highly stable with no dimensional changes being observed after 30 days, whilst Poisson's ratios of approximately –0.3 were recorded in compression.

2.2.1.5 Vac-bag auxetic fabrication

Bianchi *et al.* [138] recently presented a novel manufacturing methodology using a vac-bag system. Unlike classical manufacturing methods that are limited to rectangular or cylindrical geometries and to limited volumes; the vac-bag fabrication is capable of producing samples with complex shapes, such as arcs, and large volumes (30 cm × 16 cm × 3 cm). The vac-bag method requires a sheet of conventional foam to be placed upon a semi-circular mould and layered over with a non-porous fluorinated ethylene propylene release film followed by a medium weight polyester non-woven breather blanket which covers both the mould and the foam sample. After sealing the bag, a vacuum pump is employed to reduce the internal pressure down to 0.7 bar causing the foam to be drawn into the mould and to gain the mould curvature. The mould and foam are then placed into a furnace at 200°C and heated for 30 minutes. After removal from the mould, the foam displayed auxeticity and the natural curvature of the mould. SEM analysis further confirmed the auxeticity of the foam although each side of the sample presented different configurations. Through tensile and cyclic loading testing, it was found that the maximum negative Poisson's ratio achieved by this foam was –1.26 at 5% strain and the maximum energy dissipation was 1.42 mJ cm^{-3}. The Poisson's ratio of approx. –1.26 indicates that the sample produced was anisotropic.

2.2.1.6 Dual density auxetic fabrication

Bianchi *et al.* [139] have also recently presented a more classical example of auxetic fabrication resulting in large changes of the density of the auxetic foams. Manufacturing saw two batches of foam samples of varying dimensions placed into a metallic tube mould and compressed. The mould was then placed into an oven and heated at 200°C for 15, 45 and 60 minutes to temperatures of 135°C, 150°C and 170°C, respectively. Samples heated for 15 minutes were cooled at room temperature (20°C) for 5 minutes, whilst the 45 and 60 minute samples were instantly removed from the moulds, stretched then allowed to cool at room temperature.

The removal of the foam from the mould instantly after the heating step creates a differentiated microstructure between the external and internal part of the specimen: a stiff outer layer and a less dense core. This behaviour is suggested to be directly caused by the non-homogenous temperature distribution in the foam body, where only the higher temperatures penetrate the external regions of the sample, and not the interior. Densities were also found to be affected based upon the time a sample spent waiting to be removed, with those waiting longer exhibiting higher densities. This feature is likely to be the result of the samples being tri-axially constrained whilst cooling, thus stopping the ribs from protruding towards their original structure. Samples fabricated through this novel route were also found to only exhibit a negative Poisson's ratio under compression due to the non-homogenous microstructure caused in manufacture. The greatest negative Poisson's ratio achieved in this instance was –0.34.

2.2.2   Additive Manufacturing (3D printing)

A more unconventional method for producing auxetic structures can be associated with additive manufacturing (AM) technologies (also known as 3D printing). First introduced in 1984 by Charles Hull [140] AM is a rapid prototyping (RP) technique that unlike other prototyping techniques, creates physical models from digital CAD data by layering thin cross-section (derived from the CAD model) of material (plastics or metals) to form an approximation of the original design. The overall accuracy of the resulting physical models is dependent upon the layer thickness, where thinner layers create models that are closer to the original design [140]. As a rule of thumb, the nominal layer thickness for most commercially available AM systems is around 0.1 mm, however many systems do have the capability to vary the layer thickness to increase fabrication speed by sacrificing accuracy [140].

To date AM has been used for a number of purposes including: visual aids, presentation models, functional models, fit and assembly, patterns for prototype tooling, patterns for metal castings, tooling components and direct digital/rapid manufacturing [141]. The key advantage of using AM over other techniques is that there are almost virtually no design limitations so that, a limited understanding as to how AM works and the materials available is known [140, 142]. This makes AM manufacturing a fitting technique for not only replicating the complex auxetic structures reported in literature, but for also exploring and generating novel auxetic designs. To date, a limited number of studies have been undertaken in literature utilising various AM techniques and materials to produce auxetic structures. These studies are discussed below. Other advantages offered by AM include ease of design and modification, decreased lead time from concept to product, and lower overall costs of the product [143].

Currently, there are a number of commercially available AM technologies on the market, that differ by their usable materials, how the layers are created, how the layers are bonded together, layer thickness and overall working environment dimensions. Such differences will determine factors such as the accuracy of the final model, its mechanical and material properties, model manufacture time, how much post processing is required and overall cost [140]. While the Table 2.1 provides a summary of these different technologies, a comprehensive overview can be found in [140].

Table 2.1: Current additive manufacturing technologies [140].

Technology	Materials
Fused Deposition Modelling (FDM)	Polycarbonate (PC), Acrylonitrile Butadiene Styrene (ABS), Polyphenylsulfone (PPSF), PC-ABS blends, PC-ISO
Direct Metal Laser Sintering (DMLS)	Metal Alloys
Electron Beam Melting (EBM)	Metal Alloys
Selective Laser Melting (SLM)	Polymers, Metals and Ceramics
Selective Heat Sintering (SHS)	Thermoplastics
Selective Laser Sintering (SLS)	Plastics, Metals, Polymers, Ceramics, Composites
Laminated Object Manufacturing (LOM)	Paper, Composites, Metals, Polymers
Stereolithography (SL)	Photopolymers
Digital Light Processing (DLP)	Photopolymers
3DP	Composites, Elastomers, Polymers, Ceramics
Prometal	Metals, Ceramics
Polyjet	Photopolymers
LENS	Metals

The following section discusses various studies undertaken in literature to produce auxetic structures both directly and indirectly (for example using additive manufacturing to generate a mould, which auxetic samples are then fabricated from).

2.2.2.1 Direct fabrication:

One study involving the direct fabrication of metal auxetic structures using additive manufacturing is reported by Yang *et al.* [144]. In this work, four different re-entrant foam-like structures were manufactured from a Ti6Al4V powder, using Electron Beam Melting (EBM), followed by compression testing to strains in excess of 50% strain.

From compression testing, it was observed that unlike regular foam structures that exhibit stress-strain curves with distinct linear elastic, plateau and densification stages, the tested re-entrant structures exhibited a periodic behaviour Figure 2.10 that did not indicate any obvious plateau stage until several layers of structure had collapsed. It was suspected that this behaviour stems from the fact that the re-entrant lattice structures are periodic three-dimensional (3D) structures that have distinct layers normal to the compressive direction.
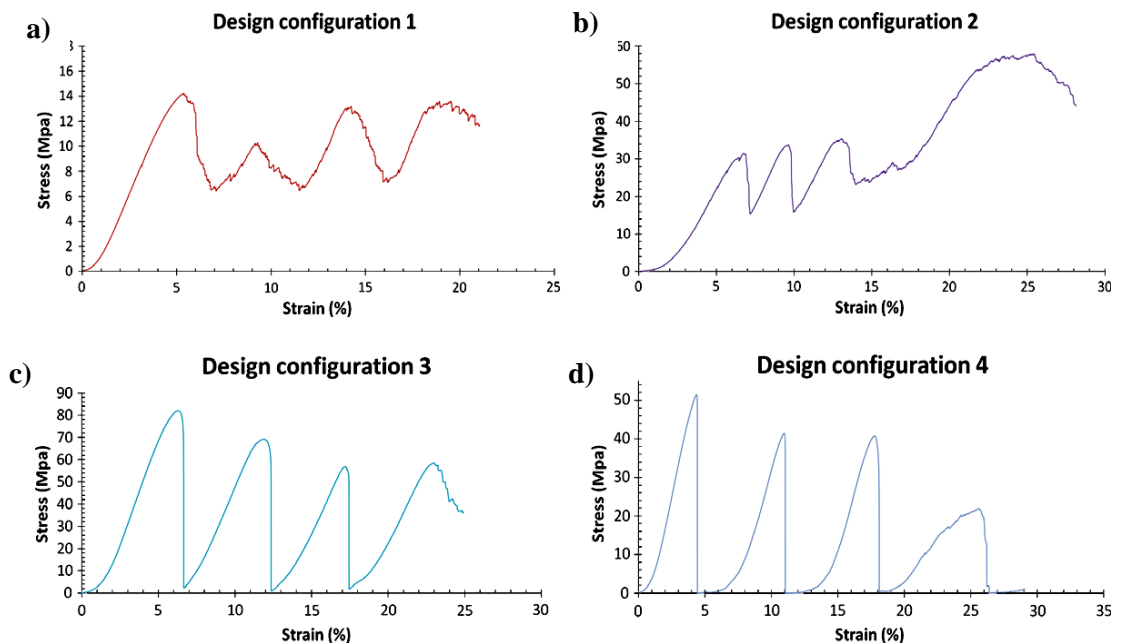
Figure 2.10: Periodic stress-strain behaviour of: **a)** design configuration 1, **b)** design configuration 2, **c)** design configuration 3 and **d)** design configuration 4 [144].

In addition to compressive stress-strain behaviour, the influence of the re-entrant designs structural characteristics (Poisson's ratio and relative density) upon its compressive strength and modulus were explored. For the designs in which the Poisson's ratio was fixed, it was reported that both modulus and compressive strength both increased with respect to an increase in relative density of the re-entrant design. As a designs relative density is directly

linked to length of its struts, it was therefore suggested a design can be tuned to a specific strength or stiffness by varying its struts. Interestingly, when the relative density of designs were kept comparable, it was found that the compressive strength and modulus both increased significantly as the Poisson's ratio becomes increasingly negative. This led the authors to conclude that a design's Poisson's ratio has a more dominant effect on its compressive modulus and strength than relative density. Similar conclusions were also drawn by Schwerdtfeger *et al.* [142], when they studied the compressive properties of re-entrant structures manufactured from a Ti-6Al-4V powder, using EBM. In a similar study by Yang *et al.* [145] two distinct auxetic foam-like structures were manufactured from a powdered Ti6Al4V using EBM, followed by bending and compression tests. When compared against the designs theoretical Poisson's ratios, the experimental Poisson's ratios were found to be significantly lower. Both designs did exhibit a negative Poisson's ratio (−0.052 and −0.097 for design 1 and 2, respectively), with design 2 being more negative due to its greater re-entrant angle and cell rib ratio. Furthermore, when assessed against the original designs, slight differences between the theoretical and actual samples existed, due to the manufacturing process.

From the mechanical tests, design 1 was found to exhibit a significantly higher average modulus, and fracture strength, whilst design 2 demonstrated higher total energy absorption before fracture, due its greater strut thickness. Interestingly, when compared against regular sandwich panel structures presented throughout literature, the auxetic samples without solid skins on either the upper or lower faces were able to match their bend strength. The auxetic designs however did not match the sandwich panels in compressive strength and energy absorption, due to fabrication defects and their periodic stress-strain behaviour.

Direct auxetic structures have also been manufactured from polymer materials. In the study by Hu *et al.* [146], samples with randomly embedded re-entrant inclusions were fabricated using an Objet 3D printer and modelled using FEA. The inclusions comprised of struts (with empty space in between) and were fabricated from a rubber material with high stiffness (TangoBlack FLX9895), whilst the matrix of the sample was fabricated from a low stiffness polymer material (TangoBlack Plus FLX9850).

Upon completion of fabrication, samples were subjected to uniaxial compression tests up to a strain of 20%, where it was observed that the composite samples exhibited an almost zero Poisson's ratio (0.007). Interestingly, while the FE model over predicted the Poisson's ratio (0.095), a good stress-strain curve agreement between the model and experimental was shown up to 0.1 strain. From 0.1 onwards, the FEA model over predicts the stress-strain

curve, which suggests the difference originates from possible local buckling in some parts of the sample, reducing its load-bearing capacity.

An additional study that directly fabricates auxetic structures from polymer materials is reported by Shen *et al.* [147]. In this study, auxetic structures were manufactured from a silicone based rubber material (TangoBlack) using an Objet Connext350 3D printer and compression tested to ascertain if a design favoured a specific buckling mode. After identification of the favoured buckling mode, it was introduced to the designs microstructure as an initial imperfection, where it was found that by varying the magnitude of this imperfection, different negative Poisson's ratios were achievable. Furthermore, it was found that the negative Poisson's ratio behaviour was retained over a wide range of applied strains and can be altered by varying the magnitude of imperfection and initial volume fraction. Fozdar *et al.* [148] have also utilised polymer materials to directly produce single and double layered in-plane auxetic structures (designs based from literature: Re-entrant, Missing Rib and intact) from an acrylated- polyethylene glycol (PEG) hydrogel, using a digital micromirror device projection printing system.

The single and double layered designs were then tensile tested (to ascertain the Poisson's ratio) and compared against analytical mathematical models. From testing it was observed that the re-entrant and missing rib designs both exhibited negative Poisson's ratios in both single and double layered states, while the intact cells exhibited a positive Poisson's ratio. Interestingly, it was found that little difference in Poisson's ratio existed between single and double layer samples, leading the authors to conclude that additional layers do not have a significant influence upon the Poisson's ratio. The Poisson's ratios were also found to be consistent with those predicted analytically.

Interestingly not all directly fabricated auxetic structures utilising additive manufacturing presented in literature have been used for scientific testing. In [149, 150], real world auxetic and regular foam structures were replicated (structure extracted using MicroCT) from a fragile incompressible polymer (material not given), as a proof of concept and visual aid.

2.2.2.2 Indirect fabrication:
In addition to directly manufacturing auxetic structures, additive manufacturing can also be used to make auxetic structures through indirect methods such as bespoke moulds. In the study by Babaee *et al.* [151], 3D materials with a negative Poisson's ratio using novel Bucklicrystals were explored. Unlike most other auxetics designs produced through moulding, the individual Bucklicrystals cells were cast from a mould (mould fabricated

using an Objet Connex500 3D printer) as one half of a spherical shell from a silicone-based rubber (Elite Double 32, Zhermack) before being joined using the same polymer as an adhesive agent. After preparing the required number of spherical shells, all the shells were joined using the polymer adhesive agent and tested under uniaxial compression, with microCT monitoring microstructure evolution, in order to ascertain Poisson's ratio at various strain. From the strains investigated, the Bucklicrystal exhibited a negative Poisson's for all tested strain intervals.

Another example of using additive manufactured moulds to produce auxetics is reported by Xu *et al.* [152]. In this study, auxetic structures comprised of a range of auxetic cells were manufactured using a mould fabricated from a polymer (polydimethylsiloxane) using three soft lithography technologies: micro-transfer moulding, micro-moulding in capillaries, and micro-embossing. The resulting moulds were then filled with different materials including polyurethane, carbon, epoxy, nickel and polyvinylene difluoride, to produce planar structures with negative Poisson's ratios. Through testing it was found that for the two representative structures tested, negative Poisson's ratios of -1.08 and -0.58 were demonstrated.

Since the inception of the original auxetic fabrication process in 1987, auxetic foams have been fabricated through a number of different fabrication methodologies, however the overall core principles of these methodologies is fundamentally the same, i.e., volumetric compression followed by heating (either through thermo or chemical processes or a combination of both) and cooling. However, since the advancements and the increased accessibility of AM, there appears to be an increase in literature reporting auxetic fabrication using these techniques. AM offers a potential solution to the reported difficulties in making reliable and predictable auxetic materials [140] as AM is inherently a repeatable process. Furthermore, AM has the capacity to enable real world testing of novel auxetic foam designs as there is almost virtually no design limitations that additive manufacturing cannot reproduce.

Other benefits of this methodology include the ability to model sample behaviour prior to fabrication (via an FEA approach), ease of sample modification and the capability to share sample designs throughout the research community or any other interested parties. One of the negative aspects of this technology is the current high setup and materials costs incurred however as this technology continues to develop it is highly likely that these costs will significantly reduce.

2.2.3 Parameters affecting the manufacture of auxetic foams

2.2.3.1 Effect of temperature and heating time

In the original auxetic fabrication literature, Lakes heated a polyester open-cell foam contained within a mould to a temperature slightly above the softening temperature of the foam material, which was reported to be between 163° to 171°C [103]. This statement was then followed by numerous studies attempting to determine the methodology and the justification behind this choice of temperature. In 1997, Chan and Evans [13] employed a thermocouple placed in the centre of a foam specimen to determine the softening temperature of the material, which was assumed to occur at the temperature when the cell ribs began to collapse. It was noticed that for the tested polyester urethane (PECO) foam, the softening temperature was found to occur around 180°C, which lead the authors to suggest that the temperature employed to achieve successful auxetic conversion should be between 5 and 20 °C lower than the softening temperature, in order to maximise stress relaxation and minimise cell rib adhesion. Conversely, Lee, T. and Lakes, R. S. [153] and Wang *et al.* [134] suggested that the conversion temperature should be *equal or greater* than the softening temperature of the material. From the results reported, it is reasonable to assume that Chan and Evans` [13] suggestion of keeping the conversion temperature below the materials softening temperature (e.g., 180°C) was incorrect and instead the temperature employed should in fact be equal or above the softening temperature of the conventional polymeric foam, as this allows for the softening of the polymeric ribs to occur.

Interestingly, in later studies by Bianchi *et al* [130], auxetic foams were produced using temperatures as low as 135°C. While the temperature was significantly lower than those previously reported, it was found through DSC that the PU-based foams exhibit two distinct glass transition (T_g) temperatures at –53 and 114°C. The led the authors to suggest that heating above the upper T_g is required in order to process the materials into the auxetic phase.

Whilst attempting to determine the reasons behind the temperature values published by Lakes [103], Chan and Evans [13] reported several interesting observations. They observed that if the heating time was too long, the foam would either decompose or melt with the cell ribs sticking together to form a dense block of material [13] and if the heating time was too short, the foam could not be 'set' into its new re-entrant structure and would soon begin to expand back to its original size. Choi and Lakes [131] and Bianchi *et al.* [106] further confirmed this behaviour; the rate at which a sample lost its negative Poisson's ratio fluctuated from a few days to a few months. Furthermore, Chan and Evans [13] noticed that

the heating time needed to turn a conventional porous material into an auxetic one depended on the exact type of foam (e.g. initial base material and porosity). Wang *et al.* confirmed these observations and further suggested that the cell size was also an important factor influencing the auxetic fabrication [134]. It was found that polyurethane foams having a smaller cell size required higher heating temperatures and heating times compared to foams with larger pore size. It was speculated that this behaviour could be due to either the surface tension effects within smaller cells or to a possible difference in the chemistry of the material [134].

Other notable effects of the temperature on the auxetic conversion process have been reported when studying the early stages of heating and cooling. During the early stages of heating at temperatures of 100 – 135°C, Bianchi *et al.* [130] noticed using thermogravimetric analysis that conventional foams experience an approximate 2% loss in weight. It is suggested that the loss in weight could potentially explain the difference in mechanical properties between conventional and auxetic materials during the multi-phase conversion (phase 1: conventional, phase 2: first auxetic, phase 3: returned conventional and phase 4: second auxetic). During cooling, numerous studies [13, 103, 131] have shown that the specimens should be cooled at room temperature, as set out by Lakes [103]. In 2008, Bianchi *et al.* [106] introduced an alternative cooling method in which samples were cooled in water for 5 minutes. Specimens cooled in water exhibited unusual density values compared to samples that were cooled in air; the numerical differences are unknown as Bianchi *et al.* [106] did not report the actual numerical values. It was further noted that by employing water cooling a more uniform temperature distribution was obtained; it was speculated that uniform temperature distribution and alternative density values occur as the water jet induces a significant thermal shock to the sample [106].

Many authors have studied the effects of temperature on the fabrication of auxetic materials but there are still discrepancies associated with determining an optimum temperature and heating time to be employed. These discrepancies are likely the result of the variance in materials and equipment that each individual researcher has employed for the experiments. Numerous temperature-time combinations have been reported in the published literature where the heating times vary from 6 min [13] to 60 min [139], but the majority of the time-temperature combinations lasted less than 20 min. The temperature applied varied between 135°C [13, 106, 130] and 220°C [134]. This wide temperature range can be explained considering the finding reported by Wang *et al.* [134]: foams with smaller cell size need higher heating temperatures and shorter processing times compared to foams with larger pore sizes.

The wide ranges in which both the heating time and the temperature have been varied seem extreme and therefore more studies are needed to understand the effect that these two variables have on the auxetic conversion process.

2.2.3.2 Effects of the cell shape

Since the auxetic materials were first produced [103], the most commonly reported auxetic foams produced were thermoplastic (polyester urethane, polyether urethane), thermosetting (silicon rubber) and metallic (copper) [12]. However, the foam most employed has been the open-cell polyurethane foam due to its availability and ease of application [22], as shown in Table 2.2. Even though polyurethane has been widely studied [11, 13, 17, 18, 103, 106, 107, 117, 118, 120, 123, 125, 137, 153, 154] only few studies have investigated the effect that pore size plays on the auxetic conversion process.

Table 2.2: Examples of foams employed by various research groups

Authors	Year	Material	Porosity/ pores per linear inch	Density / kg m^{-3}	Reference
Lakes	1987	Open-cell polymer foam	Not Given	30	[103]
Chan & Evans	1997	Closed-cell polyester urethane foam	60	39.9	[13]
Chan & Evans	1997	Reticulated polyester urethane foam	60	33.7	[13]
Chan & Evans	1997	Open-cell polyether urethane foam	10	24.1	[13]
Chan & Evans	1997	Open-cell polyether urethane foam	30	24.5	[13]
Chan & Evans	1997	Open-cell polyether urethane foam	60	21.7	[13]
Wang *et al.*	2001	Open-cell polyurethane foam	20	30	[134]
Wang *et al.*	2001	Open-cell polyurethane foam	65	30	[134]
Wang *et al.*	2001	Open-cell polyurethane foam	100	33	[134]
Scarpa *et al.*	2002	Open-cell polyurethane foam	Not Given	32	[18]
Scarpa *et al.*	2004	Open-cell polyurethane foam	30-35	32	[129]
Scarpa *et al.*	2005	Open-cell polyurethane foam	30-35	27	[24]
Bianchi *et al.*	2008	Open-cell polyurethane foam	30-35	27.2	[106]
Bianchi *et al.*	2010	Open-cell polyurethane foam	30-35	27.2	[107]
Bianchi *et al.*	2010	Open-cell polyurethane foam	52-57	27	[107]
Bianchi *et al.*	2010	Open-cell polyurethane foam	30-35	27.2	[130]
Bianchi *et al.*	2010	Open-cell polyurethane foam	52-57	27	[130]
Chekkal *et al.*	2010	Open-cell polyurethane foam	Not Given	27	[155]
Bianchi *et al.*	2010	Open-cell polyurethane–polyethylene foam	28-35	27	[139]
Bianchi *et al.*	2010	Open-cell polyurethane–polyethylene foam	30-35	27	[139]
Pierron *et al.*	2013	Open-cell polyurethane foam	45	30	[156]
Sanami *et al.*	2014	Open-cell polyurethane foam	45	26-32	[157]

One of the more comprehensive studies on the effect that cell shape and size have on the properties of the foam was reported by Chan and Evans [158]. They specifically studied the

microstructure and the deformation mechanisms of conventional and auxetic open-cell foams and observed that the cell size was not the dominating factor in determining the mechanical properties, while the cell shape and geometry were found to be greater contributors, as also reported in [159]. The cell geometry is influenced by the manufacture process of the conventional foam that is formed by injecting gas in the semi-liquid material, the gas dissipates throughout the material then the liquid is cooled to the solid state retaining the air pockets formed by the gas. The air pockets are somewhat elongated and therefore the foam could be anisotropic [158, 160].

Chan and Evans [158] studied and modelled the cell geometries and volumes in two / three dimensions for conventional (Figure 2.11) and auxetic foams (see Figure 2.12). To achieve a sufficient statistical analysis of the data, approximately 100 specimens were measured. They observed that once the conventional foam was converted to auxetic the cell geometry it no longer resembles an ellipsoid (Figure 2.11), but becomes more similar to a bow-tie re-entrant microstructure (Figure 2.12). This conversion also affects the length of the cell. Both models for the auxetic and conventional pores are described in more details below.
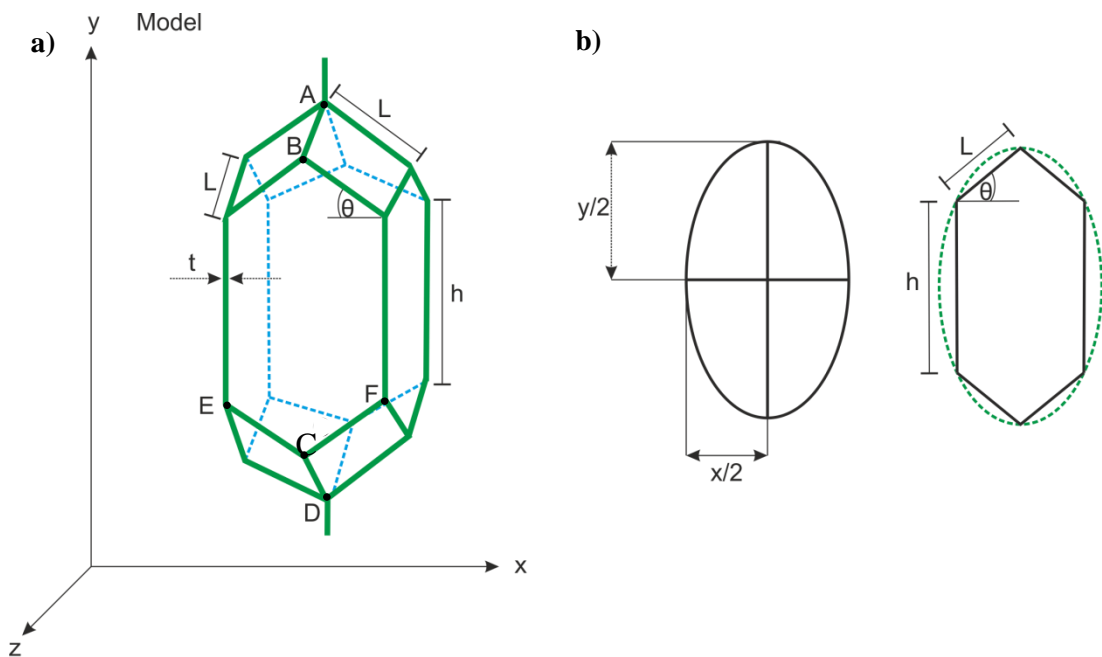
Figure 2.11: Schematic representation of **a)** a three-dimensional geometry for a conventional foam and **b)** a two-dimensional geometry of the same pore type (adapted from [158]).
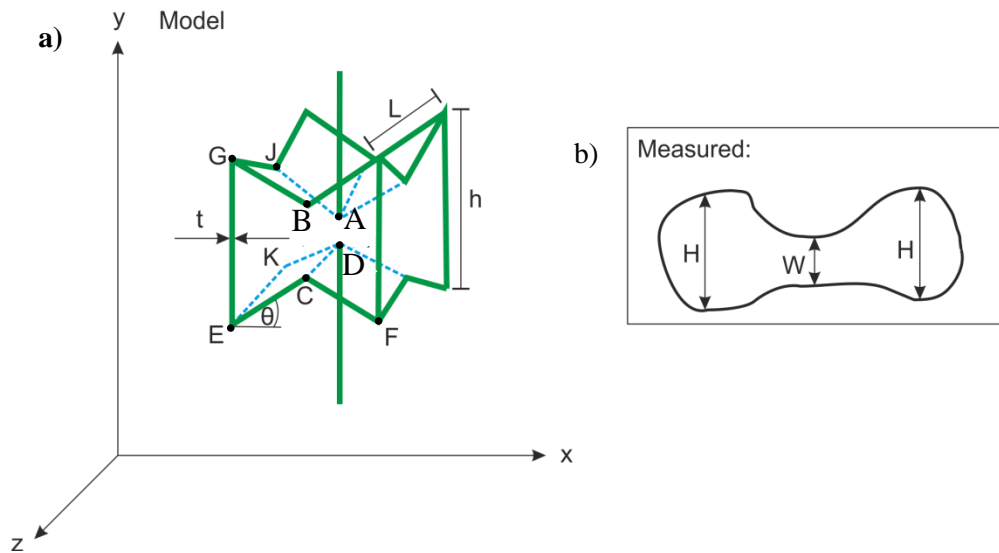
Figure 2.12: Diagrammatic representation of **a)** three-dimensional geometry of an auxetic pore and **b)** two-dimensional geometry of the same auxetic pore (adapted from [158]).

2.2.3.2.1 Conventional Model

For conventional foams reported in Figure 2.12, the cell length can be calculated using the following equations [158]:

Maximum:	$AD = h + 4L \sin\theta$	(Equation 2.1)
Minimum:	$BC = h + 2L \sin\theta$	(Equation 2.2)
Average:	$y = h + 3L \sin\theta$	(Equation 2.3)

and the cell width at any point can be taken as [158]:

Normal:	$EF = 2L \cos\theta$	(Equation 2.4)
Average:	$x = 2L \cos\theta$	(Equation 2.5)

2.2.3.2.2 Auxetic model

For auxetic foams the cell length can be given by the following equations [158]:

Maximum:	$GE = h$	(Equation 2.6)
Minimum:	$BC = h - 2L \sin\theta$	(Equation 2.7)
Average:	$H = h - L \sin\theta$	(Equation 2.8)

the auxetic cell width can be obtain by [158]:

Normal:	$EF = 2L \cos\theta$	(Equation 2.9)

and the auxetic mid-plane waist height is calculated using [158]:

Maximum: $JK = h - 2L \sin\theta$ (Equation 2.10)

Minimum: $AD = h - 4L \sin\theta$ (Equation 2.11)

Average: $W = h - 3L \sin\theta$ (Equation 2.12)

It is important to highlight that although these models allow the cell geometry to be estimated, real samples contain numerous cellular and structural anomalies. A foam specimen contains a variety of cell shapes with four to six sides [158] and a wide range of cell sizes, some of which are so small that deformation is not possible and therefore act as junction points within the foam. It was also observed that the foams tested were slightly elongated due to the foam manufacturing process [158]. While each of these anomalies discredits somewhat the proposed mathematical model, the model should not be disregarded, since it can still provide insightful information for the cell geometry.

2.2.3.3 Effects of the cell size

The material porosity and, therefore, the cell-size is a further factor affecting the auxetic conversion process. Wang *et al.* [134] tested three polyurethane foams with porosity of 20, 65 and 100 PPI. In order to explore the effects that the pore size has on the Poisson's ratio, Scott reticulated 100 PPI white foam was subjected to a screening process where samples were manufactured at temperatures between 120°C and 280°C and processing time between 5 and 21 min at a volumetric compression ratio of approximately 2.5, yielding a total of 48 samples. The data are shown in Figure 2.13.
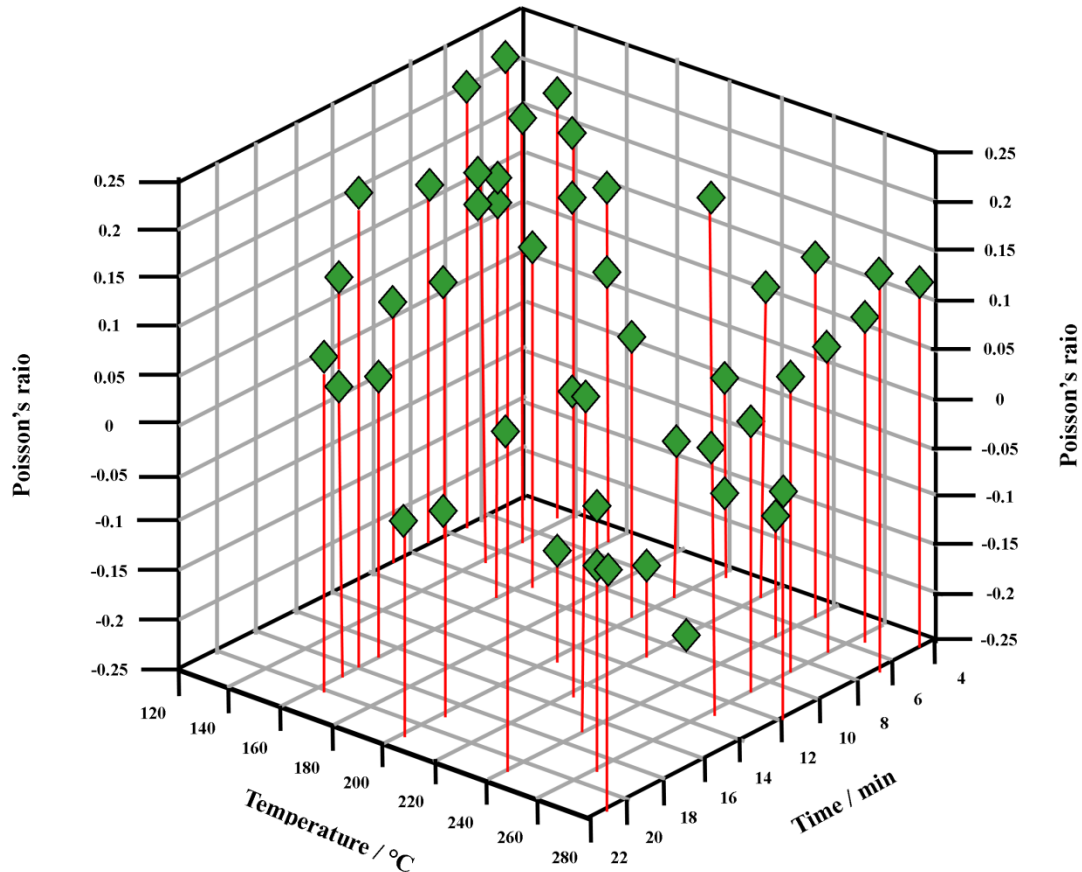
Figure 2.13: Comparison of the 100 PPI samples manufactured in different conditions for the screening process to test the effects of pore size, adapted from [134].

It was found that for the 100 PPI foam, the optimal processing parameters for creating negative Poisson's ratio foams were a heating time between 8 and 12 min, at a temperature between 210°C and 230°C. Whereas the best conditions for the 20 and 60 PPI foam specimens were a heating times of 17 and 13 min and a temperature of 170°C and 190°C, respectively. These results show that smaller cell size foams require higher temperatures and shorter heating time.

2.2.3.4 The effect of the applied volumetric compression ratio

The *volumetric compression ratio* (R_c) is defined as the ratio between the original volume (V_o) and the final volume (V_f) after the auxetic conversion of the specimen [13]. The volumetric compression ratio plays a critical role in the auxetic conversion process and it has been observed that failure to apply a value within the optimum range can result in an unsuccessful conversion process. It has been reported in the literature that different types of materials exhibit different maximum volumetric compression ratio values. For example, Lakes [103] stated that for the open-cell polymeric foam the optimal volumetric compression ratio was between 1.4 and 4.0. More recently, Choi and Lakes [134, 161] reported that in order to have a successful auxetic conversion the volumetric compression

ratio had to be between 2 and 5. Although optimum compression ratio ranges have been suggested, it has to be remembered that the optimum permanent compression to achieve the best negative Poisson's ratio depends on the initial foam density and appears to have a purely geometrical origin, as the same negative Poisson's ratio value was observed for metallic and polymeric foams with the same relative density [161]. The majority of R_c values reported in the literature occurred within this range [10, 17, 24, 129, 130, 162], however experiments with greater volumetric compression ratios have also been reported [133] but only with respect to mechanical testing and not volumetric effects.

The compression ratio has also been described in terms of volumetric percentage change [24, 163], and in comparison with the volumetric compression ratio, no optimum percentage range has been outlined. However, from estimates given in the literature, the optimal percentage range may be approximated as being between 30% and 94% of the original volume. Converting these values into volumetric compression ratios, it can be found that the optimal range is between 1.43 and 16.1. While this range seems too wide to be considered as a useful optimal range, it is in agreement with the commonly accepted 2 to 5 range previously defined by Lakes [134, 161], which as a percentage equates to 50% - 80% of the original volume.

The volumetric compression ratio has been suggested to be the most important and influential parameter in the auxetic fabrication [106, 107, 130, 134], as it has been observed to influence both the auxetic microstructure and the mechanical properties of the foam. However, the volumetric compression ratio is also susceptible to the effects of other variables, such as temperature and pore size. For example, Choi and Lakes [131] reported that when a large volumetric compression ratio is applied together with time and temperature values outside the optimum conditions, the ribs in the foam become stuck together. It has been observed that applying smaller volumetric compression ratios produces samples with a very low negative or almost positive Poisson`s ratio values [129]. However, Wang *et al.* [134] noted that, within the optimum volumetric compression range of 2 to 5, specimens with lower volumetric compression ratios were found to exhibit greater negative Poisson's ratios. This behaviour was once again observed by Bianchi *et al.* [130], where it was further noted that lower volumetric compression ratios produced greater tangent modulus values.
From the literature [106, 107, 129, 130, 134], it is clear that there are many variables influencing the manufacture of auxetic foams, such as the composition of the material, its relative density and cell size, the processing temperature and heating-time, the humidity and the volumetric compression ratio applied [131]. There is still much debate regarding which are the key factors influencing the process. Wang *et al.* [134], for example, stated that the

main physical parameters influencing the auxetic transformation process are the volumetric compression ratio, the processing temperature and the heating time. However, Bianchi *et al.* [106, 107, 130] consider only the volumetric compression ratio as the main parameter responsible for a successful conversion, with the other parameters acting as secondary influence. Although an exact relationship between the fabrication parameters is unknown, some attempts have been to identify relationships between the fabrication parameters and material properties (density, Poisson's ratio, stiffness and energy dissipation) [106], but it is clear that further work is required in this area.

2.2.4   Foam structure and deformation mechanism

The cellular structure of conventional polymeric foams is well-known, and during the auxetic conversion process the cellular structure completely changes and therefore it is fundamental to understand the deformation mechanisms involved. In order to understand the counterintuitive behaviour of auxetic foams, numerous researchers have analysed how the cell ribs and the foam structure changes under compression and tensile loading and proposed numerous theories that will be summarised below.

2.2.4.1 Bow-tie or re-entrant model

In the earliest studies reported by Lakes [103] the permanent inward protrusion of the cell ribs during the conversion process forming a 'bow-tie' structure was highlighted; this structure is also known as re-entrant cellular structure. Further work by Lakes confirmed that the performance of the auxetic foams is a result of the rib behaviour [14]. Following these observations, the re-entrant cell model shown in Figure 2.14 was established, where according to this model, the application of a tensile load results in deformation of the cell ribs through bending, which in turn leads to the cells unfolding to their original structure. In Figure 2.15, when a tensile load is applied in the *x*-direction, nodal points A and B expand further apart attempting to achieve the original hexagonal geometry of the cell, while points C and D maintain a fixed position; the expansion of A-B produces an increase in volume.
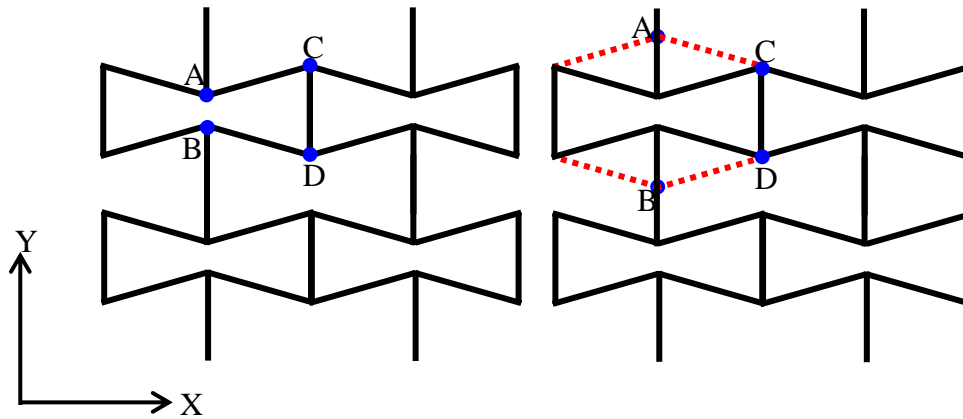
Figure 2.14: Model describing the rib behaviour under tensile loading, where blue circles represent nodal points. Image adapted from Lakes *et al.* [14].

This behaviour however is anisotropic, as loading in the y-axis will not yield the same results as loading in the *x*-axis [158]. Conversely, Lakes stated that although some materials experienced anisotropic behaviour not all auxetic materials are anisotropic [103, 158]. To date, the effect of the cell units design parameters (rib length, rib thickness and internal angle) on 2D unit cell models, have been extensively investigated [128, 159, 164-168]. Among these investigations [159], a set of equations have been proposed that numerically predict the in-plane Poisson's ratio and Young's modulus relative to honeycombs cellular structure experiencing linear-elastic deformation. By considering the unit cells presented in Figure 2.16, when a load is applied in either the X or Y direction, the cell walls bend.
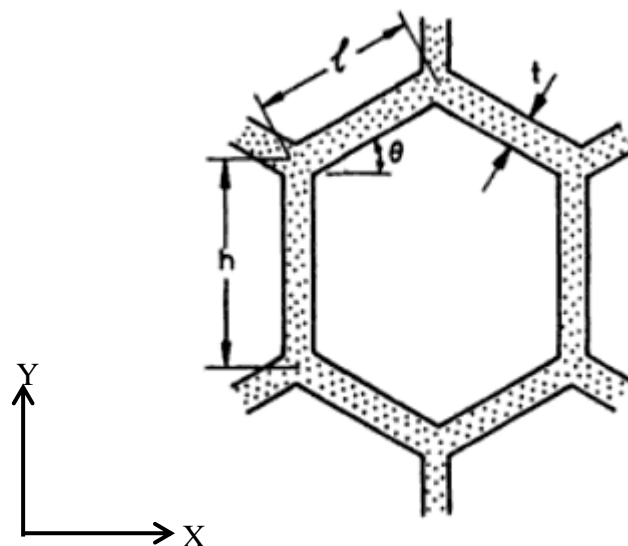
Figure 2.15: Diagrammatic representation of a honeycomb cell [159].

By measuring the magnitude of deflections caused by the bending, the Poisson's ratio and Young's modulus can be calculated by:

$$\frac{E_x^*}{E_s} = \left(\frac{t}{l}\right)^3 \frac{cos\theta}{(\frac{h}{l} + sin\theta)sin^2\theta}$$

(Equation 2.13)

$$\frac{E_y^*}{E_s} = \left(\frac{t}{l}\right)^3 \frac{(\frac{h}{l} + sin\theta)}{cos^3\theta}$$

(Equation 2.14)

$$v_{xy}^* = \frac{cos^2\theta}{(\frac{h}{l} + sin\theta)sin\theta}$$

(Equation 2.15)

$$v_{yx}^* = \frac{(\frac{h}{l} + sin\theta)sin\theta}{cos^2\theta}$$

(Equation 2.16)

where, E_x* E_y* are the Young's moduli in the x and y axis, $v_x{}^*{}_y$ and $v_y{}^*{}_x$ are the Poisson's rations in the x and y-axis and E_s is the modulus of the cell wall material, respectively.

2.2.4.2 Missing rib model

Smith *et al.* [128] proposed *the missing rib foam model* because, at the time of publication, they [128] believed that the models proposed by other groups were satisfactory in describing the stress-strain behaviour of conventional foams but were limited in describing the auxetic behaviour. In this model the cellular internal angles are not subjected to angular changes, but a fraction of the cell ribs are removed, as shown in Figure 2.16. This model is best employed in the calculation of strain-dependent Poisson's ratio function, opposed to small-strain Poisson's ratios, as defined by Berthelot [169]. The advantage of this model is that both auxetic and conventional materials can be described using realistic geometries and stress-strain behaviours could be predicted slightly more accurately. The disadvantages of this model result from both the assumption that needs to be made (real world foams contain already broken ribs which are randomly distributed) and its inability to accurately describe the compression/heating effects on fabrication. From this model Smith *et al.* [128] suggested that during several scenarios of sample fabrication, it is plausible to presume that there are multiple mechanisms causing the auxetic conversion, *i.e.*, concaved re-entrant cells and missing ribs.
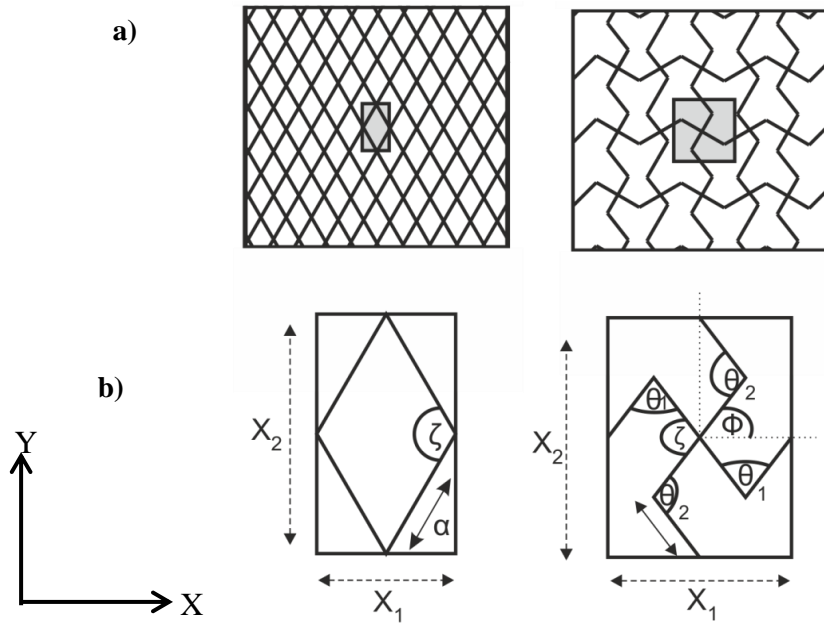
Figure 2.16: Schematic of the missing rib foam model showing **a)** an intact conventional foam structure and the cut version with cell units shaded, **b)** more detailed version of selected cells for both intact and cut versions alongside their geometry parameters (adapted from Smith *et al.* [128]).

2.2.4.3 Rigid triangle model

In 2005 Grima *et al.* [163] proposed a further model to explain the 2D behaviour of the auxetic foams. This model assumed that the microstructural changes induced during the compression/heating stage of the fabrication preserved the cell joint geometry, whilst the rib lengths were subjected to the main deformations, resulting in buckling. Furthermore, this model assumed that due to the increased thickness at the cell vertices it is possible to treat the joints as rigid, thus allowing the behaviour to be described in terms of beam mechanics, rotation and perfectly rigid equilateral triangles; although, in reality the ribs, joints or microstructure are not perfect. When the foam is loaded, the model predicts that the triangular joints rotate to return to their original arrangement causing the rib to twist and unfold producing a volumetric expansion, as shown in Figure 2.17. Based on this method the auxeticity depends mainly on the joint rigidity and the flexibility of the connection ribs, with other factors being less influential. Grima *et al.* [163] believe that this type of model presents a dominant mechanism responsible for the auxetic behaviour found after fabrication. Since 2005, several additional rotating geometry models have been proposed including: stretching squares [170], tetrahedra [171], generic triangles [172-174], squares [175-178], rectangles [177, 179], parallelograms [180], rhombi [181] and stars [182].
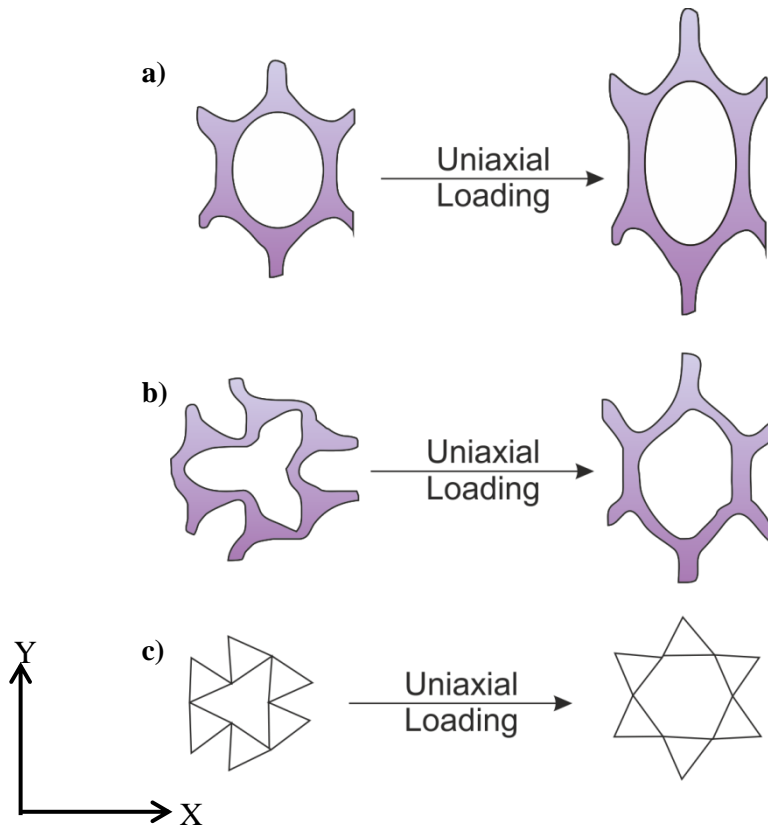
Figure 2.17: Steps in the rigid triangle model: **a)** hexagonal honeycomb model for a conventional foam, **b)** rotation of rigid units model for auxetic foams and **c)** ideal model for the rotating rib model where joints are shown as perfect rigid equilateral triangles (adapted from Grima *et al.* [163]).

2.2.4.4 Heterogeneous models

Although several homogenous 2D models have been suggested to explain auxetic behaviour in auxetic foams, these geometric structures often bear little resemblance to the true heterogeneous structure. To rectify this, Gaspar *et al* [183], modelled heterogeneity of auxetic foams by adapting mean field approximations of granular mechanics. This approach identified that the presence of a heterogeneous structure can result in a negative Poisson's ratio locally while additionally quantifying the differences in material properties, failure modes and isotropy between a homogeneous and heterogeneous materials. The authors however reported a concern that even if the models using mean field theory agreed with experimental results, it is unclear whether the model parameters in the model accurately reflect the microstructure of the foam.

Alternatively, Horrigan *et al.* [184] modelled heterogeneity of an auxetic structure by first constructing an arrangement of 2D honeycomb grids which were then subjected to two different optimisation techniques: (*i*) a genetic algorithm (GA) and (*ii*) a differential evolutionary algorithm (DE). Although both techniques produced optimal heterogeneous negative Poisson's ratio, a different solution was obtained. Unlike the DE technique which

explores a range of possible surface solutions based on pre-determined user variables (rib length, node distribution) coupled with manual evaluation through finite element analysis (FEA), the GE technique applies range changes to the original structure, creating a number of 'offspring'. These new geometries were then assessed (using FEA), with respect to user inputted criteria, where the most optimal structure was then selected and once more randomised creating more offspring until reaching the allocated offspring limit. It should however be noted that due to the iterative process, the final structure did not necessarily exhibit the greatest negative Poisson's ratio. By using the optimisation techniques to produce heterogeneous structures, it was found that a negative Poisson's ratio can be created simply be adding disorder to a positive Poisson's ratio structure; these subtle structural changes however must be of a particular type (not yet quantified). This observation was further confirmed by Gaspar *et al* [185, 186] and Koenders [187].

A similar behaviour was described by Blumenfeld and Edwards [188, 189], where they argued that within an arrangement of 'auxetons' (Figure 2.18) of irregular sizes, shapes and orientation, the global auxetic behaviour was the resultant of local folding and rotation of the 'auxetons' when stressed.
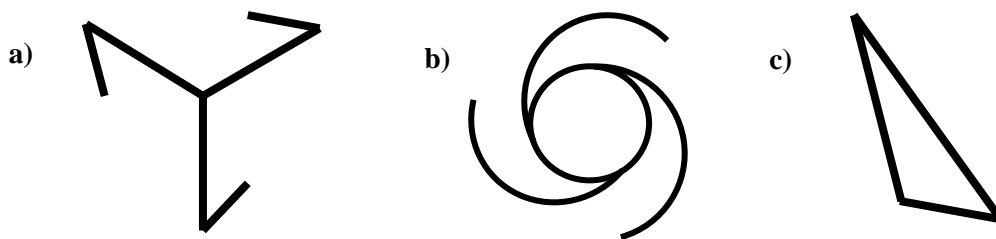
Figure 2.18: Examples of auxetons: **a)** three-armed star, **b)** folding element and **c)** a rigid triangle. Adapted from Blumenfeld and Edwards [188, 189].

2.2.4.5 *Three-dimensional model*

Although numerous models in 2D have been suggested and accepted, a 3D model has yet to be agreed. Numerous authors have attempted to produce a 3D model starting from the 2D model and applying to it an extra axis utilising dodecahedrons and tetrakaidecahedrons [163, 190-197]. This approach is acceptable for a simplistic analysis, such as those performed by FEA, as the overall auxetic foam structure and behaviour are reverted to a basic level, where little to no variation to the structure is considered.

In order to determine the true mechanisms of the auxetic foams, some researchers have begun to study cell interactions in 3D analysing a small area and applying the results to the whole specimen body. One such study was undertaken by Chan and Evans [158, 192] using

microscopy to examine the microstructure and deformation mechanisms of conventional and auxetic materials. They observed that applying a compressive or tensile load the cell ribs in both conventional and auxetic foams undergo a range of deformation, with the dominant deformation mechanism dependent on the loading type and the foam cell structure. Conventional foams in compression deform primarily by flexure and buckling of the ribs when high strains are applied. During tensile loading, the ribs perpendicular to the load also deform by flexure. When a tensile load is applied, the cell ribs of conventional foams deform through a combination of hinging, stretching and flexing mechanisms. Failure finally occurs as a result of tensile fracture. In auxetic foams, it was found that compressive and tensile loading produce the same deformation mechanisms observed in conventional foams, with the addition of rib rotations. Based on these observations, Chan and Evans [158] suggested that, as a general rule, auxetic and conventional foams under compression are dominated by flexure and that under tensile loading they are controlled by flexure and stretching.

Although each of the current models provides some value if not limited insight, these models are too simplistic, often requiring the presence of perfect microstructure geometry [196]. However, should various aspects of the previously suggested models be considered alongside imaging techniques such as computed tomography (CT), a more accurate model could be produced. Unlike optical microscopy and SEM, CT is capable of producing true three-dimensional data, not only of the surface but throughout the volume of a body. For auxetic foams this is extremely important, as the auxetic ribs deform in three-dimensions. CT is capable of analysing large samples, but the achievable resolution is affected by both the area to be scanned and the type of equipment employed. CT is a non-destructive technique and therefore allows studying the changes in microstructure under various experimental conditions. CT can also be utilised in the application of finite element analysis, an area rarely studied in current literature. An example of this work can be seen in Figure 2.19, where a real world auxetic foam sample of 45 PPI at a volumetric compression ratio of 4.88 was scanned, meshed and analysed in an attempt to understand localised rib movement under tensile loading conditions. Some initial work using the CT technique has been reported by Elliott *et al.* [198], Gasper *et al.* [199], McDonald *et al.* [132] and Lisiecki *et al.* [199].
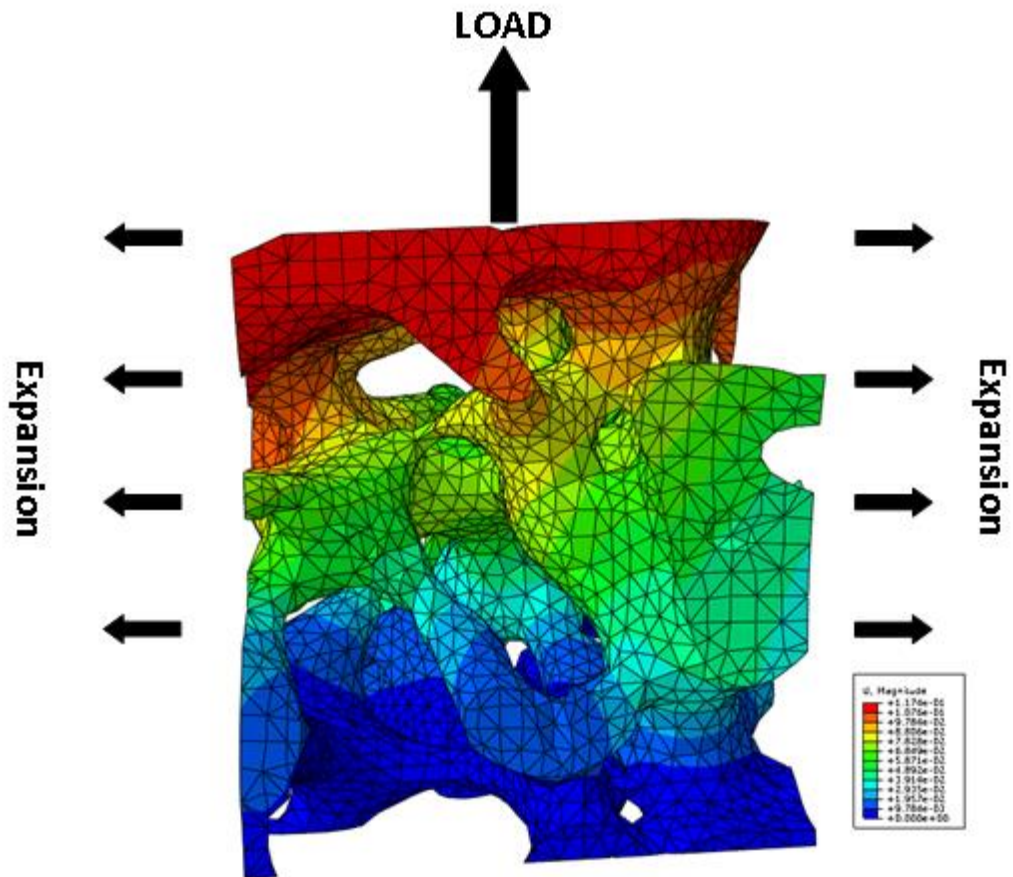
Figure 2.19: A finite element sample (2.2 mm^3) of an auxetic foam of 45 PPI, demonstrating the response to tensile loading conditions, undertaken by Richard Critchley at the University of Southampton.

2.2.5 Mechanical properties of auxetic foams

Understanding the mechanical properties of a material is fundamental to highlight its strengths and weaknesses and to evaluate any possible application. It has been reported that the conversion process of conventional polymeric and metallic foams into auxetics enhances the mechanical properties compared to the starting material [119]. Many of the observed improvements in mechanical properties are directly linked to the change in the cellular structure and the increase in density of the material due to the volumetric compression ratio applied [10, 14, 16, 158]. The increase in mechanical properties has been observed in both isotropic and anisotropic materials [13] and has been noticed to affect the shear resistance [10-15], the indentation resistance [10, 12, 13, 16-21], the fracture toughness [10, 12-14, 16, 22, 23], the shear modulus [13, 14], the stiffness [22, 24], and acoustic dampening [10, 14, 16, 25, 26],

The improvements in mechanical properties observed after the auxetic conversion have led numerous researchers to consider many possible applications for auxetic foams ranging from smart filtration systems [12] to protective sports equipment [16]. The mechanical

enhancements observed are due to the changes to the four elastic constants of the material: Young's modulus (E), shear modulus (G), bulk modulus (K) and Poisson's ratio (υ), which respectively measure stiffness, rigidity, compressibility and volumetric change under strain [12]. For these constants there is not a discernible characteristic length scale which implies that microstructural dimensions smaller than 1 μm could exhibit a negative Poisson's ratio [103]. The following equations show how the elastic constants are related to each other and why altering one of the elastic constants will affect the others [105].

$$E = 3K(1 - 2\upsilon)$$ (Equation 2.17)

$$G = \frac{E}{2(1+\upsilon)}$$ (Equation 2.18)

$$K = \frac{E}{3(1-2\upsilon)}$$ (Equation 2.19)

$$\upsilon = \frac{1}{2}\left(\frac{3K-2G}{3K+G}\right)$$ (Equation 2.20)

These equations also allow an understanding of the enhancements in properties exhibited by auxetic materials. The two main mechanical properties of auxetic foams studied in the literature have been: *hardness* (indentation) and toughness (energy absorption) and they will be described below. Both properties are well-established as the primary applications of the conventional foams are packaging and cushioning [131].

2.2.5.1 Indentation of auxetic foams

Lakes first studied the effects of indentation on an auxetic foam by assuming a localised pressure distribution, where the pressure is proportional to $(1-\upsilon^2) / E$ [103, 200]; from this equation it is clear that for a material with a Poisson's ratio close to −1 the indentation is very difficult. At the same time this material becomes extremely compressible because the shear modulus exceeds the bulk modulus. This behaviour is due to the connection between the bulk modulus, the shear modulus and the Poisson's ratio via equation:

$$K = \frac{2G(1 + \upsilon)}{3(1 - 2\upsilon)}$$ (Equation 2.21)

Alternatively, a material with a Poisson's ratio approaching 0.5, *i.e.*, rubber is incompressible because its bulk modulus is greater than the shear modulus.

In addition, Lakes studied the effects of indentation on a wrestling mat made of elastomeric foams ($\upsilon \approx 1/3$) [11]. He assumed that the indentation could be described as indentation rigidity:

$$\frac{P}{w} = \frac{E}{2a(1-v^2)}$$

(Equation 2.22)

where a is the radius of a circular localised pressure, P is the localised pressure and w is the indentation depth, as described by Timoshenko [200]. The indentations experienced by the wrestling mat were further analysed for small and large impacts [11]. For small impacts (narrow) it was assumed that the circular pressure distribution could be taken as an elastic half space yielding:

$$\left[\frac{F}{u}\right]_{narrow} = \frac{Ga_n}{(1-v)}$$

(Equation 2.23)

where F is the indentation force, u and a_n are the maximum displacement and the radius respectfully. For impacts greater than the mat thickness (wide), it is assumed that both compression and force are uniformly distributed, with the Poisson's ratio effect controlled giving:

$$\left[\frac{F}{u}\right]_{wide} = \frac{\frac{Ga_{w2}}{2H(1+v)}}{(1-2v)}$$

(Equation 2.24)

where H is the mat thickness.

From this study, Lakes suggested that the continuum theory of elasticity was probably not the best theory to describe the auxetic behaviour and proposed to use the Cosserat theory of elasticity [201, 202], that takes into account both the maximum stresses and a natural length scale to allow microstructural size to be incorporated into the prediction of failure [11]. Evans and Alderson [12] confirmed the theory presented by Lakes treating the indentation as an effect of uniform pressure distribution that for an isotropic material can be described as proportional to $[(1-v^2) / E]^{-1}$ (Figure 2.20). By applying the classic theory of elasticity, it can be seen that the indentation resistance increases towards infinity for a negative Poisson's ratio, tending to the limiting value of -1.
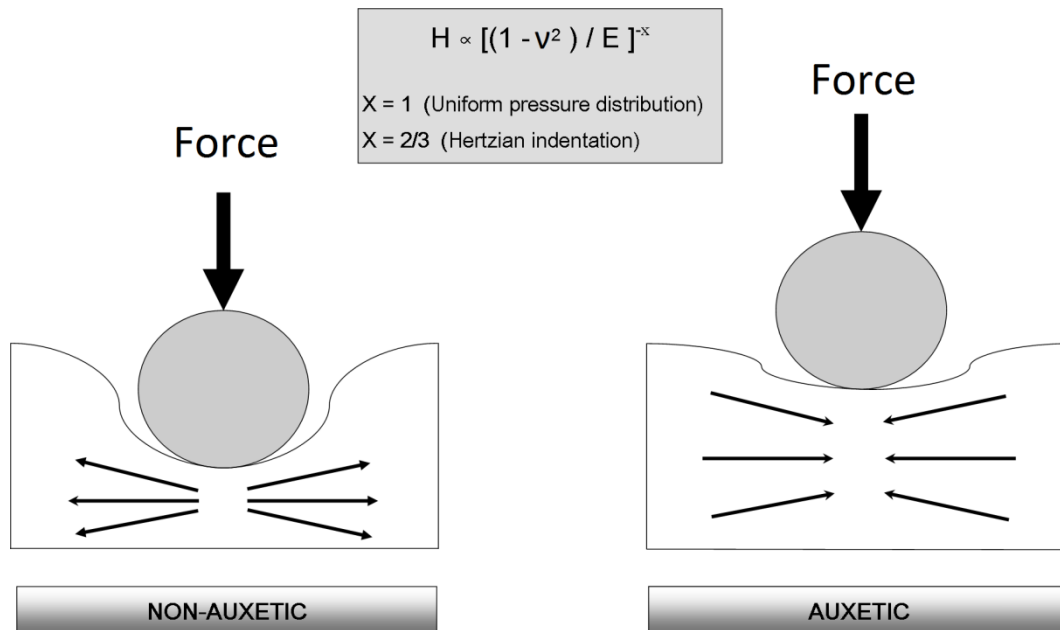
Figure 2.20: Reaction of conventional and auxetic materials to indentation loading, adapted from [12].

Furthermore, Evans and Alderson [12] presented a relationship to describe how the elastic constants affect one another with respect to the shear modulus (G):

$$G = \frac{3K(1-2v)}{2(1+v)}$$

(Equation 2.25)

Which when re-written in terms of bulk modulus K, yields Equation 2.21

When the original literature [103] is compared to the work of Evans and Alderson [12], it can be seen that the equation presented in the later literature is set to the power of −1, a value unaccounted for in the original work. The discrepancies continue when assessing the relationship between the elastic constraints, with the work presented by Lakes [103] lacking of a 3 in the denominator, compared to the equations reported by other authors [12, 203]. Although it is unclear why these discrepancies occurred, they are likely the resultant of a typing / publishing error and as such the work by Evans and Alderson [12] and the equations that they present should be considered to be correct as they are supported by other authors [203].

In a more recent study, Argatov *et al.* [204] explored the influence of a negative Poisson's ratio on local indentation from a continuum mechanics viewpoint for isotropic homogenous materials. In this study a selection of indenter geometries and scenarios were explored with regard to quasi-static and dynamic loading conditions. For each of the indenter scenarios studied, the change in indentation compliance, (which at its simplest definition is given as

normal contact force applied to the indenter, over the corresponding displacement of the indenter) was explored with respect to Poisson's ratio. In each of the scenarios explored it was found that as the Poisson's ratio approached it lowest limit of −1 indentation compliance converged towards zero, indicating an increase in indentation resistance. Furthermore it was observed that the friction at the contact interface between the indenter and the surface of an elastic medium increases indentation resistance.

2.2.5.2 Toughness and energy dissipation

Despite the fact that a number of researchers have studied the effects of hardness upon auxetic foam, many others have proceeded to look at the effects that the auxetic foams have on toughness. Toughness is an important mechanical property for a polymeric porous material since it determines the amount of energy absorption of the foam per unit volume, and can be determined by taking the integral of a stress-strain curve, which is given as:

$$\frac{\text{Energy}}{\text{Volume}} = \int_{0}^{\varepsilon_f} \sigma d\epsilon$$

(Equation 2.26)

where ε and ε_f are the strain and the strain upon failure and σ is the stress [159].

In 1987 Lakes [103] observed that the Poisson's ratio affects the toughness of the auxetic materials and that as the Poisson's ratio approaches −1, the material is expected to become extremely tough. Using the critical tensile stress:

$$\sigma = \frac{\pi E T}{2r(1 - v^2)}$$

(Equation 2.27)

where T is the surface tension, E the Young's modulus and 'r' the circular crack radius [11, 103, 205], this behaviour can be explained. Further to elastic constraints, the material toughness and the Young's modulus are also affected by both its non-linear properties and structural aspects [14]. This initial work was continued by Lakes and Choi [131] where the differences were outlined between conventional and auxetic foams in terms of material toughness. It was observed that re-entrant foams have an initial lower stiffness (Young's modulus) compared to conventional ones, but as a result of non-linear behaviour during a large deformation, the energy density is higher. Furthermore, the energy absorption can be increased by using conventional foams with higher densities; this however is not always desirable as it results in a higher stiffness [18, 131]. In order to understand the full effect of energy absorption for auxetic and conventional foams, Lakes and Choi [131] studied the behaviour of foams subjected to a range of volumetric compression ratios under compressive

and tensile stresses. They found that for each of the re-entrant specimens tested, toughness increased with an increase in volumetric compression ratio.

In an alternative study, Bezazi and Scarpa [22] studied the material toughness under quasi-static cyclic loading via a fatigue test. It was observed that the auxetic foams exhibited significantly higher stiffness degradation, energy absorption and lower rigidity loss over a large number of cycles when compared to their conventional counterparts. For N number of cycles, the energy dissipated per unit volume (E_d) is given by:

$$E_d = \int_{\varepsilon_{min}}^{\varepsilon_{max}} \sigma d\varepsilon$$

(Equation 2.28)

where ε_{min} and ε_{max} are the minimum and maximum strain.

The graphical data reported in Figure 2.21, where loading levels 'r' are defined as [206]:

$$r = \frac{U_{max}}{U_r}$$

(Equation 2.29)

where U_{max} and U_r are the maximum displacement at a particular level and at failure (measured in mm), show a greater area and therefore greater energy absorption for the hysteresis loops of auxetic foams; which with support of the stress-strain curves of static testing demonstrates the increase in resistance to failure and mechanical resilience. The hysteresis cycle areas for both auxetic and conventional foam increased with the load applied, where on average auxetic foams dissipate 2.4 times the amount of energy dissipated by conventional foams for the first cycle under different loadings. Furthermore, Bezazi and Scarpa [22] observed that there was different stiffness degradation behaviour for tension-tension and compression-compression loading, however, the difference between each could not be directly linked to the energy absorption.
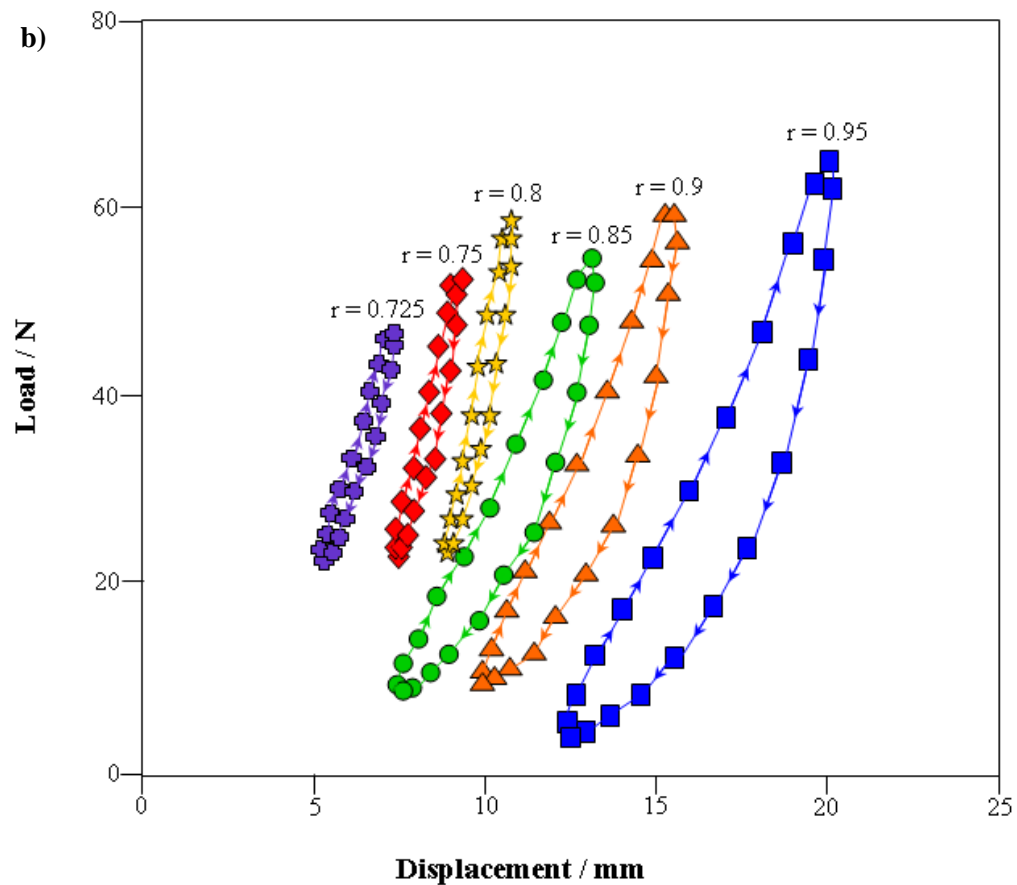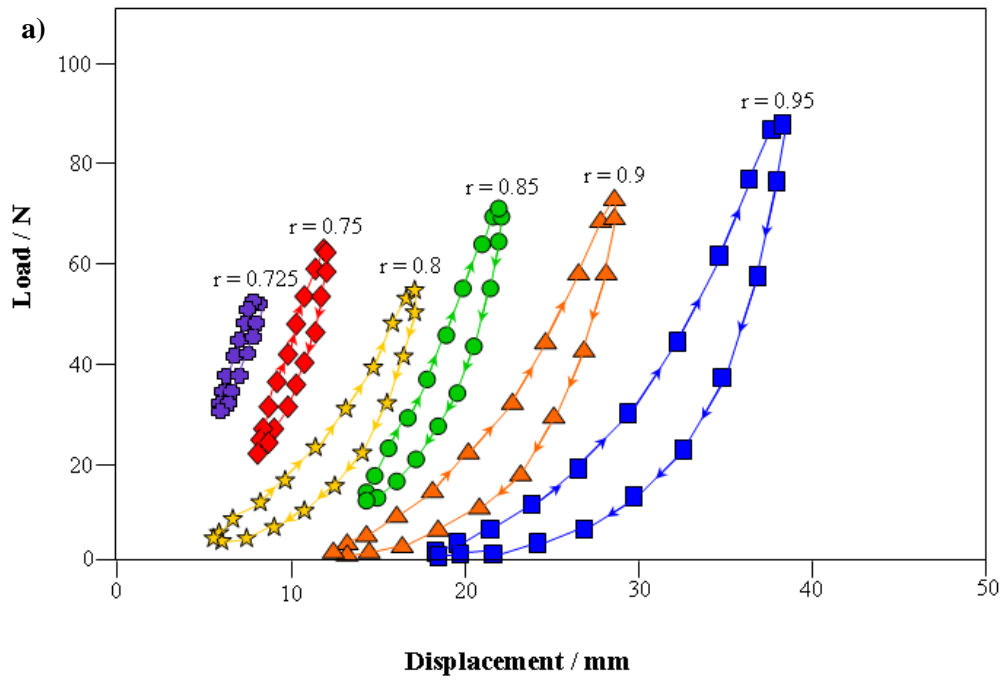
Figure 2.21: Load *vs*. displacement for different levels of loading for: **a)** auxetic and **b)** conventional foams, adapted from [22].

Bianchi *et al.* [106] continued to study the energy dissipation during quasi-static and cyclic loading under tension. They observed that when the negative Poisson's ratio approached zero the energy dissipation decreased, albeit there was no evident presence of clusters

between batches nor was there a statistically significant correlation. Furthermore, it was reported from the results of the quasi-static cyclic tests that the conventional foam exhibited greater energy dissipation than the average value of the auxetic version, with energy dissipation up to an order of magnitude higher than the auxetics. The analysis carried out in their work highlighted a different behaviour than that reported by Bezazi and Scarpa, where they reported that the energy dissipation of conventional foam was lower than the auxetic foam (based on an average result). The reason suggested for this was due to the difference in testing conditions (e.g., quasi-static tensile without preload versus dynamic compressive preload lest).

To further understand the mechanical properties of auxetic foams, Bianchi *et al.* [107] studied how the energy dissipation during both tension and compression is affected when the foam is subjected to a four phase fabrication process, as described in Section 2.1.2. The data obtained in this study is shown in Figure 2.22. The most interesting observation is that the energy dissipation is on average greater for second phase auxetics than for first phase auxetics, although first phase auxetic experienced far less scattering of the results. It was further observed, that on average, the specimens in the returned phase specimens exhibited a lower mean value of energy dissipation compared to its original conventional state, both in terms of compression and tension loading. The authors further report that the mechanical stiffness of the auxetic specimens up to one order of magnitude lower when compared to the conventional and returned foams as also confirmed by Smith et al [21].
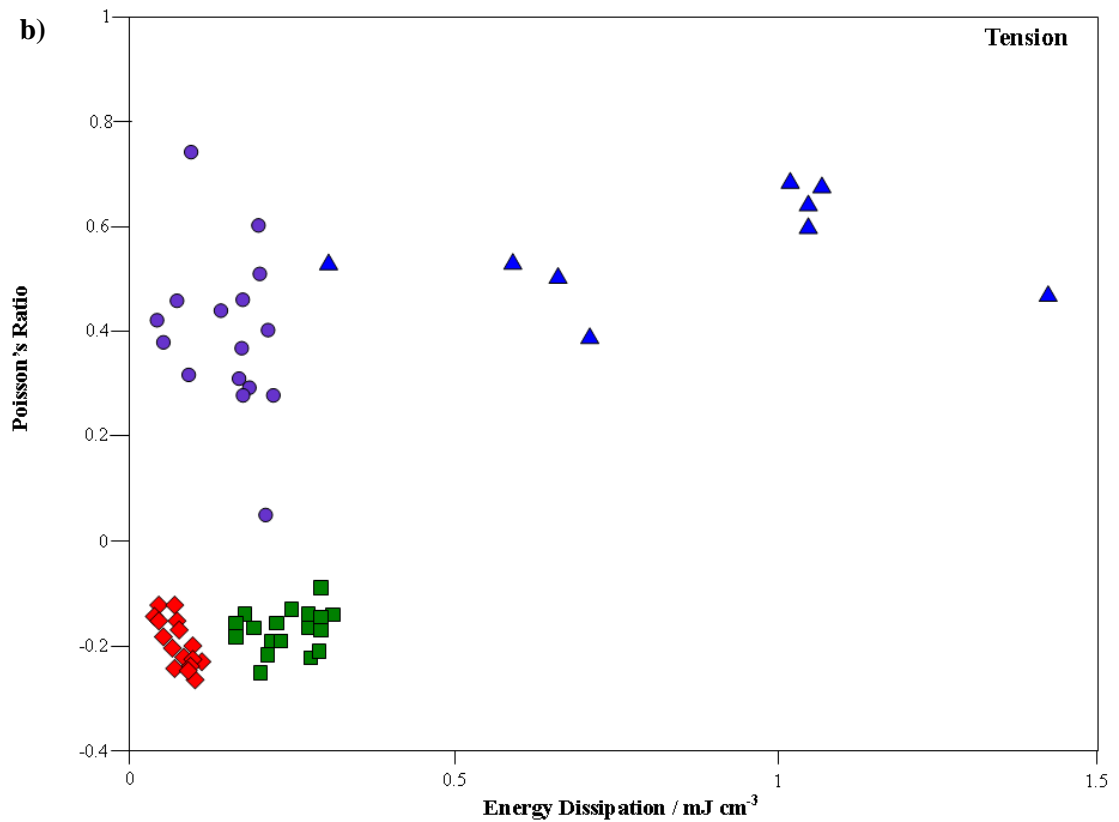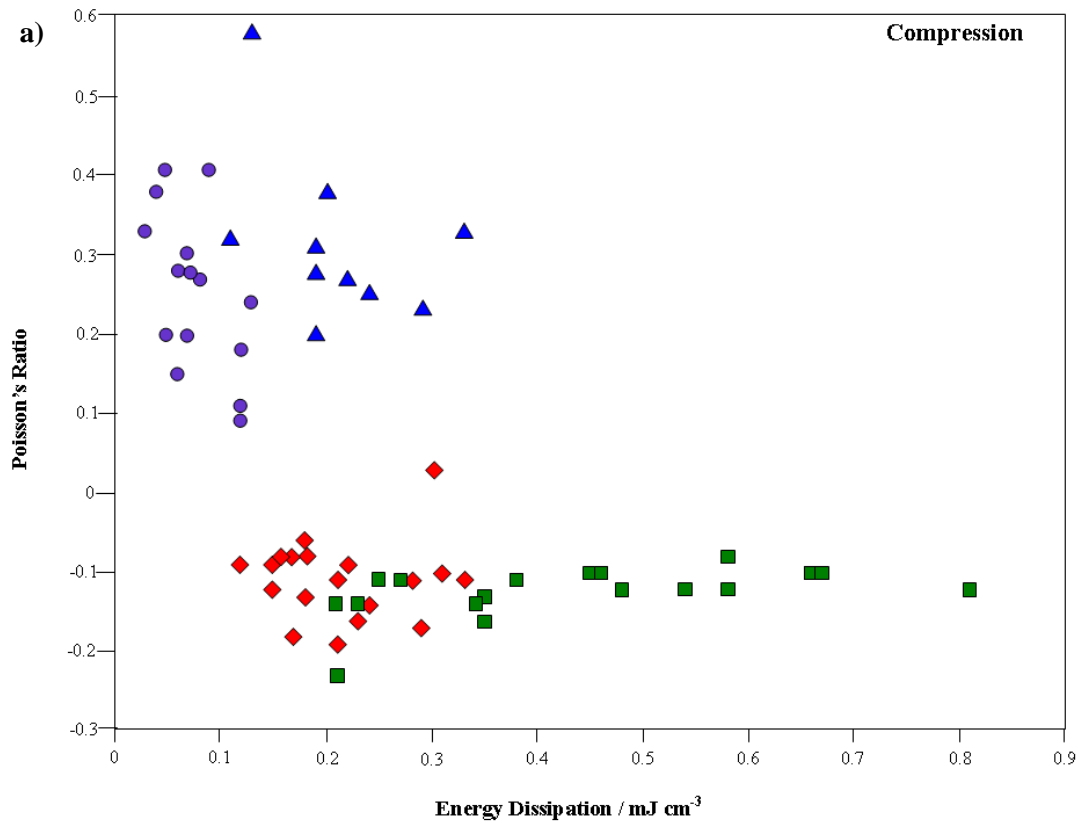
Figure 2.22: Energy dissipation under: **a)** compression and **b)** tension for as received (▲), returned (●), first auxetic (♦) and second auxetic (■) phases for polyurethane foam, adapted from [107].

In addition to quasi-static cyclic loading, Scarpa *et al.* [24] studied the energy absorption of conventional, auxetic and iso-volumetric materials at different strain rates under tensile loading. Strain rates of 8, 10 and 12 s^{-1} and instrument head displacements of 120, 150 and 180 mm s^{-1}, respectively, were applied to 19 mm diameter, 15 mm long samples [24]; the small sample size was employed to achieve the desired strain rate. From the testing, it was observed that by increasing the tensile strain, the Poisson's ratio converged towards zero before becoming positive. Furthermore, the authors also noticed that for all the auxetic samples the mechanical properties, *e.g*., mechanical strength and stiffness, were influenced by the fabrication method and that the auxetic foams had an order of magnitude increase compared to the conventional foams.

Similar work was undertaken by Scarpa *et al.* [129] where energy absorption was studied at strain rates of 15 and 38 s^{-1} (comparable to velocities of 1.5 and 3.8 m s^{-1}, respectively). They noticed that during dynamic crushing the auxetic foams showed a clear time-load history while the conventional foams failed to demonstrate any form of loading resilience. This behaviour can be associated with micro-inertia (an extension of the classic continuum mechanics theory that includes spatial gradients of acceleration to be considered into motion equations [207]), localisation effects and strain rates effect the dynamic crushing behaviour within the foams [17, 18, 129, 159]. Furthermore, the auxetic specimens were found to have a low sensitivity to strains for stresses lower than 0.54 MPa and once this value was exceeded, the specimen began to exhibit stiffening effects during the densification process. Lisiecki *et al.* [154] have also studied the energy dissipation of auxetic foams, but with a focus on different fabrication parameters including, fabrication process iterations, sample size, and volumetric compression. Utilising an MTS810 machine equipped with a 10kN force transducer, samples were initially compressed three times to 30% strain before being compressed to 77% strain in the *z*-axis, at displacement rate of 100 mm s^{-1}. From the tests it was shown that the auxetic sample with the highest volumetric compression ratio demonstrated the highest stiffness and widest hysteresis loops.

To better explore the variance of the samples, each of the tested samples was then cut in to nine smaller subsamples and tested using the previous methodology, in both the Z and Y direction (undertaken 72 h after the *z*-direction tests). Interestingly, when plotted, it was found that for every tested subsample, energy dissipation was higher in the Y direction even though the Z direction exhibited larger maximum stress values. This behaviour was put down to the fact that although the maximum stress determines the height of the hysteresis curve, total energy absorption is an integral and is dependent upon the total shape of the curve.

Each of the subsamples were also plotted with respect to their energy dissipation verses their sample density (Figure 2.23). From the plot, it is apparent that a sample's energy dissipation is highly dependent on density of a foam sample, (and in turn its volumetric compression ratio). Unfortunately the authors note that as the volumetric compression ratio is increased (and in turn increasing its density), a foam tends to bottom more easily, leading to a significant degradation in its cushioning properties. Furthermore, it was observed that for a given set of subsamples, sample density was somewhat scattered. This variance, however, was explained by the boundary effects during manufacturing, which causes inhomogeneous compression to occur throughout the sample.
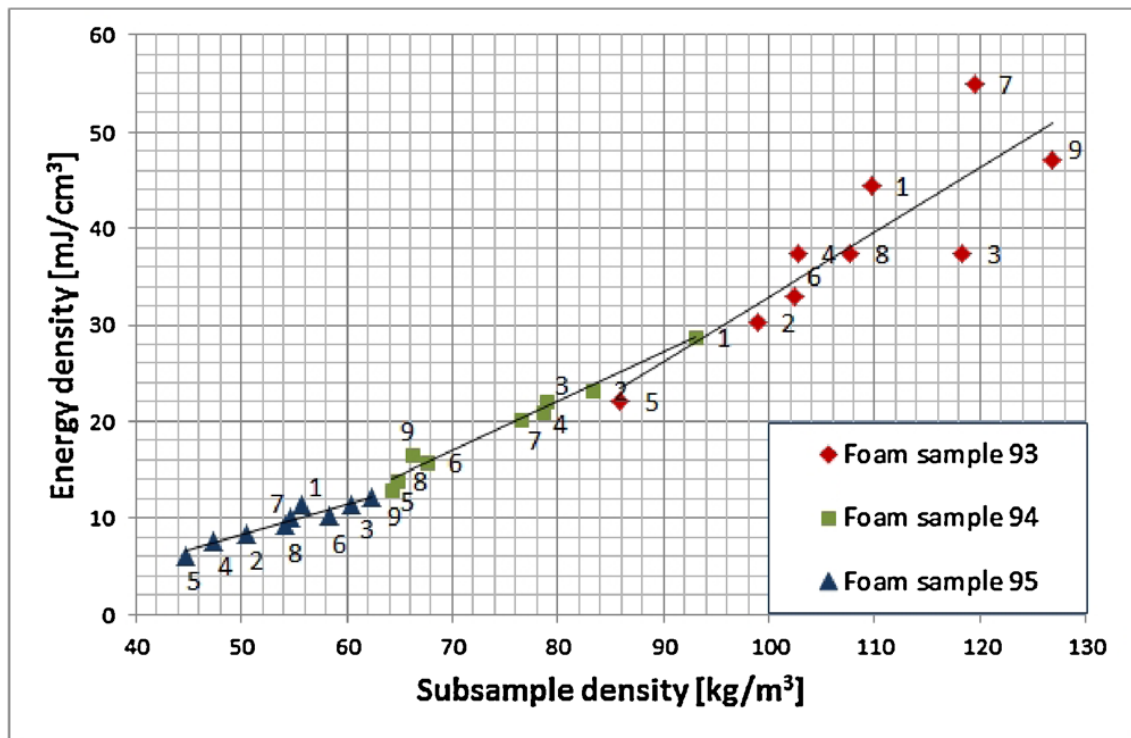
Figure 2.23: Energy dissipation vs subsample density [154].

In an additional study, Lisiecki *et al.*[137] also studied the energy dissipation of auxetic and conventional foams using static and dynamic testing. Utilising an MTS810.23 machine equipped with a 5 kN force sensor, three foam types (one auxetic, two conventional), were initially compressed three times to 30% strain before being compressed to 80% strain in the z-axis, at displacement rate of 100 mm s^{-1}. From the resulting hysteresis curves it was found that for a single cycle, the auxetic foam dissipated the most energy (due to exhibiting the largest curve), but were also stiffer than the conventional foams due to their higher relative density. Unfortunately, as a result of this increase in stiffness, the auxetic foams when subjected to impact testing were found to be significantly worse than the conventional foams at mitigating impact, due to their lower deceleration of the impactor.

71

Lim *et al.* [208] have also studied the effects of impacting of auxetic and conventional foams. In this study, auxetic and conventional foam rods were subjected to a number of different impacts upon their face surface from a Dynatup Impact Tester with a wedge-shaped tip at energies ranging between 42 J to 174 J. For low (42 J) and moderate (85 J) impacts, the authors report that little visible damage to the foam rods was observable. However, for the high energy impacts (165 J – 174 J) the auxetic samples were observed to have sustained more damage than their conventional counterparts. It was suggested that the reasons for the greater damage to the auxetic foam is due to its microstructure.

Whilst the work presented here covers literature relating to auxetic foams under impact, impact behaviour of non-foam based auxetic materials and structures including carbon fibre laminates and sandwich structures, are reported in [209-212]. It is interesting to note that in the majority of these studies, the presence of a negative Poisson's ratio has resulted in a range of positive effects including: increased in-plane ballistic performance [209], enhanced in-plane perforation resistance [211], reduction in damage areas directly under the area of load for composite structures [210] and an increase in energy absorption under crushing conditions [212]. In other instances, the presence of a negative Poisson's ratio has been shown to be beneficial as it allowed for the introduction of directionally dependent deformation [210] under impact loading.

The majority of the authors [24, 129, 137, 154] report that overall auxetic foams dissipate more energy than their conventional counterparts. There is however some conflicting work, as Bianchi et al [106] observed that conventional foam exhibited greater energy dissipation than the average auxetic foam when quasi-static cyclic tested where conventional foam was found to exhibit energy dissipation up to an order of magnitude higher than the auxetics. Although it cannot be stated with complete certainty, it is likely that the source of this anomaly may lie in the compression aspect of fabrication. While the authors applied radial and axial compressions within the 2 – 5 optimal range, the resulting overall volumetric compression ratio of sample can be seen to be as high as 19.15. Therefore the evidence presented, supports the assertion that auxetic foams do dissipate more energy than their conventional counterparts.

2.2.6 Applications of auxetic foams

The enhancements in mechanical properties offered by auxetic foams compared to conventional foams have led several researchers to consider possible applications for this new class of materials. Currently conventional foams are utilised in applications such as packaging, cushioning, air filtration, shock absorption and sound insulation [12, 18]. It could

be anticipated that in the future conventional foams will be replaced by auxetic foams in many of these applications as a result of their enhanced mechanical properties. Further novel applications for the auxetic foam technology have been suggested. Smart filtration systems [12] allow through the pores only particles with a certain size that could be varied by varying the pore size of the foam by applying different loads. This application could be taken a step further and be applied for smart drug delivery to patients. In this case the amount of drugs delivered could be controlled by whether or not the pores are open or closed and this could be influenced by the swelling of the body and the consequent pressure exerted on the foam [116]. Another application of auxetic foam could result from their characteristic double curvature reported by Lakes [103]. The dome-like shape observed when the foam is bent could be applied in mattresses to give support to the doubly curved human body [12].

Other notable uses for auxetic foams stem from military applications, where auxetic foams and other auxetic materials are being studied for use in ballistic protection, while Mitsubishi have recently patented a bullet design where one component is made of auxetic material, in an attempt to create an overall zero Poisson's ratio. By achieving a negative Poisson's ratio, lateral expansion would be reduced when travelling down the gun barrel [12].

Another possible application proposed by Choi and Lakes [10] is a press fit fastener. The press fit fastener would work by tangentially contracting when placed into a socket, and expanding when attempted to be removed from the socket [10]. An additional application suggested by Lakes [11] is for a wrestling mat that experiences both small localised impacts (knees) and large distributed impacts (human torso) during its use, which can be calculated through Equations 2.23 and 2.24 [11]. Currently, wrestling mats contain elastomeric foams with Poisson's ratio of approximately 0.3. However, Lakes proposes that due to the enhanced indentation and energy distribution mechanisms of negative Poisson's ratio materials, auxetic foam would offer the greatest performance, as opposed to rubber, which is considered to be the worst. Other possible applications include structural integrity structures [24, 108], sandwich components [10, 16, 24, 114, 213], smart structures [12, 129], biomedical components [118, 214], dynamic and multi-physics applications [18, 129, 215-218], knee pads [16], tear resistant sponges [16] and sounds absorbing materials [16].

2.3 Summary

There has been a considerable amount of work undertaken in relation to body armour. While most of the work has focused upon improving an armour's ability to protect the wearer from bullet penetration, there has been little work undertaken in relation to reducing the spectrum of non-penetrating injuries (BABT) that arise from the backface deformation of personal armour onto the wearer's torso following projectile impact.

From the limited work reported, low density foams placed between the armour and the torso are an effective means of decreasing trauma, as they attenuate the impact energy through absorption, dissipation and/or redistribution, by allowing energy to be transferred gradually to the wearer's torso.

As auxetic foams have been reported to demonstrate numerous mechanical property enhancements (including energy absorption) over conventional foams, this has led to their consideration for use as a trauma reducing material. Unfortunately, while much has been done in the field of auxetic foams, in order assess their potential usability for use within an armour system to combat the effects of BABT, further studies are required. The following are suggested studies required for this assessment.

Influence of a NPR on impact behaviour – In order to consider auxetic foams as a potential material as a suitable TAB material, it is important to understand the influence that a negative Poisson's ratio can have on a material under impact conditions. To date, very little literature has been published focusing upon the auxetic foams under impact, although some work has been done with other materials and structures.

High Strain Impact – Although not directly impacted with an armour system, the transition of energy through the protective armour plate after projectile impact has been shown to cause the material to protrude, thus impacting the object behind. Some initial work has been undertaken by Scarpa *et al.* [129], however, this study only investigated auxetic foam fabricated at only one combination of heating time, volumetric compression ratio and porosity at strain rates of 15 and 38 s^{-1}.

Behind sample analysis – As set out in NIJ standards [8], following projectile impact to an armour system, crater depths left upon a clay body (as described in standards) are not permitted to exceed 44 mm. To investigate how the auxetics perform with respect to these requirements and as a viable material for the reduction in BABT a similar study is required.

Repeatable fabrication method – As previously stated within the literature, auxetic foams are known to be highly unrepeatable (properties) within their fabrication [127] and are currently not usable for commercial applications. In order to make auxetic foams usable with body armour, it is imperative that the auxetic fabrication process is extensively explored with the aim of introducing sample repeatability.

Chapter 3: Methodology

3.1 Introduction

The following chapter outlines the methodology and materials utilised throughout the experimental programme of this thesis. Experimental decisions are discussed, which are coupled to a brief justification for the chosen technique used.

3.2 Materials

3.2.1 Polyurethane Foam

Commercially available black 45 and 10 pores per inch (PPI) polyurethane foam, with dimensions of 1500 mm $\times$ 2000 mm $\times$ 50 mm and densities 27 and 34 kg m^{-3} were supplied by Recticel, UK.

3.2.2 Roma Plastelina Clay No.1

Roma Plastelina No.1 is a non-hardening, homogeneous and non-compressible oil-based clay is used as a backing material for testing of ballistic vests, in accordance with the NIJ and HOSDB (Home Office Scientific Development Branch) standards [219]. Blocks of Roma Plastelina No.1 weighing 907 g and measuring 140 mm $\times$ 63.5 mm $\times$ 76 mm were supplied by Advanced Defence Materials Ltd., UK.

3.2.3 Objet Rapid Prototyping Polymers

Three polymer composites were used in conjunction with a Connex 350 rapid prototyping system to produce composite polymer models (Table 3.1, Table 3.2 and Table 3.3). Through a combination of these materials, a range of rubber-like materials of different mechanical properties can be produced. It is through this methodology that TangoBlack85 is created.

Table 3.1: Chemical composition of TangoBlackplus rapid prototyping material [29].

Name	Concentration / %wt.
Acrylic oligomer	< 70
Exo-1, 7, 7-trimethylbicyclo[2.2.1]hept-2-yl ester	< 25
Photo initiator	< 2
Xylenes (o-, m-, p- isomers)	0.1-1
Benzyl alcohol	< 0.5
Acrylic acid ester	< 0.3
Propylene glycol monomethyl ether acetate	< 0.1
Isoamyl acetate	< 0.1
n-butyl acetate	< 0.1
Carbon black	< 0.1
Ethylbenzene	< 0.1
Citral	< 0.1
Dipentene	< 0.1
2,6-Di-tert-butyl-p-cresol	< 0.01
Geraniol	< 0.01

Table 3.2: Chemical composition of VeroClear rapid prototyping material [31]

Name	Concentration / %wt.
Acrylic monomer	< 30
Isobornyl acrylate	<25
Acrylate oligomer	<15
Photoinitiator	<2
Acrylic acid ester	<0.3

Table 3.3: Chemical composition of Support 705 rapid prototyping support material [220]

Name	Concentration / %w.t
Acrylic monomer	20 - 40
Polyethylene glycol 400	< 40
Propane-1,2-diol	< 40
Glycerol	< 20
Photoinitiator	< 1

3.3 Manufacture of the auxetic foams

3.3.1 Conventional three stage auxetic fabrication of volumetric compression, heating and cooling

Foam samples with dimensions (height × width × length) 50 mm × 50 mm × 200 mm, 50 mm × 50 mm × 160 mm and 50 mm × 50 mm × 120 mm were cut using a mechanical knife (to limit structural damage), from both the 10 and 45 PPI polyurethane foam sheets, and

subjected to the conventional auxetic transformation process [103] of tri-axial compression, heating and cooling.

Aluminium moulds with an internal cross section of 32 mm × 32 mm and a length of 200 mm were utilised for the bi-axial compression to the foam samples. Two aluminium compression blocks with dimensions 32 mm × 32 mm × 50 mm were then positioned at either end of the moulds in order to compress the sample in the third axis, thus, providing the tri-axial compression arrangement. These blocks were held in place by two steel end plates connected via 5 mm threaded rods 250 mm long (Figure 3.1). The sample lengths affect the imposed tri-axial compression resulting in volumetric compression ratios of 4.88, 3.91 and 2.93 for lengths of 200 mm, 160 mm and 120 mm, respectively.
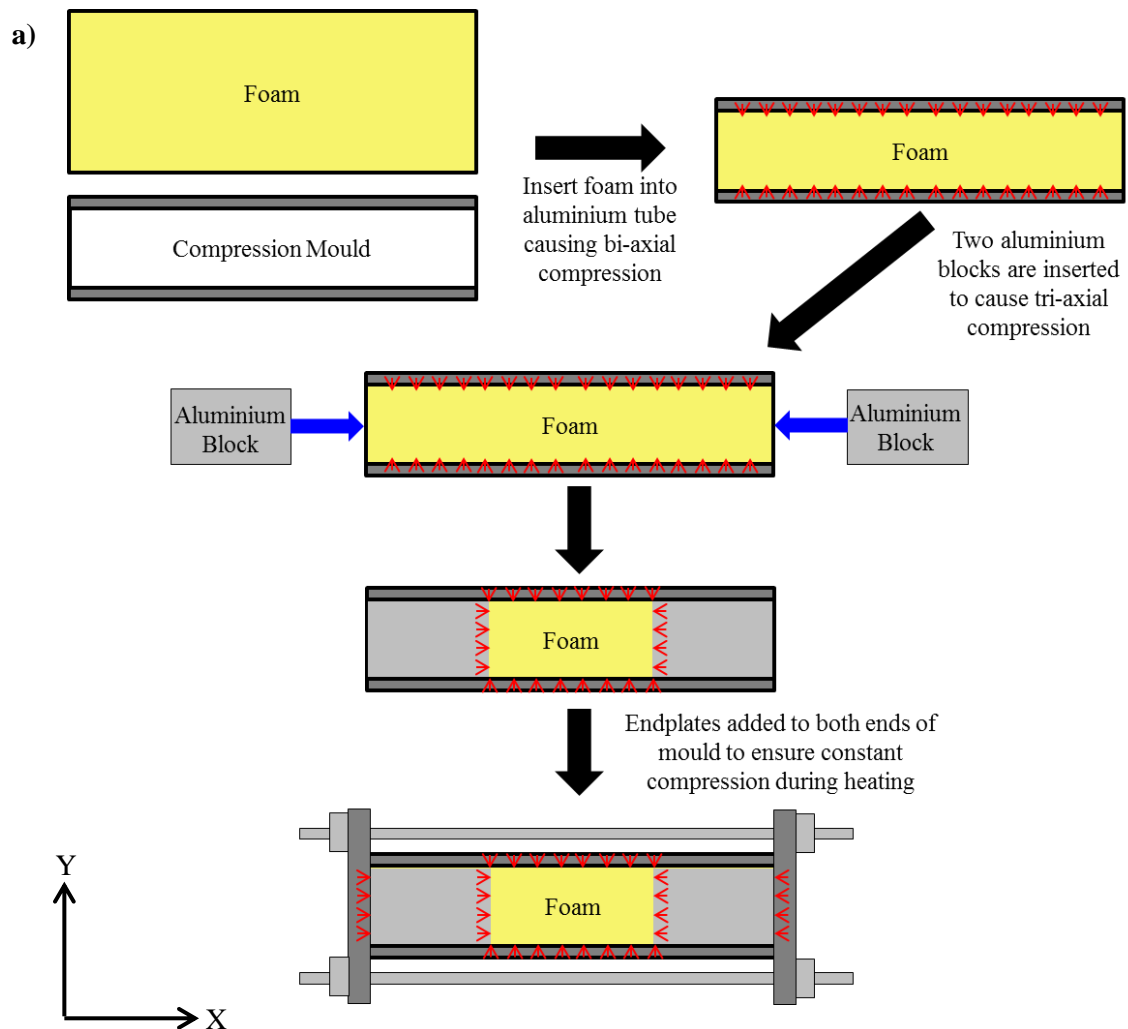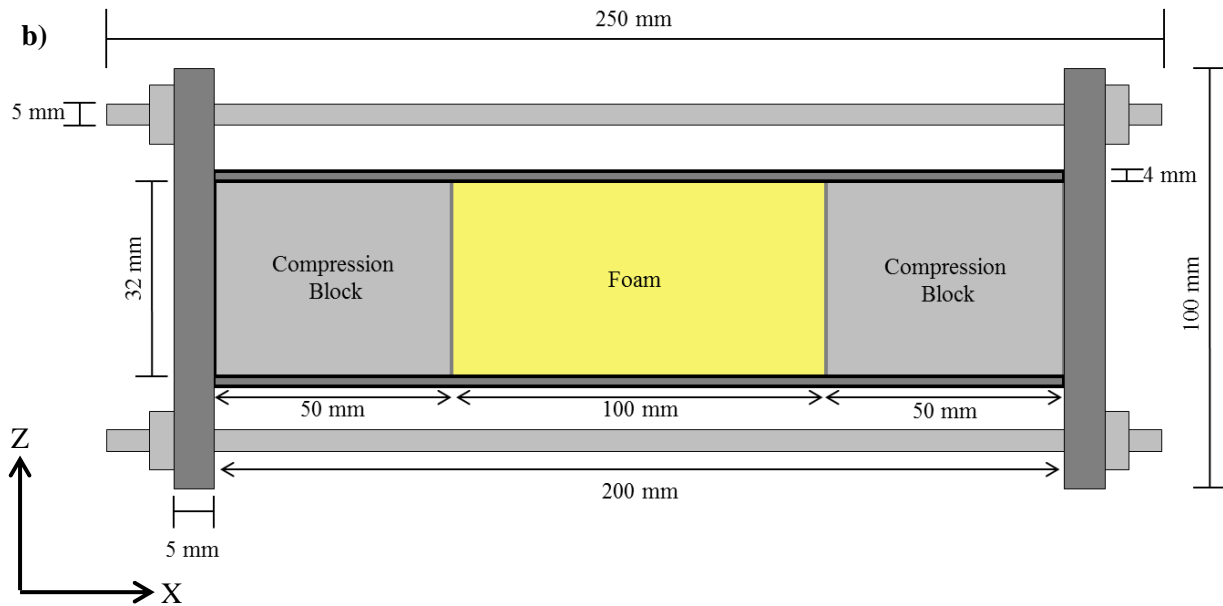
Figure 3.1: Diagram showing **a)** the fabrication process utilising tri-axial compression of the polyurethane foams, where red arrows indicate applied forces and **b)** rig dimensions upon completion of tri-axial compression**.**

Constrained samples were then placed into a Binder FD 115 series oven pre-heated at 200°C (this value was selected as it represents the upper repeated value reported in literature, while also exceeding the glass transition temperature of polyurethane which is reported as 114°C [130]) for a set time (as outlined in Table 3.4). In some experiments a thermocouple was employed to monitor the internal temperature of the sample during fabrication to determine how long it took for the heat to diffuse to the centre of the sample. On completion of the heating cycle, the aluminium moulds were removed from the oven and allowed to cool for at least 2 h until both sample and mould reached ambient room temperature (typically 23°C) allowing the auxetic microstructure to be fixed. Samples were then removed from the mould and hand stretched along the longitudinal direction to relax the sample. The mass and dimensions of the samples were then measured using a Sartorius Talent, TE2145S electronic balance (± 0.0001 g) while a ruler of accuracy ± 0.5 mm was used to measure three positions across the X, Y and Z axes (rise direction) and averaged. Samples were then immediately mechanically tested.

To understand the intrinsic anisotropic nature of the auxetic foams [103, 158, 185], both the longitudinal and the latitudinal axes of the sample have been tested (Figure 3.2). For latitudinal testing, cubic samples (30 mm × 30 mm × 30 mm) were removed from the centre third of the initial sample in order to negate the influence of the localised high density regions that occur at the extremities [24, 153]. The longitudinal samples were left uncut since the testing occurred directly in the centre third of the sample.
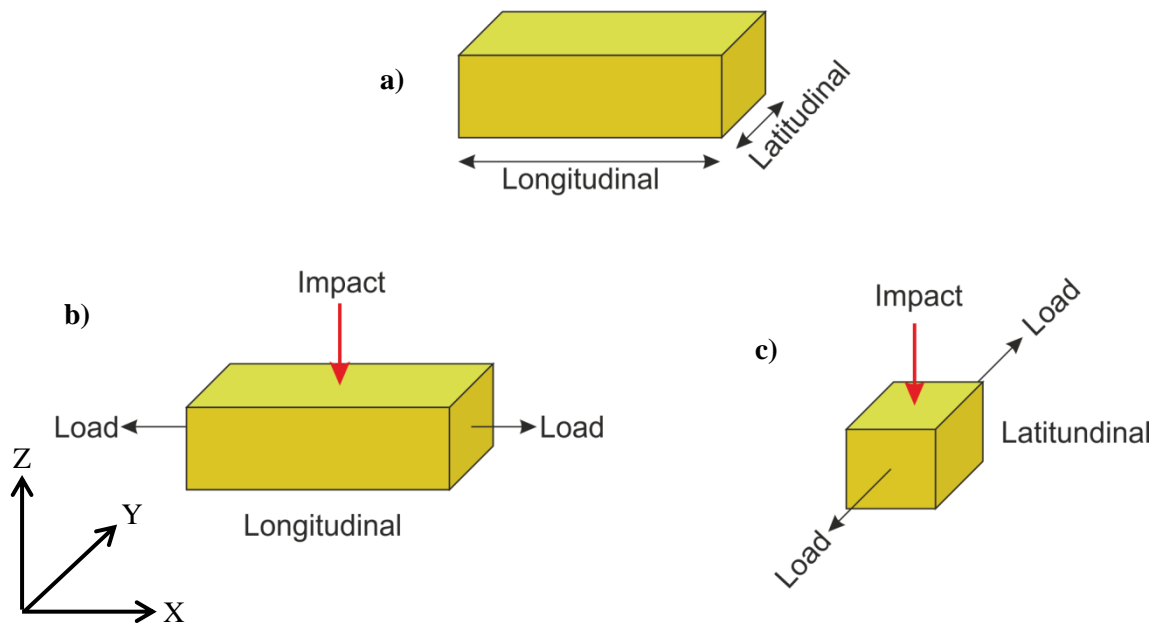
Figure 3.2: Diagrammatic representation of: **a)** sample as removed from oven, **b)** testing parameters for longitudinal samples, and **c)** testing parameters for latitudinal samples.

Overall, a total of 288 (192 longitudinal and 96 latitudinal) samples were fabricated using this methodology, resulting in the fabrication matrix shown in Table 3.4 and Table 3.5. All variables within this test matrix were chosen to encompass the various volumetric compression ratios and heating times discussed throughout the literature.

Table 3.4: Longitudinal samples fabrication matrix.

Longitudinal Samples			
Base foam porosity: 45		**Base foam porosity: 10**	
Volumetric compression ratio: 4.88			
Heating Time / min	Number of Samples	Heating Time / min	Number of Samples
60	4	60	4
55	4	55	4
50	4	50	4
45	4	45	4
40	4	40	4
35	4	35	4
30	4	30	4
25	4	25	4
Volumetric compression ratio: 3.91			
Heating Time / min	Number of Samples	Heating Time / min	Number of Samples
60	4	60	4
55	4	55	4
50	4	50	4
45	4	45	4
40	4	40	4
35	4	35	4
30	4	30	4
25	4	25	4
Volumetric compression ratio: 2.93			
Heating Time / min	Number of Samples	Heating Time / min	Number of Samples
60	4	60	4
55	4	55	4
50	4	50	4
45	4	45	4
40	4	40	4
35	4	35	4
30	4	30	4
25	4	25	4

Table 3.5: Latitudinal samples fabrication matrix.

Latitudinal Samples			
Base foam porosity: 45		**Base foam porosity: 10**	
Volumetric compression ratio: 4.88			
Heating Time / min	Number of Samples	Heating Time / min	Number of Samples
60	4	60	4
50	4	50	4
40	4	40	4
30	4	30	4
Volumetric compression ratio: 3.91			
Heating Time / min	Number of Samples	Heating Time / min	Number of Samples
60	4	60	4
50	4	50	4
40	4	40	4
30	4	30	4
Volumetric compression ratio: 2.93			
Heating Time / min	Number of Samples	Heating Time / min	Number of Samples
60	4	60	4
50	4	50	4
40	4	40	4
30	4	30	4

3.3.2   Heat Study

3.3.2.1 Thermocouples

A K-Type thermocouple supplied by RS Components, UK was directly inserted in to the centre of a tri-axially compressed 45 PPI and 10 PPI foam samples of volumetric compression ratios of 4.88, 3.91 and 2.93 (Figure 3.1). Samples were then individually placed in to the centre of a Binder FD 115 series oven pre-heated at 200°C and heated for 2 h where a DAQ card recorded the temperature change at a rate of 10 samples per second. On completion of the heating, the samples were removed from the oven and allowed to cool for at least 2 h until both sample and mould reached ambient room temperature (typically 23°C).

3.3.2.2 Heat Model

To study the temperature variation experienced during auxetic fabrication a two-dimensional heat transfer model was created using COMSOL Multiphysics Version 4.4 software. The model comprised of three distinct regions, each with their own properties (Table 3.6), coupled with a heating source, set at a consistent 200°C, and a cold region to represent convection between the hot oven and cold mould (Figure 3.3).
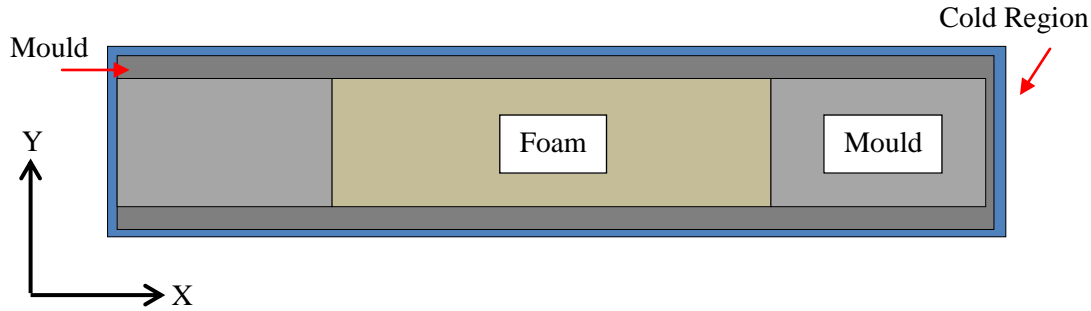
Figure 3.3: 2D COMSOL model used for the calculation of heat transfer.

Although graphically represented, the model calculates temperature variations with respect to time, using the heat equation [221], which is given as:

$$\frac{\partial u}{\partial t} = \alpha \left(\frac{\partial^2 u}{\partial x^2} + \frac{\partial^2 u}{\partial y^2} + \frac{\partial^2 u}{\partial z^2} \right)$$

(Equation 3.1)

Where:

$\frac{\partial u}{\partial t}$ = is the rate of change of temperature at a point with time.

$\left(\frac{\partial^2 u}{\partial x^2} + \frac{\partial^2 u}{\partial y^2} \quad \frac{\partial^2 u}{\partial z^2} \right)$ = temperature as a function of space and time[3]

$\alpha = \frac{k}{c_p \rho}$ = is the thermal diffusivity

k = thermal conductivity (W m^{-1} K^{-1})
ρ = density (kg m^{-3})
c_{p} = specific heat capacity (J kg^{-1} K^{-1})

---

[3] Can eliminate dependant on if model is 1D, 2D or 3D.

Table 3.6: Heat model parameters, where values were provide by CES edupack [222].

Foam Properties			
45 PPI			
Volumetric compression:	4.88	3.91	2.93
Density (kg m^{-3})	140	113	83
Thermal conductivity (W m^{-1} K^{-1})	0.045	0.04	0.036
Specific heat capacity (J kg^{-1} K^{-1})	1650	1650	1650
45 PPI			
Volumetric compression:	4.88	3.91	2.93
Density (kg m^{-3})	176	139	103
Thermal conductivity (W m^{-1} K^{-1})	0.05	0.045	0.04
Specific heat capacity (J kg^{-1} K^{-1})	1650	1650	1650
Mould properties (aluminium 7020):			
Material	(aluminium 7020)		
Density (kg m^{-3})	2810		
Thermal conductivity (W m^{-1} K^{-1})	143		
Specific heat capacity (J kg^{-1} K^{-1})	911		
Cold Region			
Material	Air		
Density (kg m^{-3})	1.205		
Thermal conductivity (W m^{-1} K^{-1})	0.0257		
Specific heat capacity (J kg^{-1} K^{-1})	1.005		

After assigning all properties, the model was meshed (using a fine element size) and then calibrated against the mean empirical thermocouple data (45 PPI foam compressed at a volumetric compression ratio of 4.88). This was achieved by varying the size of the cold region over a series of simulations (run on a computer of specifications: Windows 7 64 bit, 8 gigabyte RAM, GEFORCE GTX 680 2048 megabyte graphics card with an Intel i5 750 four core processor running at 2.67 GHz per core) until the theoretical and empirical time-temperature profiles converged. Once calibrated, the model was then utilised to predict the influence of volumetric compression ratio and heating time by varying the foam region properties (outlined in Table 3.6) prior to running the simulations.

3.3.3   3D printing

Idealised auxetic and conventional foam cellular structures, as originally proposed in the literature [14] were computationally designed using Solidworks® 2012 (64 bit). Modelled cells were initially produced as 2D structures (Figure 3.4), then merged together to form symmetrical cells. When these cells were designed they were initially based upon real world measurements of the 10 PPI foams (the largest used in this document), due to a combination

of systematic limitations of the Connex350 3D Printer, the aggressive nature of the support material removal process and the desire to achieve auxetic and conventional foams with matching densities. An appropriate cell size was achieved through a trial and error process, where the original 10 PPI dimensions were used as the base at the commencement of the procedure.
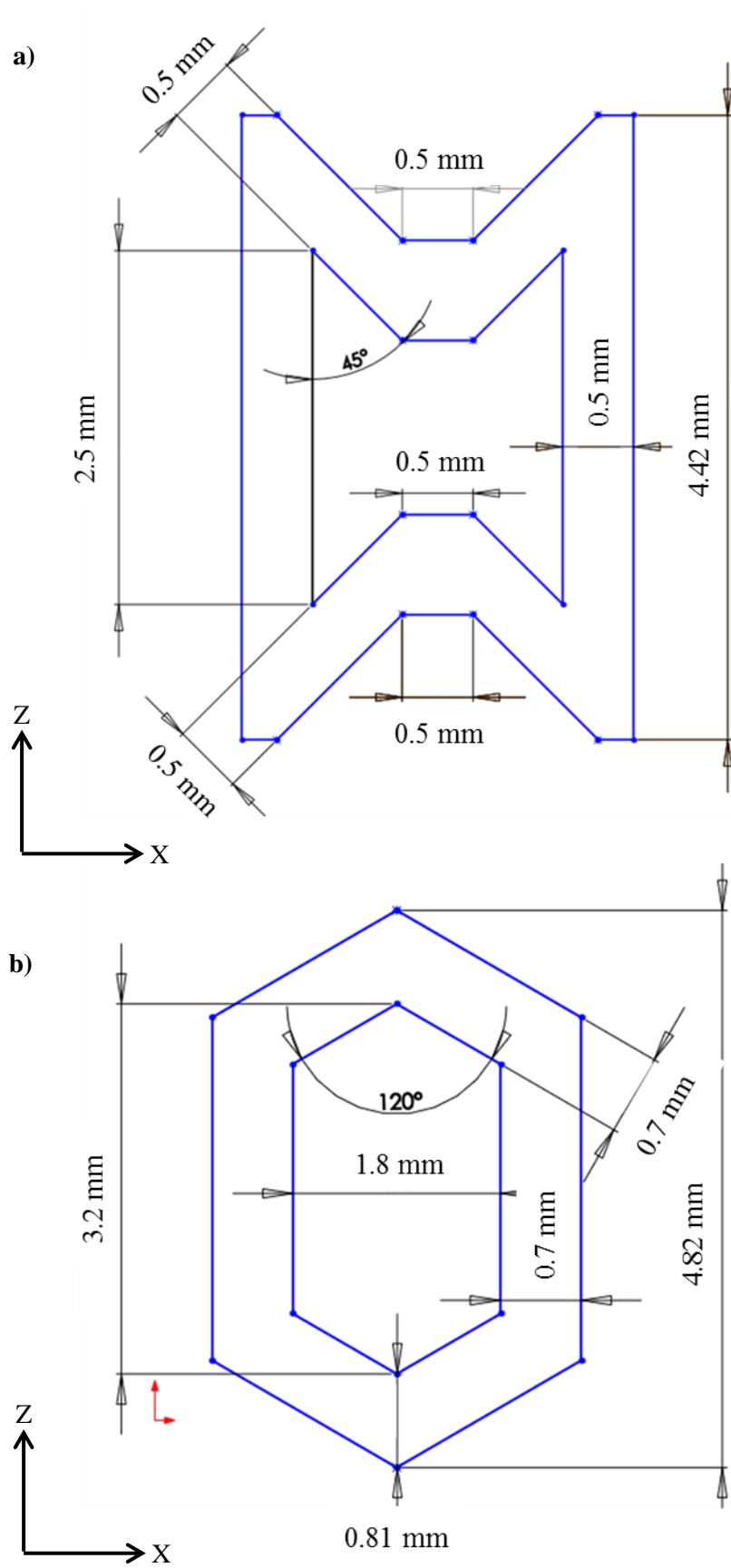
Figure 3.4: a) auxetic and **b)** conventional 3D printed cell dimensions.

These new 3D cells was then merged perpendicularly with another identical unit cell to form the symmetrical 3D cells before being layered into various arrangements to produce samples for both tensile and impact testing (Table 3.7). Finally, where required, endplates of 1 mm thickness and dimensions matching the *X* and *Y* sample dimensions are added to each end of the unit cell layup to provide a flat interface in order to bond the foam samples for tensile or impact testing. On completion of the design phase, the digital foam structures were converted to a single part (.STL) for use with a Connex 350 Objet printer, where samples were fabricated from the polymeric composites TangoBlack and TangoBlack85. To minimise systematic effects all samples manufactured within this study were "built upwards" about the Z axis, unless otherwise stated. Overall, a total of 29 samples were fabricated using this methodology.

Table 3.7: 3D printed sample parameters.

Diagrammatic representation	Cell structure	Test Type	Dimensions			Endplate	Number of samples
			X / mm	Y / mm	Z / mm		
Figure 3.5a	Auxetic	Tensile	20	20	40	Y	6
Figure 3.5c	Auxetic	Impact – High mass, low velocity	30	30	30	N	3
Figure 3.5e	Auxetic	Impact – Low mass, high velocity	30	30	15	Y	6
Figure 3.5b	Conventional	Tensile	20	20	40	Y	6
Figure 3.5d	Conventional	Impact – High mass, low velocity	30	30	30	N	3
Figure 3.5f	Conventional	Impact – Low mass, high velocity	30	30	15	Y	3
Figure 3.5g	Solid block	Impact - Low mass, high velocity	30	30	15	N/A	2
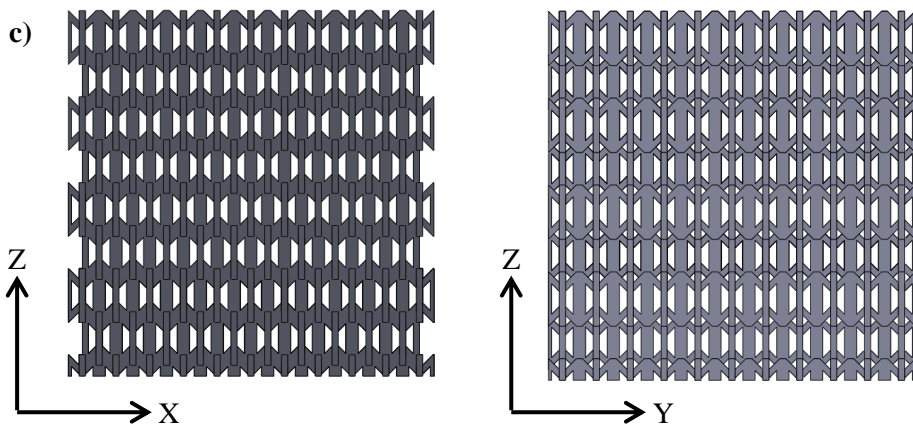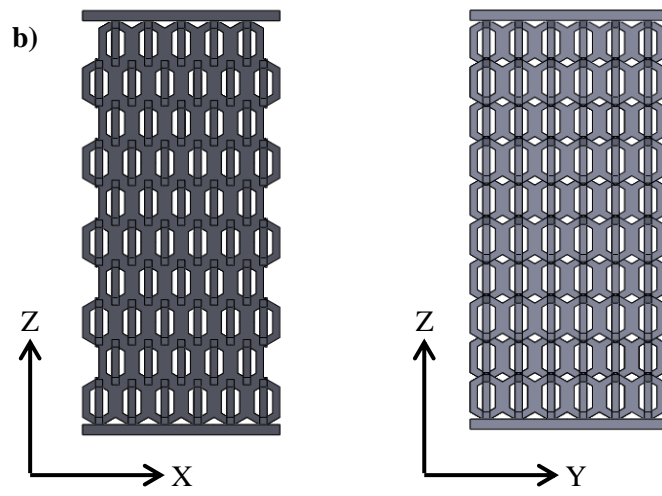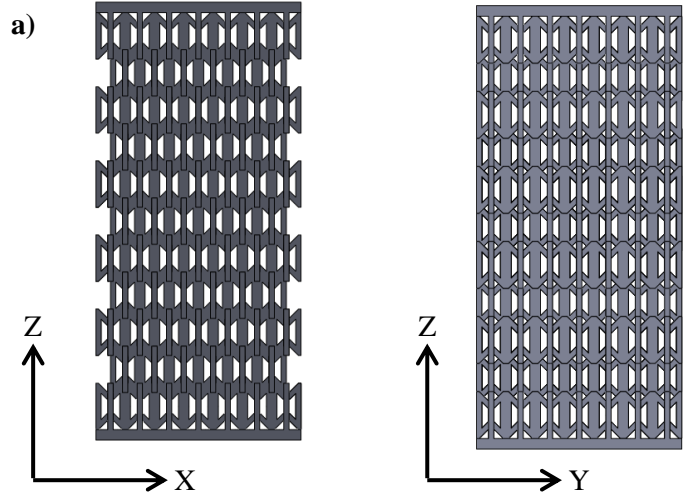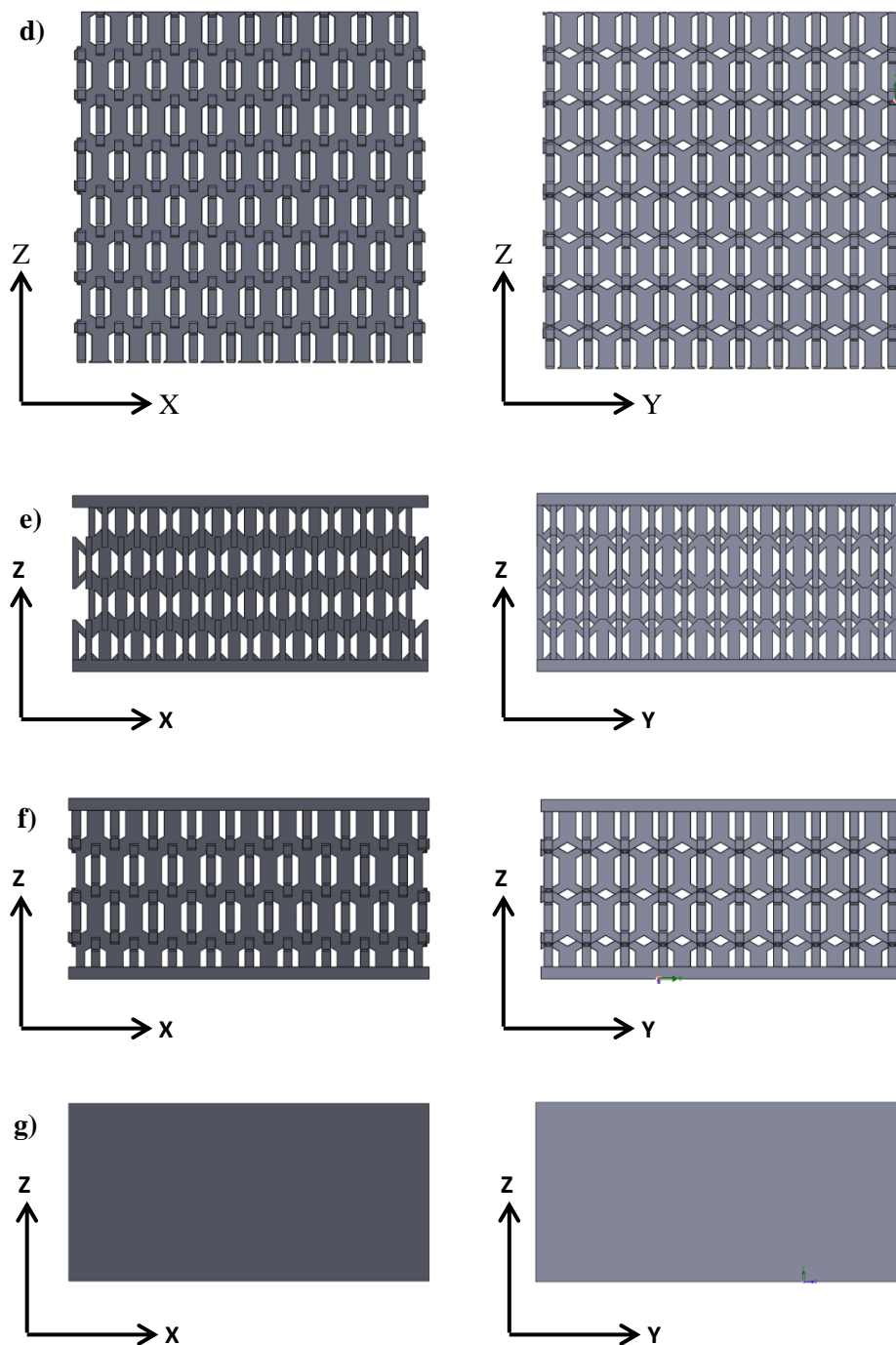
Figure 3.5: Solidworks designs in the X and Y axis for each 3D printed sample type where: **a)** auxetic tensile, **b)** conventional tensile, **c)** auxetic high mass, low velocity, **d)** conventional high mass, low velocity, **e)** auxetic low mass, high velocity, **f)** conventional low mass, high velocity and **g)** solid block low mass, high velocity.

One drawback of this technique is the deposition of support material throughout the sample structures, as part of the printing process. To chemically soften and facilitate removal of the support material, each sample was placed in an aqueous 50 g L^{-1} potassium hydroxide (KOH) solution at ambient temperature (typically 23°C) and agitated using either electronic

rollers or sparged using an Interpet AP2 Aquarium Air Pump for 24 h, after which, samples were thoroughly rinsed with tap water and allowed to dry. If any support material remained, the sample was placed in freshly prepared potassium hydroxide solution and agitated for a further 24 h.

3.4 Impact testing

A free fall drop tower designed and manufactured in-house (Figure 3.6) was used to test the response of auxetic foams under a compressive load of $\approx$ 7.2 J; each sample was impacted only once. The compressive load was delivered via a steel cylindrical datum bar with a semi-sphere end (radius 6 mm and mass = 1.262 kg) dropped from a fixed height of 600 mm onto a sample resting on Roma Plastilina Clay. The clay was enclosed in an aluminium box of internal dimensions 137 mm $\times$ 69 mm $\times$ 64 mm, in accordance with current testing methods [223].
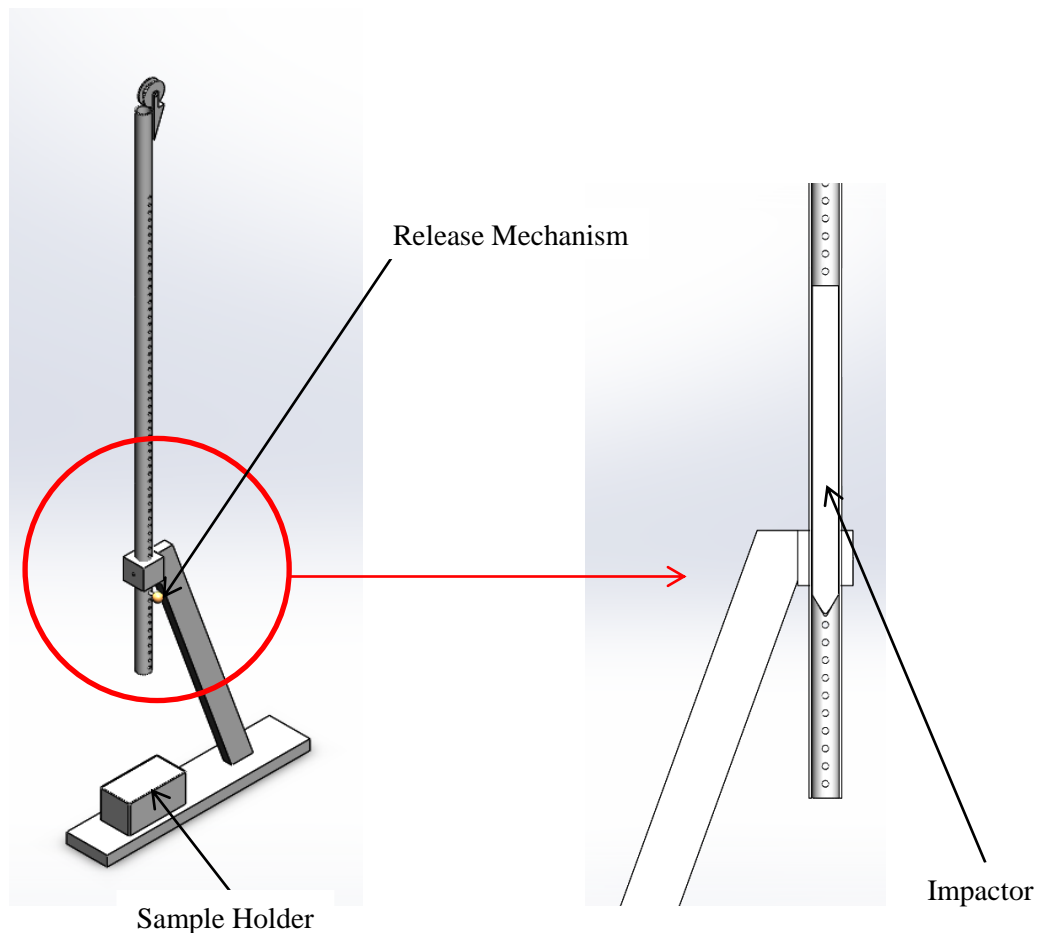
Figure 3.6: Drop tower rig schematic.

Interaction between the datum and sample / clay combination causes a transfer of kinetic energy, resulting in deformation of the clay body to form craters. By considering the energy

absorption per unit volume of the clay (E_{unit}) as a constant, the relationship between the impact energy (E_{impact}) and volume of a crater (V_{crater}) can be assumed to be:

$$E_{unit} = E_{impact} / V_{crater} \qquad \text{(Equation 3.2)}$$

In order to calculate the energy absorbed by a sample, calibration tests were performed in which the datum directly impacted the clay body. It is assumed that all the energy is transferred to the clay during impact, thus negating energy loss through friction and the environment. Since the potential energy of the datum and the volume of the crater are known, E_{unit} can be calculated.

Following calculation of E_{unit} it is then possible to calculate the total energy absorbed. By assuming that for a given impact of a sample resting on a clay body all energy is absorbed by either the foam or clay, the following must be true:

$$E_{impact} = E_{Clay} + E_{Foam} \qquad \text{(Equation 3.3)}$$

As the total energy absorbed per unit volume was previously calculated via Equation 3.2, E_{clay} is given by:

$$E_{clay} = E_{unit} \times V_{crater} \qquad \text{(Equation 3.4)}$$

The total energy absorbed per sample is then calculated by re-arranging Equation 3.2 to give:

$$\text{Total energy absorption} = E_{impact} - E_{sample} \qquad \text{(Equation 3.5)}$$

After impacting a sample, the foam and the aluminium box containing the clay were removed and substituted with non-impacted replacements. Before carrying out each experimental session, a calibration experiment was undertaken.

3.5 Compression Testing

To assess the compressive properties, uniaxial compression tests were undertaken using an Instron test machine outfitted with a 50 kN load cell and m2 0.00-0.25 grips each containing a fixed steel plate of dimensions 35 mm × 40 mm × 2.5 mm. Two test profiles were utilised throughout this study; one for materials fabricated through the traditional auxetic manufacturing method, and one for the 3D printed samples. For traditional method samples

compression was undertaken at a rate 5mm per minute, while 3D printed samples were compressed at a rate of 2 mm per minute (Table 3.8). In both tests compression was undertaken about the Z axis.

Table 3.8: Compression testing parameters.

Sample	Dimensions			Rate of Compression / mm min^{-1}	Maximum strain
	X / mm	Y / mm	Z / mm		
Conventional Foam	30	30	30	5	83
Auxetic Foam	30	30	30	5	83
3D Print Conventional	30	30	15	2	67
3D Print Auxetic	30	30	15	2	67

3.6 Ballistic rig – high velocity, low mass

To assess the auxetic and conventional structure response under a high velocity, low mass impact, a high strain rig as shown in Figure 3.7 was designed in-house and manufactured by Safire Design Engineers Ltd, Southampton, UK.

Due to the high velocities (up to 190 m s^{-1} when a 9 mm steel ball bearing of mass 3 g is projected using 160 psi of compressed air) that the rig delivers, both auxetic and conventional foam samples were bonded (using double sided tape) to a hard outer layer of 32 ply carbon fibre, supplied by Cytec, UK.
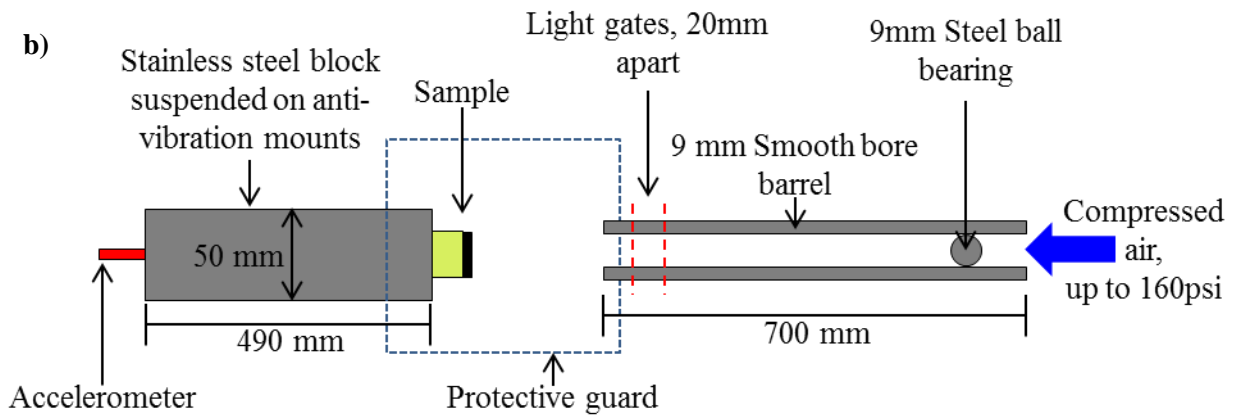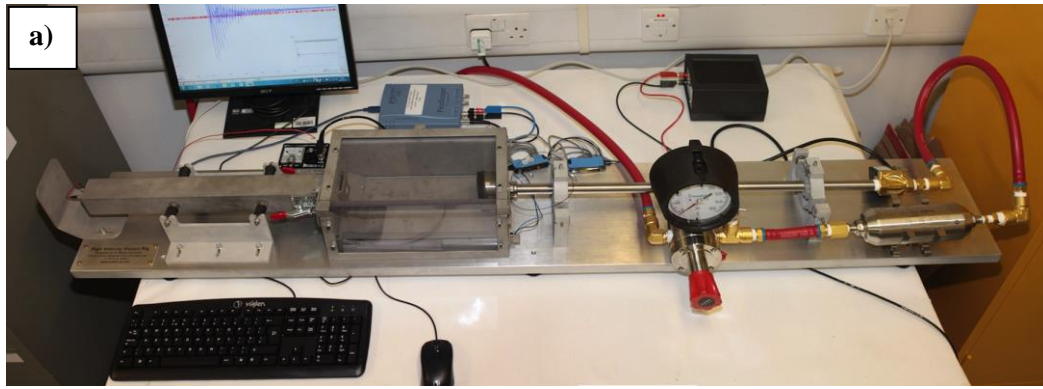
Figure 3.7: a) The high speed impact rig and **b)** schematic representation.

Impact was achieved by projecting an AISI52100 chrome steel 9 mm diameter ball bearing using a smooth bore barrel, (using a variable compressed air system) at a sample, suspended via vacuum grease on the end of a type 316 stainless steel half metre long block, that rests upon four anti-vibration mounts. Two light gates were mounted directly within the smooth bore barrel, which not only measured the velocity of the projectile, but initiated the capture of the accelerometer data.

In order to capture the impact event, and thus detect the transferred energy through the sample, an accelerometer was attached at the opposite end of the suspended block to detect the various transmitted waves that occur after sample impact. To ensure that a discernible wave form can be detected from the impact event, three interchangeable accelerometers from Dytran Instruments Inc. (Chatsworth, California) of g-force measurement ranges 50,000, 10,000 and 500 were employed at the rear end of the suspended block (Table 3.9) and powered with a 4105C battery powered current source power unit of gain ×1, ×10 and ×100, giving frequency responses between 0.1 Hz to 100 kHz, 0.1 Hz to 50 kHz and 0.1 Hz to 10 kHz, respectfully.

Table 3.9: Specification of the three available accelerometers.

Range	Model	Sensitivity / mV g⁻¹	Frequency Range / Hz
±500 g	3019A	0.1	1 - 10,000 (±5%)
±10,000 g	3200B4	0.5	0.35 - 10,000 (±10%)
±50,000 g	3200B2	0.1	0.35 - 10,000 (±10%)

Once an impact event has been captured by the accelerometer, a Blackman filter was applied to the raw data in order to smooth the signal noise, and plotted to form graphs of time (ms) versus acceleration (m s^{-2}).

Although this smoothed data indicates the first detectable signal from the impact event, identification of the wave time period only associated with the impact is difficult. In order to find this region, the time for the wave to travel through the sample and 316 stainless steel block must first be known. As the P-wave (Primary wave) is known to be the fastest travelling wave type in an impact event, the velocity of a P-wave can be calculated in a homogeneous isotropic medium by Equation 3.6 [224],

$$V_p = \sqrt{\frac{K + \frac{4}{3}G}{\rho}}$$

(Equation 3.6)

Where V_p is P-wave velocity (m s^{-1}), K is the bulk modulus (Pa), G is the shear modulus (Pa) and ρ is the density of isotropic medium (kg m^{-3}). When considered for the 316 stainless steel block, the P-wave velocity was calculated to be 5555 m s^{-1}, while the total travel time for the wave in the block and sample of length 0.495 m is 89.1 μs.

However, as the impact event is comprised of multiple wave types including shear and Rayleigh waves, the calculated time of 89.1 μs must be considered as the time taken to detect the start of the impact event, as other wave types travel slower. Consequently, the time period associated with the initial impact can be said to the total time it takes for the P-wave to be detected once more after the initial detection, which is calculated to be 178.2 μs. As the wave travels the 0.495 m twice due to boundary reflexion, as indicated in Figure 3.8 where it can be seen that as the wave travels through the solid stainless steel block and comes in to contact with fixed boundary 2, the wave will be reflected back down the length of the block until encountering boundary 1, another fixed end which again will reflect the wave back (towards the accelerometer). This wave reflection continues to occur, until the block comes to rest due to wave attenuation and resistive forces against the block's movement.
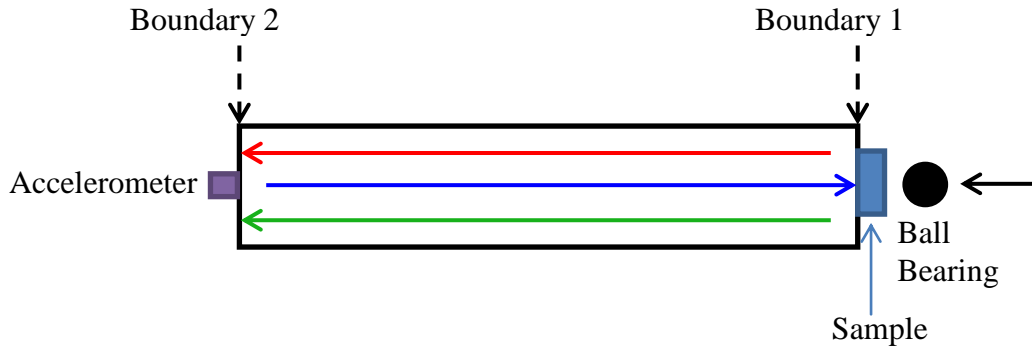
Figure 3.8: Diagrammatic representation of how the wave travels in the type 316 stainless steel block, where the red arrow represents the initial detection of P-wave, blue arrow represents reflected wave and green arrow represents second detection of initial P-wave.

By determining the length of time that it takes for the P-wave to be re-detected, the energy transmitted through the sample can then calculated using the following equation:

$$Kinetic\ energy = \frac{1}{2}mv^2$$

(Equation 3.7)

Where *m* is the mass of the ball bearing (kg) and v is the summed integral of positive area under the curve (negative peaks not considered due to negative waves represent movement away from the accelerometer, (Figure 3.9) of the acceleration *vs.* time plot, from the first positive detectable peak until a time of 178.2 μs later, as indicated in Figure 3.9.
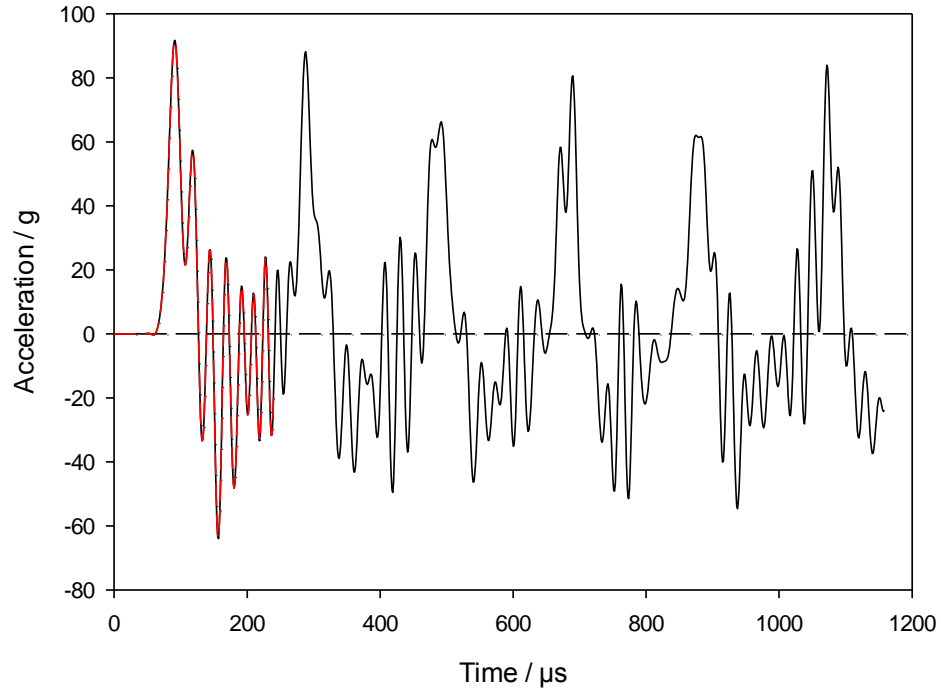
Figure 3.9: Graph showing acceleration *vs.* time trace (black line) of a 3D printed honeycomb structure with 32 ply hard outer coating hit at a velocity of 124 m s^{-1} delivering an energy of 22.9 J, where the red dashed line indicates time period used for calculating energy.

3.7   Characterisation Techniques

Characterisation of samples is a vital component in understanding the relationship between heating time, volumetric compression and porosity of the auxetic fabrication process, where employment of the wrong technique can result in unreliable quantitative data being obtained.

3.7.1   Density

Since auxetic foams have been reported to exhibit a natural tendency to increase in density after conversion [24, 107] the sample masses and dimensional measurements were recorded after removal from the mould, after stretching and before mechanical testing. The density of the samples was calculated by measuring the mass with a Sartorius Talent, TE2145S electronic balance (± 0.0001 g) and the volume by measuring with a ruler (± 0.5 mm) in three positions across the *x*, *y* and *z* axes and averaged to produce a sample's mean volume.

3.7.2   Volumetric Compression Ratio

By considering the original volume of the sample, the internal volume of the moulds (V_{mould}) and the measured volumes of the sample after conversion (V_{actual}), both imposed volume compression ratio (VCR$_{imposed}$) and actual volumetric compression ratio (VCR$_{actual}$) were calculated using:

$$VCR_{imposed} = \frac{V_{original}}{V_{mould}}$$

(Equation 3.8)

$$VCR_{actual} = \frac{V_{original}}{V_{actual}}$$

(Equation 3.9)

3.7.3   Poisson's ratio

3.7.3.1 Tension

A Hounsfield A10 tensometer was employed to measure the Poisson's ratio, where samples were loaded along the longitudinal and latitudinal directions up to strain of 1 at 0.1 intervals at a rate of 32.5 mm min^{-1}. To enable testing, and to ensure uniform straining, foam samples were bonded to two steel endplates of dimensions 35 mm × 40 mm × 2.5 mm (Figure 3.10), using a two part epoxy resin and allowed to cure at 23°C for 24 h. After being cured, the fixtures were visually assessed to check for any noticeable problem between the foam and fixture. Samples were then fixed into the manual tensile test machine and displaced to a strain of 1. If any evidence of failure was observed, testing was immediately stopped. For each interval of strain, sample displacement was temporally halted, and the change in sample length ($d\varepsilon_{length}$) and width ($d\varepsilon_{width}$) was measured using a hand ruler with an accuracy of ±0.5 mm. Poisson's ratio (υ) was then calculated using the following equation:

$$\upsilon = -\frac{d\varepsilon_{width}}{d\varepsilon_{length}}$$

(Equation 3.10)
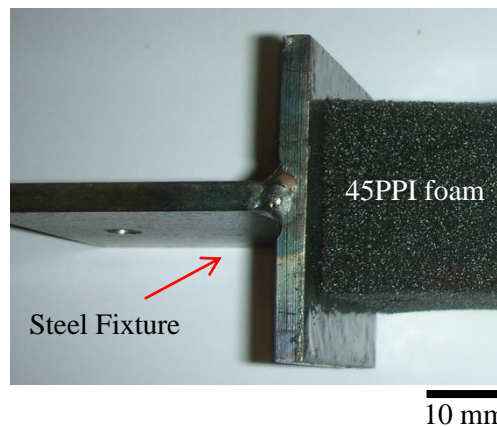
Figure 3.10: Foam sample bonded to the tensile fixture.

3.7.3.2 *Compression*

To assess the compressive Poisson's ratio, samples were subjected to the methodology outlined in 3.5. where a Canon 600D camera utilising an 18-55 mm F_{stock} 3.5 − 5.6 lens recorded the experimental procedure at a resolution of 1920 × 1080 (High definition) at a rate of 25 frames per second, with two Zaila Nila LED lights providing the light source. Prior to testing, a hand rule of accuracy (± 0.5 mm) was placed in line with the sample to allow conversion of pixels into millimetres.

On completion of the testing, the video files were cropped in to regions of interest and batch processed into tiff image files utilising Adobe After Effects. Every twenty-fifth image, (relating to one second of footage), was extracted using FIJI (an open source image processing software). Poisson's ratio was then calculated for each 0.1 strain interval by measuring (using a macro) the transverse strain at pre-marked region at every 60 images (relating to 10 mm extension), where a compensation factor was applied to account for any sample movement away or towards the stationary camera.

3.7.4   Optical microscopy

Optical microscopy is one of the more commonly implemented techniques for the analysis of auxetic foams as it offers the ability to produce quick non-destructive images of samples, with minimal training required. Combined with minimal sample preparation, the acquisition time of images is further reduced.

Akin to all equipment, the optical microscope has its disadvantages, such as the ability to only image a two-dimensional plane, the limited depth of field and resolution provided by cheaper equipment models that often makes it difficult to obtain clear, useable images. Since auxetic behaviour in foams is known to be triggered by the three-dimensional (3D) convoluted interconnected microstructural networks across the volume of the material these limitations are problematic.

Two optical microscopy systems: a WILD M410 Zoom macroscope and Keyence 'VHX-600' with magnification ranges up to ×32 and ×5000, respectively, were used to study the surface of the samples. Both systems contained embedded digital cameras allowing for the capture of digital images.

3.7.5 Scanning electron microscopy (SEM)

An alternative to optical microscopy can be found in SEM, which offers a variety of enhancements including resolution. Unlike optical systems that are limited to a theoretical resolution of approximately 200 nm [225], SEM is capable of achieving around 0.02 nm, resulting in greater observable details. Coupled with SEM's comprehensive magnification range up to ×1,000,000 and enhanced depth of field, it is possible to achieve high magnification, high resolution images of a samples surface [226]. SEM also includes features that are not available to optical microscopy, such as the ability to produce 3D images of surfaces using special software; this feature works by taking numerous images at various angles and using the information to generate 3D. Subsurface and internal features however cannot be obtained.

Unlike optical microscopy, SEM requires samples to be both small in size and electronically conductive. Since the foams are non-conductive there was a requirement to coat with a conductive material such as gold (i.e., gold sputtering). Unfortunately the coating procedure results in samples becoming unusable for any further experiments, thus SEM must be considered to be a destructive analytical technique. SEM images can be found throughout the literature, especially when individual auxetic pores are studied [17, 153, 158, 198, 227-229].

A JEOL JSM-6500F SEM and a JEOL JCM-6000 NeoScope with magnifications up to ×500,000 and ×60,000 with maximum resolutions up to 1.5 nm were employed to study the surface topography of conventional, auxetic and 3D printed samples (Table 3.10 details the various parameters used throughout this study). As the samples were intrinsically non-conductive a Polaron E5100 Series II Sputter Coater was used to gold coat the samples, the details of this process can be found in [230].

Table 3.10: SEM parameters used throughout study.

Figure	SEM System	Voltage / kV	Magnification	Working Distance / mm
4.7	JSM 6500F	15	x27	13.3
4.9	JSM 6500F	15	x25	13.3
6.1d	JSM 6500F	10	x12	29.8
6.2a	JCM 6000	15	x40	32
6.2b	JCM 6000	15	x17	30
6.3c	JCM 6000	15	x34	32

3.7.6 Computed Tomography (CT)

Unlike optical microscopy and SEM, CT is capable of producing 3-D data not only of the sample surface but throughout the volume of a body. For auxetic foams, this ability is very

important as auxetic microstructural ribs deform three-dimensionally. CT is capable of analysing large samples but achievable resolution is affected by both the area to be scanned and the equipment itself. Like optical microscopy, CT is a non-destructive technique and allows for *in-situ* experiments to be undertaken. This is a useful feature when dealing with auxetic foams, as experiments can be set up to study the changes in microstructure under various experimental conditions.

However, CT is the most expensive of the analytical imaging techniques described because of the high costs of the equipment, software and maintenance. Costs are further increased through the need to train expert researchers and users. CT is also a very time-consuming technique since it can take several hours to scan and digitally reconstruct a 3D volume. The lead time is further increased by sample preparation and the safety training required before any scans are undertaken. Some initial work has been reported by McDonald [132] and Gasper *et al.* [199], where the auxetic microstructure has been explored under tension and geometrically, respectively.

In this work an X-Tek (Now Nikon) benchtop CT system with a maximum scanning area of 200×200 mm and a resolution up to 5 µm [231] was used to investigate the compression aspect of the auxetic fabrication process where conventional foam samples were imaged in both uncompressed and compressed states. To replicate the volumetric compression within the CT scanner, moulds and endplates of the same dimensions as those described in Section 3.3.1, were manufactured from Perspex to enable a greater contrast between the mould and the foam material resulting in clearer images.

To optimise the number of scans, data and scan time required, symmetry about the mould's centre was assumed, resulting in region of interests of dimensions 30 mm $\times$ 30 mm $\times$ 50 mm being imaged using an X-ray source of 110 kV with a voxel resolution of 0.0433 mm. The scan data was then reconstructed using CTPro via filtered back projection algorithm [232] before being cropped, concatenated and converted to 8-bit grayscale using FIJI.

3.7.6.1 *Foam Density:*

The foam relative density change was then calculated via the following processes. 8-bit volumes were binarised (*i.e.,* image digitisation into 0 / 1) using an ISO50 threshold standard [233] to extract the foam structure. A region was cropped to include the internal region of the foam and exclude artefacts that were in the upper and lower 50 voxels of the scan. The relative density was calculated by dividing the number of voxels representing the foam

structure by the total number of voxels within a given slice. This was achieved using the standard voxel counter included within FIJI tool to represent relative density as a function of distance in the *z*-axis. As symmetry was previously assumed about the centre, the change in relative density was reflected at this point to represent complete samples.

3.7.6.2 Rib Structure:

To evaluate the rib structure of a foam sample, five local volume of dimensions 7 mm × 7 mm × 3 mm were extracted at random (random coordinates generated using [234]) locations from the previously binarised volumes. Each local volume was then processed by a standard skeletonisation tool using FIJI software, that essentially 'burns' away the foam material, retaining only its connectivity as a series of linear branches that begin and end at junctions [235]. On completion of the skeletonisation process, a results table is then outputted by the software, detailing various parameters including rib lengths, number of ribs, frequency of ribs and number of ribs per junction within a region of interest can be measured.

3.7.7   Impact Crater Measurements

In order to understand how a sample performed in absorbing energy, the impact craters left on the clay were measured using a Taicaan XYRIS 2000 surface profilometer. Unlike a physical surface profilometer, the Taicaan utilises a triangulation laser sensor vertically aligned towards a surface at a standoff distance. When initiated, the beam reflects from the surface to a pair of position sensing detectors mounted at opposing observation angles to the laser (43°). The dual sensor configuration stabilises the positional read out induced through absorbency changes (surface colour) and obstruction of the return beam (shadowing) caused by large features upon the surface.

Taicaan is a fully automated non-contact technique capable of scanning surfaces up to 100 mm × 100 mm at a working *z*-range of 25 mm (-12.5 mm to 12.5 mm). Coupled with a maximum resolution of 0.1 μm, complex crater geometries can be measured to a greater accuracy than the previous two methods discussed. If the region of interest exceeds the working area, it is possible to run multiple scans and stitch them together either vertically or horizontally, using the specialist software BODIES, as supplied by Taicaan. The BODIES software can also be used to extract quantitative data from the 3D surfaces. In this case the volume of the crater can be determined by normalizing the clay surface by applying a best fit plane.

The normalized surface separates volumes above (material that has been displaced during impact) and below (the crater) the plane and both volumes are considered as the total displacement volume due to impact. Should any data points fail to be obtained a median 3×3 filter can be applied to obtain them.

Furthermore, Taicaan outputs scan data as Cartesian coordinates in a readable digital format that can be accessed by third party software such as Microsoft Excel. This not only results in a permanent digital copy of the impact crater for future analysis but, due to the Cartesian coordinates, software such as Solidworks can reconstruct the data as models for further Finite Element Analysis. Although Taicaan is capable of achieving high resolution scans over a large area, increasing either the scanning area or resolution will result in an increase in the total scan time.

In order to maximise the data extracted from the samples and experimental methods, analysis of the auxetic foams was achieved through a combination of techniques. A range of quantifiable data was recorded including the physical geometry (ruler, digital vernier callipers), *ex situ* microstructure (optical microscopy, SEM), internal microstructure (computed tomography), energy absorption and crater depth (Taicaan surface profilometer). In many instances, the data obtained through these techniques can be exported for use with computer software, allowing for further quantification to be undertaken through image processing, computer simulations and rapid prototyping.

3.7.8   Digital volume correlation

Digital Volume Correlation (DVC) is a powerful computation tool used for mapping and detailing full field deformations of 3D volumes through pattern correlation algorithms. Generally, there are two main approaches used to quantify continuum level strain measurements: local correlation and global correlation. However, for the work presented here only the local correlation was considered. Local correlation consists of taking two volumes (reference and deformed) and dividing them in to sub-volumes, before being independently correlated through a fast Fourier transform (FFT), as detailed in (Figure 3.11) [28]. Should the user choose, this process can be set to run in a multi-pass approach, in which displacement gradient data from previous passes is used to deform the sub-volumes prior to the next pass of cross-correlation [28, 236].
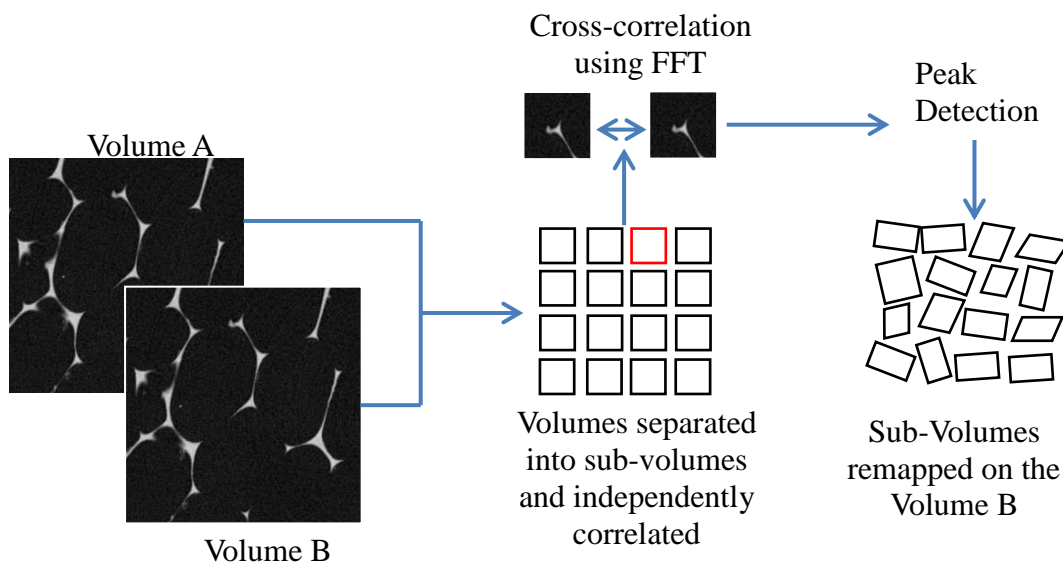
Figure 3.11: Diagrammatic representation of DVC employing a local correlation approach.

To enable the use of this technique auxetic and conventional foams were individually placed into an in-house designed quasi-static compression rig, comprising of a cylindrical Perspex (to allow more uniform X-ray penetration over 360° rotation, and good contrast) tube with an internal diameter of 50 mm and height of 200 mm, coupled with a hemispherical polystyrene ball (diameter 10 mm) connected via a 6 mm threaded rod to the tube (Figure 3.12).
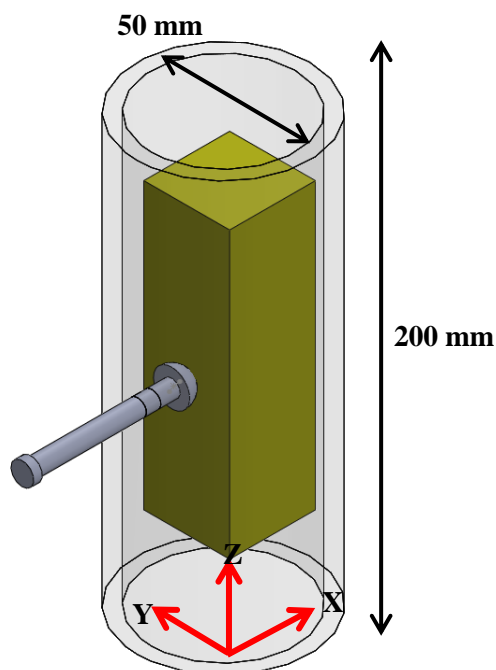
Figure 3.12: Quasi-static compression rig for use with computed tomography.

The quasi-static compression rig containing a foam sample was then placed into an HMX X-Ray computed tomography scanner (detailed in Section 3.7.6) and a full 3D scan was performed across 2000 radiographs with a 38.4 μm voxel resolution, in a vertical orientation. When the scan was completed, the threaded polystyrene indenter was rotated by a one full rotation, inducing a displacement of 1.1 mm in the *X* orientation. The full scan programme per sample is shown in Table 3.11.

Table 3.11: DVC scan experimental plan.

Scan Title	Description
A	Pre-scan, no displacement of the foam – used as part of the measurement noise study.
B	Second pre-scan, no displacement of the foam – used as second dataset in the measurement noise study.
C	Five pixel displacement in the Z-axis to assess the rigid body movement feature of the software – used to align datasets that are offset.
D	Indenter displaced 1.1 mm into the foam sample by one rotation.
E	Indenter displaced 1.1 mm into the foam sample by one rotation.

On completion of the CT scans, the radiographs of a sample in each compressive state (Table 3.12) were reconstructed using CT Pro, before being imported into LaVision's DaVis strain mapping software to determine the 3D pattern correlations with respect to the parameters set by the user. Once the strain mapping was completed, the data was then exported into Matlab 64-bit where the in house created scripts were used to output the vector field data.

Table 3.12: DVC user input parameters with a sub volume percentage overlap of 50%.

Sub volume dimensions (Pixels)	Number of passes run
160×160×160	2
128×128×128	2
96×96×96	2
64×64×64	2
48×48×48	2
32×32×32	2

Chapter 4: The effects of fabrication parameters on auxetic foams

4.1 Introduction

For auxetic foams to be considered for the application of trauma attenuating backings, it is important to first ascertain the influence of the fabrication parameters on Poisson's ratio. Unlike conventional polyurethane foams, that are known to have a positive Poisson's ratio of approximately 0.3 [222], auxetic foams are often reported to be anisotropic [13, 103, 158, 185], thus requiring assessment of both their longitudinal and latitudinal orientations in order to fully characterise the effect of the fabrication parameters.

Overall, in this study a total of 72 fabrication parameter combinations (based on published literature and in-house experiments) were quasi-static tensile tested (four samples per combination), over a strain range of zero to +1 at 0.1 intervals, in accordance with the methodology described in Chapter 3.

Following tensile testing, the fabrication parameter combinations were then assessed for their variability and repeatability to produce a negative Poisson's ratio. By utilising a tensile loading methodology prior to compressive testing, not only can the effect of the fabrication parameters be explored, but volumetrically unstable samples may also be identified prior to impact testing by any large permanent volumetric changes, as observed in literature [24, 107].

Auxetic fabrication parameters (including volumetric compression ratio and heating time) were individually explored to ascertain their influence on the auxetic fabrication process and in turn the variability induced in the material systems.

4.1.1 Results and discussion

4.1.1.1 Poisson's ratio vs. strain

Figure 4.1 to Figure 4.4 show the mean Poisson's ratio per unit strain for each combination of the fabrication parameters (pore per inch, heating times and volume compression ratios), *i.e.,* longitudinal and latitudinal orientations for 10 PPI and 45 PPI foams. Error bars are intentionally absent in order to convey the data in a clear manner, however, an example of a raw dataset of a Poisson's ratio with error bars, coupled with a worked example of Poisson's ratio measurement can be found in Appendix 4A.
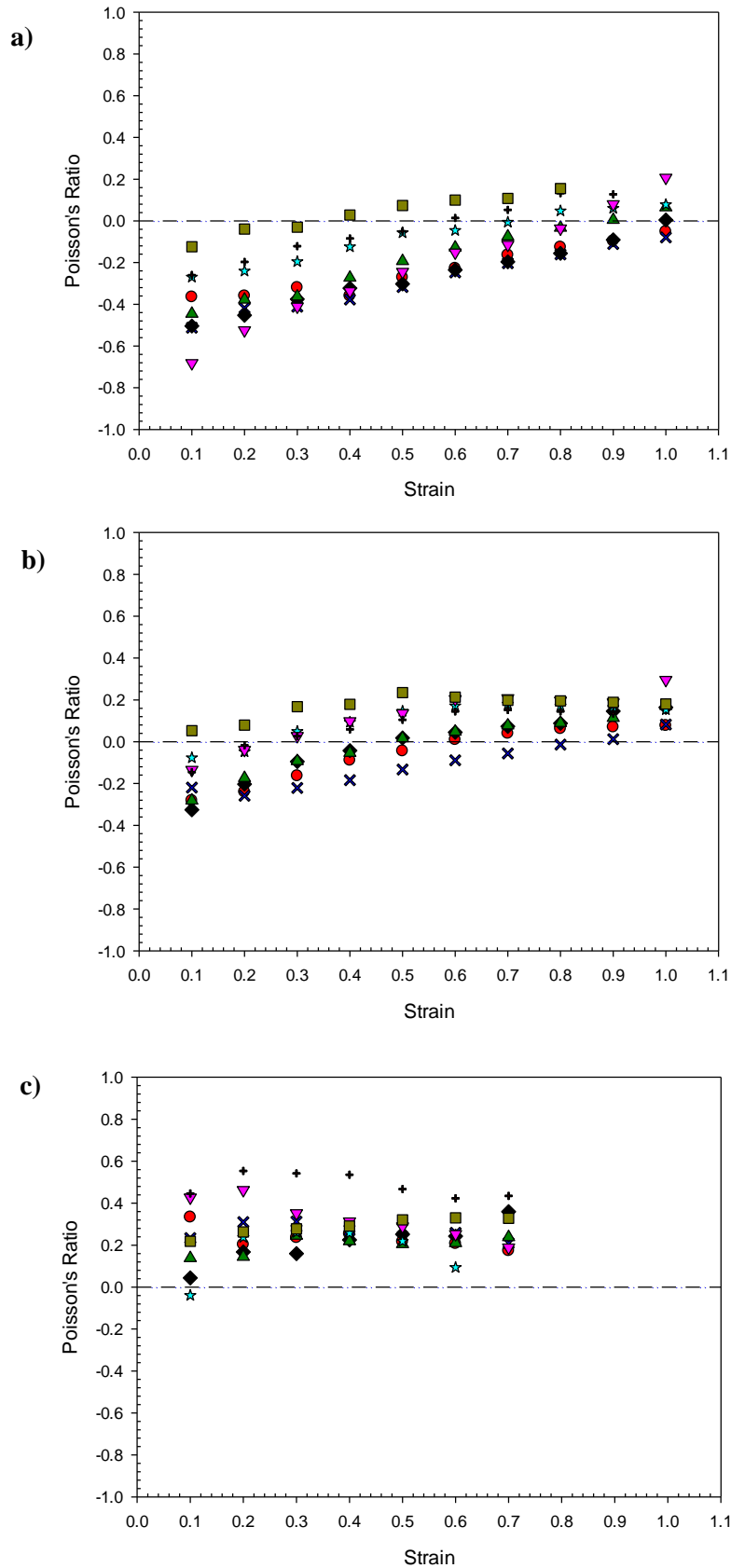
Figure 4.1 Poisson's ratio behaviour with respect to strain and heating times: 60 minutes (●), 55 minutes (×), 50 minutes (♦), 45 minutes (▲), 40 minutes (★), 35 minutes (▼), 30 minutes (+) and 25 minutes (■) for the longitudinal 45 PPI polyurethane foam: **(a)** 4.88, **(b)** 3.91 and **(c)** 2.93 volumetric compressions, where the dashed line denotes the negative and positive Poisson's ratio boundary.
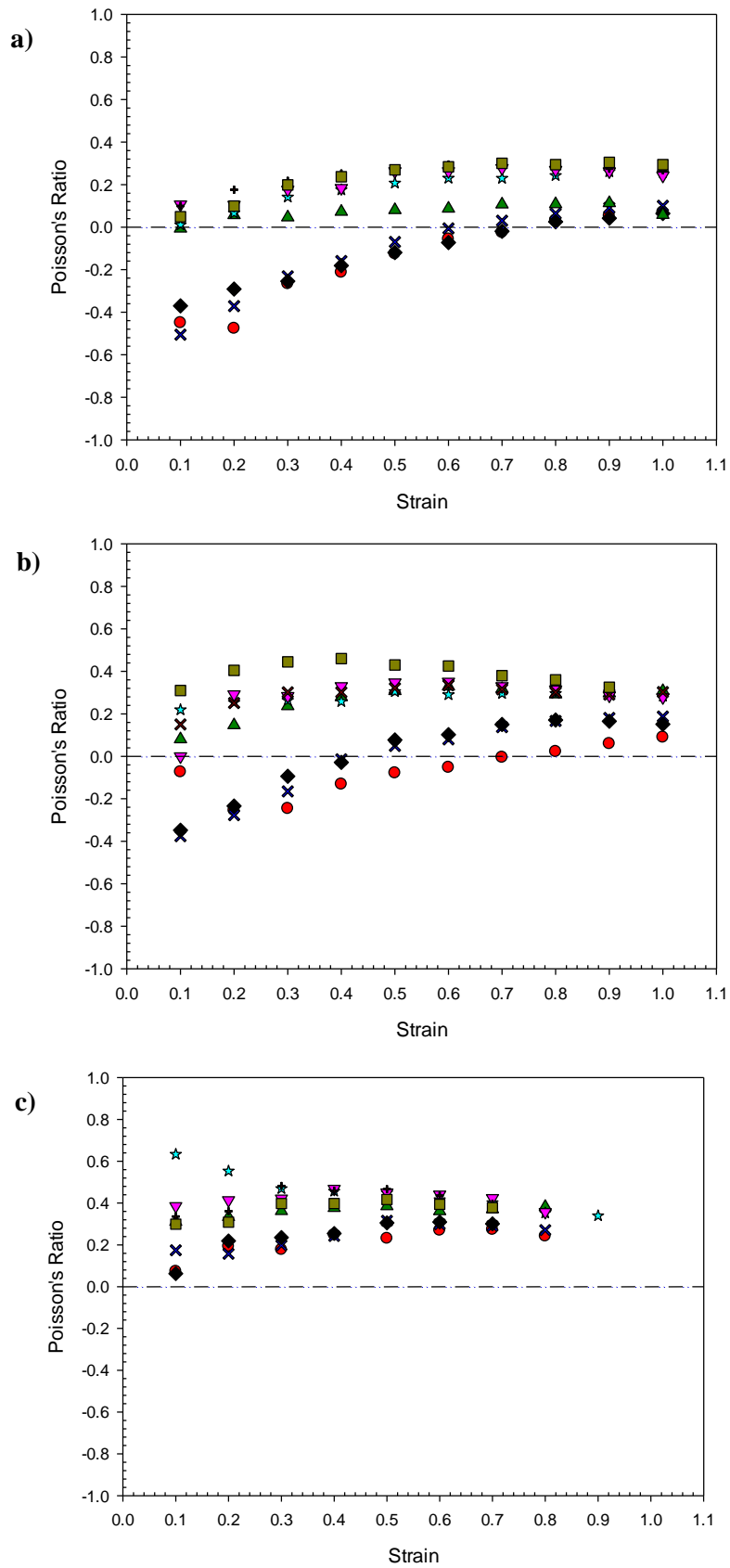
Figure 4.2: : Poisson's ratio behaviour with respect to strain and heating times: 60 minutes (●), 55 minutes (×), 50 minutes (♦), 45 minutes (▲), 40 minutes (★), 35 minutes (▼), 30 minutes (+) and 25 minutes (■) for the longitudinal 10 PPI polyurethane foam: **(a)** 4.88, **(b)** 3.91 and **(c)** 2.93 volumetric compressions, where the dashed line denotes the negative and positive Poisson's ratio boundary.
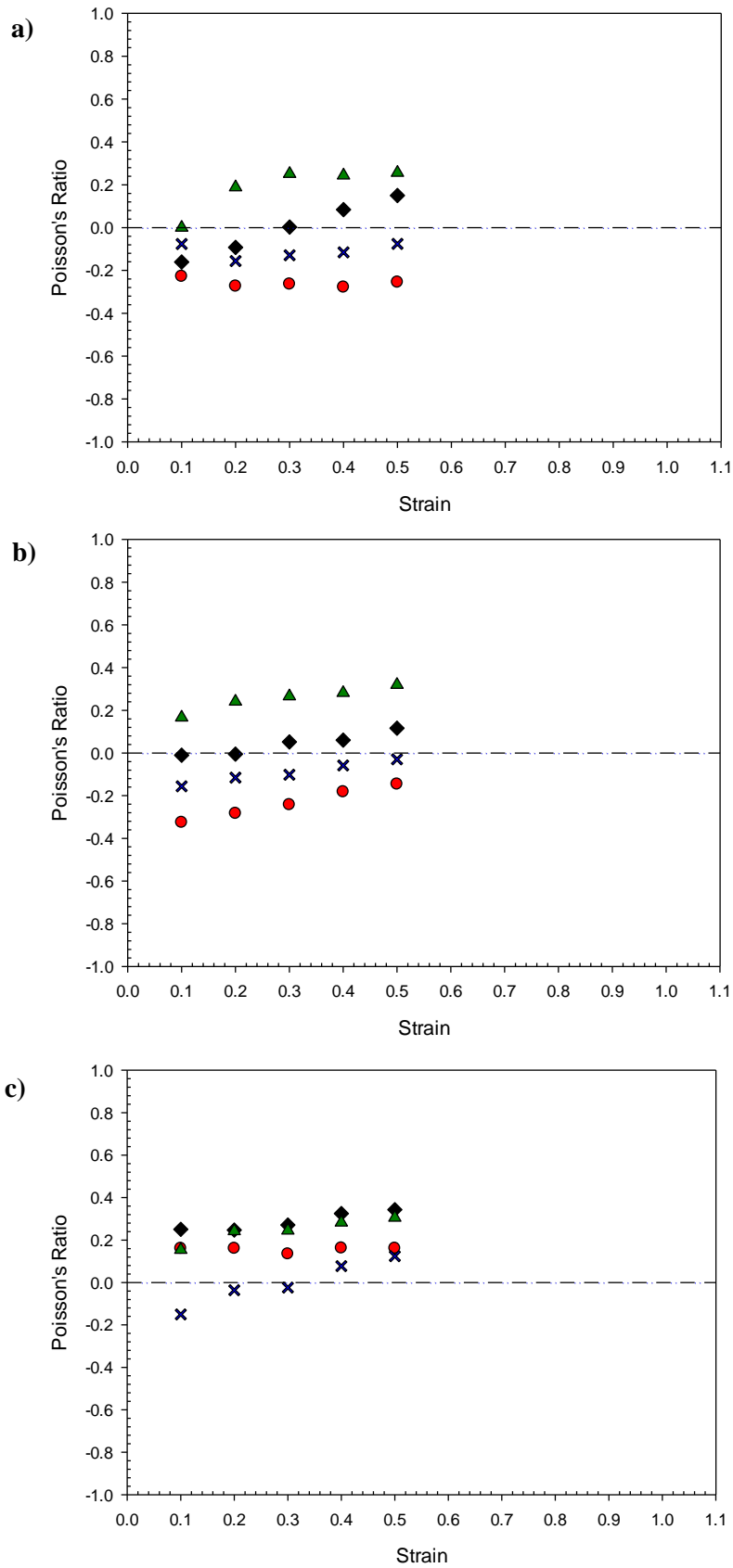
Figure 4.3: Poisson's ratio behaviour with respect to strain and heating times: 60 minutes (●), 50 minutes (×), 40 minutes (♦) and 30 minutes (▲) for the latitudinal 45 PPI polyurethane foam: **(a)** 4.88, **(b)** 3.91 and **(c)** 2.93 volumetric compressions, where the dashed line denotes the negative and positive Poisson's ratio boundary.
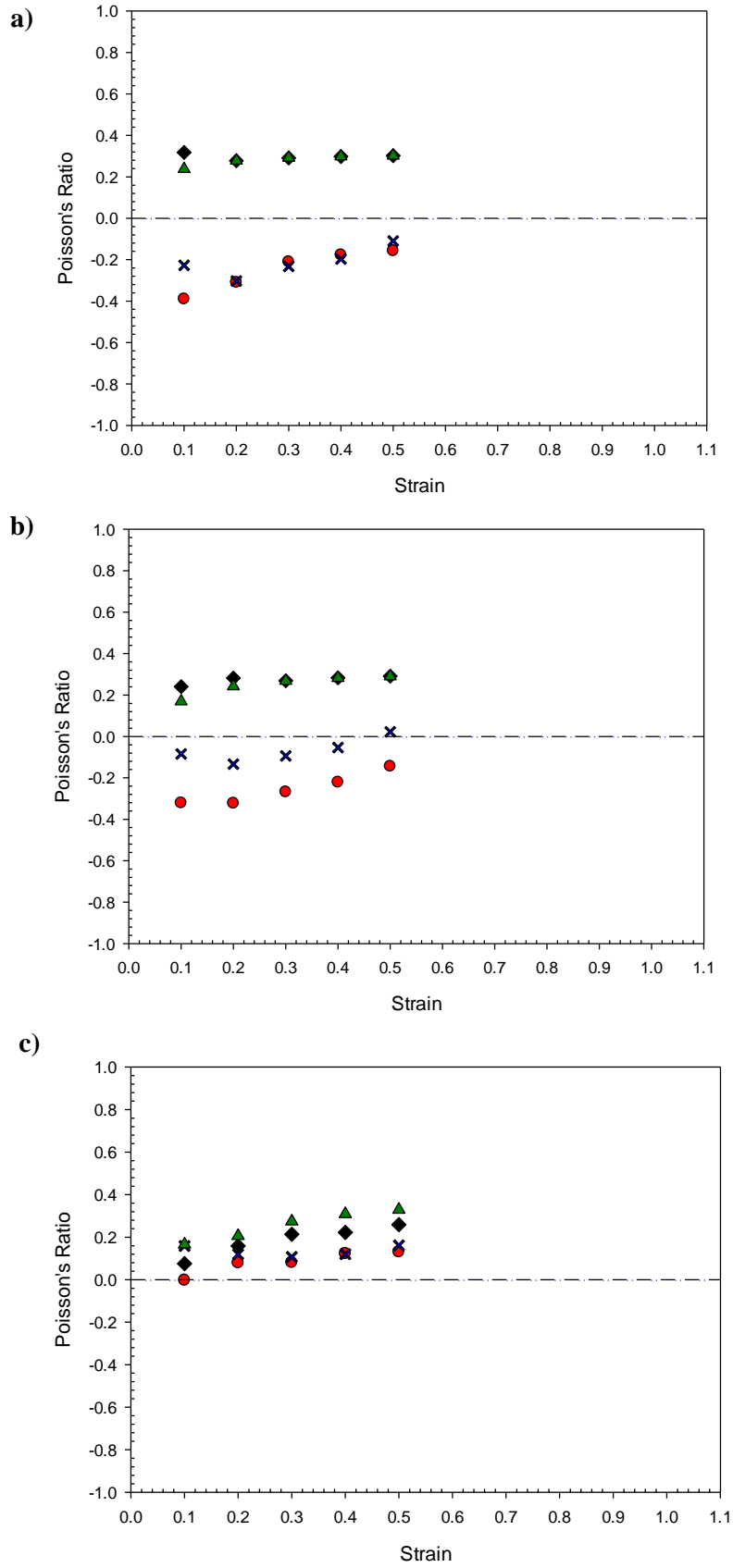
Figure 4.4: Poisson's ratio behaviour with respect to strain and heating times: 60 minutes (●), 50 minutes (×), 40 minutes (♦) and 30 minutes (▲) for the latitudinal 10 PPI polyurethane foam: **(a)** 4.88, **(b)** 3.91 and **(c)** 2.93 volumetric compressions, where the dashed line denotes the negative and positive Poisson's ratio boundary.

For the longitudinal oriented 45 PPI and 10 PPI foams, both 4.88 and 3.91 volumetric compression ratios demonstrate an almost linear convergence towards a positive Poisson's ratio with respect to strain (Figure 4.1a, Figure 4.1b, Figure 4.2a and Figure 4.2b). This behaviour was additionally shown to occur for the latitudinal 45 PPI and 10 PPI foams fabricated at 4.88 and 3.91 volumetric compressions (Figure 4.3a, Figure 4.3b, Figure 4.4a and Figure 4.4b), but only for a limited number of heating times. Once a positive Poisson's ratio was achieved, the Poisson's ratio exhibits a plateau effect for the remaining intervals of strain, indicating the return to a conventional foam performance.

Alternatively, should the fabrication process fail to induce a negative Poisson's ratio (as shown at the lowest volumetric compression ratio of 2.93 (Figure 4.1c, Figure 4.2c, Figure 4.3c and Figure 4.4d), with the exception of the latitudinal 45 PPI, 50 minute sample) in nearly all instances, the Poisson's ratio fluctuates between 0.1 and 0.3 per interval strain until either the applied load ceases or failure occurs. There are however some instances when this behaviour does not occur, (for example the longitudinal 40 minutes 10 PPI samples), due to one or more of the four samples produced for a given combination of parameters exhibiting potentially erroneous data, as shown in Figure 4.5 and Figure 4.6.
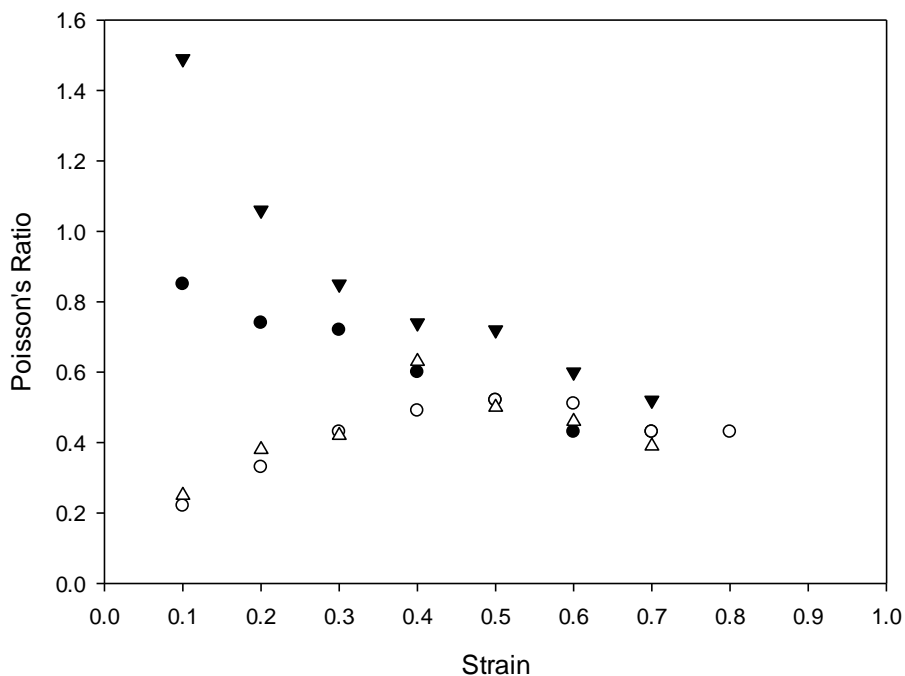
Figure 4.5: Poisson's ratio *vs*. strain for all four longitudinal samples produced at 40 minutes for a 10 PPI foam.
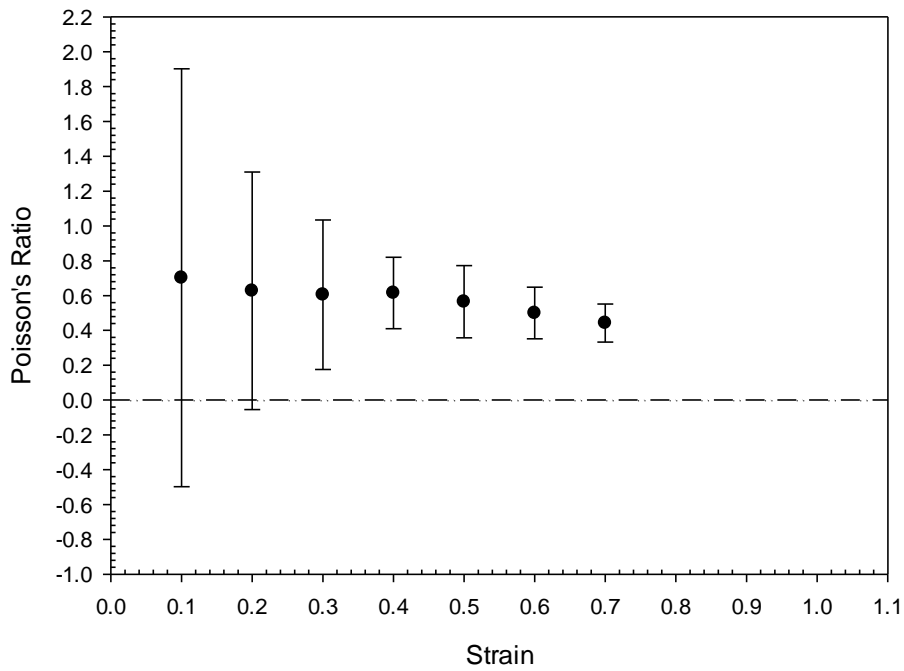
Figure 4.6: Mean Poisson's ratio *vs.* strain for all longitudinal samples produced at 40 minutes for a 10 PPI foam, where error bars are provided by a 95% confidence interval.

For any given foam, the overall Poisson's ratio behaviour exhibited can be attributed to its cellular microstructure. For example, during the auxetic phase, where a foam displays a negative Poisson's ratio, the cellular microstructure is in a random concaved configuration (Figure 4.7), comprised of cellular ribs orientated via rotation, bending and stretching [158] which are induced by compression during fabrication. When a tensile load is applied (causing a strain), the cell ribs displace in multiple directions in an attempt to return to their original microstructure (Figure 4.8 and Figure 4.9). On returning to a conventional microstructure, further loading will cause the foam to once more behave as a regular foam material (with a positive Poisson's ratio) until either the applied load ceases or failure occurs.
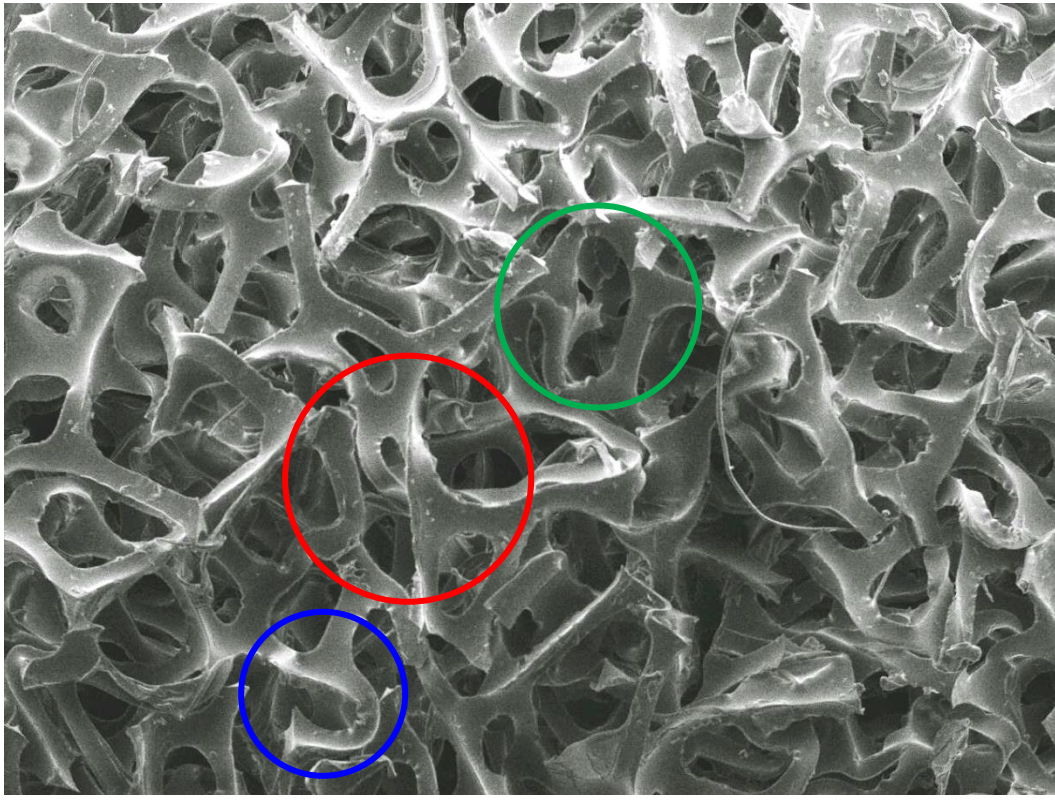
1 mm

Figure 4.7: SEM showing the random cellular rib structure and its deformation mechanisms of rotation (red circle), bending (blue circle) and stretching (green circle) of an auxetic polyurethane foam (45 PPI), fabricated at a 4.88 volumetric compression ratio and 60 minutes heating.
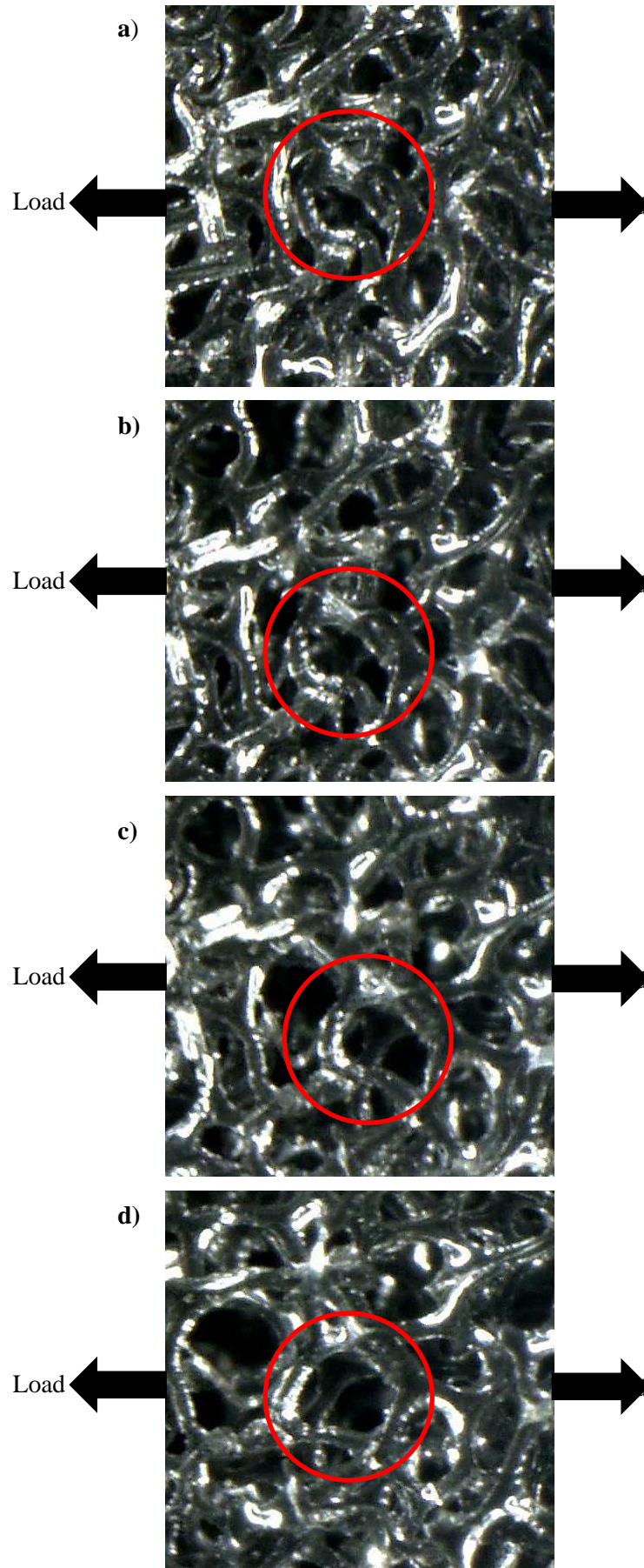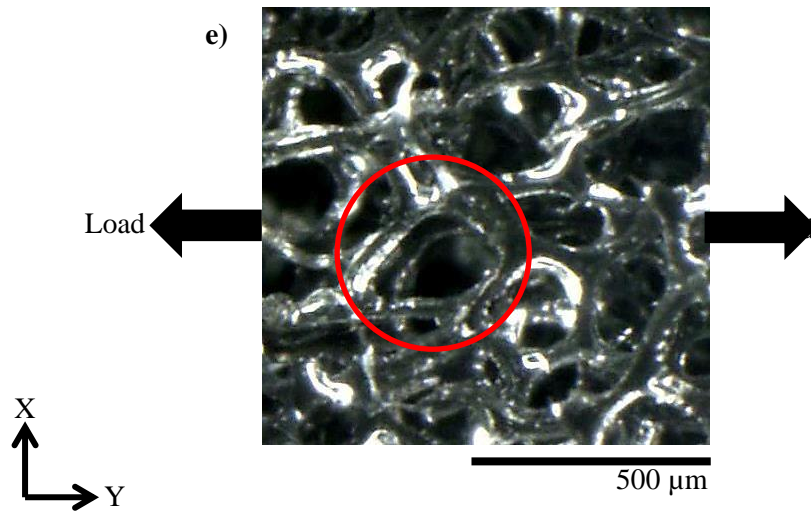
Figure 4.8: Optical microscopy showing strain induced structural changes from **(a)** auxetic to **(e)** conventional, in an auxetic polyurethane foam (45 PPI), fabricated at a 4.88 volumetric compression ratio and 60 minutes heating. The strains were assessed as follows: **a)** 0, **b)** 0.26, **c)** 0.43, **d)** 0.6 and **e)** 0.88.
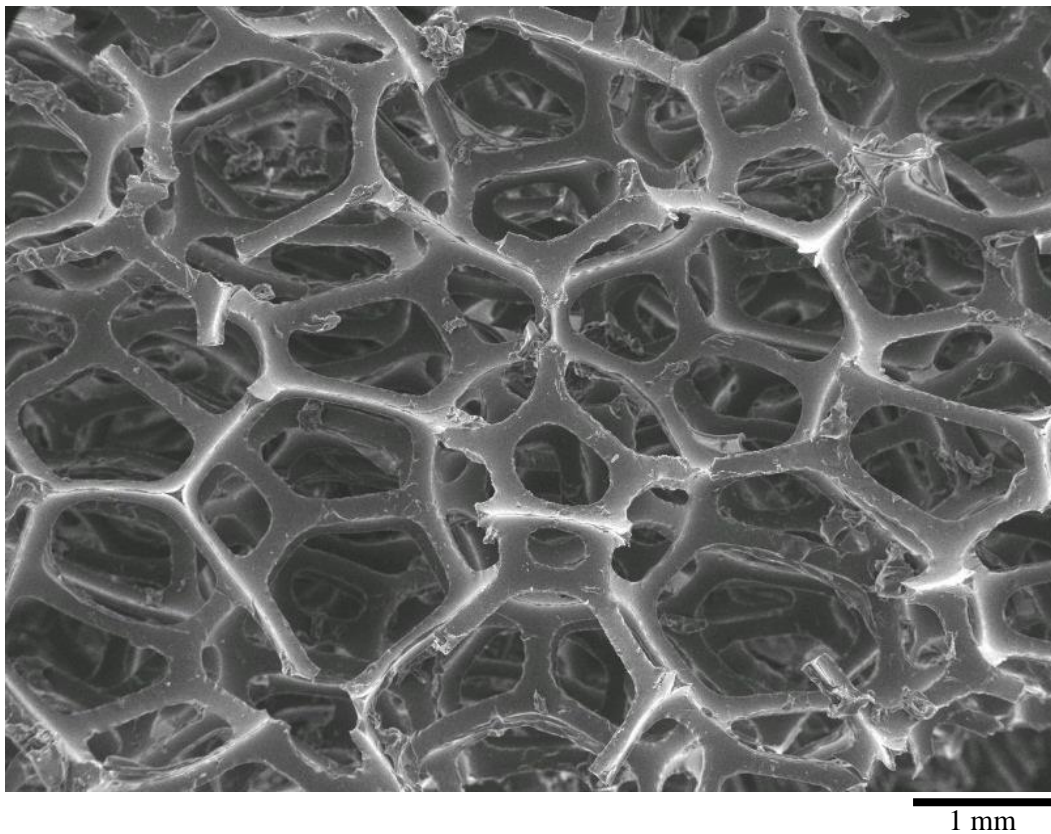
Figure 4.9: SEM of the open cellular microstructure of a conventional 45 PPI polyurethane foam.

Unfortunately, when considered with respect to a 95% confidence interval, the relationships shown in Figure 4.1 to Figure 4.4 are only applicable for mean values, as large errors frequently cause data ranges to overlap, indicating that a foam has equal chance of falling between the values plotted. In the majority of datasets, the largest error is often shown to

occur at the 0.1 strain interval, which decreases with an increase in strain [153]. This can be attributed to sample positioning before any loading has been applied. While the utmost care is taken to ensure samples are positioned within the tensometer in a flat, taut state, often when an initial strain is applied, an increase in tautness and not displacement occurs. Error also stems from the measuring of the transverse strain by hand. While a reference line was drawn across the centre of the sample to enable transverse strain change at the same location per interval strain, due to the line thickness, coupled with human error and equipment inaccuracies it is unlikely the correct position or measurement will be recorded [153]. To explore the extent of this error, conventional 45 PPI foams were tensile loaded utilising an Instron test machine at a rate of 10 mm min^{-1} (1.6×10^{-3} s^{-1}), where a Canon 600D camera visually captured the event as detailed in Section 3.7.3.2.

It was found, that the Instron and Hounsfield tensile tensometer method, led to differences in calculated Poisson's ratio for the same material systems, as shown in Figure 4.10. This difference led to a higher range of Poisson's ratios, up to 0.13, being recorded by the Hounsfield tensometer method. The cause of these differences is likely to be attributable to the measurement accuracy utilised, *i.e.,* a ruler with a resolution of 0.5 mm *vs.* the Canon camera setup with a resolution of ≈0.1 mm for the Hounsfield and Intron methods, respectively. These differences make it difficult to compare the Poisson's ratio in material systems when conducted across the two different methods. To better enable comparison of material systems conducted on different test methods, differences in Poisson's ratio above 0.13 are required.
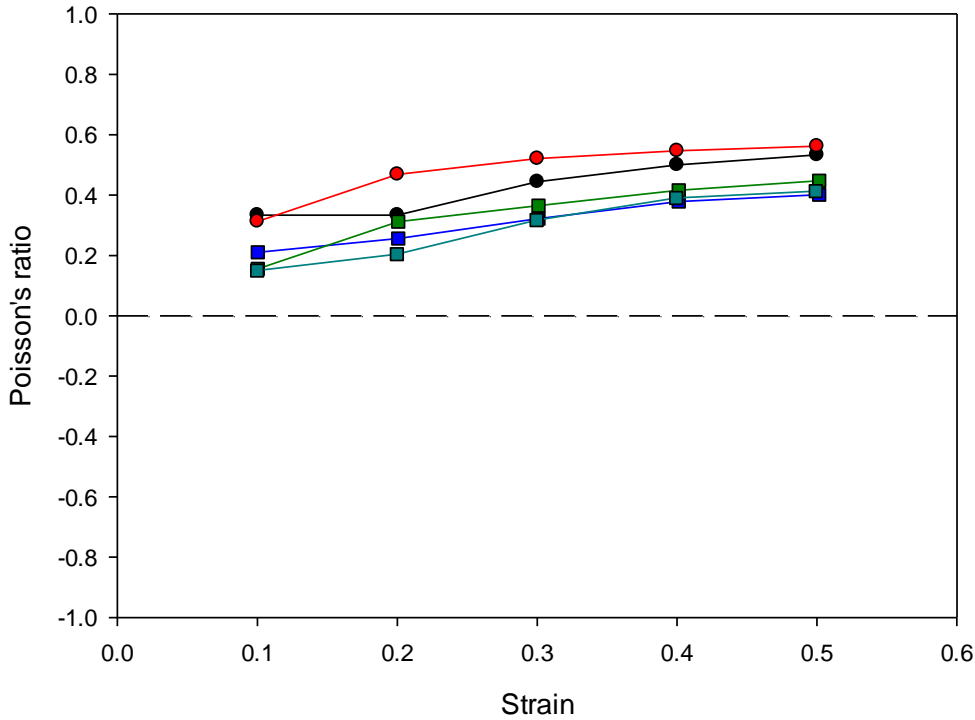
Figure 4.10: Poisson's ratio relative to strain for conventional 45 PPI foam measured using a Hounsfield hand tensometer (red and black lines) and an Instron (blue, green and cyan lines).

Tensometer measurements brings into question the integrity of Poisson's ratio calculated using these methods regarding the accuracy and techniques used in deriving this parameter, in addition to local geometrical variations attributed to the material. Both tensometer measurements rely on the longitudinal and transverse displacement to calculate the overall average strains along these two axes. Additionally, the Poisson's ratio was calculated along the central reference line resulting in only the average Poisson's ratio being calculated for a given strain interval. This has implications in calculating the Poisson's ratio as it was shown in a previous study [156], utilising digital volume correlation (DVC), that both auxetic and conventional foams are heterogeneous and exhibit local and quite significant variations in Poisson's ratio and strains (attributed to localised irregularities in cell sizes and wall thicknesses) [156].

Furthermore, by measuring the Poisson's ratio at a pre-defined area, such as a reference line, the influence of edge effects in accordance to Saint-Venant's principle, must also be considered. According to Saint-Venant, when a load is applied to a cross-sectional area (such as that experienced by a sample during tensile loading), the resulting internal stresses (and in turn the strains) from these loads are only significant over a portion of the body equivalent to the width of the cross-sectional area. In other words, higher stresses are exhibited nearest to the boundary load conditions, which decay at an effective distance equivalent to the cross-sectional width [237, 238]. However, according to Lakes [11], the

decay of Saint-Venant's effects is also influenced by a sample's geometry and Poisson's ratio, as shown in Figure 4.11.

In this study, two foam sample geometries were used, *i.e.,* longitudinal (30 mm × 30 mm × 100 mm) and latitudinal (30 mm × 30 mm × 30 mm). Due to the geometries used in the latitudinal case, Saint-Venant's effects are likely to influence the measured Poisson's ratio. Conversely, the measured reference line for the longitudinal samples are outside the range denoted by the Saint-Venant's region and are unlikely to experience this phenomenon. The influence of Saints-Venant's effects with respect to Poisson's ratio was not explored in this study. However, this may be an important phenomenon regarding the geometry of the sample tested.
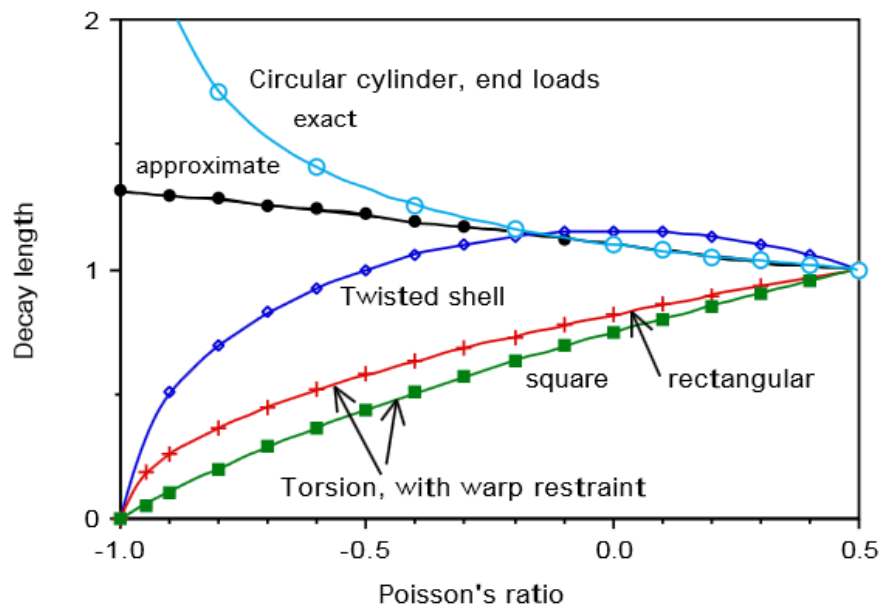
Figure 4.11: Saint-Venant's decay length *vs*. Poisson's ratio for different sample geometries [11].

The limitations of the current auxetic fabrication methodology must also be considered. The volumetric compression aspect of fabrication, coupled with the already heterogeneity of the base foam [158, 160], results in an uncontrollable distribution of deformed cells. Where consistency in manufacturing is considered, each foam sample has a very different, if not unique, cell arrangement. To add to this complexity, the fabrication process has the potential to induce surface artefacts, or crumpling zones [13, 128], which can significantly affect the overall Poisson's ratio, due to further irregular rib unfolding. The influence of sample test direction must also be considered as polyurethane foams have a natural elongation direction as a result of their production process [159, 160]. This elongation is of particular note, as when coupled with auxetic fabrication process, there is evidence to

suggest from Figure 4.7 and 4.8 that cells favour deformation about their longest ribs. By favouring the elongation direction for cell deformation, the foam samples will be anisotropic [158], resulting in axially different Poisson's ratios, as supported by Refs [14], *i.e.,* the manufacturing process introduces anisotropic behaviour into the material's system.

4.1.1.2 Sample analysis

The success rate of producing foam samples with negative Poisson's ratios are shown in Figure 4.12 and Figure 4.13, as a function of heating time, compression ratios, porosities and sample orientation. In total 39% of the samples were found to demonstrate a negative Poisson's ratio, across the range of heating times, volumetric compression ratios and porosities studied. Longitudinal 45 PPI foams were found to be the most successful at auxetic conversion, where 57% demonstrated a negative Poisson's ratio, while conversion rates of only 21%, 42% and 33% were found for the longitudinal 10 PPI, latitudinal 45 PPI and latitudinal 10 PPI, respectively. For each foam type and orientation, as the heating time and volumetric compression ratio decreases, the probability of producing a negative Poisson's ratio decreases, indicating that auxetic fabrication is reliant on both heating time and volumetric compression, as supported by Wang *et al.* [134]. This observation however fails to explain why for a given heating time and volumetric compression ratio variability in the Poisson's ratio exists. To understand this behaviour, volumetric compression ratio and heating time were individually explored to ascertain their influence on the auxetic fabrication process and in turn the variability induced in the material systems.
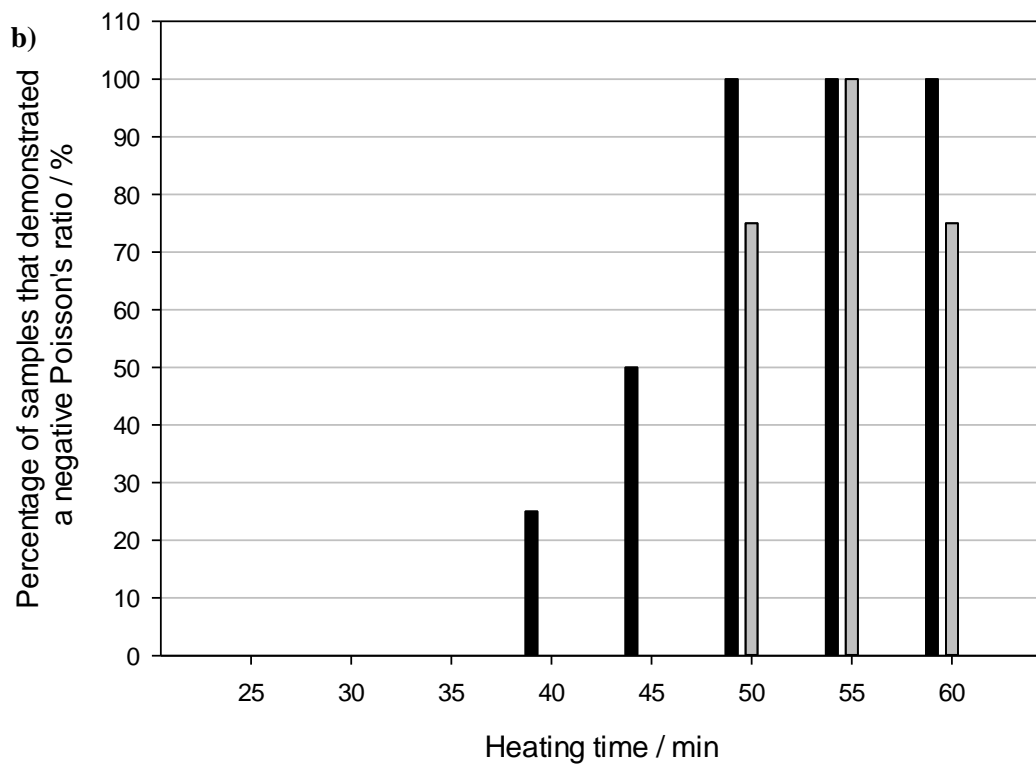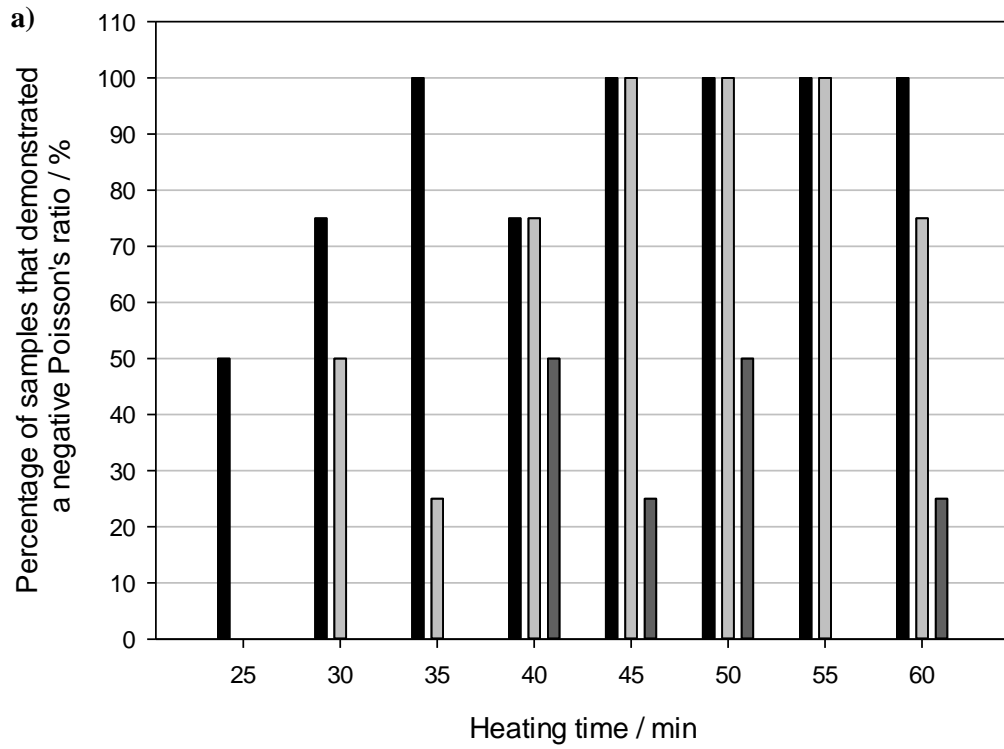
Figure 4.12: Percentage of longitudinal orientated foam samples that demonstrated a negative Poisson's ratio for a given heating time and volumetric compression ratios of 4.88 (black bar), 3.91 (light grey bar) and 2.93 (dark grey bar) for: **(a)** 45 PPI and **(b)** 10 PPI polyurethane foams.
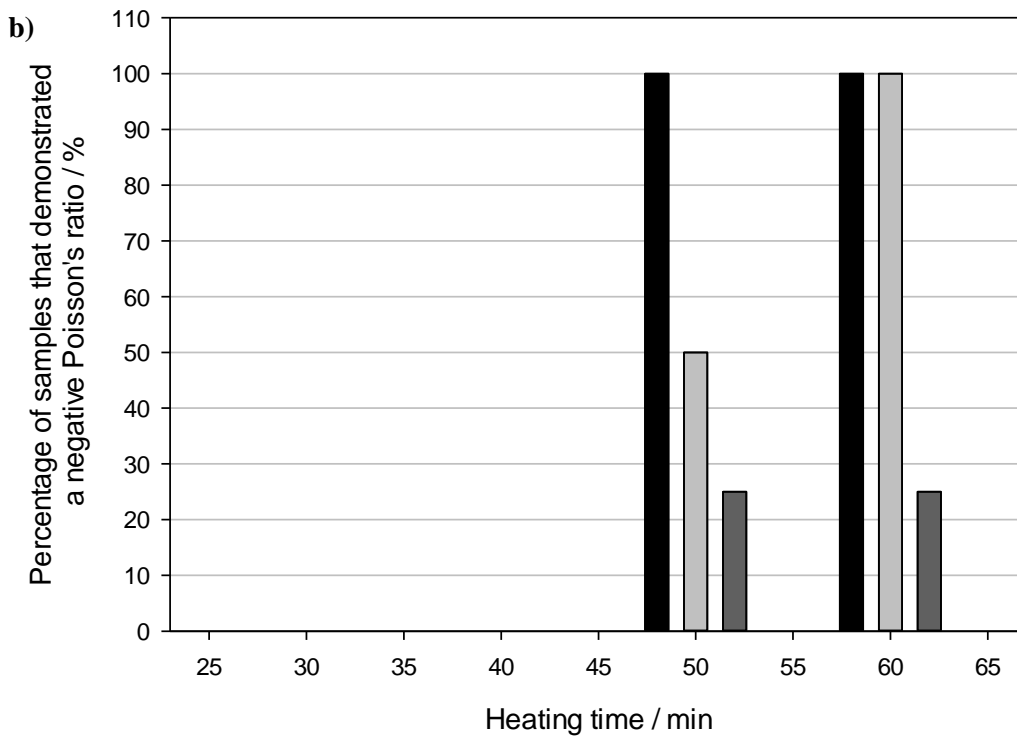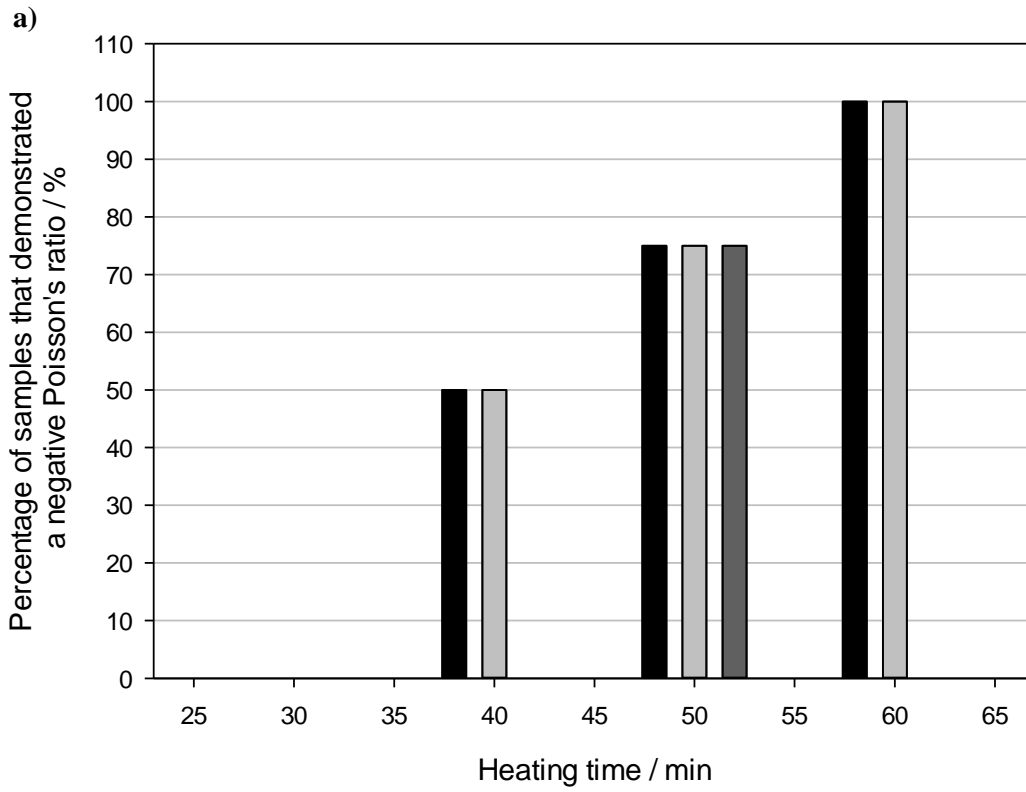
Figure 4.13: Percentage of latitudinal oriented foam samples that demonstrated a negative Poisson's ratio for a given heating time and volumetric compression ratios of 4.88 (black bar), 3.91 (light grey bar) and 2.93 (dark grey bar) for: **(a)** 45 PPI and **(b)** 10 PPI polyurethane foams.

4.1.1.3 Influence of heating and volumetric compression ratio

For the manufacture of auxetic materials, a critical softening temperature is required to be obtained by the material system to instil the new auxetic foam structure [103, 130]. It is important to know the heating time required to achieve this temperature, which varies but is not limited to the following: relative density, sample size, foam porosity and base material. To minimise the complexity of this study, only parameters previously outlined in Chapter 3, are considered.

Figure 4.14 shows the temperature-time profile measured at the centre of the sample for 45 and 10 PPI foams subjected to volumetric compressions of 2.93, 3.91 and 4.88. It is clear from the 45 PPI system that lower compression ratios lead to quicker heating times; in this instance by up to 14%. This is attributed to a higher heat capacity in the polyurethane base material, compared to the air, which is three orders of magnitude greater [222]. Thus, higher compression ratios increase the relative density of the foam material, *i.e.,* increasing the ratio of polyurethane base material to air, which therefore increases the heat required to raise the temperature of the foam. It is interesting to note, that when comparing 45 PPI against 10 PPI, the former system heats marginally quicker, despite having higher relative densities. It is suspected that as heating occurs through thermal conductivity and convection, the differences in cell size between the two systems could account for these differences in heating time. This behaviour has also been reported by Wang *et al.* [134], where it was observed that foams with smaller cell sizes require shorter auxetic fabrication processing times. What is clear from figure 4.14a and figure 4.14b is that relative density and cell size, influence heating time. These are important parameters that should be considered when modelling the thermal behaviour to predict heating times as will be discussed later.
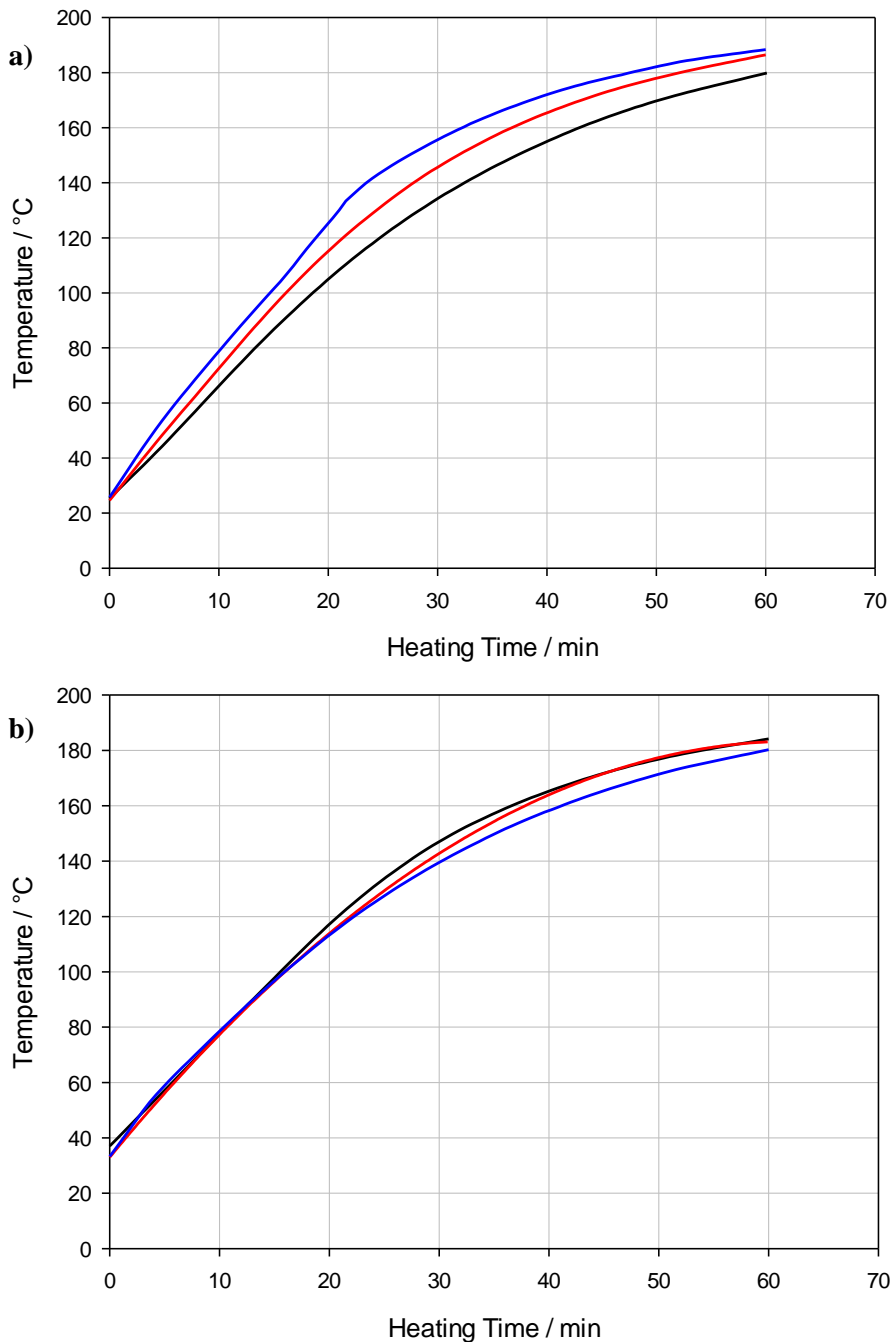
Figure 4.14: Experimental thermocouple data: **a)** 45 PPI and **b)** 10 PPI foam subjected to a volumetric compression ratio of 4.88 (black line), 3.91 (red line) and 2.93 (blue line)**.**

4.1.1.3.1   Heat Model:

To ascertain the influence of heating time on auxetic fabrication, a two-dimensional heat transfer COMSOL Multiphysics model was created. This model was comprised of three distinct regions (each with their own properties, coupled with a uniform heating source, set at 200°C, and a cold region to represent convection between the hot oven and cold mould. The model was then calibrated against mean empirical thermocouple data (45 PPI foam

compressed at a volumetric compression ratio of 4.88 as shown in Appendix 4B) by varying the size of the cold region, until the theoretical and empirical time-temperature profiles converged (Figure 4.15).
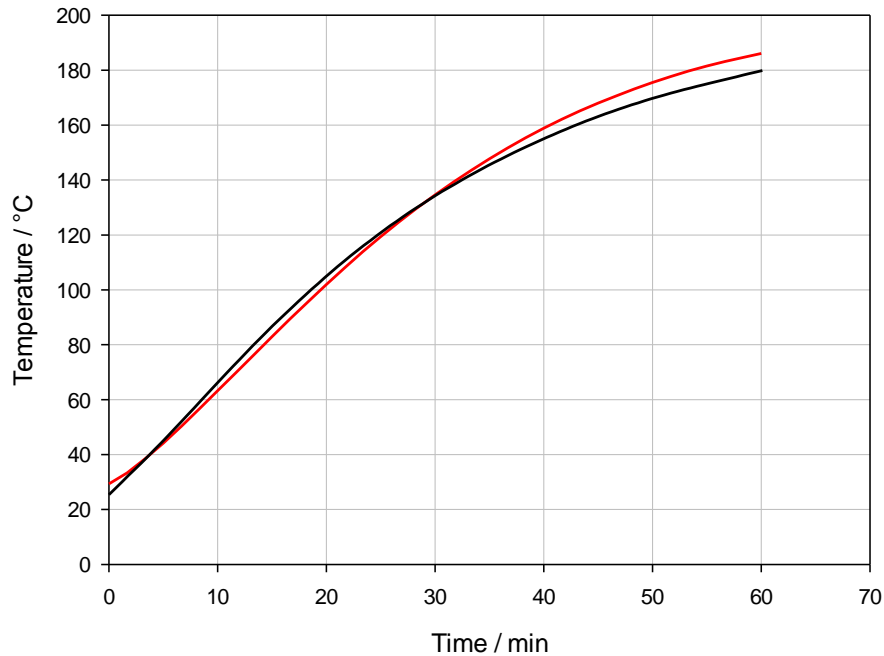
Figure 4.15: Mean experimental thermocouple data of 45 PPI foam subjected to a volumetric compression ratio of 4.88 (black line) *vs*. model data (red line).

It was found that when compared to the experimental data, the model exhibited an initial heating rate slightly slower than the experimental data. As the heating time increased, the heating rate of the model converged to the experimental data at approximately 29 minutes, until finally exceeding it. On completion of the 60 minutes heating cycle, the model was shown to overestimate the internal temperature by 6°C. Following calibration, it is then possible to establish the influence of the volumetric compression ratio and heating time by varying the properties of the foam region and running the simulations (Figure 4.16).
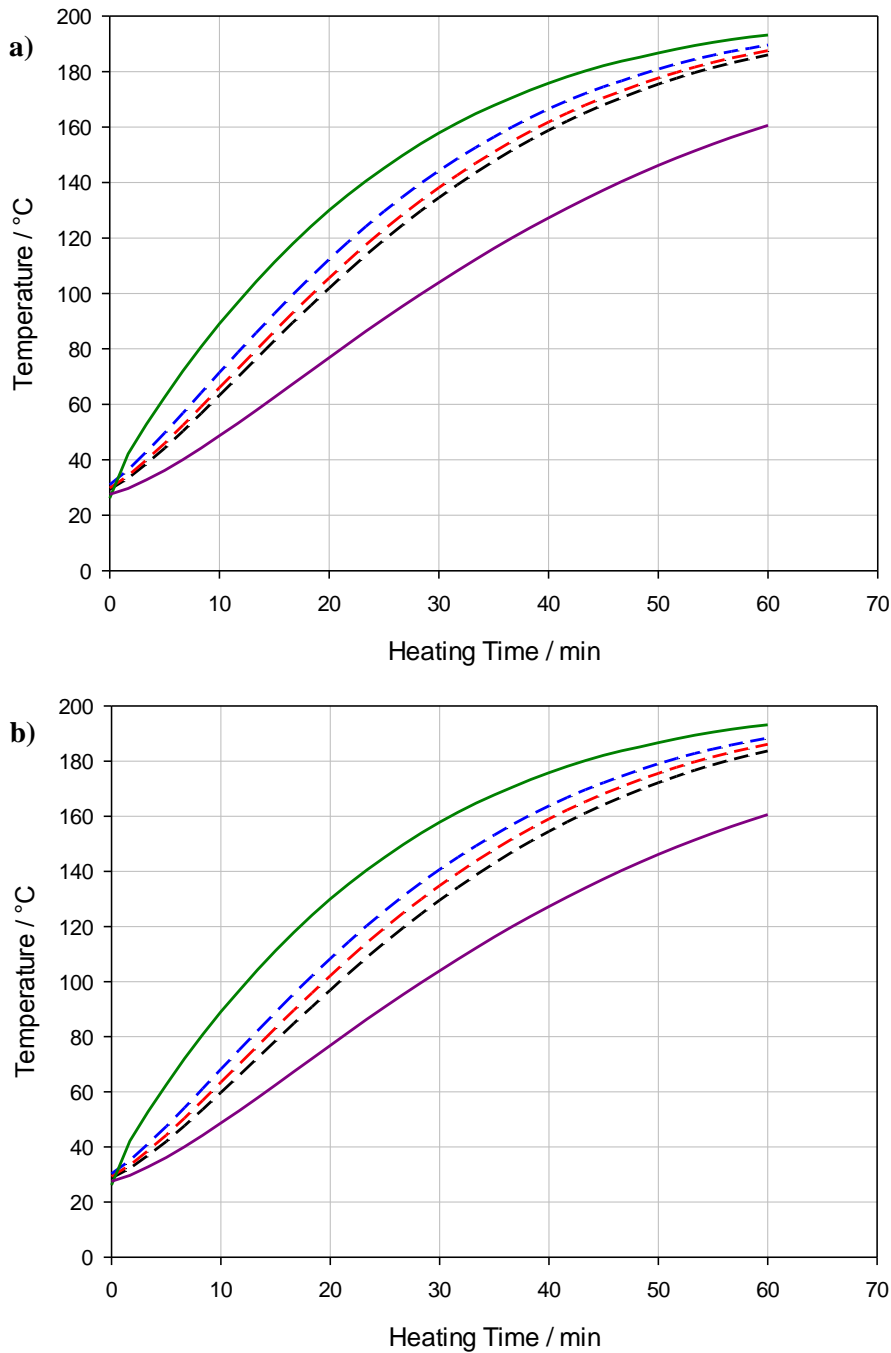
Figure 4.16: COMSOL model simulations for **a)** 45 PPI and **b)** 10 PPI foam subjected to a volumetric compression ratio of 4.88 (black line), 3.91 (red line) and 2.93 (blue line). Air and solid polyurethane are represented by solid green and purple lines, respectively.

Figure 4.16 shows the results of the COMSOL model simulations for each volumetric compression ratio per porosity. Solid polyurethane and air (at room temperature) were also included to indicate the extremes of this model, as foams are a ratio of air and solid material [159]. When compared against their experimental counterparts, the ranking order predicted by the model regarding the heating times for a given compression ratio complied with the experimental data for the 45 PPI foams, but different for the 10 PPI foams. It is currently inconclusive why the 10 PPI foam models fail to converge towards the experimental plots,

however, it is suspected that factors such as cell size and localised density effects, could influence this behaviour. For all fabrication combinations studied, after the maximum heating time of 60 minutes, temperatures between 185°C and 190°C were measured in the foam centre. When this region of interest was expanded to a cross-sectional measurement, a non-uniform temperature distribution was shown to exist throughout the sample body (Figure 4.17 and Figure 4.18). This signified that thermal equilibrium between the samples and oven was yet to occur. It should however be possible to accelerate this process by a number of approaches including: smaller sample sizes, longer heating and higher temperatures.

For any given sample, the temperature at any position within the sample body is relative to its distance from the heat source and heating time as described by the heat equation (Chapter 3). It is conceivable that this non-uniform temperature distribution could explain the rapid sample volume changes observed in literature [24, 107]. Within these samples, if the softening temperature region is greater than the non-softening region, the increased stiffness of the auxetic region should be sufficient to resist the volumetric change. However, if the alternative scenario occurs, then it is likely volume change will occur. Furthermore, this non-uniform temperature distribution would also explain why it is was possible to produce auxetic foams at temperatures as low as 25 minutes, where from Figure 4.17 it can be seen that portions of samples have yet to exceed the T_g at all regions of the sample.
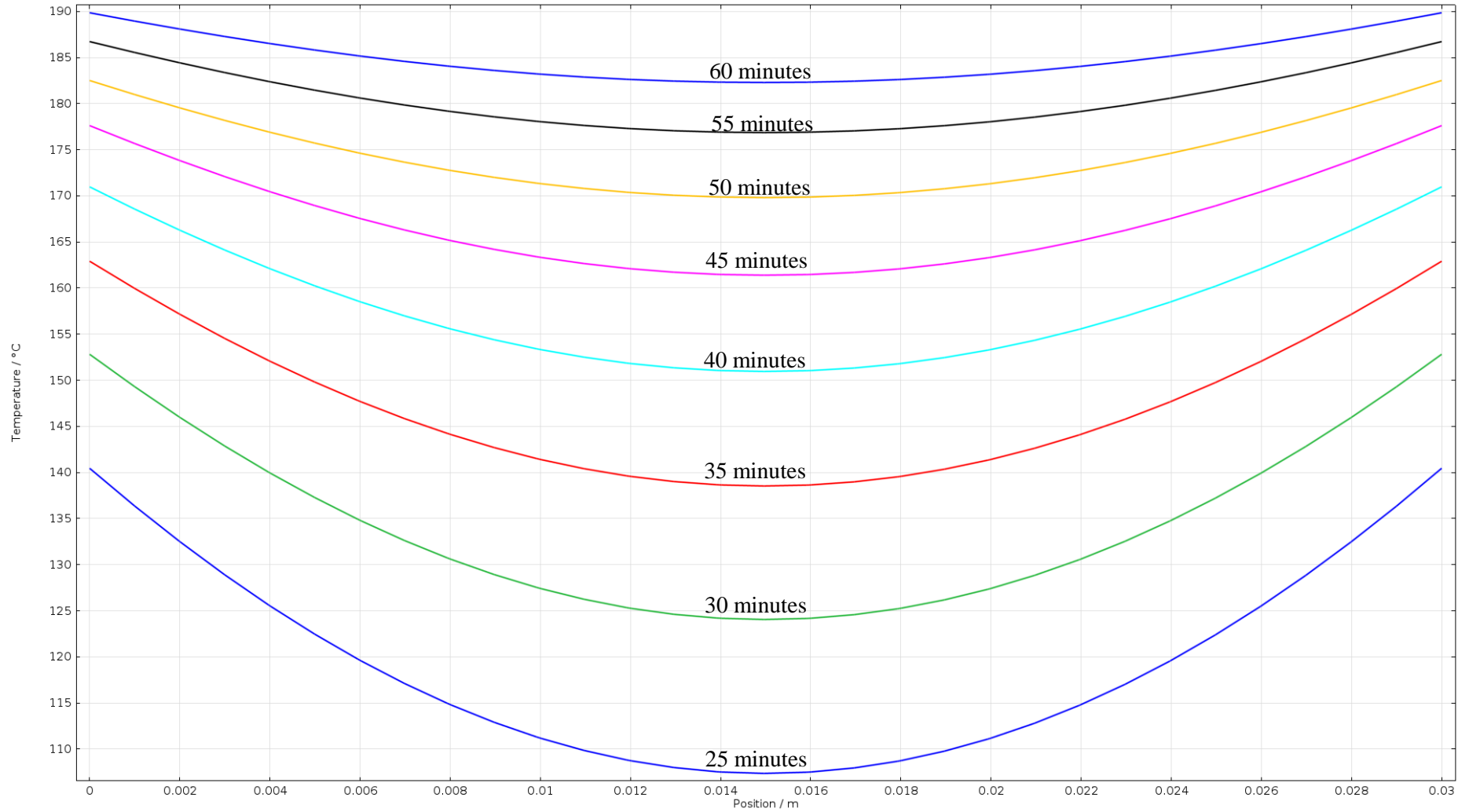
Figure 4.17: Temperature change across the *x*-axis at sample centre versus time, for a foams produced from a volumetric compression of 4.88 from 45 PPI foam.
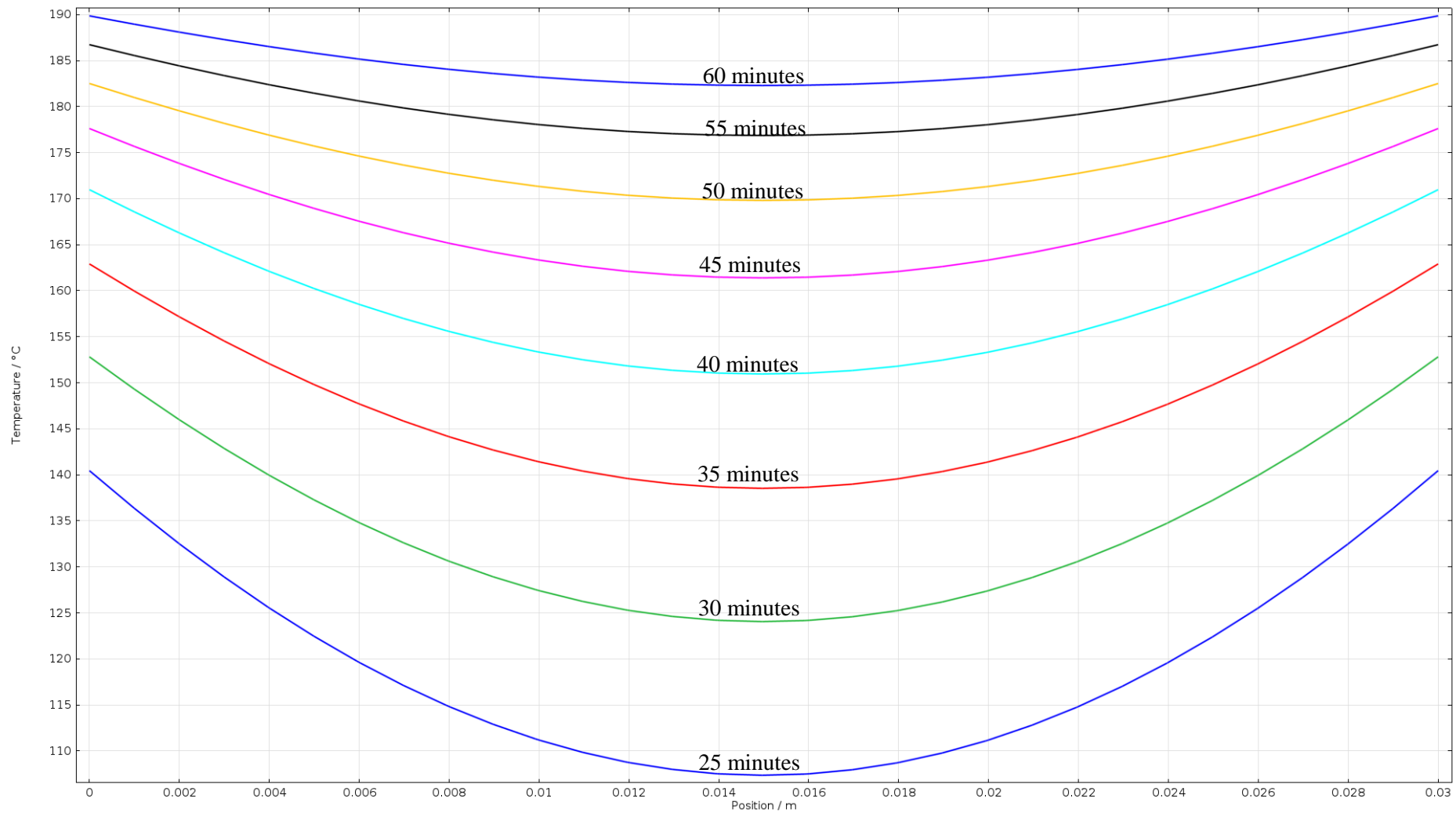
Figure 4.18: Temperature change across the *y*-axis at sample centre versus time, for a foams produced from a volumetric compression of 4.88 from 45 PPI foam.

4.1.1.3.2 Density:

To explore the compression aspect of the auxetic fabrication process, conventional 45 PPI and 10 PPI foams were imaged using micro tomography in both uncompressed and compressed states. To replicate the volumetric compression conditions of the auxetic fabrication process within micro tomography scanner, moulds and endplates of the same dimensions as those described in Chapter 3.3.1, were manufactured from Perspex. By using Perspex, a greater contrast between the mould and the foam material can be achieved, resulting in clearer images.

To optimise the number of scans, data and scan time required, symmetry about the mould's centre was assumed. This results in a rectangular region of interest with dimensions of 30 mm $\times$ 30 mm $\times$ 50 mm being imaged using an X-ray source in the region of 110 kV with a voxel resolution of 0.0433 mm. The scan data was reconstructed using CTPro via filtered back projection algorithm [232] before being cropped, concatenated and converted to 8-bit grayscale using FIJI.

The foam relative density change was then calculated via the following processes. 8-bit volumes were binarised (*i.e.,* image digitisation into 0 / 1) using an ISO50 threshold standard [233] to extract the foam structure. A region was cropped to include the internal region of the foam and exclude artefacts that were in the upper and lower 50 voxels of the scan. The relative density was calculated by dividing the number of voxels representing the foam structure by the total number of voxels within a given slice. This was achieved using the standard voxel counter included within FIJI tool to represent relative density as a function of distance in the *z*-axis. As symmetry was previously assumed about the centre, the change in relative density was reflected at this point to represent complete samples (Figure 4.19).
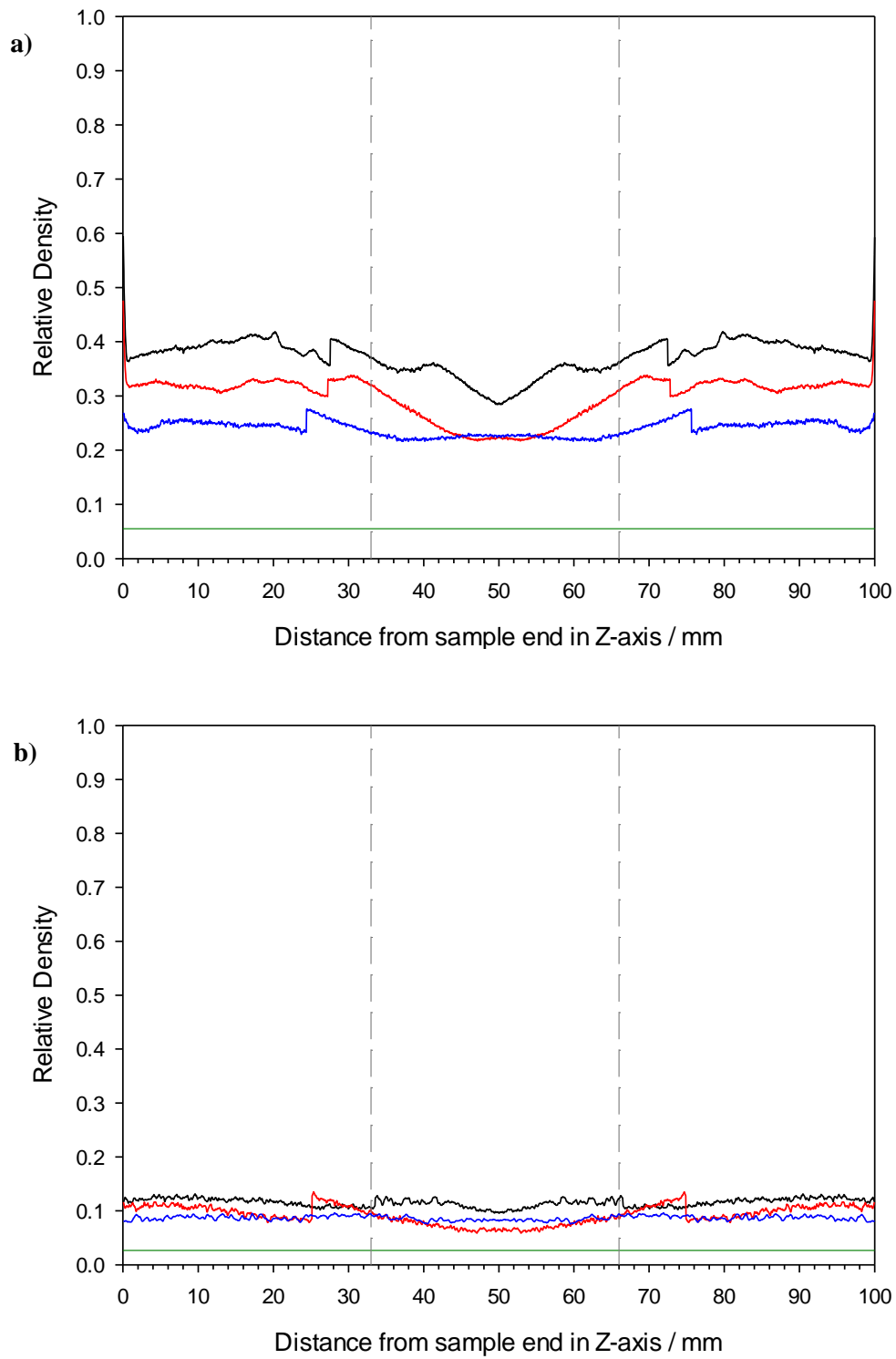
Figure 4.19: Relative density change with respect to distance from sample edge: **a)** 45 PPI and **b)** 10 PPI foams for volumetric compression ratios of 4.88 (black line), 3.91 (Red line) and 2.93 (blue line) where dashed lines represent the boundaries between the centre third and end thirds. Conventional foams are represented by a green line.

From Figure 4.19 it can be seen that all of the graphs exhibit distinct peaks. These peaks occur at locations where the sub-volumes were concatenated, and are the direct result of the ISO50 standard, calculating different threshold values between sub-volumes. Currently the influence

that the sub-volume offset has on density variation is unknown. However, when compared against conventional foams, the presence of a volumetric compression can be clearly shown to increase a sample's overall relative density, by approximately the magnitude of the imposed volumetric compression ratio. The relative density change was shown to be heterogeneous, whereby density fluctuates depending on the distance from the sample's end. In the majority of the datasets, the largest relative density changes exist between 0 to 33 mm from the ends of the sample (dashed grey lines). This is potentially attributed to localised collapse (crumple zones) of the cell ribs closest to the foam surface in contact with the end blocks, as previously reported in literature [198, 239].

When the distance from the end blocks exceeds 33 mm (or one-third of the volume), a decrease in relative density arises, until finally converging to its lowest value at the centre of the sample. This behaviour differs to the work presented by Elliot *et al.* [198], where compressed conventional foam exhibited a higher relative density at its centre. Although it is unclear why these variances exist, it is likely the product of the different compression methods utilised between studies.

It is because of the differences in density between the two distinct regions that the denser sections nearest the end plates are typically removed or are not considered throughout literature [24, 153]. To the author's knowledge, the differences between these regions are yet to be studied and as such are explored in the Chapter 5.

4.1.1.3.3 Skeletonisation:

Within a three-dimensional conventional foam, the cell structure comprises of two distinct components: cell ribs and vertices. While cell ribs are the beams of the structure, the vertices function as the connecting nodes between the cell ribs [160]. At any given vertex, four cell ribs meet, although this can be less, if damage has occurred to the structure. Alternatively, the cell ribs can be highly variable, especially regarding their geometrical aspects including length and tortuosity.

To evaluate the rib structure within the two distinct regions, five local volume of dimensions 7 mm × 7 mm × 3 mm (local volume dimensions were chosen to allow direct comparison against current literature [199]), were extracted at random locations from the previously binarised volumes. Each local volume was processed by a standard skeletonisation tool within FIJI, that essentially 'burns' away the foam material, retaining only its connectivity as a series of linear branches that begin and end at junctions [235]. By measuring these paths and junctions, the

various rib lengths, number of ribs, rib tortuosity, frequency of ribs and number of ribs per junction within a region of interest can be measured.

4.1.1.3.4   Vertices:

Figure 4.20 shows the mean frequency versus branches per vertex measured within the random volume selections for the compressed and conventional foams. When compared against their conventional counterparts the presence of a volumetric compression greatly increased the amount of vertices contained within a given volume. The number of vertices within a volume was shown to be directly linked to the magnitude of the compression. At higher compressions, a large proportion of the cell ribs are forced into a limited volume. As compression decreases, more space is available to the cell ribs, reducing the number of ribs within a given volume.
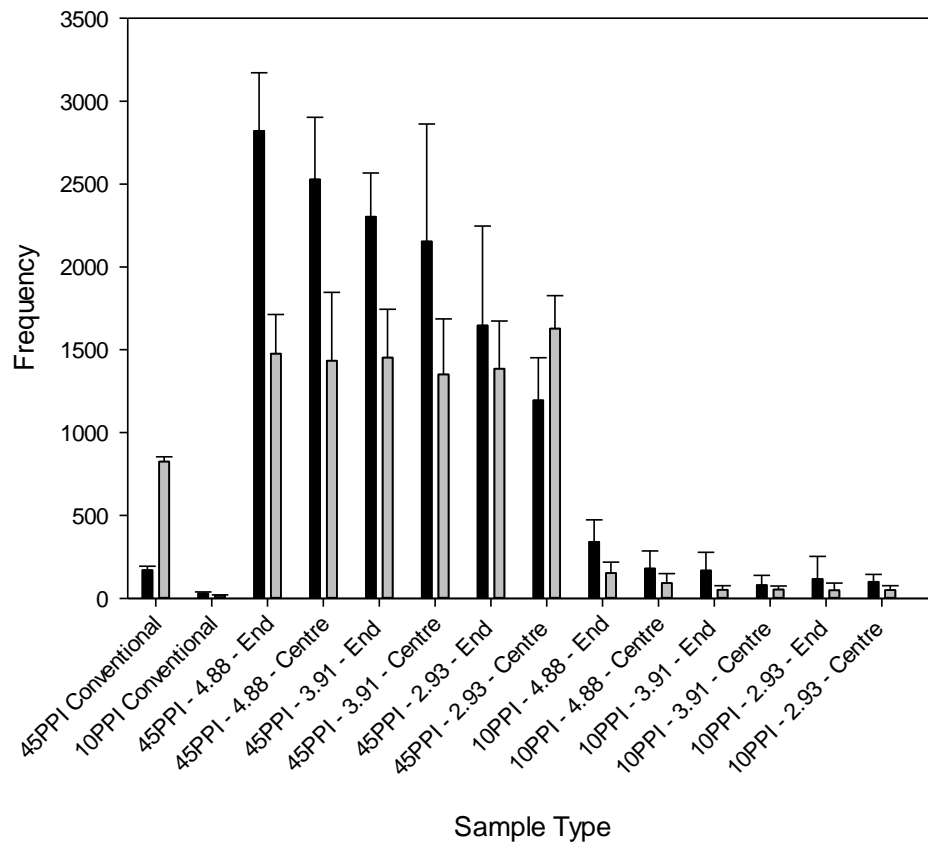
Figure 4.20: Mean frequency of vertices that exhibit triple (black bar) and quad (grey bar) branches for each studied compression and conventional foam.

In the majority of datasets, a greater frequency of vertices with three branches (rather than the expected four) was demonstrated. The only exceptions were conventional 45 PPI and 45 PPI-2.93 centre samples. This observation was found to differ from the work presented by Elliot [198] and Gaspar [199], where a greater frequency of vertices with four cell ribs per node was reported. However, it can be seen that as volumetric compression decreases, the frequency of vertices with three branches decreases, while those with four branches remain fairly consistent. It is likely that

this behaviour results from extracting and analysing small sub-volumes. By extracting sub-volumes from a larger sample, any vertices near the volume boundaries are susceptible to either being cropped, or losing cell ribs. As volumetric compression directly influences the amount of vertices and cell ribs within a given volume, at higher compressions, it is likely there are more vertices or cell ribs at the boundaries being cropped. Nevertheless, as compression decreases, fewer vertexes are now within the same area, resulting in less vertices and cell ribs being cropped, thus reducing the three branch frequency. Furthermore volumes extracted from the end regions contain a higher amount of vertices than their central counterparts. This is directly related to the higher densities within the end regions, as previously shown in Figure 4.19.

4.1.1.3.5 Branch Length:

Figures 4.21, 4.22 and 4.23 show the mean branch length versus frequency for the conventional and compressed foams. When conventional 45 PPI foams were analysed, over 45% of all branches had a length between 0.25 mm and 0.5 mm. However, the peak frequency of branches within conventional 10 PPI foam was found to fall between 0 and 0.25 mm. This is an interesting observation, as it is expected that rib lengths within the 10 PPI foam should be greater than their 45 PPI counterparts, due to their larger cells. A likely explanation for this behaviour could again be associated with the procedure of extracting sub-volumes, as previously discussed. This behaviour could also be attributed to the skeletonisation algorithm representing curved struts in the tomographic data as a series of connected straight struts. The result of which has the potential to segment larger branches into smaller ones [198].
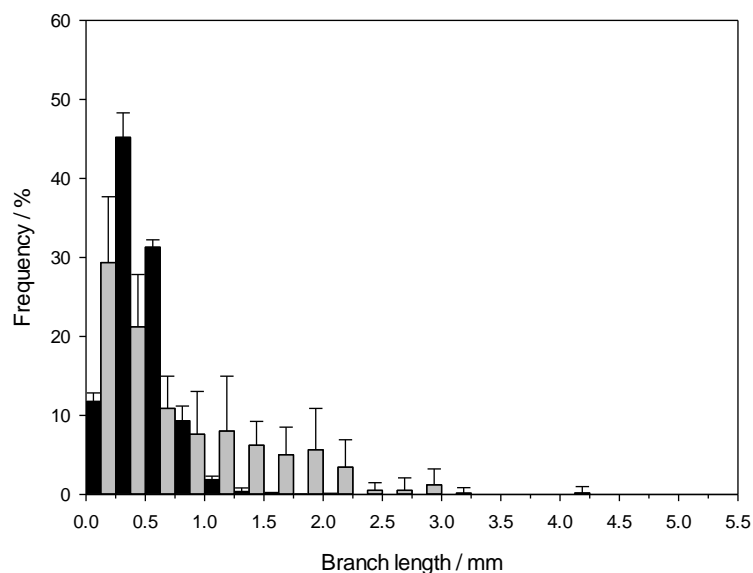
Figure 4.21: Mean branch length verse frequency for conventional 45 PPI (black bar) and 10 PPI (grey bar) foams.

Conventional 10 PPI foams were also observed to have a greater distribution tail in branch lengths compared to conventional 45 PPI, thus suggesting that there is greater variability in cell rib length throughout the foam structure. When conventional 45 PPI foam was subjected to each of the volumetric compressions, branches between 0.25 mm and 0.5 mm remained the dominant length scale throughout the foam structure at the centre and end regions. When 10 PPI foams were subjected to the same volumetric compressions, the 0.25 – 0.5 mm branch length scale was again shown to be the most dominant, in the majority of the datasets. This however differs from the uncompressed conventional 10 PPI foam.
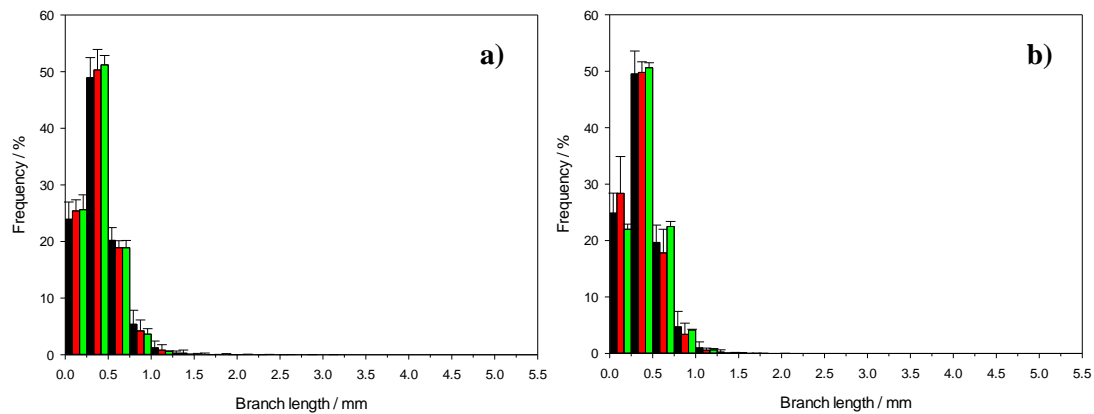
Figure 4.22: Mean branch length versus frequency for 45 PPI foams for volumetric compression ratios of 4.88 (black line), 3.91 (red line) and 2.93 (green line) using five randomly sampled volumes from: **a)** the end region and **b)** the centre region, as shown in Figure 4.19**.**
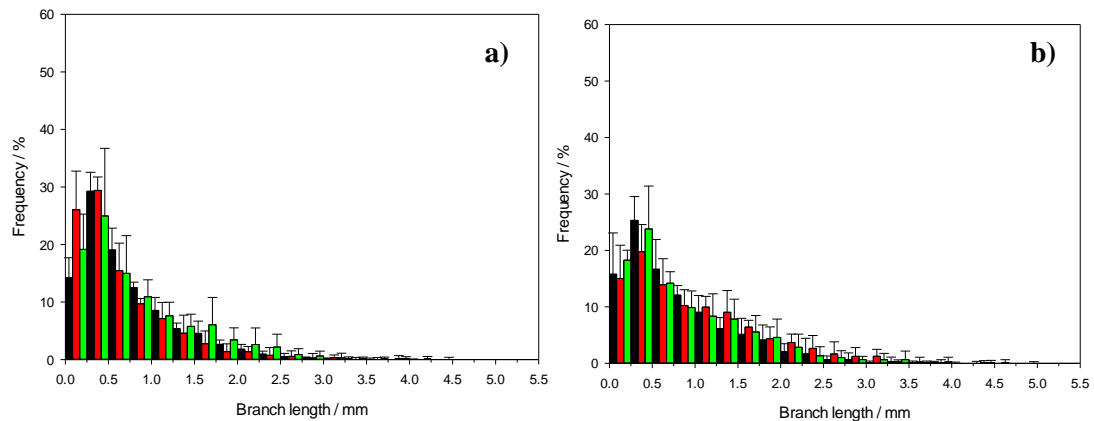
Figure 4.23: Mean branch length versus frequency for 10 PPI foams for volumetric compression ratios of 4.88 (black line), 3.91 (red line) and 2.93 (green line) using five randomly sampled volumes from: **a)** the end region and **b)** the centre region, as shown in Figure 4.19**.**

In addition to branch length, the curvatures of the branches were quantified as a measure of tortuosity. Tortuosity is given as the ratio between the arc and chord of a circle, where a ratio of one equals a straight line and infinity for a circle. Within this work, tortuosity is measured as the ratio between a branch's length and its Euclidean distances (the shortest distance between nodes at each of the branch).
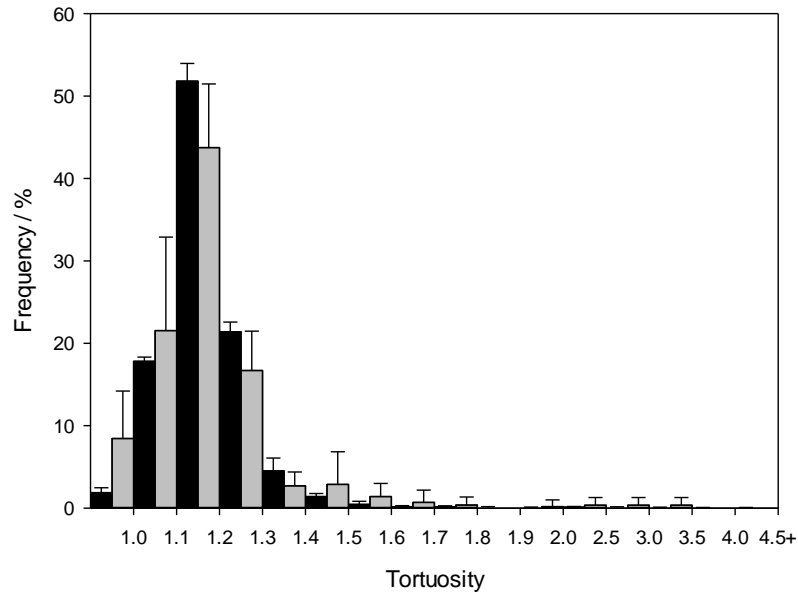
Figure 4.24: Mean branch tortuosity versus frequency for conventional 45 PPI (black bar) and 10 PPI (grey bar) foams.

Figures 4.24, 4.25 and 4.26 are the frequency of tortuosity for conventional 45 PPI and 10 PPI foam. Both foams exhibited a peak tortuosity between 1.1 and 1.2 indicating that the cell ribs are slightly curved. Peak tortuosity continued to remain between 1.1 and 1.2 for each of the volumetric compressions, but at a reduced frequency. The presence of compression did, however, induce a greater distribution in tortuosity across the foam samples. These observations were also reported by Gaspar *et al.* [199] for conventional foams. However, it was suggested that the presence of any peak other than at 1.0 for the ribs within conventional foams relates to some form of digital anomaly. To quantify the effect of digital errors associated with skeletonisation, an idealised straight line of 100 pixels was analysed. An error in tortuosity of 0.09 was identified. When this approach was replicated using the skeletonisation algorithm employed in this study, an error in tortuosity of 0.01 was confirmed. As this error is due to the skeletonisation algorithm used throughout this study, this error can be considered systematic, while its low value allows for it to be considered negligible.
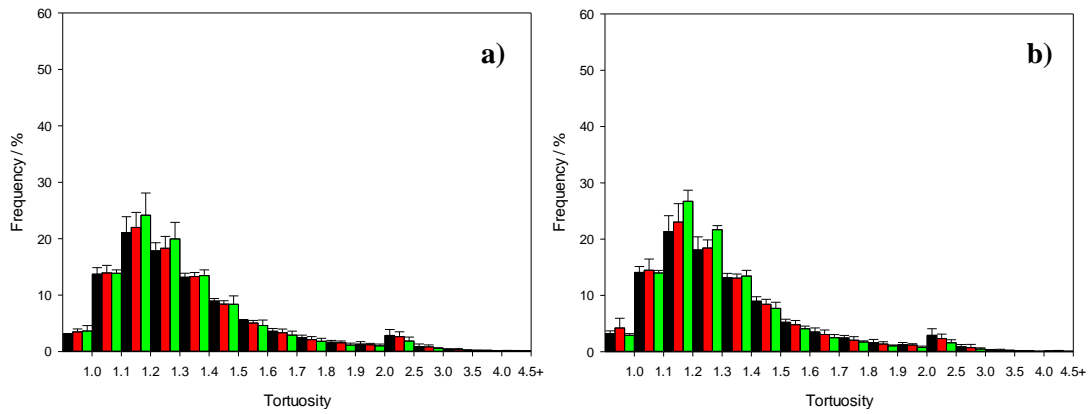
Figure 4.25: Mean tortuosity versus frequency for 45 PPI foams for volumetric compression ratios of 4.88 (black line), 3.91 (red line) and 2.93 (green line) using five randomly sampled volumes from: **a)** end region and **b)** centre region, as shown in Figure 4.19**9.**
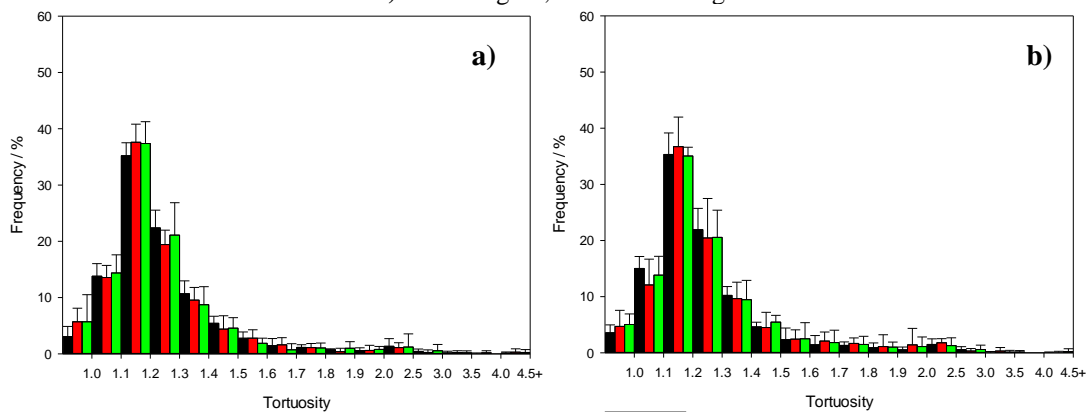
Figure 4.26: Mean tortuosity versus frequency for 10 PPI foams for volumetric compression ratios of 4.88 (black line), 3.91 (red line) and 2.93 (green line) using five randomly sampled volumes from: **a)** end region and **b)** centre region, as shown in Figure 4.19**.**

To provide an understanding of the shape associated with a given tortuosity, the branches are considered to be bent in an arc of a circle. In this simplification, helical and periodic branch shapes are ignored [199]. From Figures 4.27, 4.28 and 4.29, both conventional foams indicate that the peak bending angle for the branches falls between 0.1° and 5.0°. The peak angle continued to remain between 0.1° and 5.0° for all of the volumetric compressions, but at a reduced frequency. The presence of compression did however again induce a greater distribution in bending angles across the foam samples.
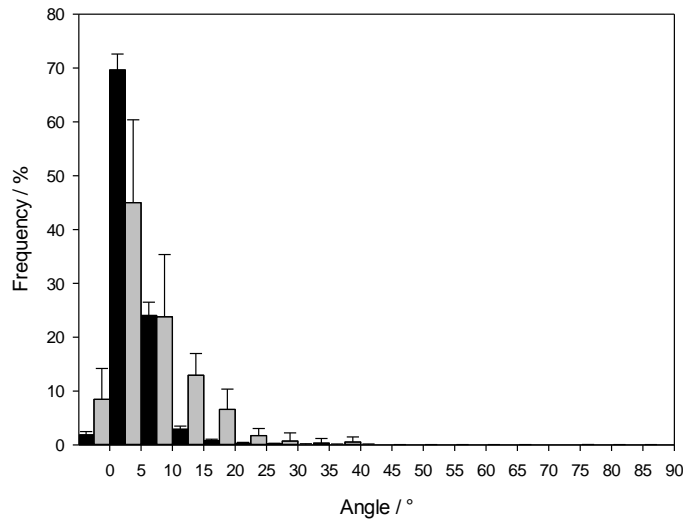
Figure 4.27: Mean branch bending angle versus frequency for conventional 45 PPI (black bar) and 10 PPI (grey bar) foams.
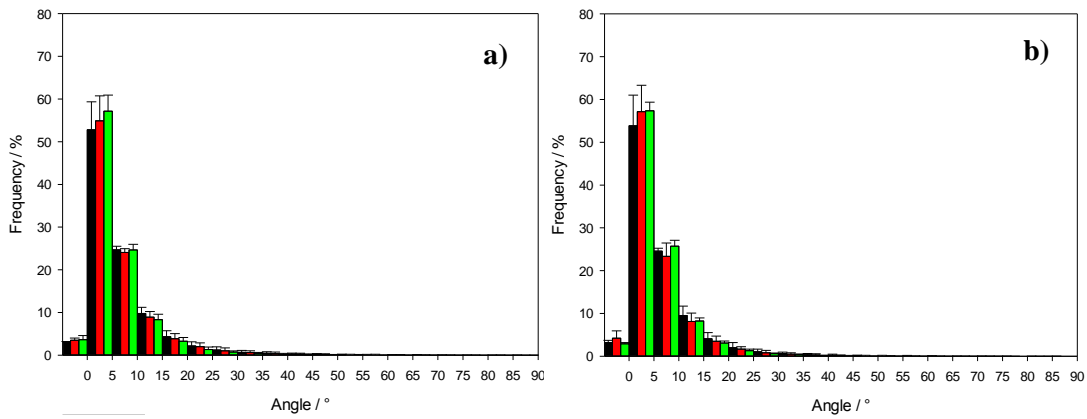
Figure 4.28: Mean branch bending angle versus frequency for 45 PPI foams for volumetric compression ratios of 4.88 (black line), 3.91 (red line) and 2.93 (green line) using five randomly sampled volumes from: **a)** the end region and **b)** the centre region, as shown in Figure 4.19**.**
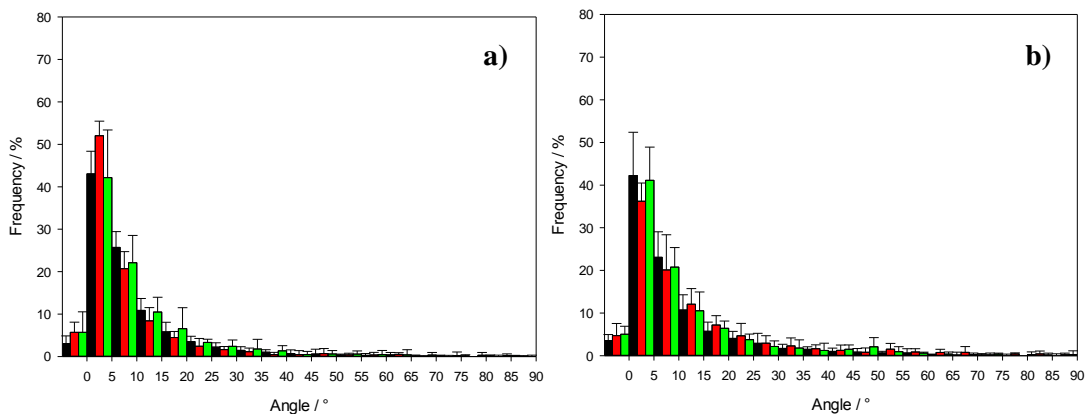
Figure 4.29: Mean branch bending angle versus frequency for 10 PPI foams for volumetric compression ratios of 4.88 (black line), 3.91 (red line) and 2.93 (green line) using five randomly sampled volumes from: **a)** the end region and **b)** the centre region, as shown in Figure 4.19**.**

4.2 Discussion

In this study, the effects of auxetic fabrication parameters (pore per inch, heating times, volume compression ratios and orientation) on inducing a negative Poisson's ratio have been explored. From the 288 samples tested, over 72 parameter combinations, only 39% of the samples demonstrated a negative Poisson's ratio. For those that exhibited a negative Poisson's ratio, an almost linear convergence towards a positive Poisson's ratio with respect to strain was shown to exist. Once positive, the Poisson's ratio exhibited a plateau effect until eventually stabilising. To date, similar Poisson's ratio behaviour to those presented here have been reported in literature [131, 153], however the Poisson's ratios in these studies is often shown to vary from study to study.

While the Poisson's ratio change with respect to strain can be attributed to cell deformation [158], the variation in the auxetic foams between studies have been suggested to be influenced by a number of factors. Wang *et al.* [134] for example, state that the main physical parameters influencing the auxetic transformation process are the volumetric compression ratio, the processing temperature and the heating time. However, other authors [106, 107, 130, 134] consider only the volumetric compression ratio as the main parameter responsible for a successful conversion, with the other parameters acting as secondary influences.

For the work presented here, Poisson's ratio was shown to be directly affected by the volumetric compression ratio imposed on a sample during the auxetic conversion process, where a decrease in volumetric compression ratio reduces the negative Poisson's ratio. Consequently a negative Poisson's ratio was no longer present when the imposed volumetric compression ratio became too small, eventually culminating with samples exhibiting a positive Poisson's ratio, but one that is lower than conventional foam.

This behaviour is the direct result of the overall compression induced on the fixed conventional foam during fabrication. At lower volumetric compression ratios the cellular ribs only deform a minimal amount, as internal space is in abundance. Once the compression increases, the amount of space the ribs can deform into decreases, resulting in ribs competing for this now limited space. Should the induced volumetric compression ratio become too high, all internal cell space becomes occupied with deformed cell ribs, and no further compression can be undertaken.

While this behaviour was confirmed through micro-tomography, and supported by the work of Gaspar *et al.* [199] and Scarpa *et al.* [129], volumetric compression was also found to result in heterogeneous compression causing variations in relative density throughout samples body. This

variation in relative density is problematic, as not only does it reduce repeatability of sample production, but can also influence a sample's local thermal properties [240]. By having variations in thermal properties, some regions of foam have the potential to heat at greater rates than others.

Heating time was also found to influence the Poisson's ratio of samples, as a decrease in heating time was shown to reduce the maximum negative Poisson's ratio that a sample attains. Interestingly, it was found that a negative Poisson's ratio were achievable at heating times as low as 25 minutes. This behaviour is supported by the model as it predicts that even at 25 minutes large amounts of the sample body have already exceeded the PU T_g presented by Bianchi *et al.*[130]. While the model does not directly explain the reasons why a decrease in heating time increases the likelihood of a sample exhibiting a positive Poisson's ratio, it does highlight that non-uniform temperature distribution exists throughout the sample body. By subjecting the sample to gradient heating, the outer regions of the samples reach a sufficient temperature for the softening of ribs turning them auxetic, while the heat deprived internal body remains conventional. By coupling this non-uniform heating with the cutting down of the samples to test dimensions, there is the potential to remove the auxetic regions of the sample.

The behaviour of heating time on a sample is important, as it directly relates to the internal temperature of the compressed polyurethane foam at its core. As heating the foam in a non-compressed form will not enable an auxetic structure to be instilled, both parameters must be considered together. For short heating times, a sample produced at low volumetric compression ratio (2.93) will experience a high positive Poisson's ratio, equal to or greater than that of its base conventional foam. This occurs as the low volumetric compression ratio allows the compressed foam to retain a significant portion of its original porosity. By retaining its porosity, foam preserves its thermal conductivity properties, which when coupled with the low heating time, prevents the internal core temperature from reaching the required softening temperature needed to fix the new auxetic microstructures in place.

As the volumetric compression is increased, the Poisson's ratio is shown to become either a low positive Poisson's ratio or low negative Poisson's ratio, depending on whether the compression is medium (3.91) or high (4.88). At these higher compression ratios, the foam starts to lose its porosity, as the original structure becomes filled (occupied) with deformed ribs, causing the foam to resemble a solid block of polyurethane. By resembling solid polyurethane, the thermal conductivity increases, allowing greater heat transfer to penetrate into the specimen and soften the cellular ribs to the new auxetic microstructure.

Alternatively, for shorter heating times, only a small number of negative Poisson's ratio samples were produced, as the limited heating time restricts the heat transfer within the interior body of the sample [139]. By subjecting the sample to a gradient heating, the outer regions of a foam reach a sufficient temperature to allow for the softening of ribs (turning them auxetic), while the unaffected internal body remains conventional. Thus, when subjected to a tensile stimulus, the surface auxetic ribs expand, while the internal cellular ribs elongate.

4.3   Summary

Auxetic and conventional polyurethane foams have been studied with respect to their Poisson's ratio, overall a set of 72 combinations of parameters including heating time, volumetric compression ratio, pores per inch and sample orientation.

Poisson's ratio was found to be highly dependent on both the volumetric compression ratio and the heating time, as shown in Table 4.1. An almost linear relationship between negative Poisson's ratio and strain, until becoming positive when the Poisson's ratio stabilised between values 0.2 and 0.3, indicating a return to conventional foam, whilst failed fabrication samples only exhibited positive Poisson's ratios that fluctuate until stabilising between 0.2 and 0.3.

Unfortunately when considered with respect to a 95% confidence interval the relationships between Poisson's ratio and fabrication parameters only applied to a sample's mean value, as large error bars frequently cause data ranges to overlap, indicating that a sample between two states of strain has equal chance of falling between the values plotted. A number of sources were suggested for these high errors including equipment limitations, anisotropic samples, user error and edge effects.

Table 4.1: Poisson's ratio relationships with respect to heating time and volumetric compression ratio (VCR).

	High heating time	**Low heating time**
High VCR	High NPR	Low NPR
Medium VCR	Medium NPR	Low NPR
Low VCR	Low NPR	High NPR

Chapter 5: Crater depth and energy absorption

5.1 Introduction

Although modern body armour may stop the penetration of a projectile, the armour must additionally dissipate appropriately the subsequent kinetic energy. Within these armour systems, energy dissipation occurs through deformation or fragmentation of the projectile, deformation of the armour and deformation of the torso body wall [44]. If the associated armour deformation is significant, the corresponding impact on the torso behind the armour can result in serious injury (such as BABT) or, for a very high energy impact, death [3, 4].

To limit the effects of BABT, the US National Institute of Justice (NIJ) [8] standard states that the impressions left in ballistic Roma Plastilina #1 clay (also known as the backface signature) must be less than 44 mm in depth in order for an armour system to be considered safe and effective. Interestingly, while the exact origins of how exactly a maximum deformation of 44 mm became the BABT standard [96, 99], it was found that it has only a 6% probability of lethality, below the initial requirement of less than or equal to 10% that was originally outlined by the lightweight soft body armour programme undertaken by researchers in the Wound Ballistics Program of the US-Army [44].

Currently, to assist in limiting the impact energy effects on the torso, and thus reduce BABT, materials that enhance energy absorption, dissipation and redistribution are placed between the armour system and body. These materials (TABs) are predominantly sold by body armour manufacturers and are often produced from specialist low-density proprietary materials.

To date, TABs are typically tested within a full armour system layup under ballistic conditions. To the author's knowledge, the testing of the trauma attenuating backings outside a full armour layup has yet to be undertaken. Based on conservation of momentum, the velocities experienced by the trauma attenuating backings are lower than those experienced by the hard outer ceramic plate, with reductions potentially down to the low velocity, high mass impact regimes. This raises the question, can the individual constituents of the armour configuration be tested, and if so, can it be replicated by high mass, low velocity impacts.

This chapter will focus on the energy absorption potential and resulting crater depth, as measured by the Roma Plastilina #1 clay, on auxetic foams subjected to low velocity impacts of 7.2 J, where the mechanical performance was tested by varying heating time, volumetric compression ratio,

porosity and sample orientation. Conventional foams were additionally studied to allow direct comparison between the foam sample types, in order to determine if the presence of an auxetic structure is beneficial.

5.2   Results

5.2.1   Crater depth

5.2.1.1 Non-auxetic

To determine whether an auxetic structure improves the ability of polymeric porous materials to dissipate the energy of an impact load, it is first necessary to understand the behaviour of the conventional open-cellular structure of base foams from which the auxetic samples were fabricated. To allow comparison between auxetic and non-auxetic, six samples of each type of conventional base foam (45 PPI and 10 PPI foams of longitudinal and latitudinal orientations) and 24 direct impacts were initially tested (control tests), each resulting in a measurable crater (an example of which is shown in Figure 5.2). For each of the datasets, the mean crater depths were calculated using a Taicaan laser surface profilometer (example data shown in Figure 5.1), where error bars are given, represent a 95% confidence interval (Figure 5.3a). An example of this raw data can be found in Appendix 5A.
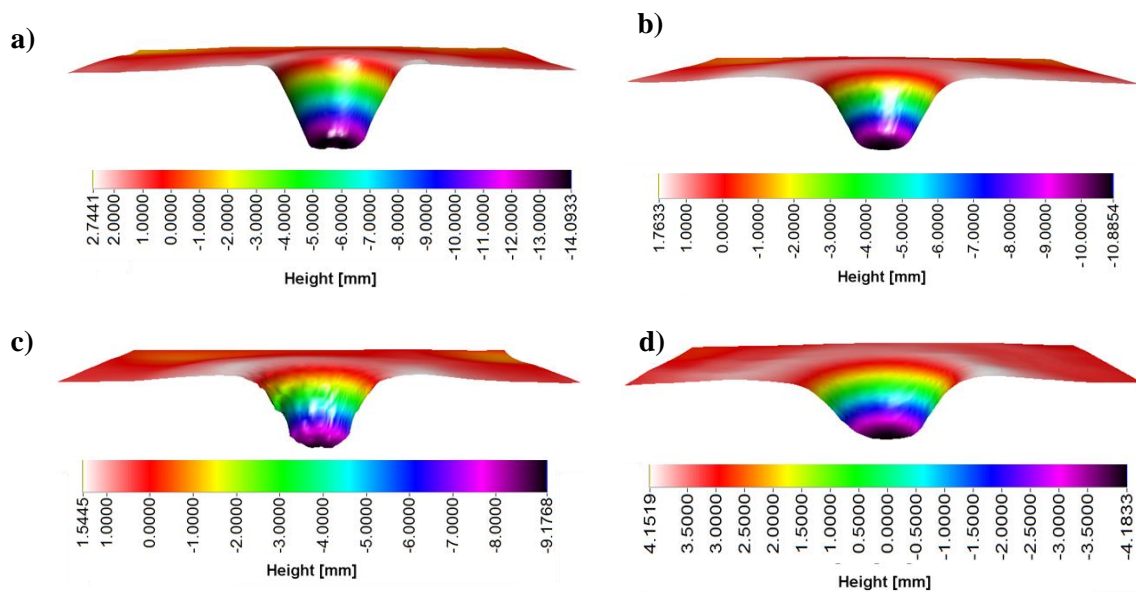
Figure 5.1: Taicaan cross-sectional representation of Roma Plastilina No. 1 clay craters produced from the impact of: **a)** direct, **b)** 45 PPI conventional foam, **c)** 10 PPI conventional foam and **d)** auxetic 45 PPI foam produced heated for 60 minutes at a volumetric compression ratio of 4.88.
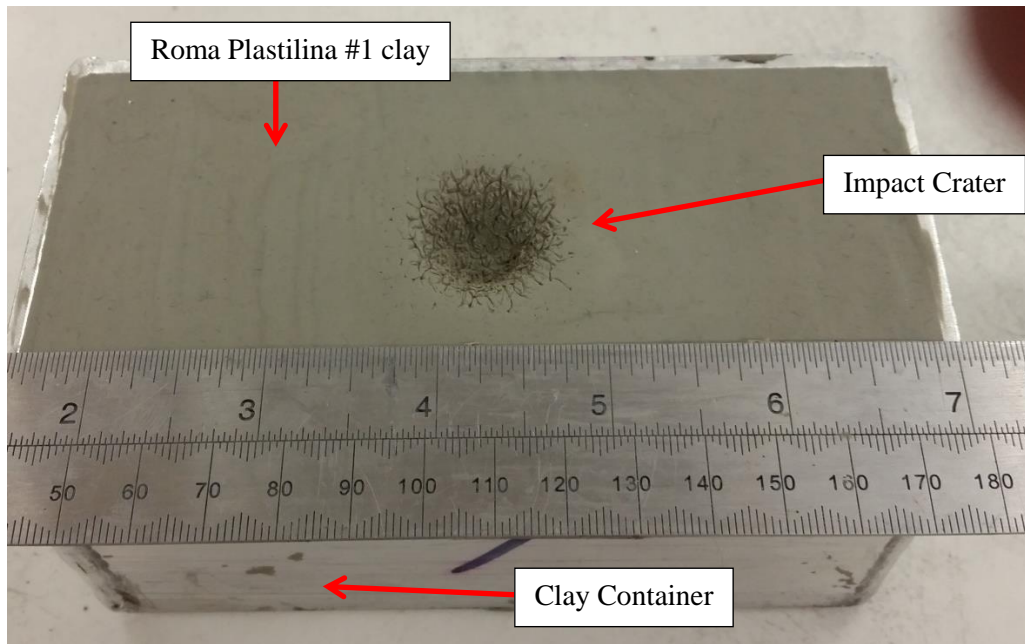
Figure 5.2: Example of a crater produced as a result of a direct impact onto conventional 45 PPI foam sample resting upon a clay body.

Overall, the control impact tests produced the highest mean crater depth of 17.3±0.5 mm, while the presence of longitudinal 45 PPI and 10 PPI foams reduced the crater depth to 12±0.3 mm and 10.5±0.2 mm, respectively. Latitudinal samples also reduced the crater depth to 11.4±0.4 mm and 11.2±0.4 mm, for 45 PPI and 10 PPI, respectively (Figure 5.3b). By determining the mean crater depths of the conventional and control impacts, these results can be utilised as boundary thresholds to allow direct comparisons to be made between the auxetic and non-auxetic foams.
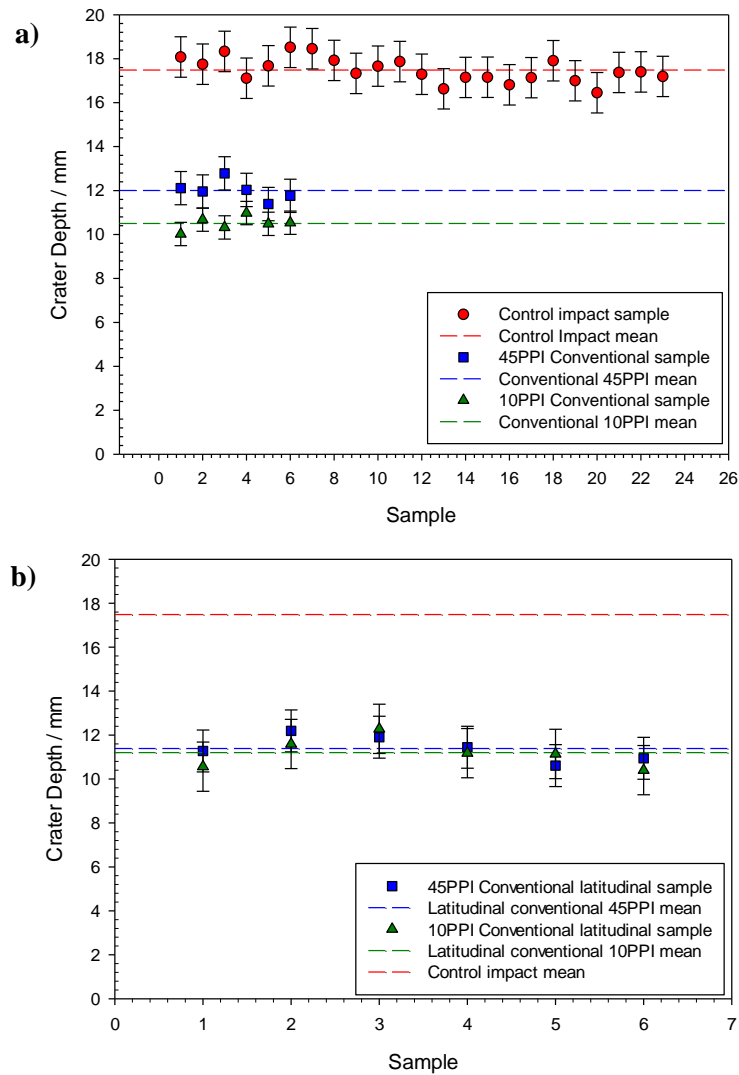
Figure 5.3: Crater depths for direct high mass / low velocity impact (7.2 J), 45 PPI conventional and 10 PPI polyurethane conventional foams for: **a)** longitudinal and **b)** latitudinal foams, where each dashed line represents the mean of the samples tested. Error bars provided by 95% confidence level.

5.2.1.2 Auxetic

Figure 5.4 to Figure 5.7 present the mean crater depths with respect to the volumetric compression ratio, heating time, base foam porosity and sample orientation. Error bars are provided by a 95% confidence interval while examples of a raw datasets utilised in the calculation of a crater depths can be found in Appendix 5A.
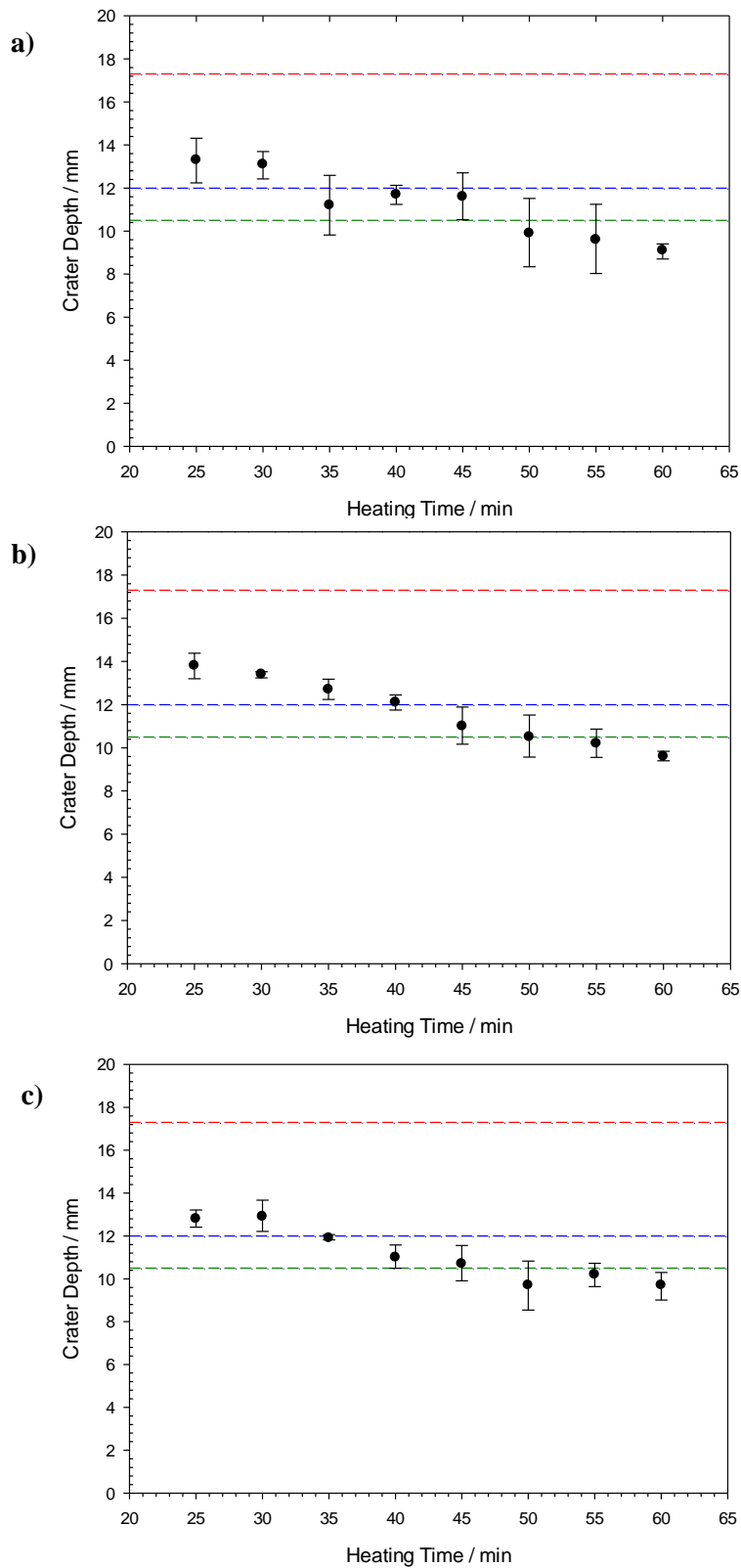
Figure 5.4: Crater depth *vs.* heating time for the 45 PPI longitudinal orientated polyurethane foams at: **a)** 4.88, **b)** 3.91 and **c)** 2.93 volumetric compression ratios, where the red dash line is the mean direct impact depth, blue dash line is the 45 PPI mean depth and green dash line is the 10 PPI mean depth. Conditions - high mass, low velocity impacts of 7.2 J. Error bars provided by 95% confidence level.
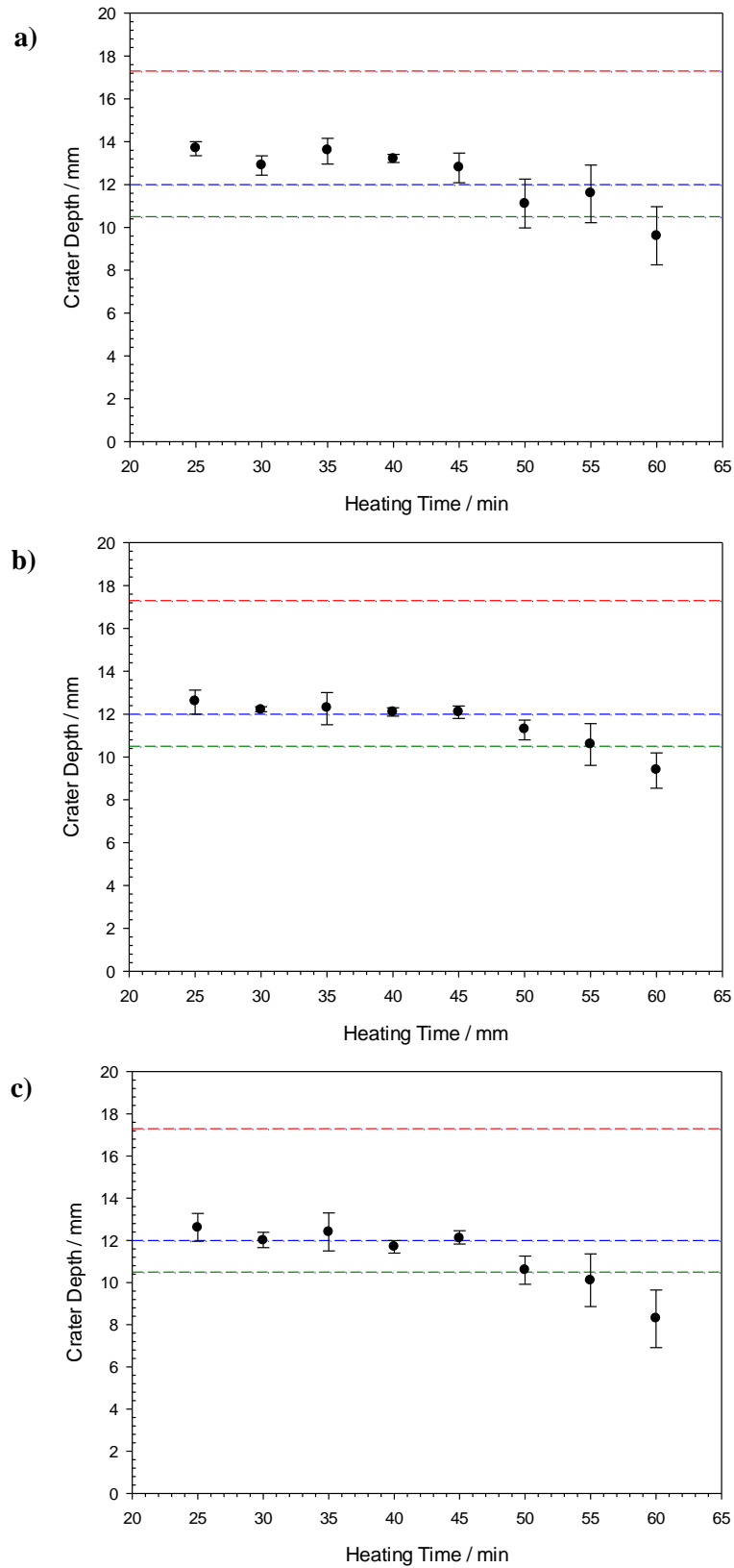
Figure 5.5: Crater depth *vs*. heating time for the 10 PPI longitudinal orientated polyurethane foams at: **a)** 4.88, **b)** 3.91 and **c)** 2.93 volumetric compression ratios, where the red dash line is the mean direct impact depth, blue dash line is the 45 PPI mean depth and green line is the 10 PPI mean depth. Conditions - high mass, low velocity impacts of 7.2 J. Error bars provided by 95% confidence level.
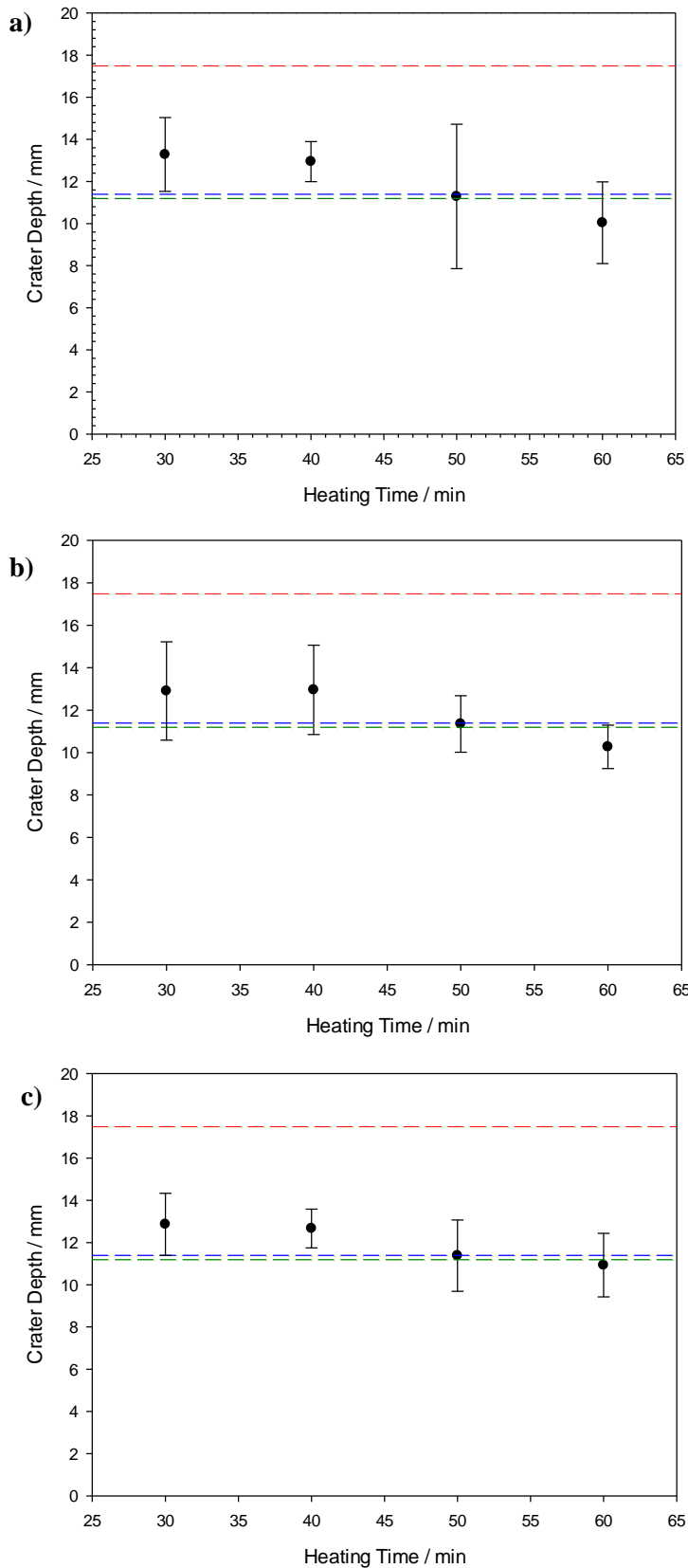
Figure 5.6: Crater depth *vs.* heating time for the 45 PPI latitudinal orientated polyurethane foams at: **a)** 4.88, **b)** 3.91 and **c)** 2.93 volumetric compression ratios, where the red dash line is the mean direct impact depth, blue dash line is the 45 PPI mean depth and green line is the 10 PPI mean depth. Conditions - high mass, low velocity impacts of 7.2 J. Error bars provided by 95% confidence level.
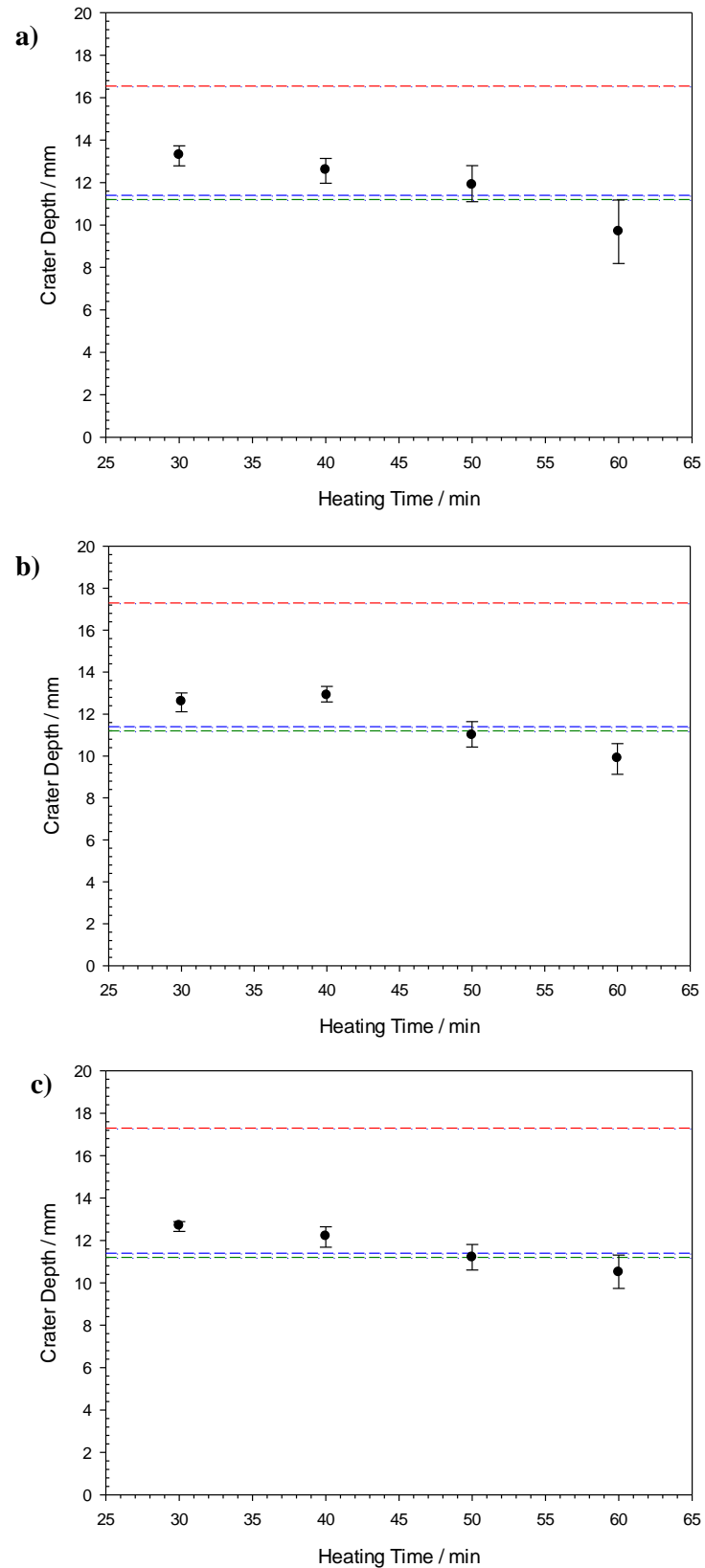
Figure 5.7: Crater depth *vs.* heating time for the 10 PPI latitudinal orientated polyurethane foams at: **a)** 4.88, **b)** 3.91 and **c)** 2.93 volumetric compression ratios, where the red dash line is the mean direct impact depth, blue dash line is the 45 PPI mean depth and green line is the 10 PPI mean depth. Conditions - high mass, low velocity impacts of 7.2 J. Error bars provided by 95% confidence level.

From Figure 5.4 and Figure 5.5, longitudinal 45 PPI and 10 PPI samples can be seen to exhibit an almost linear decrease in crater depth with increasing heating times, for all three volumetric compression ratios. Within each dataset, 60 minutes is the only heating time to consistently exhibit crater depths less than both the conventional base foams, although heating times as low as 45 minutes can also produce samples with crater depths smaller than both conventional foams, as indicated by the error bars. A further reduction in heating time however resulted in samples that were either the same or worse than the starting conventional foams. This behaviour was also shown to be exhibited by the 45 PPI and 10 PPI latitudinal samples, indicating that the relationship between crater depth and heating time is independent of sample orientation. Furthermore, as the relationship between heating time and crater depth is shown to occur for all tested volumetric compression ratios it can be assumed that crater depth is also independent of volumetric compression ratio. Overall, the lowest mean crater depth of 8.3±1.9 mm was found to occur at a 60 minute heating time for the 10 PPI foam produced at a 2.93 volumetric compression ratio at the longitudinal orientation. To determine whether a negative Poisson's ratio has an effect on the crater depth, Poisson's ratio was plotted against crater depth with respect to the volumetric compression ratio, heating time, base foam porosity and sample orientation. From Figure 5.8 to Figure 5.11 it can be seen that for the majority of datasets many of the lower values of crater depth also exhibit a negative Poisson's ratio. Interestingly, there is however no evidence to suggest that there is a relationship between a sample's Poisson's ratio and crater depth, as there are many samples with the same recorded Poisson's ratio, but different crater depths. This suggests that although the auxetic fabrication process is having an effect on the foams, the crater depth is being affected not by its negative Poisson's ratio but instead by the change in density that the fabrication process causes (as discussed in Chapter 4) [137, 154].
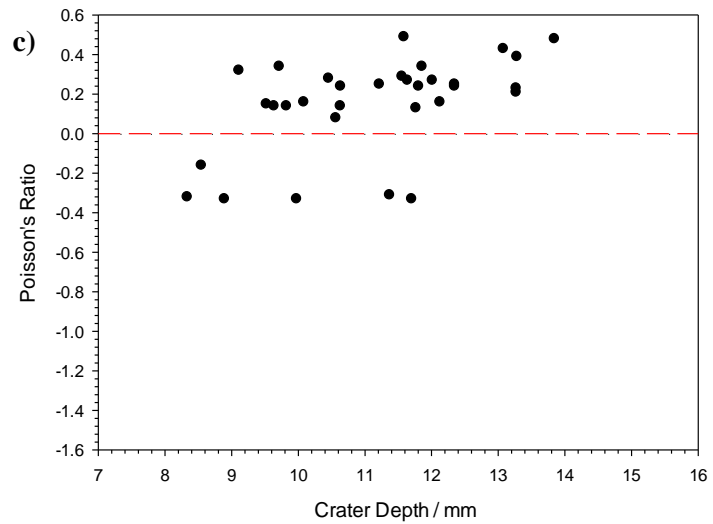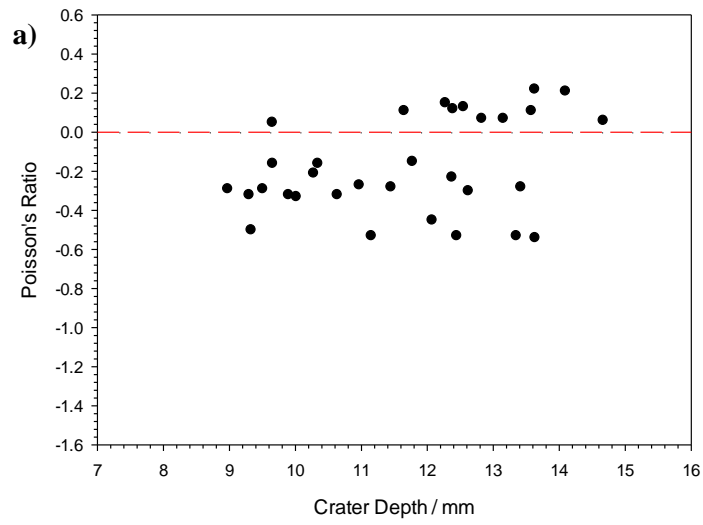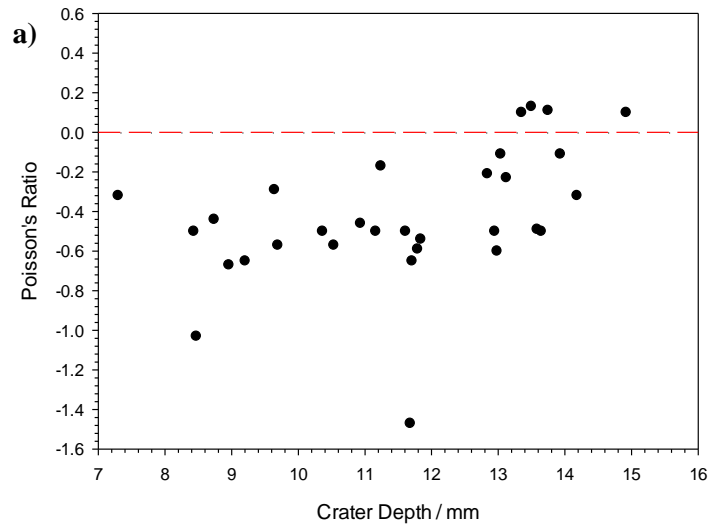
Figure 5.8: Poisson's ratio *vs.* crater depth for the 45 PPI longitudinal orientated polyurethane foams at: **a)** 4.88, **b)** 3.91 and **c)** 2.93 volumetric compression ratios. The red dash line represents the positive-negative boundary.
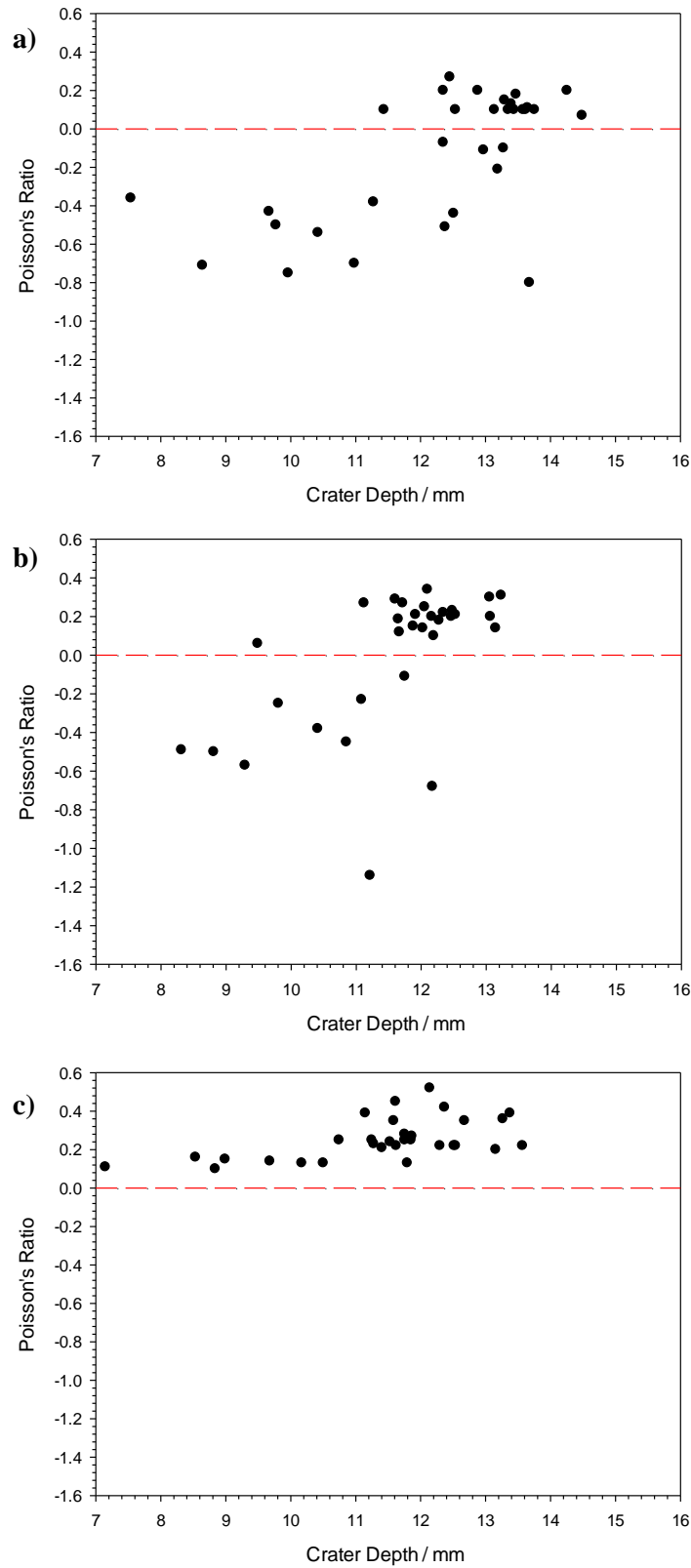
Figure 5.9: Poisson's ratio *vs.* crater depth for the 10 PPI longitudinal orientated polyurethane foams at: **a)** 4.88, **b)** 3.91 and **c)** 2.93 volumetric compression ratios. The red dash line represents the positive-negative boundary.
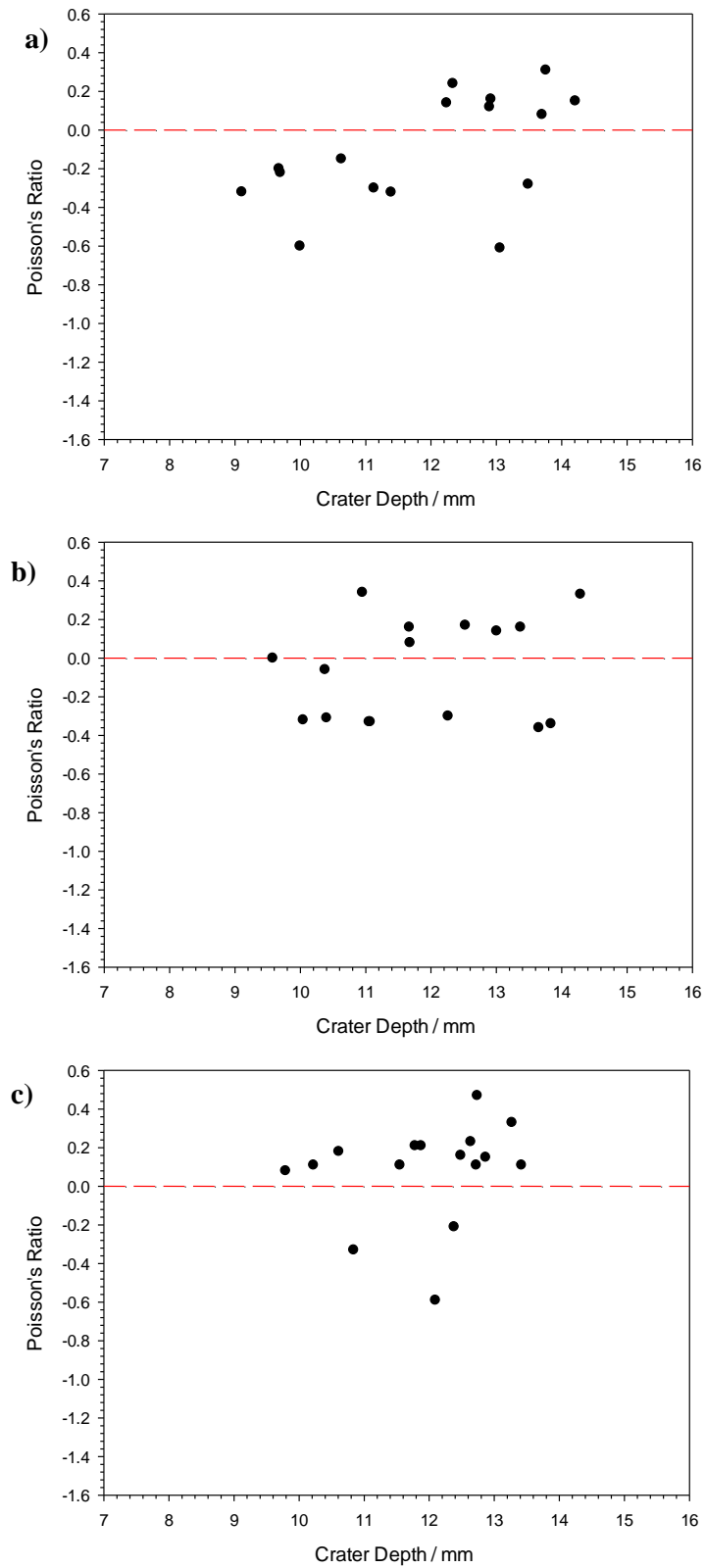
Figure 5.10: Poisson's ratio *vs.* crater depth for the 45 PPI latitudinal orientated polyurethane foams at: **a)** 4.88, **b)** 3.91 and **c)** 2.93 volumetric compression ratios. The red dash line represents the positive-negative boundary**.**
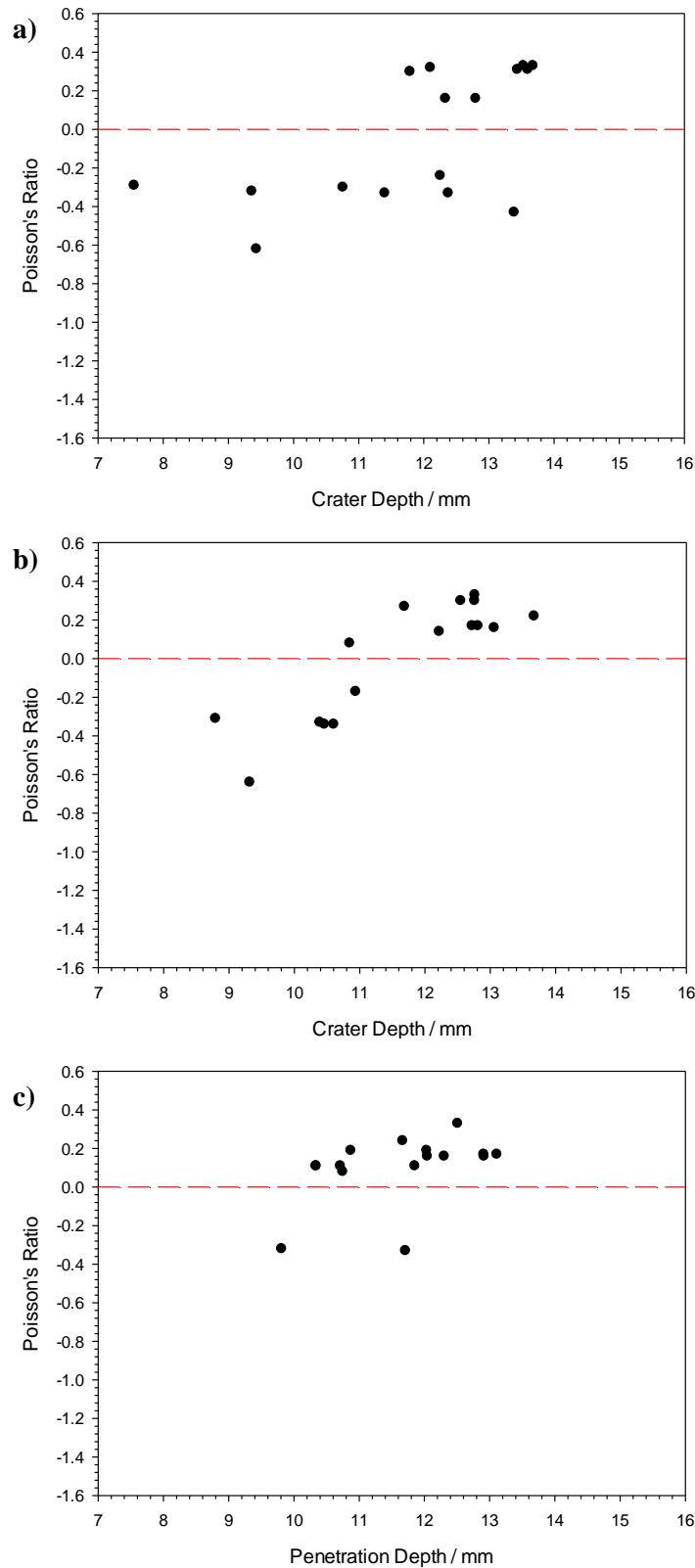
Figure 5.11: Poisson's ratio *vs.* crater depth for the 10 PPI latitudinal orientated polyurethane foams at: **a)** 4.88, **b)** 3.91 and **c)** 2.93 volumetric compression ratios. The red dash line represents the positive-negative boundary**.**

To explore the influence of foam density on the crater depths, all crater depths for a base porosity (for latitudinal samples) were plotted against density in Figure 5.12. The data from the

longitudinal samples were omitted due to the large variations in density that occur between each third of each sample [24, 153], unlike the latitudinal samples which were extracted from the central third of the auxetic foams and thus do not contain these high density regions.
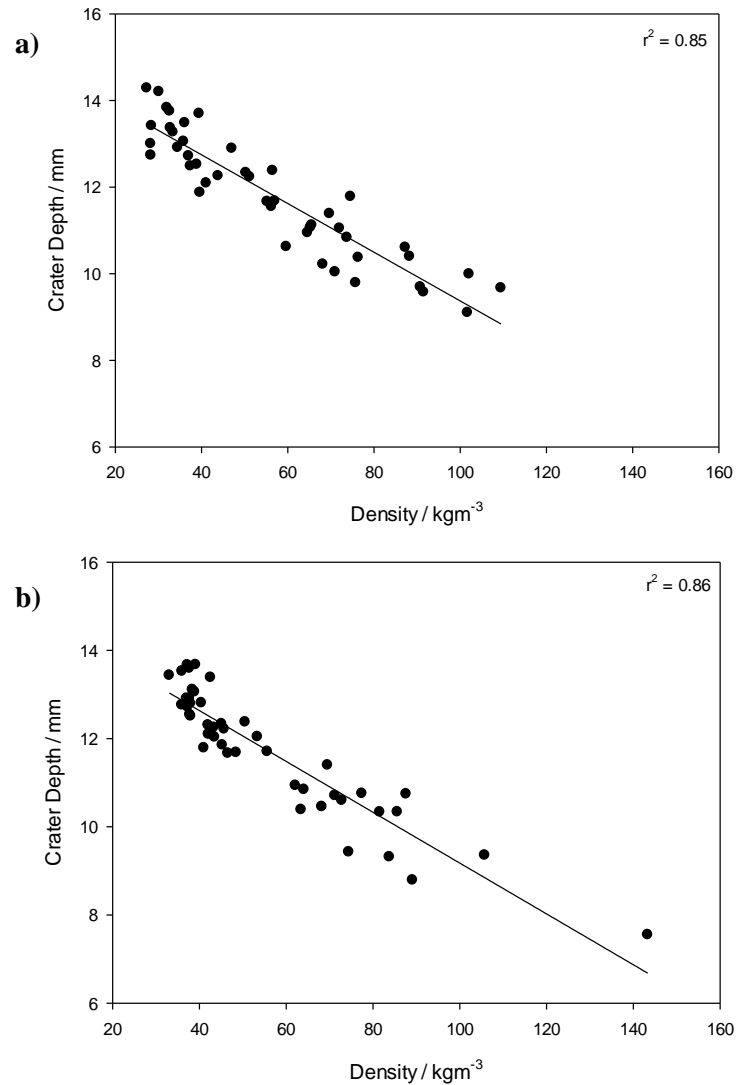
Figure 5.12: Crater depth *vs*. density for latitudinal: **a)** 45 PPI and **b)** 10 PPI polyurethane foams.

When plotted, both datasets indicated a strong linear relationship between density and crater depth, where the *R*-squared correlation coefficient was found to be 0.85 and 0.86 for 45 PPI and 10 PPI samples, respectively. Interestingly, when the mean crater depths were plotted against mean sample density for a given heating time, this relationship was again shown (Figure 5.13 and Figure 5.14).
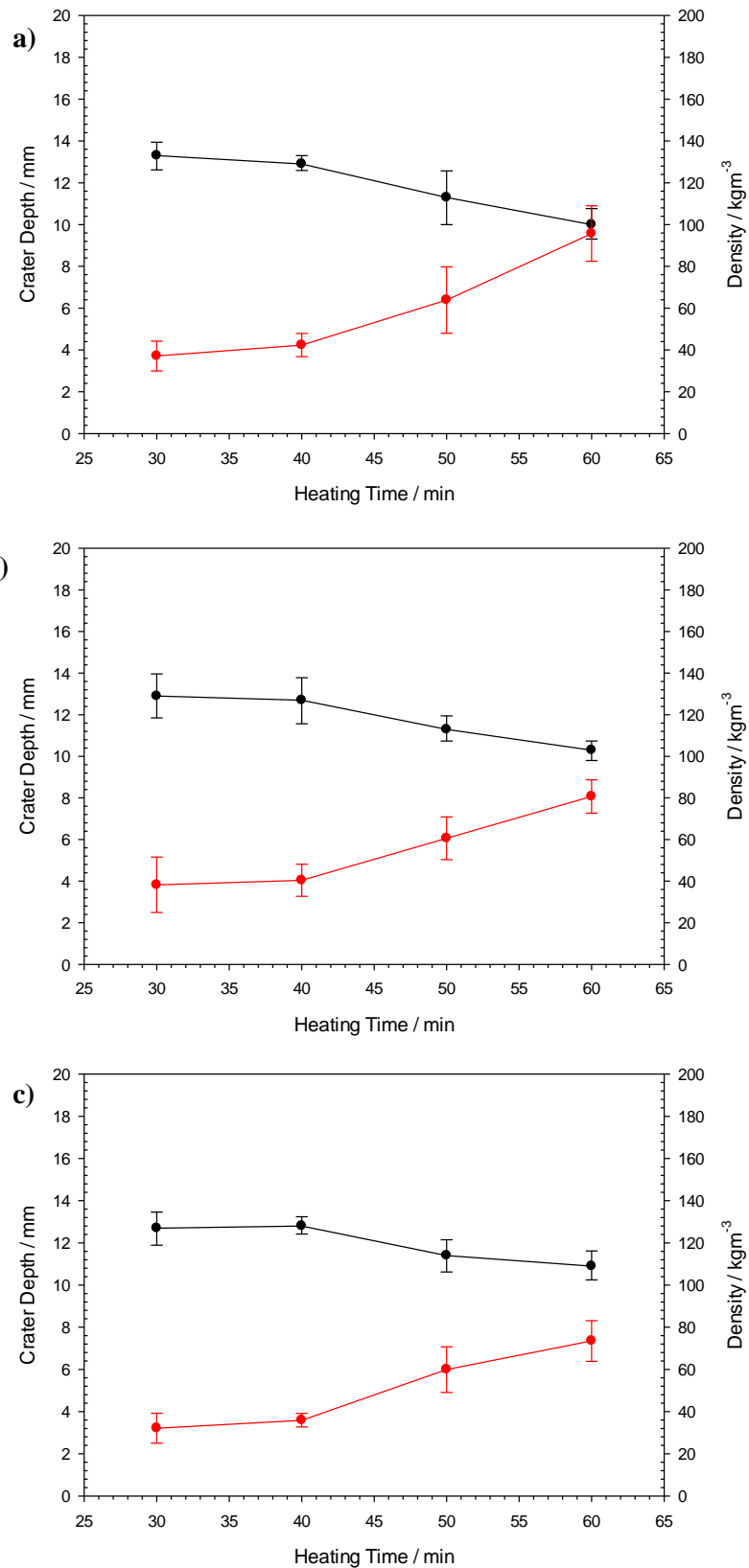
Figure 5.13: Density *vs.* crater depth for 45 PPI latitudinal orientated polyurethane foams at volumetric compressions: **a)** 4.88, **b)** 3.91 and **c)** 2.93, where black circles correspond to the crater depth and red circles to density.
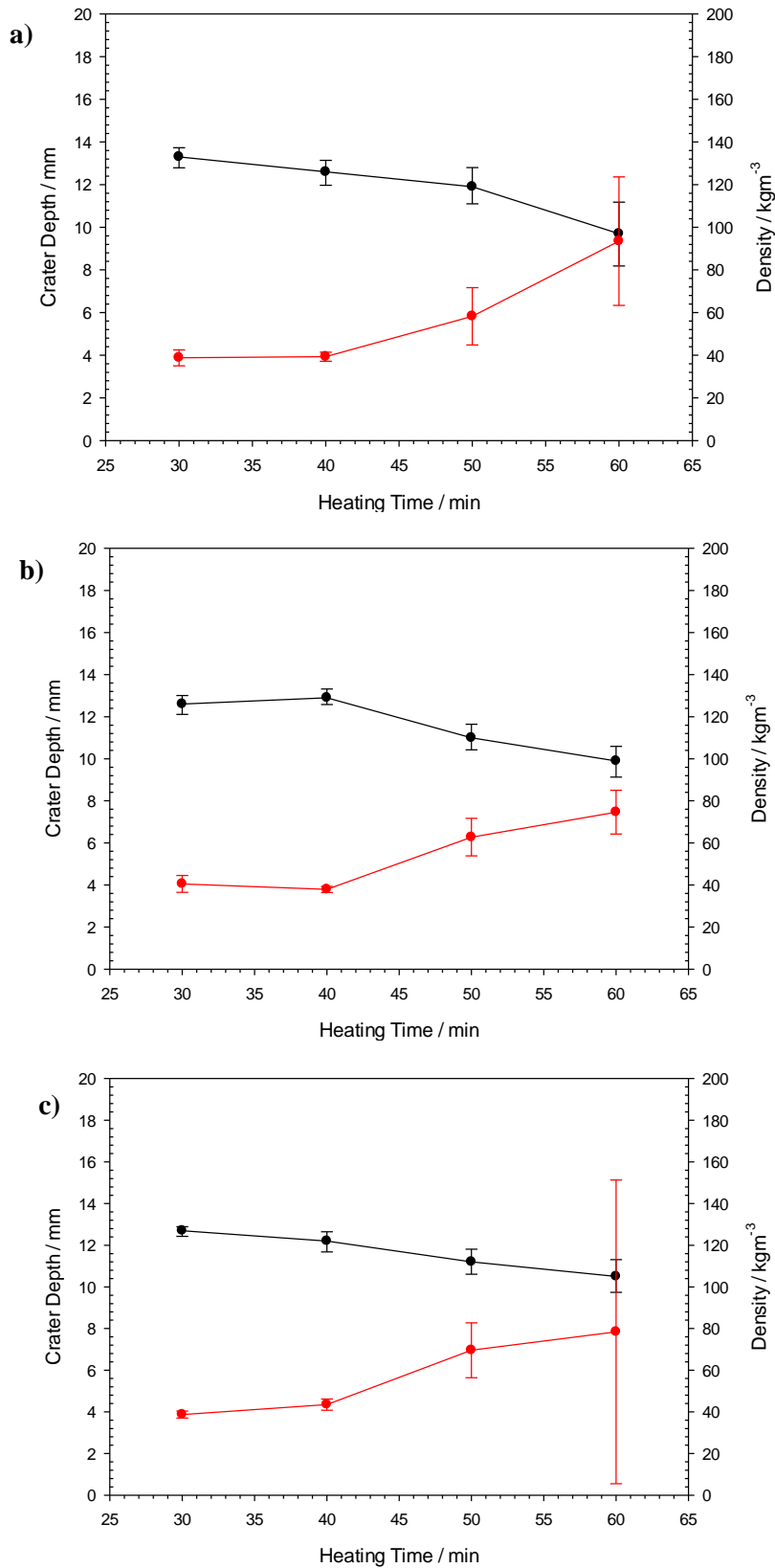
Figure 5.14: Density *vs.* crater depth for 10 PPI latitudinal orientated polyurethane foams at volumetric compressions: **a)** 4.88, **b)** 3.91 and **c)** 2.93, where black circles correspond to the crater depth and red circles to density.

5.3   Energy Absorption

5.3.1.1 Non-auxetic samples:

By studying the craters produced from impact, the amount of energy absorbed by a sample can be established. To understand the changes in energy absorption induced by the presence of auxetic samples, it is first necessary to assess the conventional foams, in both longitudinal and latitudinal orientations. For each foam type, six samples were tested and plotted in Figure 5.15, where mean values were calculated from the raw data and set as benchmarks, thus allowing a direct comparison between the auxetic and conventional foams. On average the 45 PPI and 10 PPI longitudinal conventional foams absorbed 2.2±0.2 J and 3.3±0.3 J, while the latitudinal samples of 45 PPI and 10 PPI absorbed 2.3±0.5 J and 2.8±0.4 J of the 7.4 J impact (Figure 5.15).
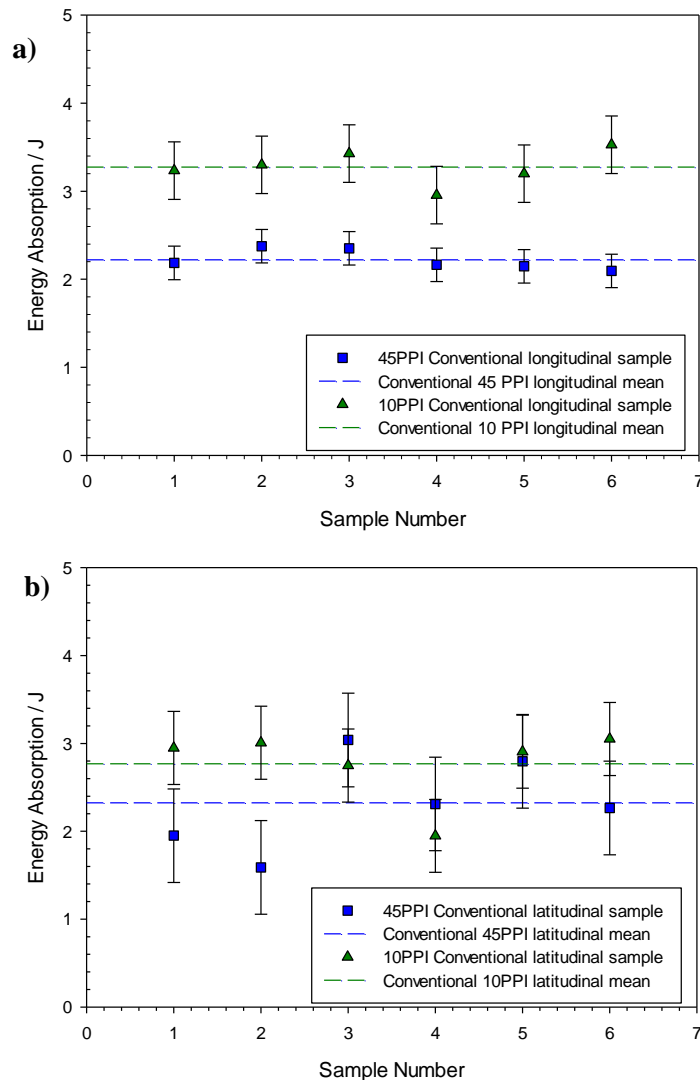
Figure 5.15: Energy absorption for the 45 PPI and 10 PPI conventional foams, where a 95% confidence interval provides the error**.**
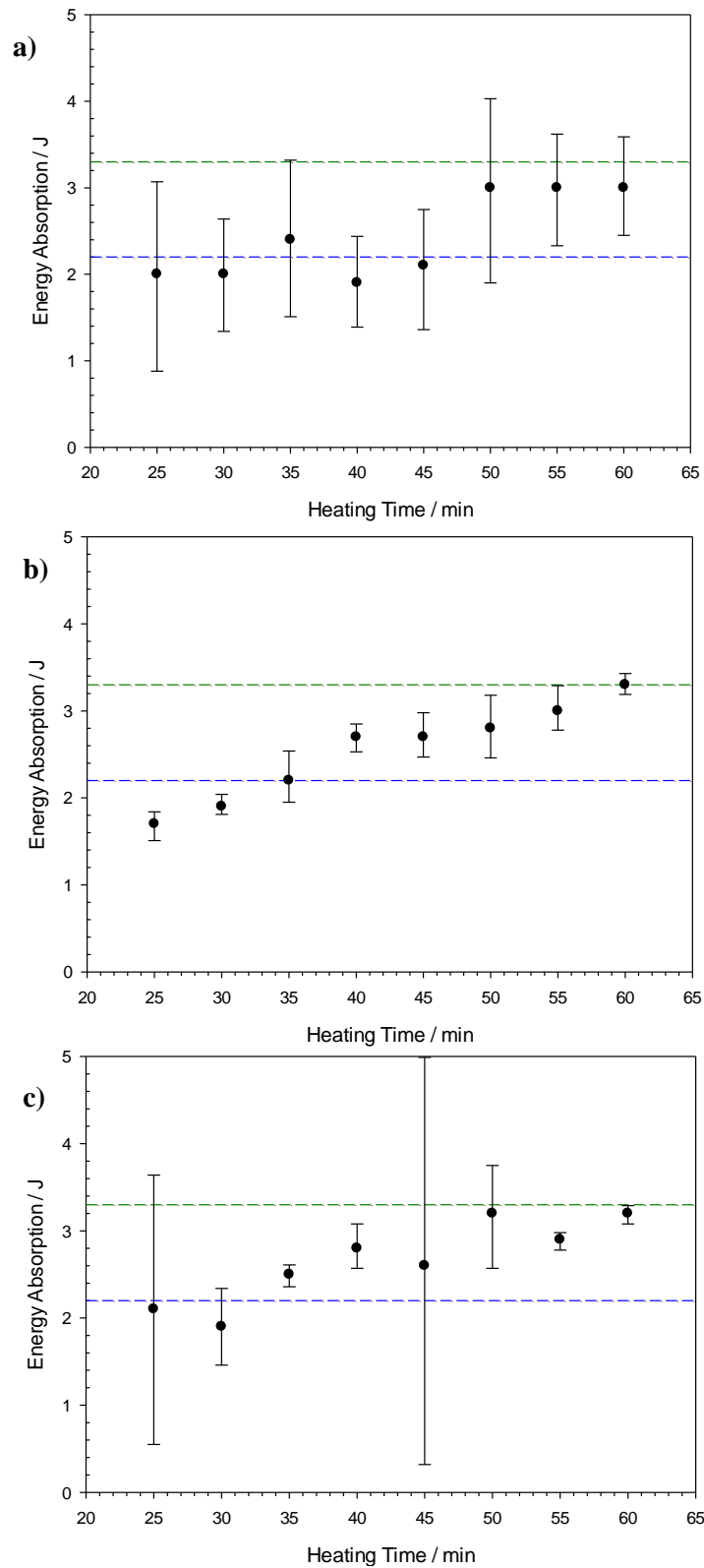
Figure 5.16: Energy absorption *vs*. heating time for longitudinal 45 PPI samples at: **a)** 4.88, **b)** 3.91 and **c)** 2.93 volumetric compression, where green dash represents the mean energy absorbed by conventional 45 PPI foam and blue dashed line is the mean energy absorbed by conventional 10 PPI foam. Error bars are provided by a 95% confidence interval**.**
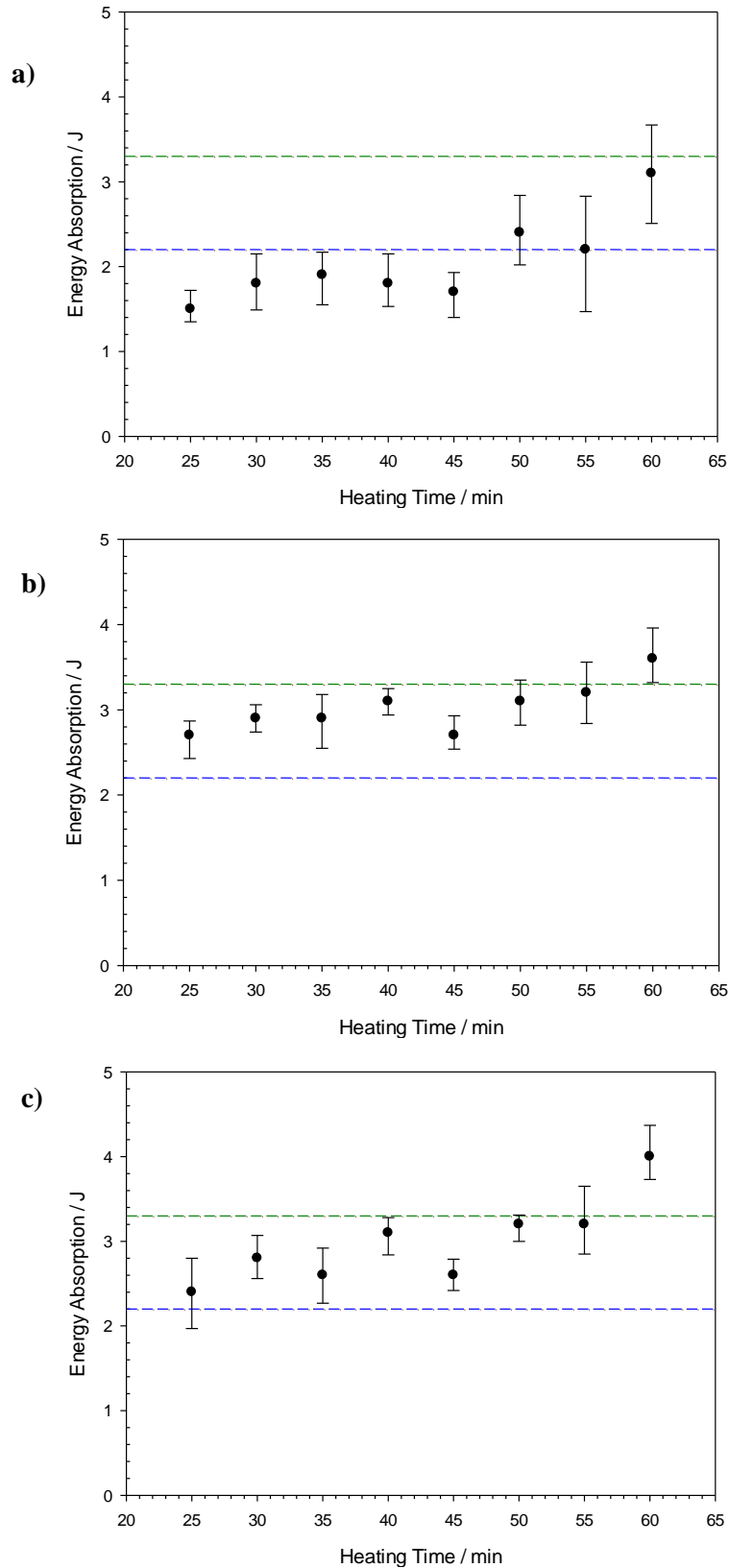
Figure 5.17: Energy absorption *vs*. heating time for longitudinal 10 PPI samples at: **a)** 4.88, **b)** 3.91 and **c)** 2.93 volumetric compression, where green dash represents the mean energy absorbed by conventional 45 PPI foam and blue dashed line is the mean energy absorbed by conventional 10 PPI foam. Error bars are provided by a 95% confidence interval**.**
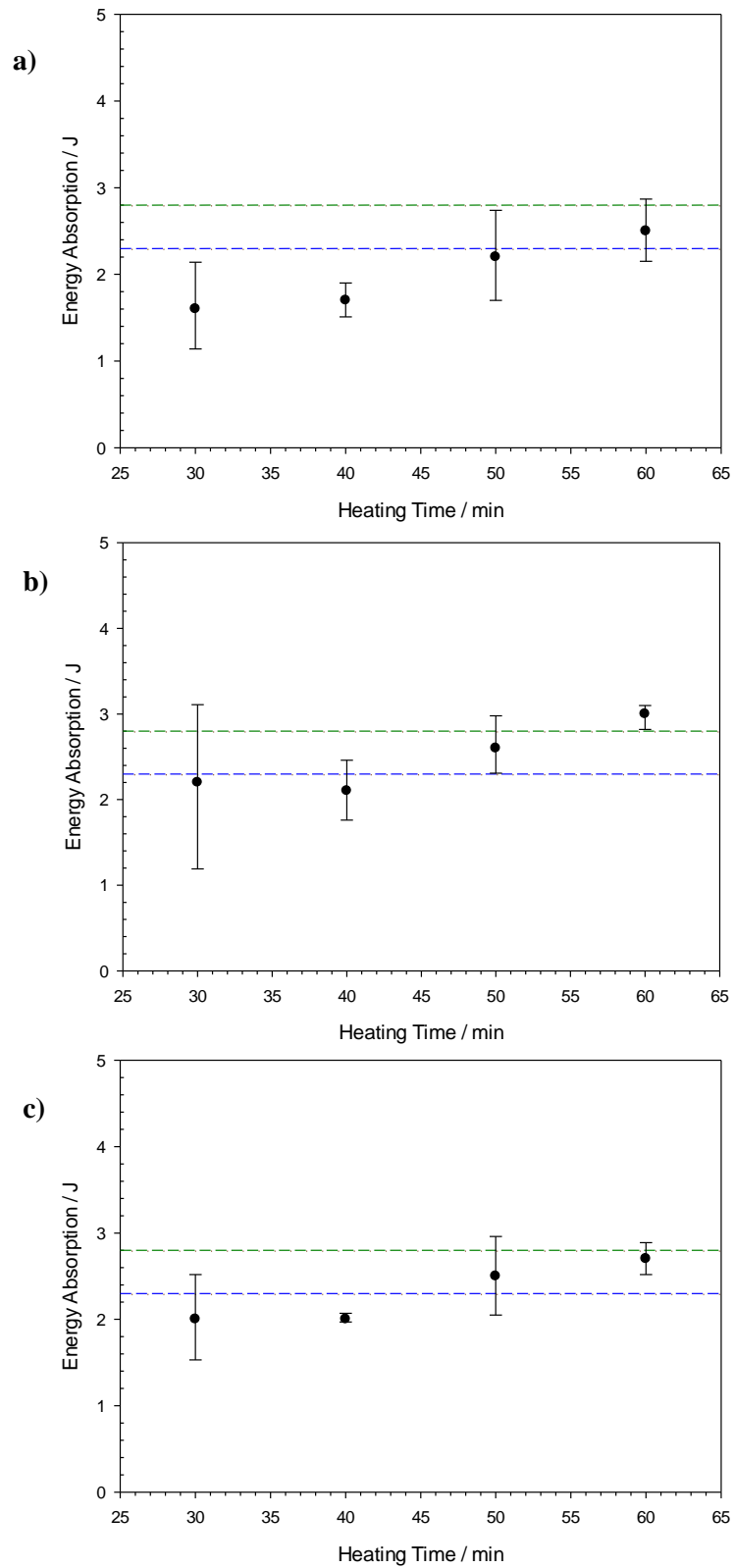
Figure 5.18: Energy absorption *vs*. heating time for latitudinal 45 PPI samples at: **a)** 4.88, **b)** 3.91 and **c)** 2.93 volumetric compression, where green dash represents the mean energy absorbed by conventional 45 PPI foam and blue dashed line is the mean energy absorbed by conventional 10 PPI foam. Error bars are provided by a 95% confidence interval.
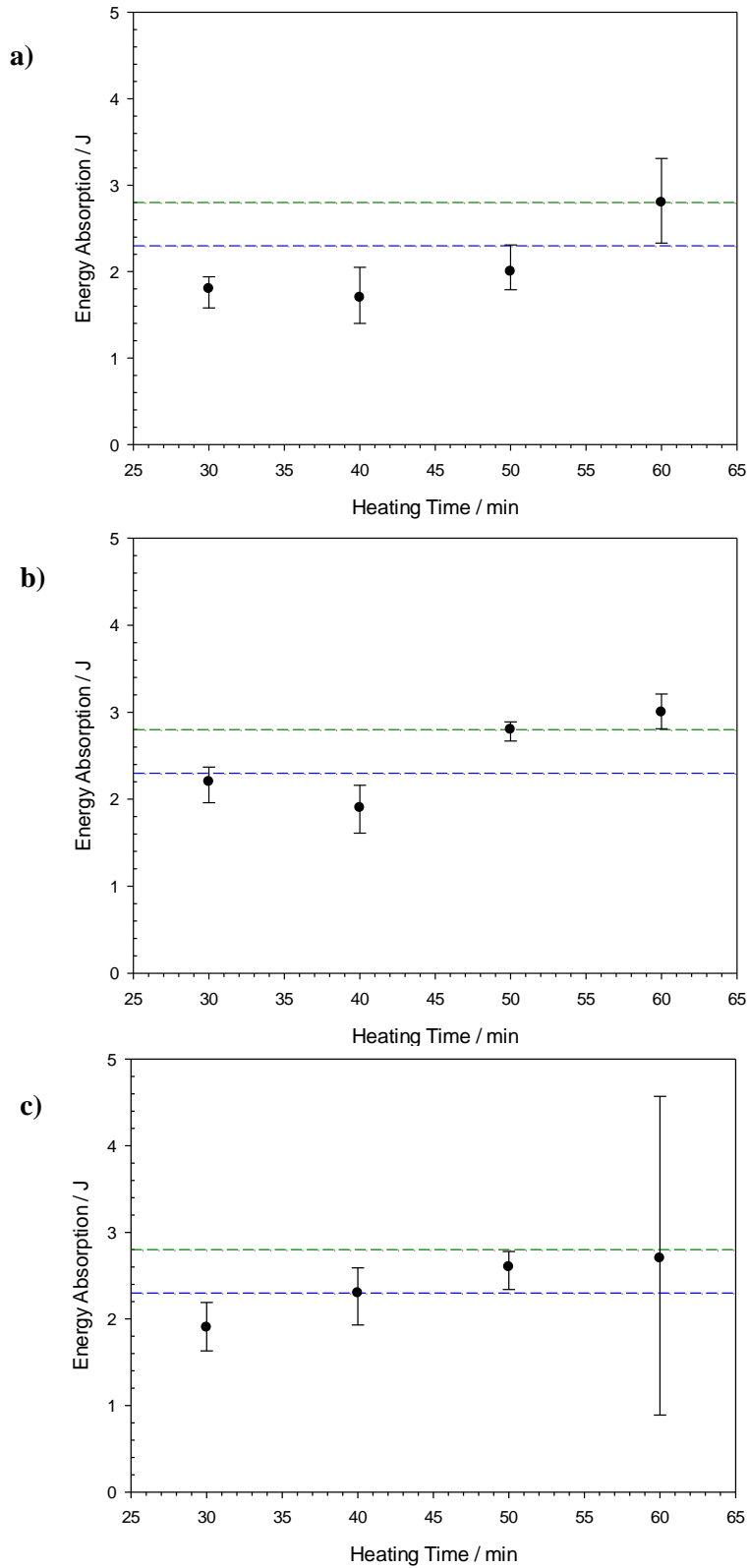
Figure 5.19: Energy absorption *vs*. heating time for latitudinal 10 PPI samples at: **a)** 4.88, **b)** 3.91 and **c)** 2.93 volumetric compression, where green dash represents the mean energy absorbed by conventional 45 PPI foam and blue dashed line is the mean energy absorbed by conventional10 PPI foam. Error bars are provided by a 95% confidence interval.

Figure 5.16 to Figure 5.19 show the mean heating time *vs*. energy absorption with respect to the volumetric compression ratio, heating time, base foam porosity and sample orientation, where, no overall discernible relationship was found to exist. Some datasets did however indicate localised trends, such as the loose linear relationships between heating time and energy absorption as shown in Figures 5.16b, and figures 5.18a, b and c.

In some instances, the auxetic materials performed worse than their conventional counterparts, from which they were fabricated. This is especially prominent for the auxetic foams fabricated from the 10 PPI foam, where only heating times between 50 to 60 minutes are shown capable of absorbing more energy than their base material. In some instances, the auxetic materials performed worse than their conventional counterparts, from which they were fabricated. This is especially prominent for the auxetic foams fabricated from the 10 PPI foam, where only heating times between 50 to 60 minutes are shown capable of absorbing more energy than their base material. While the requirement of high heating times can be explained by the temperature effects discussed in Chapter 4, it is currently unclear why samples outside of this range result in auxetic foams with energy absorption less than their conventional counterparts, as it has been identified in literature (and supported by the work in Chapter 4) [137, 154], that auxetic fabrication only requires temperatures above the material T_g (cited as approximately 114°C for polymer foams [106]. One such explanation could be that the low heating times causes the presence of both auxetic and conventional cells to exist in large quantities. These different cells could then be counter acting each other resulting in a behaviour that is neither synonymous with either foam type.

Energy absorption was then plotted (Figure 5.20 to Figure 5.23) against Poisson's ratio to establish if a negative Poisson's ratio, influenced energy absorption. Overall, no relationship between Poisson's ratio and energy absorption was shown to exist, (as confirmed by Bianchi *et al.* [106]), however in the majority of datasets, samples that absorbed the greatest amount of energy also exhibited a negative Poisson's ratio. Furthermore, Figure 5.20 to Figure 5.23 also indicated that not only can samples with the similar Poisson's ratios exhibit different energy absorptions, but also those with different Poisson's ratios can also absorb the same amount of energy. One explanation for the lack of a discernible relationship could be attributed to the fact that Poisson's ratio is a localised measurement [241] whereas energy absorption is more associated to the global behaviour of the foam sample.
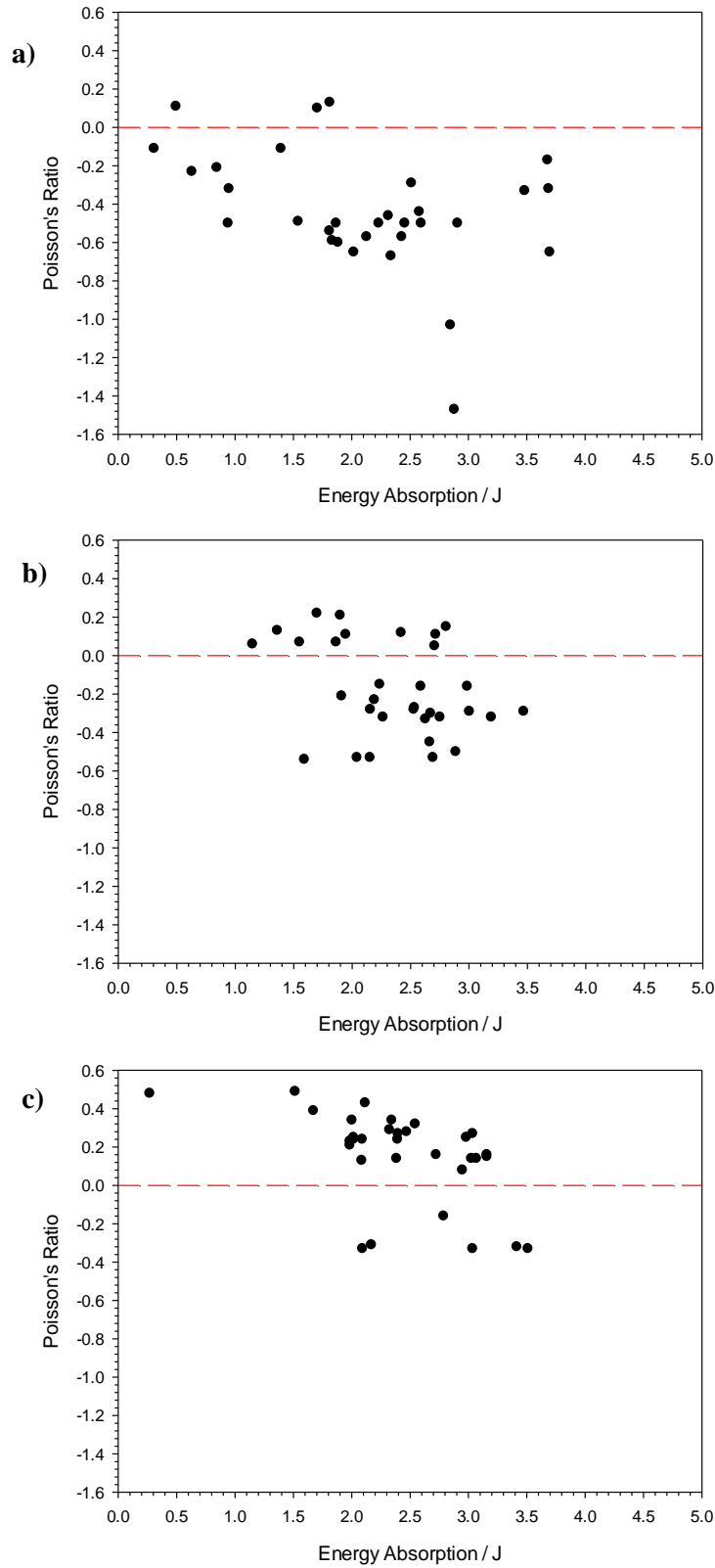
Figure 5.20: Poisson's ratio *vs.* energy absorption for the 45 PPI longitudinal orientated polyurethane foams at: **a)** 4.88, **b)** 3.91 and **c)** 2.93 volumetric compression ratios. The red dash line represents the positive-negative boundary.
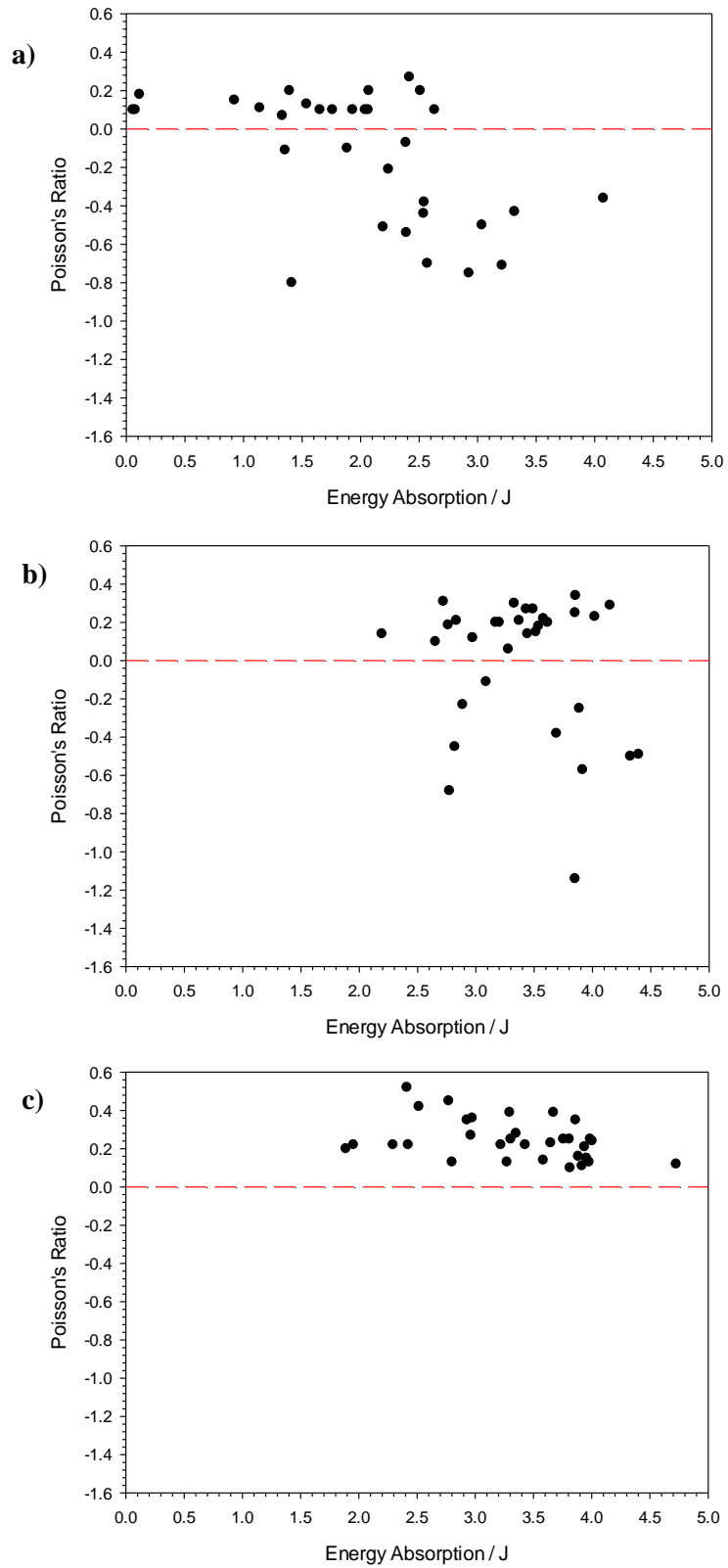
Figure 5.21: Poisson's ratio *vs.* energy absorption for the 10 PPI longitudinal orientated polyurethane foams at: **a)** 4.88, **b)** 3.91 and **c)** 2.93 volumetric compression ratios. The red dash line represents the positive-negative boundary**.**
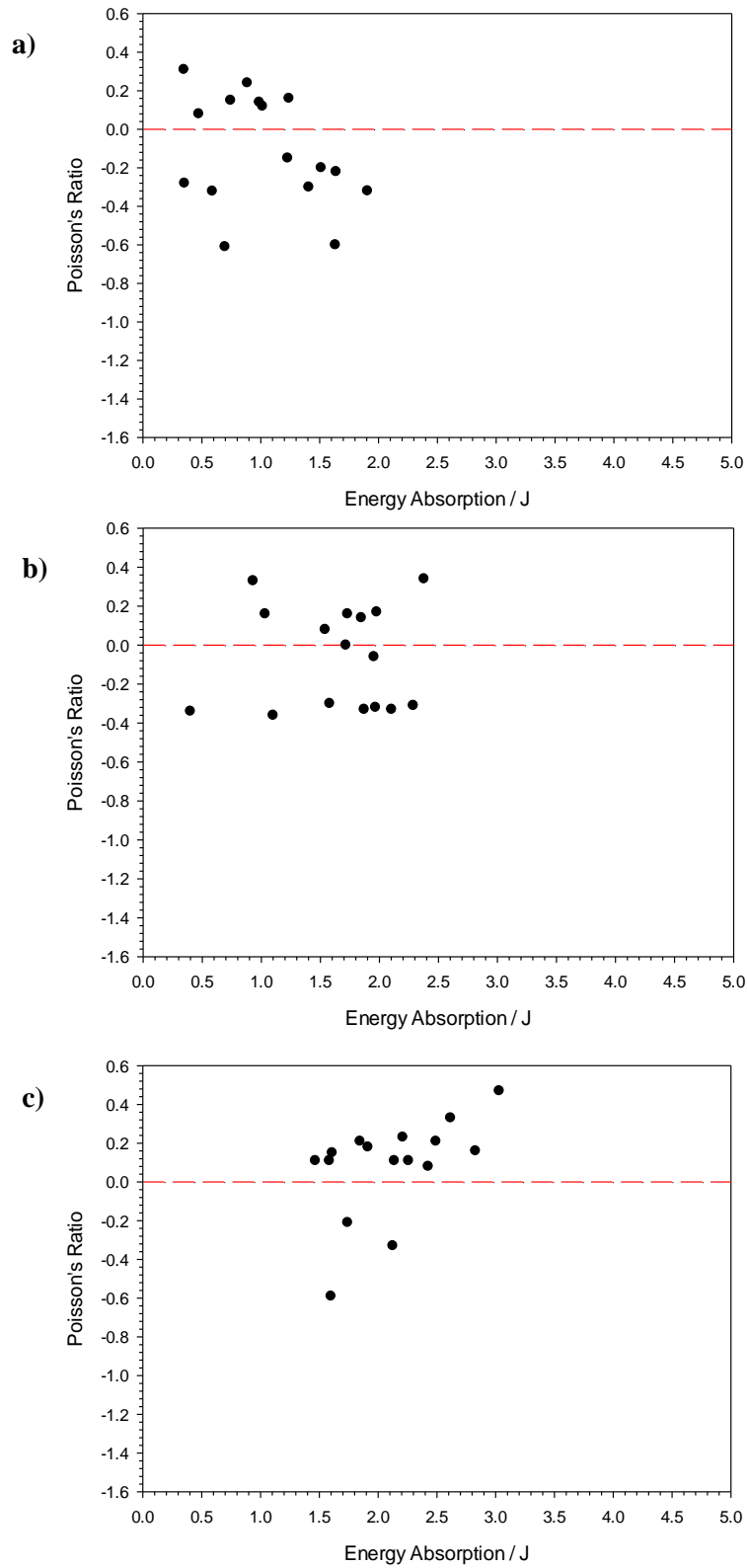
Figure 5.22: Poisson's ratio *vs.* energy absorption for the 45 PPI latitudinal orientated polyurethane foams at: **a)** 4.88, **b)** 3.91 and **c)** 2.93 volumetric compression ratios. The red dash line represents the positive-negative boundary**.**
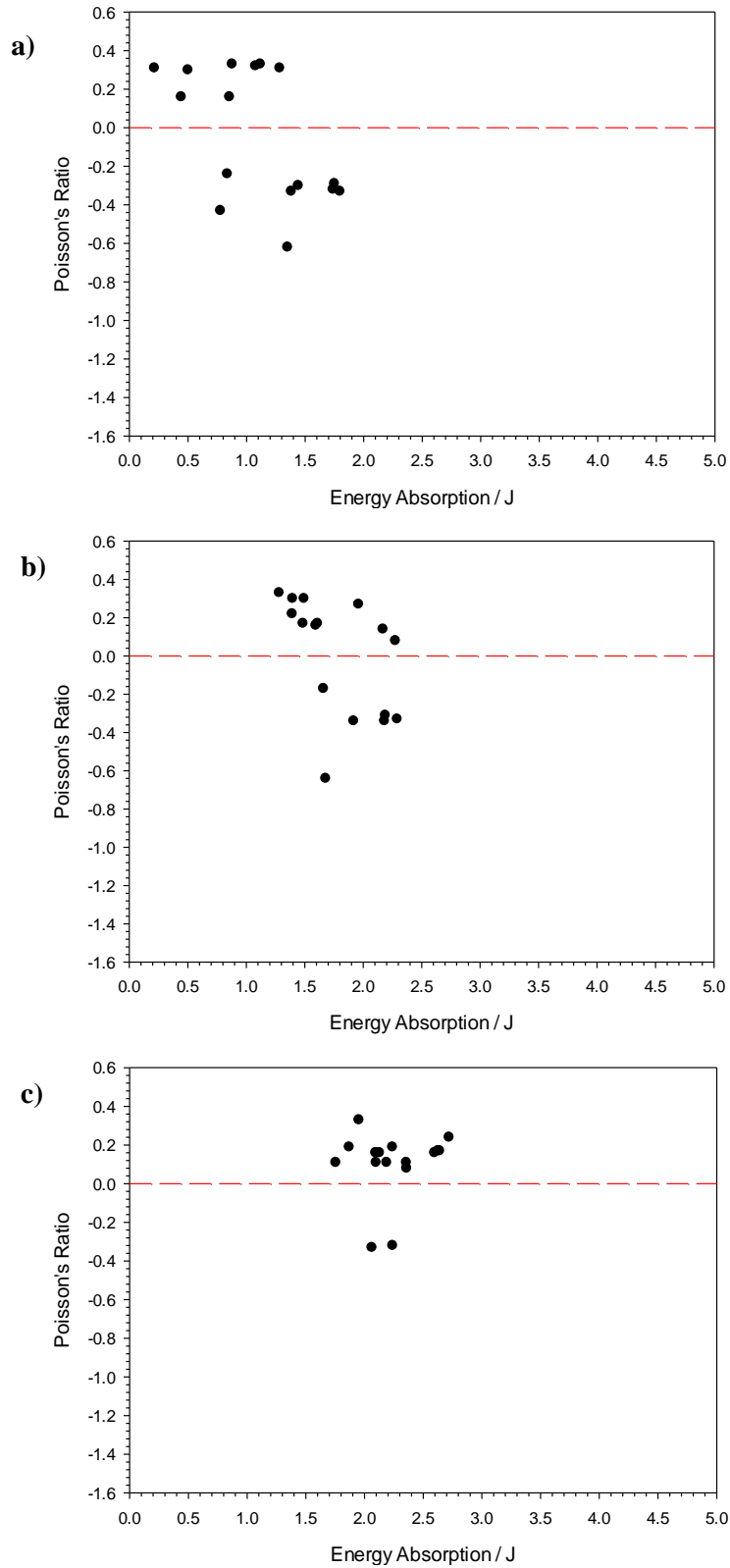
Figure 5.23: Poisson's ratio *vs.* energy absorption for the 10 PPI latitudinal orientated polyurethane foams at: **a)** 4.88, **b)** 3.91 and **c)** 2.93 volumetric compression ratios. The red dash line represents the positive-negative boundary.

While little evidence is reported to support that the presence of a negative Poisson's ratio influences energy absorption, it has been suggested by various authors throughout literature that

energy absorption of porous materials is directly linked to a foams relative density. In light of this, energy absorption vs density was explored. When energy absorption *vs.* density of the latitudinal samples (the data from the longitudinal samples were omitted due to the large variations in density that occur between each third of each sample [24, 153]) were plotted with respect to volumetric compression ratio and its porosity, no trends were shown to exist (Figure 5.24 and Figure 5.25).
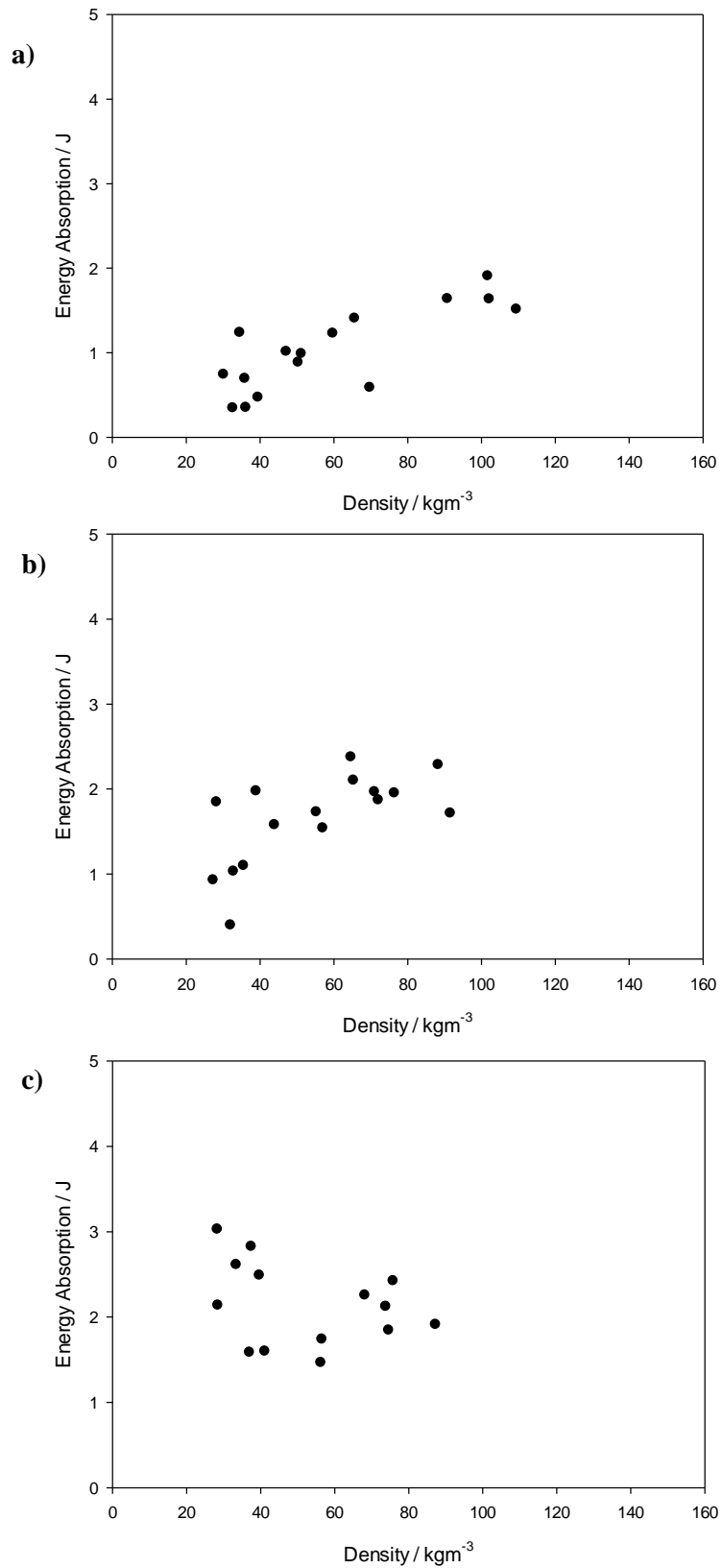
Figure 5.24: Energy absorption *vs*. density for the 45 PPI latitudinal orientated polyurethane foams: **a)** 4.88, **b)** 3.91 and **c)** 2.93 volumetric compression ratios**.**
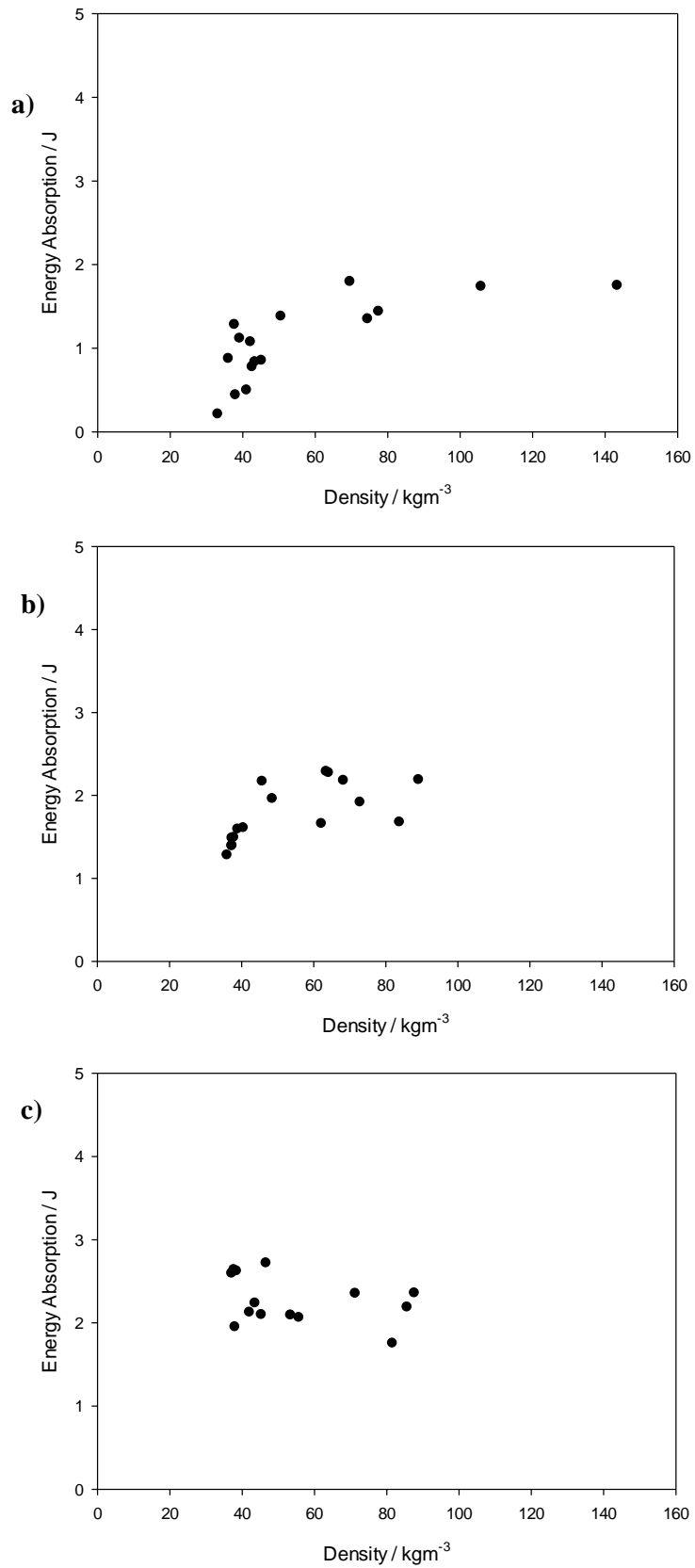
Figure 5.25: Energy absorption *vs.* density for the 10 PPI latitudinal orientated polyurethane foams: **a)** 4.88, **b)** 3.91 and **c)** 2.93 volumetric compression ratios**.**

170

However, it was only when all samples for a given porosity were plotted (Figure 5.26) against density, that a loose relationship (as indicated by *R*-squared correlation coefficients of 0.54 and 0.59 for 45 PPI and 10 PPI samples, respectively) between an increase in density causing an increase in energy absorption was discernible.
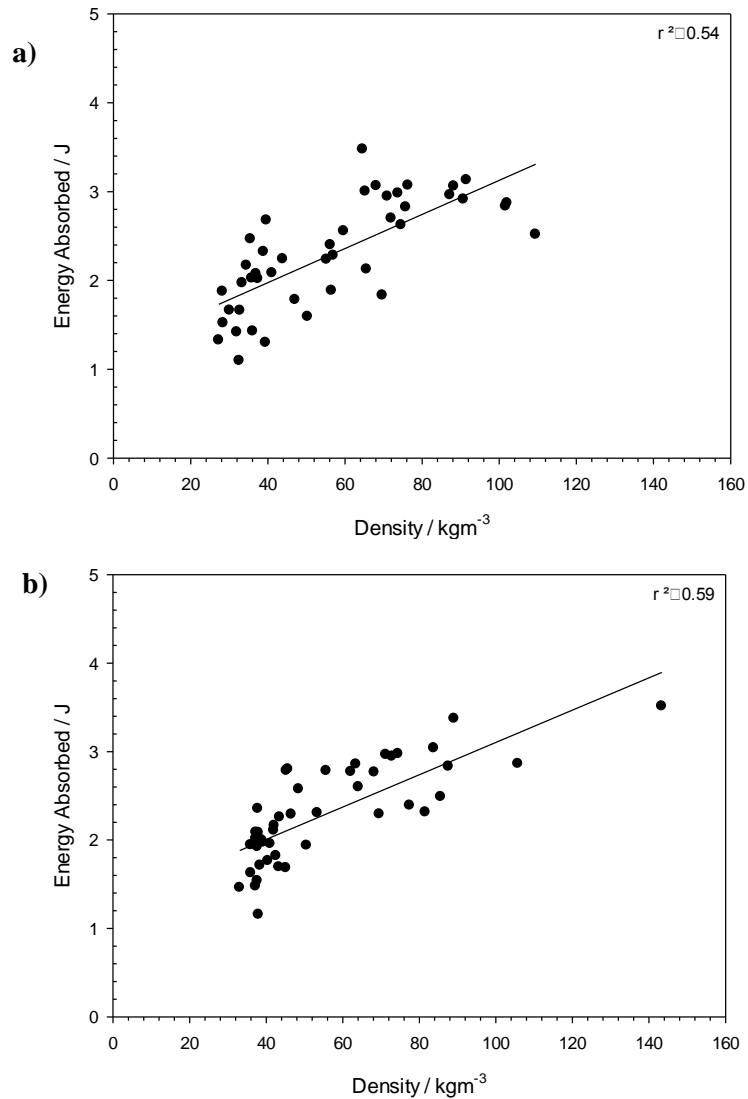
Figure 5.26: Energy absorption *vs.* density for latitudinal: **a)** 45 PPI and **b)** 10 PPI polyurethane foams.

In addition to the direct impact work, an analysis of stress-strain behaviour was undertaken in order to provide measurements of both the Poisson's ratio and Young's moduli of the cellular materials under compression loading. As it was previously identified (in Chapter 4) that samples manufactured at higher heating times together with high volumetric compression ratios, result in the highest negative Poisson's ratios, samples were manufactured at a heating time of 60 minutes at a volumetric compression ratio 4.88. The resulting samples were then extracted from the centre 1/3rd of a longitudinal sample, resulting in dimensions of approximately 30 mm × 30 mm × 33 mm. In addition to the auxetic samples, the remaining high density regions were also explored,

whilst conventional samples of the same dimensions were also tested. The results of the compression testing are shown below (Figure 5.27).

5.3.1.1.1 Poisson's Ratio:
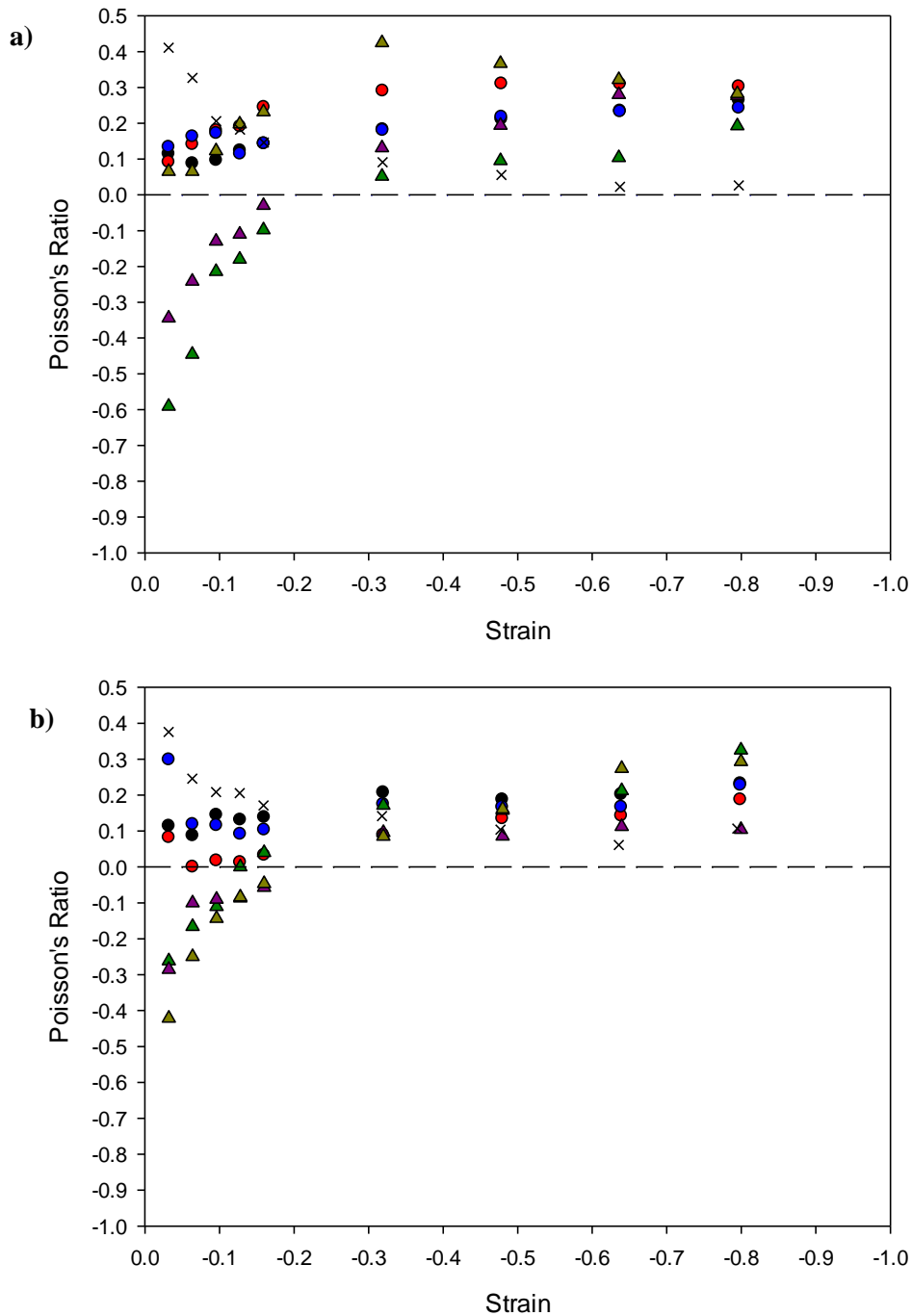
Figure 5.27: Graph showing compressive Poisson's ratio for samples manufactured at 60 minutes heating and volumetric compressions ratio of 4.88 for: **a)** 45PPI and **b)** 10 PPI foams, where ● ● ● and ▲ ▲ ▲ are the dense and central samples 1, 2 and 3, respectively. Conventional sample are denoted by ✕.

Figure 5.27 shows the Poisson's ratio *vs*. strain for all samples tested, where it can be seen that overall, all but one of the central region samples exhibited a negative Poisson's ratio. For each negative Poisson's ratio sample, as strain increased, Poisson's ratio converged towards a positive

value, as previously shown in literature [131, 137]. Once a positive Poisson's ratio was achieved, the remaining strain intervals saw the samples (within a specific dataset) converge towards a common positive Poisson's ratio between $0.2 - 0.3$ and $0.1 - 0.35$ for 45 PPI and 10 PPI foams, respectively. None of the dense region samples exhibited evidence of a NPR. Instead the majority of these samples initially exhibited a positive Poisson's ratio of approximately 0.1 that varied with respect to strain. Furthermore both conventional foams were shown to have similar behaviour, exhibited a Poisson's ratio near 0.4 at initial straining, which converge towards 0 with an increase in strain.

In addition to measuring the Poisson's ratio, the stress-strain performance of the tested foams was also explored (Figure 5.28), where all samples, first exhibited an initial linear elastic region, in which the cell walls of the foam structure elastically bend. During this region, it was shown that for the 45 PPI based samples; the dense region samples exhibited a greater modulus. However, there was no conclusive evidence to show that similar behaviour occurred with the 10 PPI samples, as central sample 2 exhibited a modulus greater than dense sample 2.
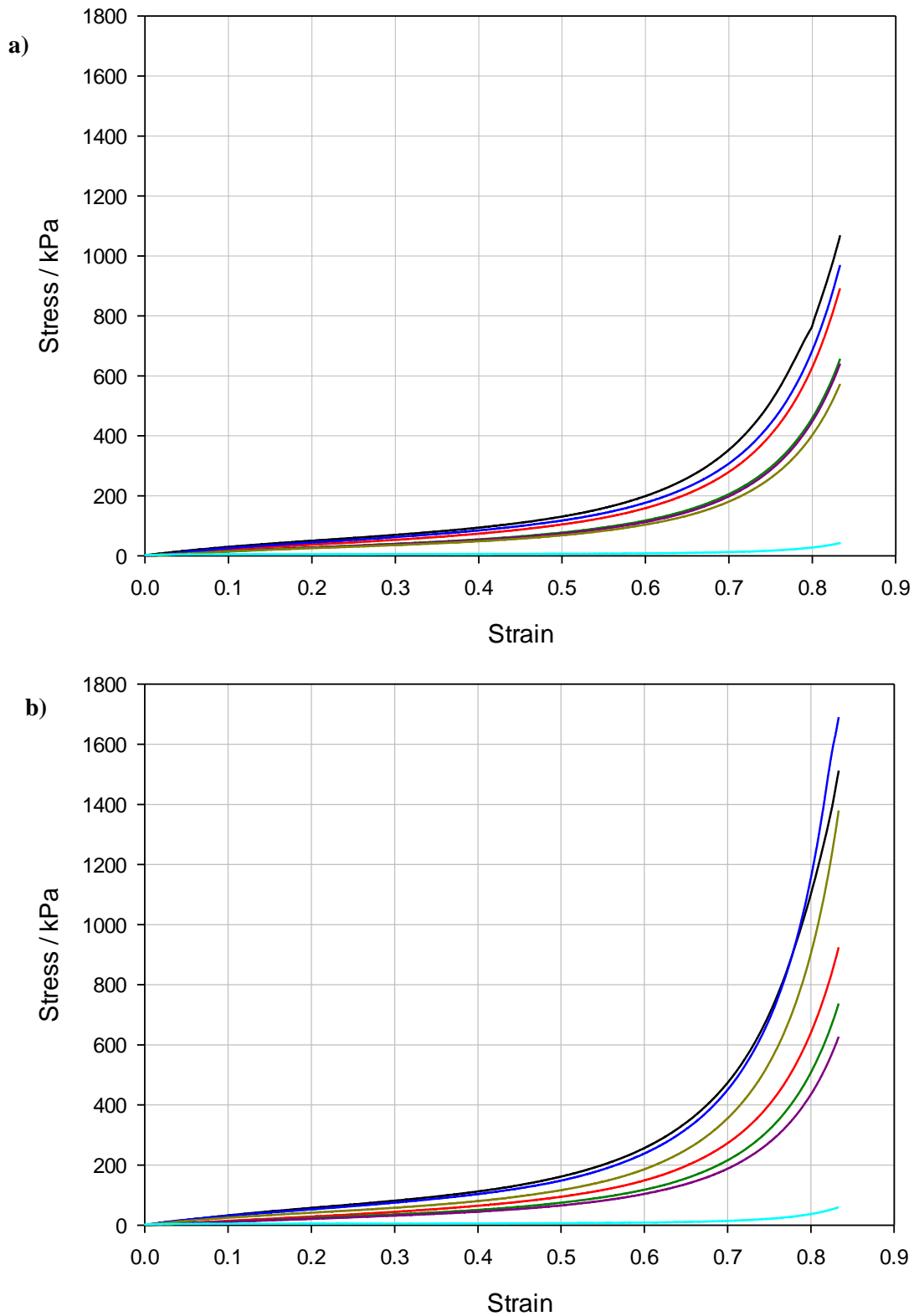
Figure 5.28: Graph showing compressive stress-strain behaviour for samples manufactured at 60 minutes heating and volumetric compressions ratio of 4.88 for: **a)** 45PPI and **b)** 10 PPI foams, where ▬ ▬ ▬ and ▬ ▬ ▬ are the dense and central samples 1, 2 and 3, respectively. Conventional sample are denoted by ▬ .

Following linear elastic behaviour, the dense regions then exhibited stress-strain behaviour that is synonymous with highly dense conventional foams. Unlike the dense samples, the central

samples featured the extended linear stress-strain behaviour synonymous with auxetic foams [131]. In addition to the increase in stiffness that the dense samples exhibited over the central samples, it was also observed that these samples transitioned into the densification phase earlier.

From the stress-strain curves, it is also possible to calculate the energy absorbed per unit volume of specific samples by the area under the curve. Overall it was found that the dense samples absorbed more energy than their central counterparts. Interestingly, when considered with respect to specific sample density, no distinct relationship between a samples density and its stress-strain behaviour was shown to occur. This observation contradicts literature, where it is reported that that stress-strain behaviour is directly influenced by a foam sample's relative density [159]. While the exact reason for this contradiction is unknown, one possible explanation could be due to the variable density that exists throughout foam samples that have been subjected to the auxetic fabrication process, as previously shown in Chapter 5.

Furthermore, the work presented here could be interpreted to suggest that auxetic foams do not exhibit greater energy absorption than their conventional counterparts due to their negative Poisson's ratio, but instead because of the increase in density that they obtain from the fabrication process [137, 154]. However without comparison between auxetic and conventional foams of matching densities, it is not possible to deduce if auxetics are better at energy absorption due to their increase in density or because of their structure.

5.4   Discussion

5.4.1   Role of density and its influence on performance

In this study, a decrease in crater depth and an increase in energy absorption of the foam, were shown to correlate with an increase in relative density; a behaviour also reported by [137, 154]. The controlling factor of density was linked to both the volumetric compression ratio and the applied heating time, where the latter controlled the stability of holding its new density, by the auxetic fabrication process, as previously discussed in Chapter 4.

Although the auxetic fabrication process produced foams with negative Poisson's ratios, it was found that these had little effect upon the crater depth and energy absorption. Instead, the improvements came from the increased density through the auxetic manufacturing process. Currently it is unclear if the behaviour of auxetic foams is better than conventional foams for a given density, as it is difficult to compare like-for-like densities due to a limited pool of open cell polyurethane foams. However an additive manufacturing technique would allow consistency and controllability of the densities to be explored, as discussed in Chapter 6.

For cellular materials, including auxetic foams [129], relative density ((ρ^* / ρ_s): where ρ^* is the density of the foam and ρ_s is the density of the solid material from which it is [159]) is the main controlling factor in determining the energy absorption per unit volume of a porous material (i.e., the integral of the stress-strain curve) [159]. Since the role of the foam during a loading event is to decelerate a payload via deformation of the cellular structure, energy absorption is achieved by three distinct phases: elastic deformation; plastic deformation; and densification (Figure 5.29). Within the linear elastic region, only a small amount of energy is absorbed through cell wall bending. Once the yield point is exceeded, the plastic 'plateau region' is entered; during this phase, large energy absorption occurs at near-constant loading, through the collapse of cells through buckling, yielding and fracturing failures [159]. Finally, when the cells have been crushed and further deformation is impeded, densification occurs. This process is shown to be highly dependent on the strain rate, composition, and density of the foam [159].
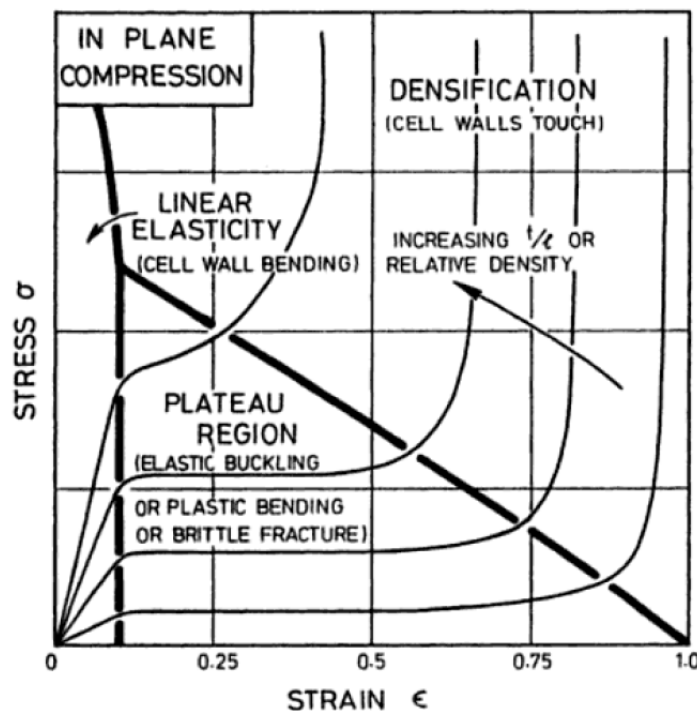
Figure 5.29: Stress-strain diagram of linear elastic, plastic plateau and densification changes with respect to relative density for a foam under compression [159].

Although not found in this work, based on the literature [159] it is suggested that there is an upper limit to the correlation between an increase in density and a reduction in crater depth. This limit might be met as increasing the density will hinder the foams ability to deform and absorb energy, due to a reduction in the free space available in which the cell ribs can deform.

For foams with very high densities, little deflection occurs, causing rapid deceleration and higher stresses owing to their relatively high stiffness. Alternatively for low density foams, limited

energy absorption occurs as little force is required to cause cellular deflection due to their relatively low stiffness, resulting in the foam to bottom out with a sharp increase in force causing the remaining impact energy to be transmitted to the substrate, in this case the Roma Plastilina clay backing. This results in the formation of a crater [43, 159], which when measured is used to calculate the energy absorbed by the foams, as presented in Section 5.2.2.

5.4.2   Sources of scatter in the data:

Scatter was more prominent in the auxetic materials, in comparison to the conventional materials and is attributed to a number of factors including:

- Defective and damaged cells;
- Inconsistencies in manufacturing of the foam;
- Elongation of cells within conventional foam;
- Systematic error;
- Operator error;
- Measurement error.

The presence of defective and damaged cells throughout the foam cellular structure weakens the local foam structure and influences the mechanical behaviour. It is reported that the loss of 5% of the cells within a structure can reduce the Young's modulus or stiffness by over 30% [47, 49, 159]. This in turn will reduce the overall energy absorption per unit volume.

Disparity within the cell geometry due to the inherent anisotropic nature of conventional foams can also attribute to the variation in energy absorption as any cell elongation or flattening will cause the properties of porous materials to become anisotropic and varied [159]. While all foams used within this current study were originally purchased from the same company (Recticel, UK) to limit this effect, due to the initial fabrication process of pumping carbon dioxide gas into liquid polyurethane [159, 242], both elongation of cells and density variation occur as the material cools [158, 160]. As such, when a sample is initially cut from the larger sheets of foam, random variations are already present, which in turn carries through to all stages of fabrication and experimentation. This behaviour was further exacerbated during the auxetic fabrication process, where heating and volumetric compression induced heterogeneous changes to the cellular geometry, resulting in foams with both conventional and auxetic microstructural cells.

Another source of scatter was due to the limited control over a number of variables during the fabrication process. While heating time and volumetric compression ratio can be controlled, it is currently not possible to control how the cellular ribs position themselves, as numerous quantities

of ribs compete for limited space. If a large number of ribs were to become fixed at a specific position within the foam body, high density pockets could form. Should a large amount of these pockets become localised within a region, the density within that region would increase while others decrease. This in turn could lead to either localised increases or decrease in energy absorption performance affecting the overall performance of the system.

Operator error also adds to the overall inaccuracies, especially when applying the volumetric compression ratio as the initial large samples have to be physically pushed into the mould by hand, often resulting in surface artefacts forming. Human error also influences other areas such as the measurement of the samples, as the pliable nature of the samples requires a hand rule to be implemented to record sample dimensional changes. Error can also be attributed to the limited amount of samples tested for each parameter combinations. By only testing a minimal amount of data points, it is difficult to ascertain reliable trends, as any significant scatter of the data will infringe statistical analysis.

5.4.3 Limitations and scope for future work

The current work utilises a low velocity impact to test the energy absorption of auxetic and conventional foams. In ballistic scenarios, when the hard ceramic plate is impacted, the armour not only defeats the bullet through fracture mechanics but also dissipates the energy over a larger area [3], before being decelerated by the TABs (if present). The deceleration of the projectile on the ceramic plate to the foam backing could change the dynamics of the loading-rate experienced by the foam. To the author's knowledge, whilst the loading-rate experienced by the foam constituent is unknown (whether it is in the regime of low, high or ballistic velocities), it raises the question whether the individual constituents of the full armour system could be tested independently and still be representative of the overall performance in a full armour system. Such understanding is important and will require further study. Should the loading-rate acting on the foam be in low-velocity regime, it will enable simplifying testing procedures and varying foam material parameters without the need to combine this with a more costly full armour system and ballistic testing. In such cases, the relevancy of this work becomes important to informing the foam's performance when used in a full armour system.

5.5 Summary

Auxetic and conventional polyurethane foams were studied with respect to the crater depths and total energy absorbed for a combination of heating times, volumetric compression ratios, porosities and samples orientations following a high mass, low velocity impact of 7.2 J.

When compared to the control impact mean crater depth of 17.5±0.9 mm, conventional off-the-shelf longitudinal foams of base porosity 45 PPI and 10 PPI reduced the mean crater depth to

12±0.3 mm and 10.5±0.2 mm, whilst latitudinal samples of the same porosities had a maximum reduction to 11.4±0.4 mm and 11.2±0.4 mm, respectively. When longitudinal orientated auxetic samples were substituted in place of conventional foams, the maximum reduction in mean crater depth was shown to be 8.3±4.3 mm at a 60 minute heating time for 10 PPI foam samples produced at a 2.93 volumetric compression ratio.

While no trends were found to exist between individual fabrication parameters and the resultant crater depths, combined, these parameters were shown to determine the overall sample density. Crater depth was found to be strongly influenced by the sample density, where an increase in density results in a reduction in crater depth. This behaviour is the result of relative density being the main controlling factor in determining the energy absorption per unit volume of a porous material, and is achieved by deformation of the foams structure through three distinct phases: elastic deformation; plastic deformation; and densification.

Overall, the greatest energy absorption of 4 J was found to occur at a 60 minute heating time for longitudinal 10 PPI foam samples produced at a 2.93 volumetric compression ratio. When considered with respect to error (provided by 95% confidence), this value increased to 4.99 J, and was now found to occur at a 60 minute heating time for at a 2.93 volumetric compression ratio, but for a longitudinal 45 PPI.

When analysed, an increase in density was shown to have a loose correlation with energy absorption, however this was explainable by the presence of defective and damaged cells throughout the foam cellular structure, coupled with disparity within the cell geometries causing anisotropic and orientation specific mechanical behaviour. This behaviour was caused by a number of factors including the cutting of the foam samples, the auxetic fabrication process and the original fabrication of the conventional polyurethane foam.

Chapter 6: 3D printing of auxetic foams

6.1   Introduction

Fabrication of auxetic foams is relatively easy to undertake, however, as demonstrated in Chapters 4 and 5 the production of consistent foams can be elusive due to the difficulties in positioning the internal cells when compressed during manufacture.   One novel method of introducing repeatability into the auxetic fabrication process is through the employment of 3D printing technologies using an additive manufacturing technique.   Through implementing these technologies, any random cell orientation is removed, as idealised auxetic foam topologies can be digitally designed, simulated and finally printed from a wide range of materials, including pliable polymers.   Auxetic microstructures can also be obtained through the scanning of conventional auxetic foam structures using computed tomography (CT) [132] and then replicated as models as demonstrated by Baker [149] in the production of auxetic spinal implants.   To date, numerous studies [144, 148, 149, 243, 244] have been published that have reproduced auxetic topologies (primarily the re-entrant structure) using a number of materials (e.g. ABS, polyethylene glycol (PEG) and Ti6Al4V).   By adapting the previously published work outlined above, this chapter will explore the fabrication of pliable polymeric auxetic re-entrant and conventional honeycomb structures through the application of 3D printing technologies before being optimised for testing under both high mass, low velocity and low mass, high velocity impact regimes.

6.2   Results and discussion

6.2.1   Sample repeatability – a preliminary study

In order to assess the feasibility of fabricating auxetic foams through 3D printing it is imperative that a preliminary study is undertaken.   While numerous structural models [124] could be replicated using the 3D printing system, the re-entrant model was selected due to its wide acceptance within the research community for understanding the cellular structure and deformation mechanisms of conventional and auxetic foams.   Furthermore, the re-entrant model offers a structure that is easily mathematically assessable, thus allowing its behaviour to be predicted and modified prior to fabrication, whilst additionally reducing sample waste, time and costing.

By extruding the re-entrant model into three dimensions, an idealised auxetic foam cellular structure was computationally designed, and printed from two photopolymer composites (TangoBlack and TangoBlack85) following the methodology described in Section 3. Figure 6.1 shows a direct qualitative comparison between the computer-designed and physically printed

pliable auxetic foam structure, respectively. The physical model (Figure 6.1b) is shown to have the same cellular structure as the CAD model (Figure 6.1a). However, some damage was present throughout the sample which was confirmed by both micro CT (Figure 6.1c) and SEM imaging (Figure 6.1d).

a)

5 mm

b)

5 mm

c)

Rib damage
caused by
swelling

10 mm
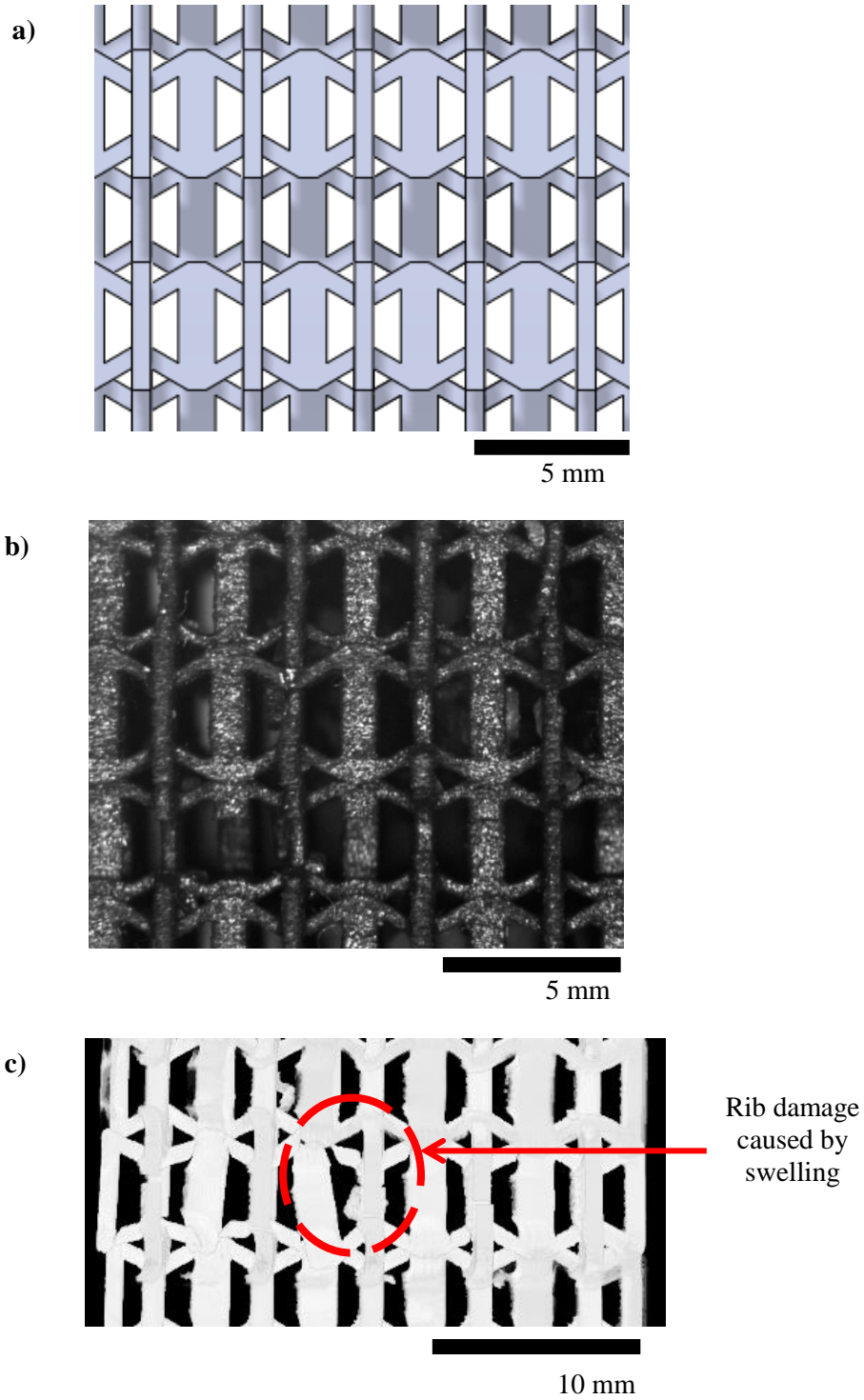
d)
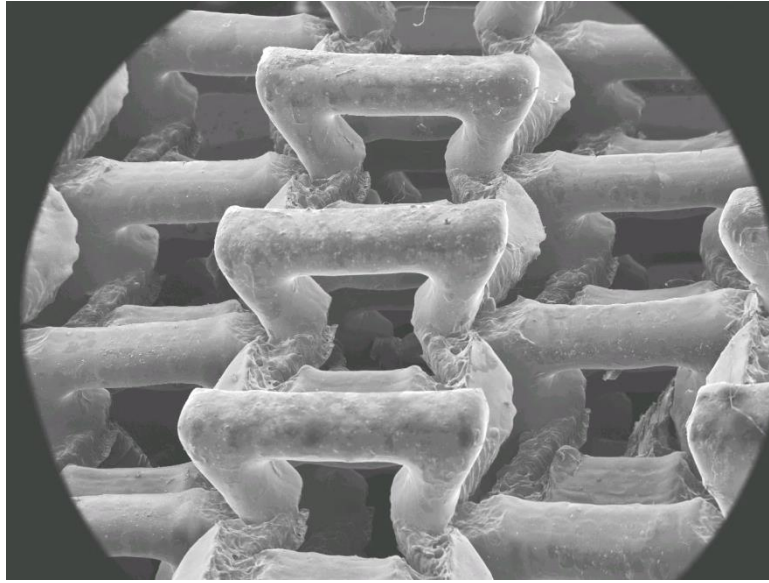
2 mm

Figure 6.1: Images showing **a)** original computer designed cellular re-entrant lattice, **b)** 3D printed cell structure captured using a WILD M410 Zoom macroscope, **c)** internal swelling damage in the polymer caused by immersion in the KOH solution, captured using micro CT and **d)** SEM image of the cellular microstructure.

This damage is directly caused by immersion of the polymer composite into the KOH cleaning solution, during which water permeates into the polymeric material resulting in swelling. This swelling causes high stresses to occur, which in turn leads to cracking and eventually fracture [245]. Interestingly, SEM analysis provides evidence of each failure mechanism seen throughout the samples (Figure 6.2) but indicated no discernible relationship between location and failure mechanism. CT imaging indicated that the swell damage was not only limited to the outer edges of the sample but can occur throughout the foam structure (Figure 6.2c). SEM imaging (Figure 6.1d) further indicated that although the bulk of the support material was removed by the KOH solution, small surface deposits (sub 100 µm in size) of support material still remained on the foam ribs.

a)

500 μm

b)

1000 μm

c)
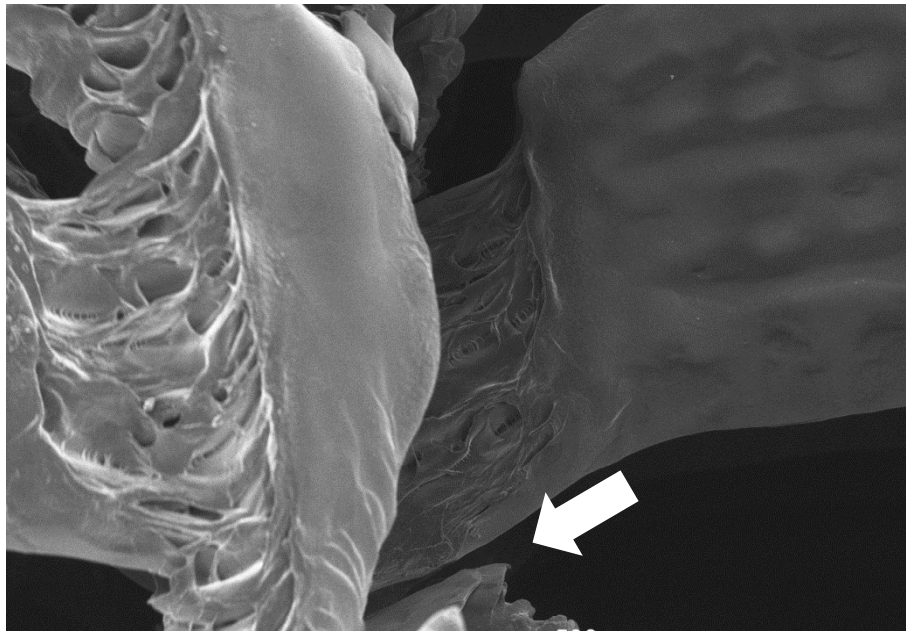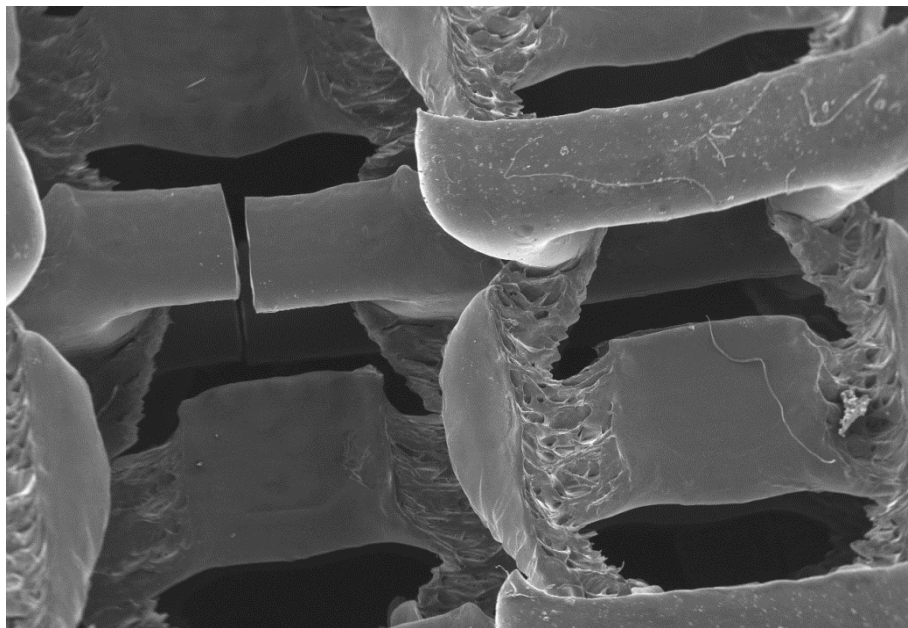
500 µm
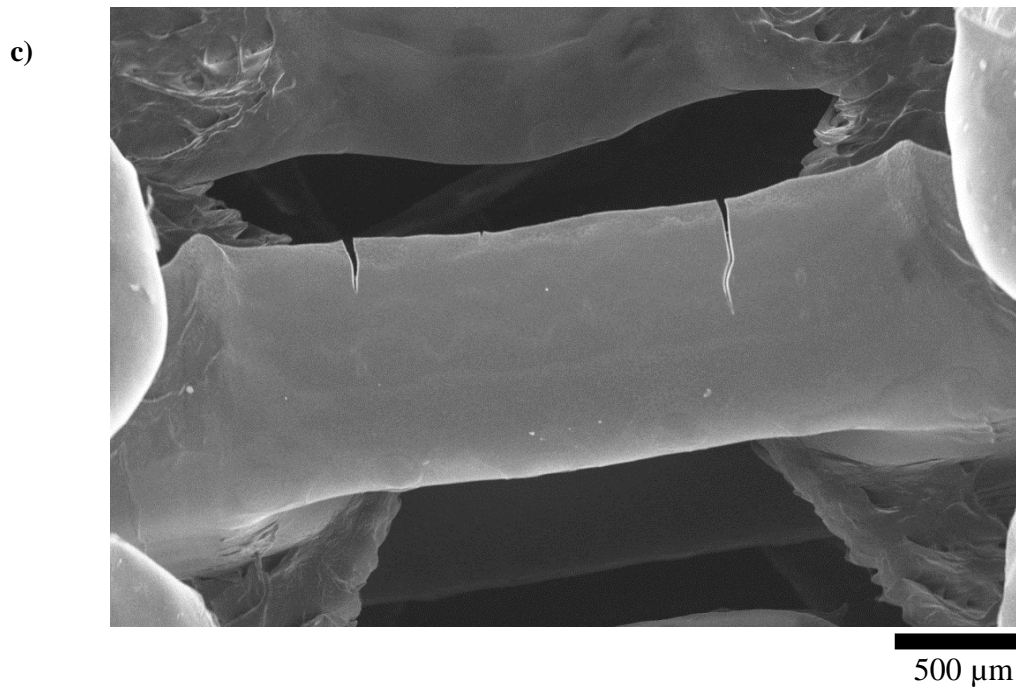
Figure 6.2: SEM images showing various damage types induced during immersion in the potassium hydroxide cleaning solution: **a)** delamination, **b)** fracture and **c)** cracking.

When studied quantitatively (measuring variation across areas A-D as shown in Figure 6.3a and Figure 6.3b, the printed samples were found to have orientation specific inaccuracies and precision (Table 6.1). The rib width (dimension C) best demonstrated this behaviour, where a re-occurring distorted geometry was found on face 1 (Figure 6.3c).

Table 6.1: Mean variation of samples produced from TangoBlack and TangoBlack85, compared to the Solidworks® model for cellular geometric areas of interest.

Dimension		Solidworks® Model / µm	TangoBlack / µm	TangoBlack85 / µm
A	Face 1	600	607 ± 76	606 ± 43
	Face 2		587 ± 26	597 ± 51
B	Face 1	2400	2319 ± 150	2330 ± 112
	Face 2		2348 ± 91	2387 ± 108
C	Face 1	600	719 ± 193	764 ± 168
	Face 2		610 ± 54	630 ± 47
D	Face 1	4140	3947 ± 152	4022 ± 229
	Face 2		3953 ± 451	4064 ± 135

a)

b)

500 μm
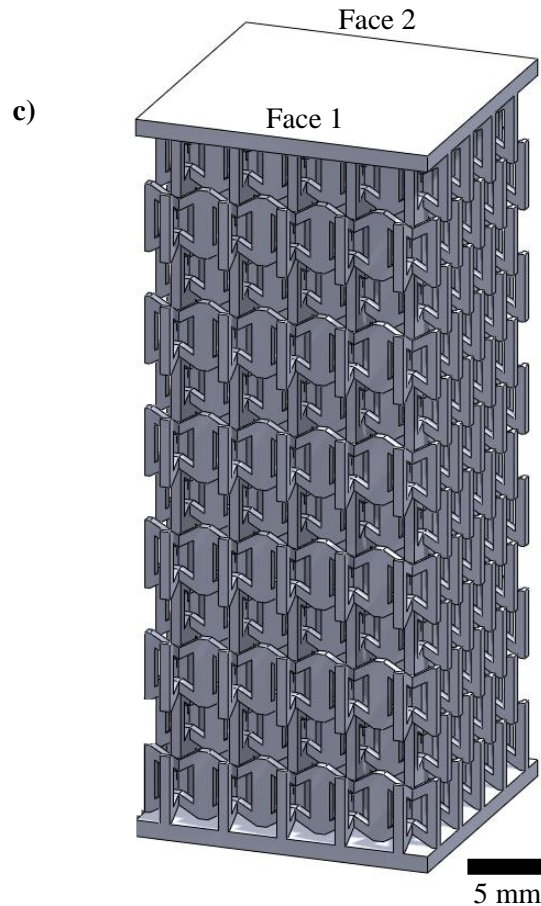
Figure 6.3: Diagrammatic representation of the computed designed: **a)** 2D auxetic cell (all measurements in mm), **b)** 3D auxetic cell and **c)** completed foam structure prior to printing**.**

These distortions were found to have a mean inaccuracy of up to 27% when compared to the original CAD model, unlike the other areas that only had a mean inaccuracy of up to 5%. This extreme geometrical distortion of 27% is directly affected by the interaction between the initial layer of support material (to assist in final removal of sample from the base) and the polymer material placed on top. Indeed, when considered along with the error, all measured dimensions (excluding face 2 of dimension D) were found to fall within the quoted systematic accuracy error of ±0.1 mm to ±0.3 mm [220], indicating that geometry distortion is systematic and thus unavoidable. Unfortunately systematic induced inaccuracies caused by the manufacturing process are a known problem, as they have been observed in other studies [144, 147, 244].

6.2.1.1 Tensile testing

Figure 6.4 shows the Poisson's ratio for the TangoBlack and Tangoblack85 samples (1 to 3 respectively) tested at each 0.05 interval of strain, until failure occurred. All samples demonstrated a negative Poisson's ratio at a 0.05 strain, where the lowest measured Poisson's ratio was −1.18.
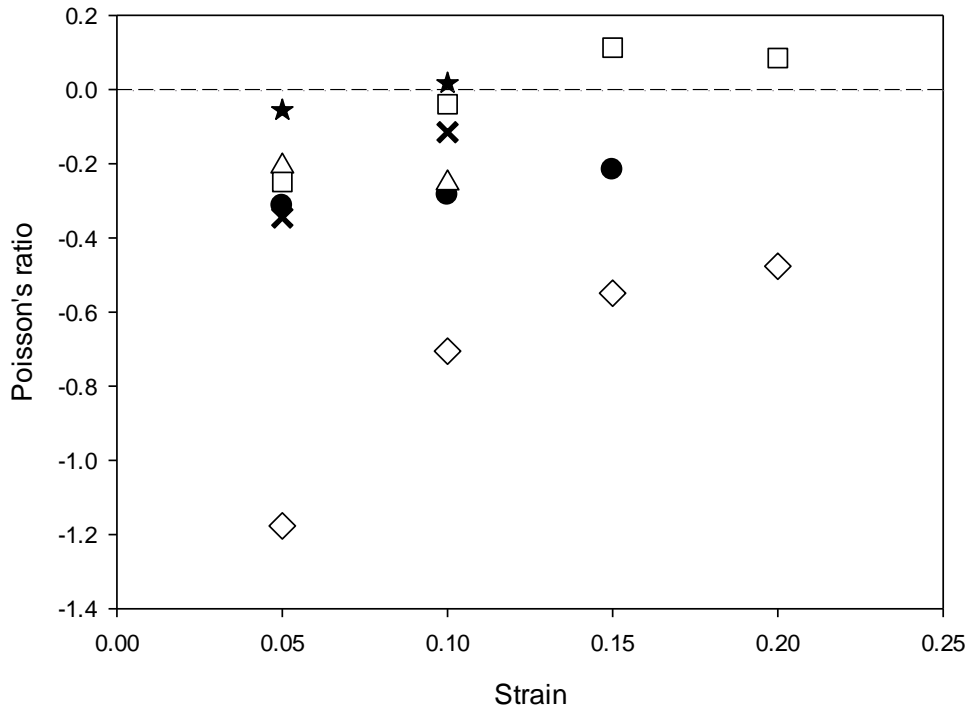
Figure 6.4: Poisson's ratio *vs.* strain data where ● △ □ and ◇ ★ ✖ are the TangoBlack and TangoBlack85 samples 1, 2 and 3, respectively.

As the applied strain increased, each unit cell within the auxetic foam structure expands from its original fabricated re-entrant structure to a clearly defined honeycomb structure with a positive Poisson's ratio (Figure 6.5) which is consistent with the auxetic behaviour. This causes the overall Poisson's ratio of the sample to transition from negative to positive with increasing strain. Conventional samples however did not experience this transitional effect since the presence of a honeycomb structure causes the Poisson's ratio to remain positive for all intervals of strain due to cellular elongation.

It was observed that the unit cells at the distal end of the sample (i.e., the furthest position from the applied tensile load) required a greater amount of strain to obtain a honeycomb structure. Where a positive Poisson's ratio develops in a sample under strain conditions, the sample will regain over time a Poisson's ratio similar to its base material (e.g., $\approx$ +0.3), which it will subsequently retain until failure occurs. Poisson's ratio can be explained by cellular displacement mechanisms, as described in [158].
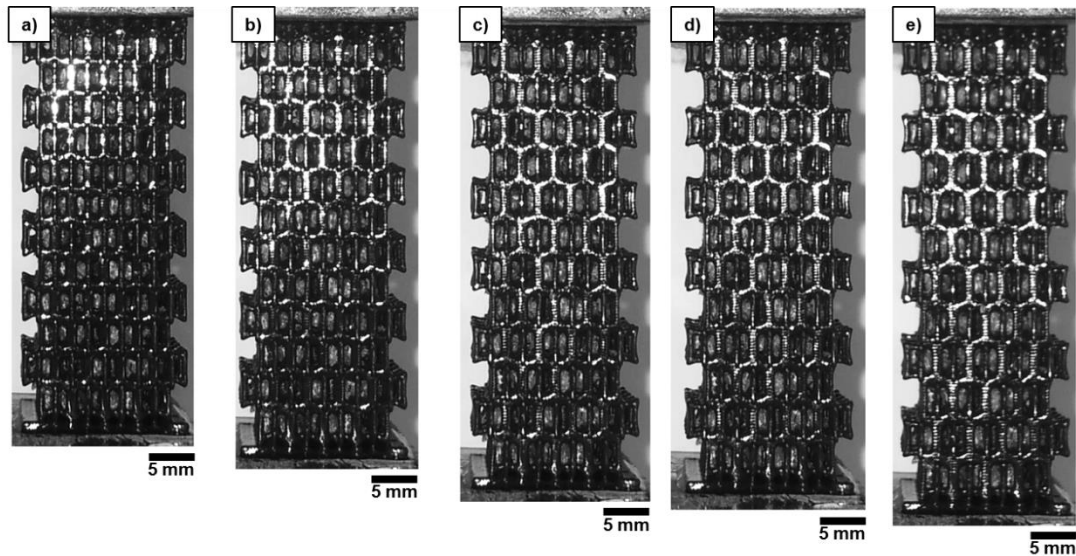
Figure 6.5: Sequence of strain induced structural changes in a real 3D printed foam: from **a)** re-entrant lattice to **e)** honeycomb structure. The strains were assessed as follows: **a)** 0%, **b)** 5%, **c)** 12%, **d)** 14%, and **e)** 19%.

Interestingly, no discernible relationship was found between both sample material types and Poisson's ratio, although the large variation can be explained by a number of reasons. The primary source of variability is associated with the fabrication method, which can cause many of the unit cells' features to vary by the systematic accuracy error of ±0.1 mm to ±0.3 mm. This variability, in turn, can change the internal angles of the re-entrant cells, which affect the overall Poisson's ratio of a cell. Other variations can also be attributed to the damage indicated in Figure 6.2. By having this pre-existing damage, uniform loading is not possible as the load can only transmit through the cell ribs that are attached [159]. This in turn causes individual cells within the structure to be loaded at various angles, thus inducing additional deformation through rotation and shear.

6.2.2 Primary 3D printing study

From the preliminary work discussed above, while evident that 3D printing of auxetic foams have some intrinsic limitations (resolution and support removal damage), the introduction of sample repeatability, together with the ability to tailor the foam structure is a desirable improvement and thus is worthy of further more detailed study. Following the preliminary work detailed in Section 6.2.1, two idealised cellular structures (auxetic and conventional) of matching densities were computationally designed and printed from a photopolymer composite (Tangoblack plus) through the methodology described in Section 3.3.3. To achieve a matching density, samples were fabricated from two different types of cells geometries as shown in Figure 3.4.

189

6.2.2.1 Poisson's ratio

Figure 6.6 shows the Poisson's ratio per unit strain for the 3D printed experimental and predicted auxetic and conventional samples where error is provided by a 95% confidence interval. As strain increases, the Poisson's ratio of the auxetic samples is shown to transition from a negative Poisson's ratio towards a positive Poisson's ratio almost linearly, as a result of the cellular geometry changing from a re-entrant to a honeycomb cell. The conventional samples were additionally shown to exhibit a Poisson's ratio change with respect to strain, however, an increase in strain caused a decrease in Poisson's ratio, until it stabilised at approximately 0.2.

In both datasets large error was shown to occur at 0.05 strain, and decreases with respect to an increase in strain due to sample stabilisation; a behaviour previously observed both in Chapter 4 and throughout the literature [153]. This characteristic is the result of sample positioning before applying a load. While the utmost care was taken to ensure a sample was placed into the tensometer in a flat, taut state, often when strain is applied to the sample it results in an increase in tautness and not displacement, thus creating large errors at the first strain interval.

To assess the manufactured samples against the design specifications, the experimental Poisson's ratio of each sample was compared to a mathematically predicted Poisson's ratio determined using the Gibson and Ashby model [159] described in Section 2.7.1. For both the auxetic and conventional designs, the mathematical model predicted an almost linear convergence towards a zero Poisson's ratio, relative to strain. When compared to the experimental data, the predictions of Poisson's ratio showed a good fit to the experimental data for the conventional foams until 0.2 strain, while no fit was apparent for the auxetics. The poor fit between the experimental and modelled Poisson's ratios is likely due to the sample manufacturing, which led to distortions in the internal angles and the length of the cell walls in comparison to the original design specifications, as previously discussed in Section 6.2.1.1.
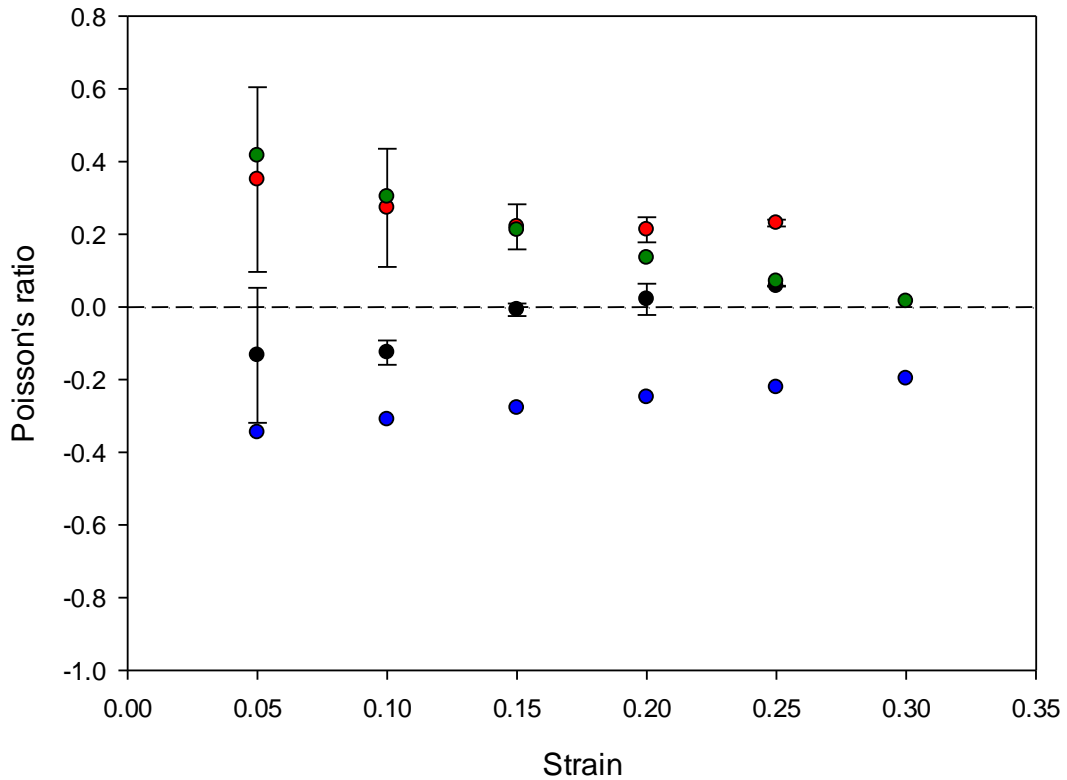
Figure 6.6: Poisson's ratio per unit strain for: experimental auxetic (●), experimental conventional (●), predicted auxetic (●) and predicted conventional (●).

6.2.2.2 Compressive stress-strain testing

To assess the mechanical performance of the auxetic and conventional foams, 3D printing samples were subjected to a uniaxial compression test, at a loading rate of 2 mm per minute leading to a strain-rate of 2.3×10^{-3} s^{-1}. In addition to measuring the compressive stress-strain response of the samples, Poisson's ratio was also measured. To keep density effects to a minimum and potentially enable differentiation between density related and foam structure related behaviour, both sample types were designed to have matching dimensions and densities as shown in Table 6.2. Unfortunately, while care was taken to ensure the test samples were identical, some variability was present, due to damage and disparities induced by the manufacturing method. Similar behaviour has been observed in other literature [144, 145, 147]. In an attempt to limit the effects of these variations, the mean compressive stress-strain curves were considered.

Table 6.2: 3D printing dimensions of auxetic and conventional samples utilised in compression test

Sample type	Dimensions			Imposed density / kg m^{-3}	Actually density / kg m^{-3}	Density variation / %
	X / mm	Y / mm	Z / mm			
Auxetic – sample 1	30	30	15	400	391	2.3
Auxetic – sample 2	30	30	15	400	385	3.8
Auxetic – sample 3	30	30	15	400	393	1.8
Conventional – sample 1	30	30	15	400	435	8.8
Conventional – sample 2	30	30	15	400	429	7.3
Conventional – sample 3	30	30	15	400	424	6

Figure 6.7 shows the Poisson's ratio *vs*. strain for the auxetic and conventional samples. Overall, both sample types were shown to exhibit high levels of repeatability, where overall the auxetic samples were shown to exhibit an almost linear transition from a negative Poisson's ratio towards a positive Poisson's ratio with respect to strain. Alternatively, the conventional samples exhibited an almost consistent Poisson's ratio of approximately 0.1 with respect to strain.
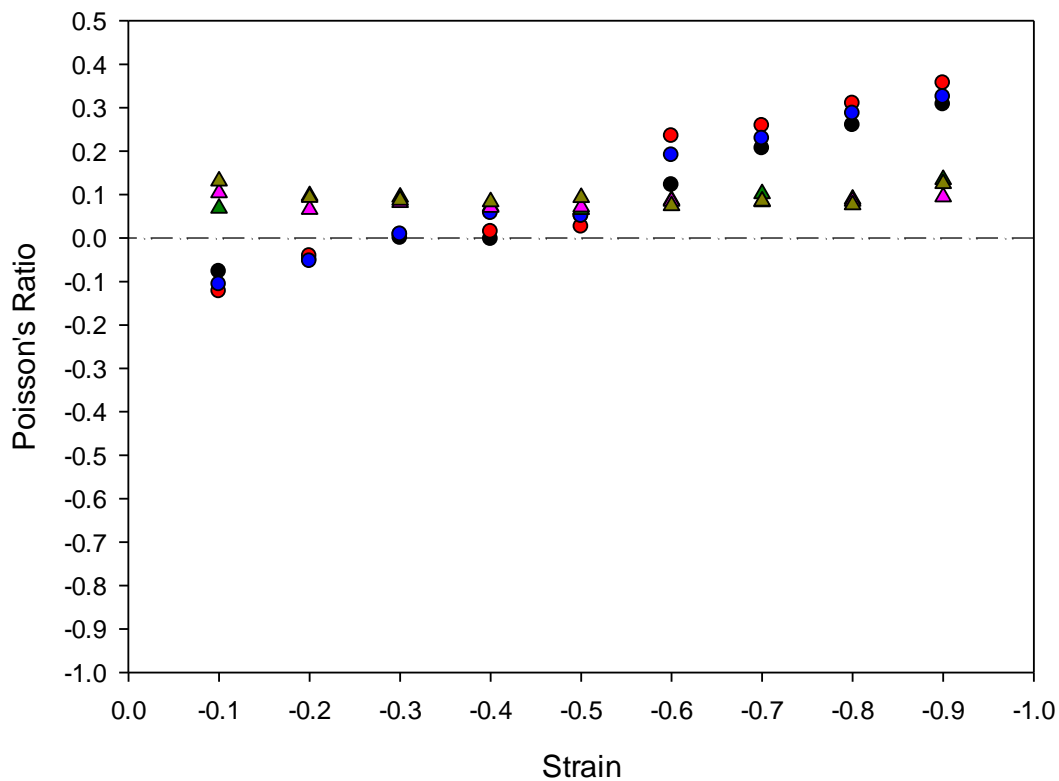
Figure 6.7: Poisson's ratio per unit strain for auxetic and conventional samples under compression where, ● ● ● and ▲ ▲ ▲ are the auxetic and conventional samples 1, 2 and 3, respectively.

Figure 6.8 and Figure 6.9 show the actual and mean compressive engineering stress-strain curves for the auxetic and conventional samples respectively. The conventional systems exhibited three distinct phases of deformation: linear elastic, plastic and densification as reported in the literature [159]. Within the linear elastic region, the cell walls of the foam structure are shown to elastically

bend. When the applied load becomes too great, the stress-strain curve enters the plateau region, where cells deform through elastic buckling of cell walls. At the start of this region, cells that are the longest or are in the most favourable orientation will be the first to buckle, while those in a less favourable orientation or smaller require higher stresses to buckle. Finally, when the cells have been crushed and further deformation is limited, densification occurs [159].
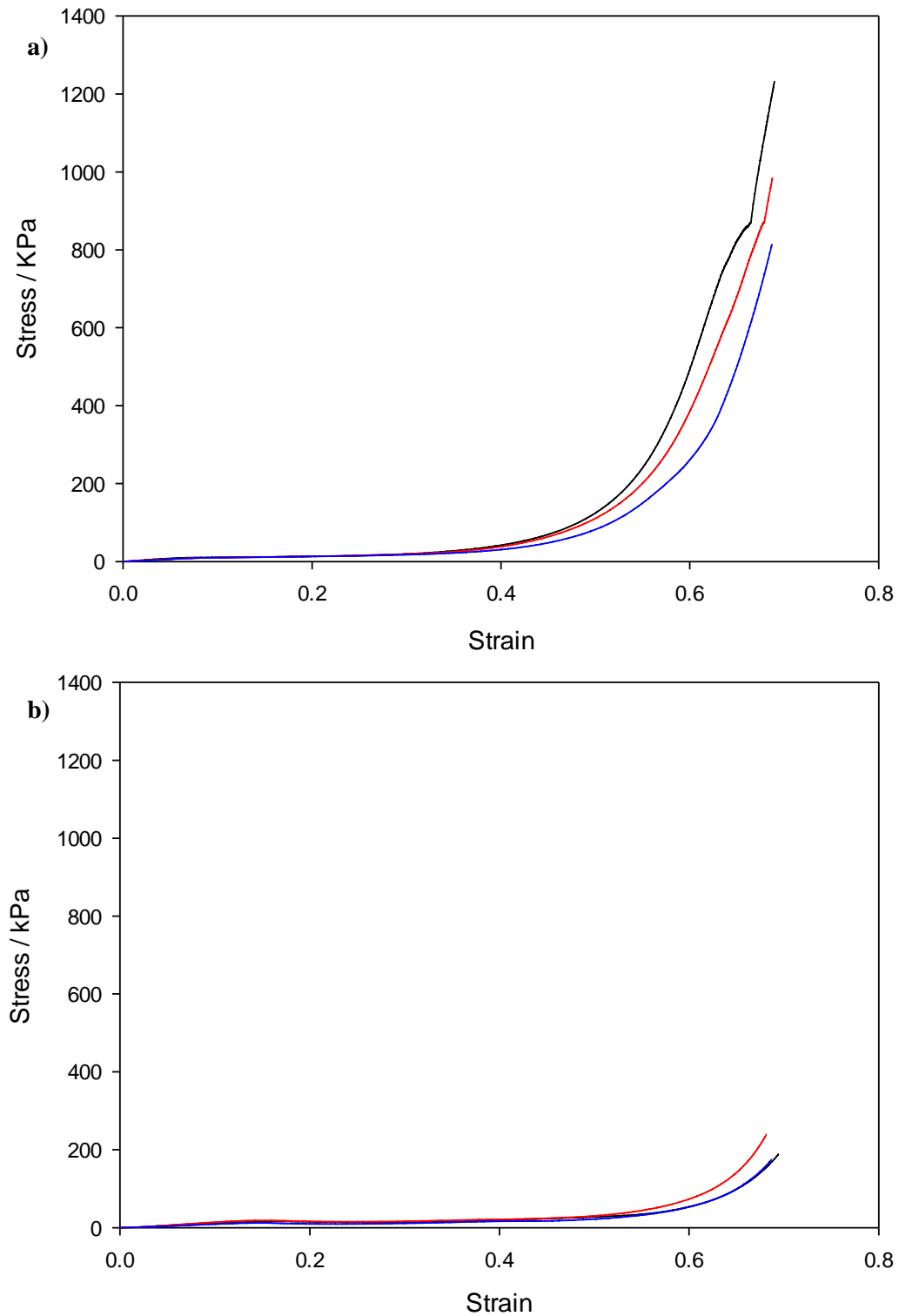
Figure 6.8: Compressive engineering stress-strain curves for: **a)** auxetic and **b)** conventional samples, where three replicate samples are represented by (━), (━) and (━), respectively.
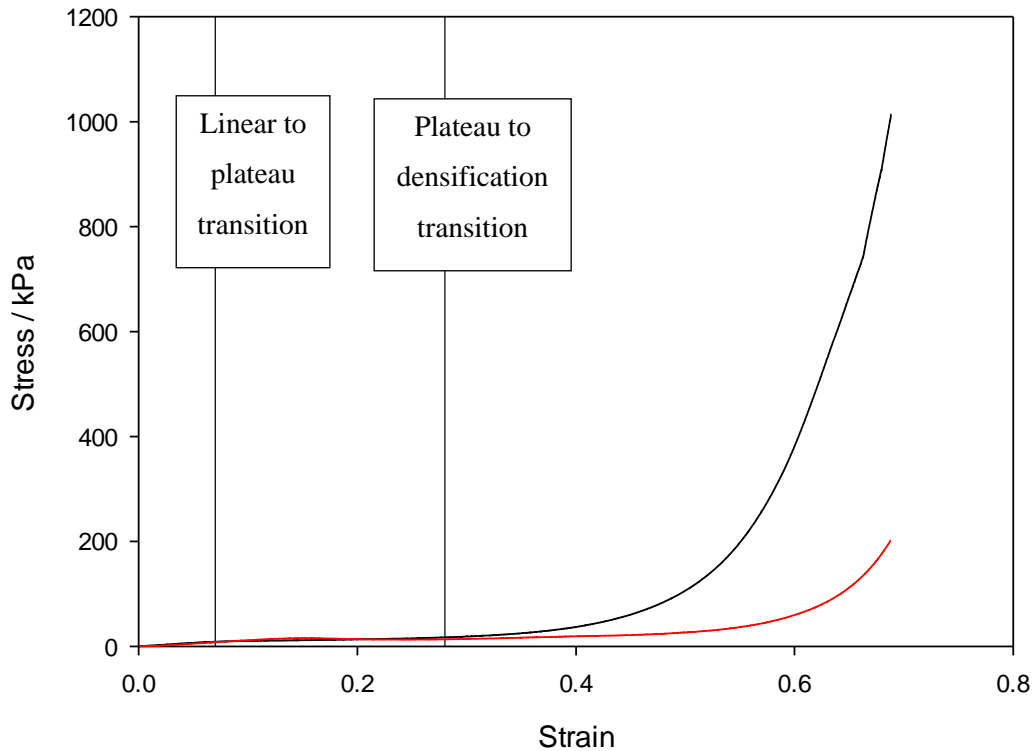
Figure 6.9: Mean compressive engineering stress-strain curves for auxetic (━) and conventional (━) samples, where boundary regions are given for experimental data.

Unlike the conventional systems, the auxetics did not exhibit the classical elastic-plateau region, but instead feature an extended linear stress-strain pattern, as the cell ribs continue to bend rather than buckle, due to them being already convoluted. This correlates with other auxetic foam materials often described in literature [131]. However when compared against the work by Yang *et al* [144], in which they studied 3D printed re-entrant structures under compressive loading, they observed that the stress-strain curves exhibited a periodic behaviour that did not indicate any obvious plateau stage until several layers of structure had collapsed. It was suspected that this behaviour stemmed as a result of re-entrant lattice structures, having distinct layers normal to the compressive direction. As this behaviour was not observed in the work presented here in which comparable structures were utilised, it is possible that the difference between the two studies could be due to the material used. In the work presented here, a pliable polymer was utilised whilst Yang *et al.* utilised a stiffer material (Ti6Al4V).

From the stress-strain curve, the energy per unit volume represented by the area under the curve is greater in the auxetic case than the conventional system for a given strain profile. Considering that both systems have approximately the same relative density, it can be inferred that on a like-for-like weight, auxetic foams can absorb more energy for a given strain profile. This is due to the earlier onset of densification. Conversely, the densification of the auxetic system could be delayed to similar levels observed in the conventional system by reducing the relative density, due

to the relationship between stress-strain and relative density in cellular solids [159]. By doing so, auxetic systems could replicate the conventional system's densification stage of the stress-strain profile at a reduced weight.

From the application of ballistic protection (TABs), the foam must not only absorb energy but also reduce the force exhibited on the wearer's torso. There is a potential trade-off as most energy absorption occurs through the densification stage, but as a consequence there are greater stresses involved which will transfer to the body increasing the likely BABT severity. Alternatively, the foam could be made thicker and the densification stage delayed further to absorb the same amount of energy whilst reducing stresses. Interestingly the effects of increasing TAB thickness of conventional foams have already been explored by Ouellet *et al.* [34], where it was found that increasing TAB thickness decreased all measured parameters relating to trauma (thoracic velocity, peak pressure and acceleration). Furthermore, it was identified that for a specific threat, there was an optimal TAB density that minimises thoracic velocity, peak pressure and acceleration. Increasing TAB thickness however must be considered with careful, as increasing the thickness, as it could impede operational requirements such as weapon carrying, aiming, sitting, crouching, body heat loss etc. Should any of these not be possible, or if performance excessively degrades, the wearer will have no confidence in the TAB, and may not be worn [30].

While the capability to produce complex, repeatable porous structures is beneficial, the ability to predict a design's mechanical behaviour prior to fabrication is also highly desirable. For the current study, theoretical stress-strain curves were constructed utilising the semi-empirical approach presented by Maiti *et al.* [246], where Equations 6.1 to 6.3 predict the linear elastic region, transition from elastic to plateau stress and the plateau region, respectively. Densification was assumed to begin when a foam's relative density satisfies the relationship of $1 - 3(\rho^* / \rho_s)$, and ends when $\rho^* / \rho_s = 1$.

$$\frac{E^*}{E_s} = C_1 \left(\frac{\rho}{\rho_s}\right)^2 \qquad\qquad \text{(Equation 6.1)}$$

$$\frac{\sigma_{el}^*}{E_s} = C_2 \left(\frac{\rho}{\rho_s}\right)^2 \qquad\qquad \text{(Equation 6.2)}$$

$$\frac{\sigma}{E_s} = C_3 \left(\frac{\rho}{\rho_s}\right)^2 \left\{\frac{1-(\rho/\rho_s)^{1/3}}{1-\left[\rho/\rho_{s\frac{1}{(1-\varepsilon)}}\right]^{1/3}}\right\}^2 \qquad\qquad \text{(Equation 6.3)}$$

Where E^* is the Young's modulus of the foam (Pa), E_s is the Young's modulus of cell wall material (Pa), ρ^* is the density of the foam at a given strain (kg m^{-3}), ρ_s is the density of the cell wall material (kg m^{-3}), ε compressive strain, σ_{el}^* stress at which transition from elastic to plateau occurs, and C_1-C_3 are dimensional constants that depend on cell-wall geometry, obtained experimentally. For the work presented by Maiti *et al.* [246], these values are given as 1, 0.05 and 0.05 for C_1- C_3, respectively.

Figure 6.10 shows the constructed theoretical stress-strain curves fitted against the mean experimental data of the auxetic and conventional systems presented in Figure 6.9. The theoretical model accurately replicated the experimental linear elastic region and the transition from the linear elastic to plateau region for both the auxetic and conventional systems. However, on transitioning into the plateau region, the model deviated from the experimental behaviour for both the conventional and auxetic systems. For the conventional systems, this manifested as an over estimation of the stress per unit strain, early prediction of densification, and a maximum peak stress 5 times greater at maximum strain than the experimental. Alternatively, for auxetic systems, the model underestimated the stress-strain behaviour, initiation of densification and the maximum peak stress at maximum strain.

While the exact reason is unclear as to why the model under and overestimates the stress-strain behaviour, when compared to the source of the equations, there is evidence to suggest that this is merely a limitation of the model. It is interesting to note that the authors presented two graphs showing theoretical and actual stress strain curves, which also provided evidence of over / under estimate depending upon relative density [246]. This is further supported in [159], where according to Ashby and Gibson, the model, along with other models proposed throughout literature [247-249] are not very satisfactory at describing the shape of the stress-strain curves of the porous materials, and instead the best approach is a semi-empirical one.

Furthermore, there is some visual evidence from the videos that suggest that the some samples do not exhibit uniform compression. This non-uniformity is likely caused by the manufacturing process, which has the capacity to induce inhomogeneity. This inhomogeneity however is neglected as the model assumes an idealised structure, resulting in its effects being disregarded. However, the extent of inhomogeneity may need to be included in future models as it does affect the macroscopic properties [154].
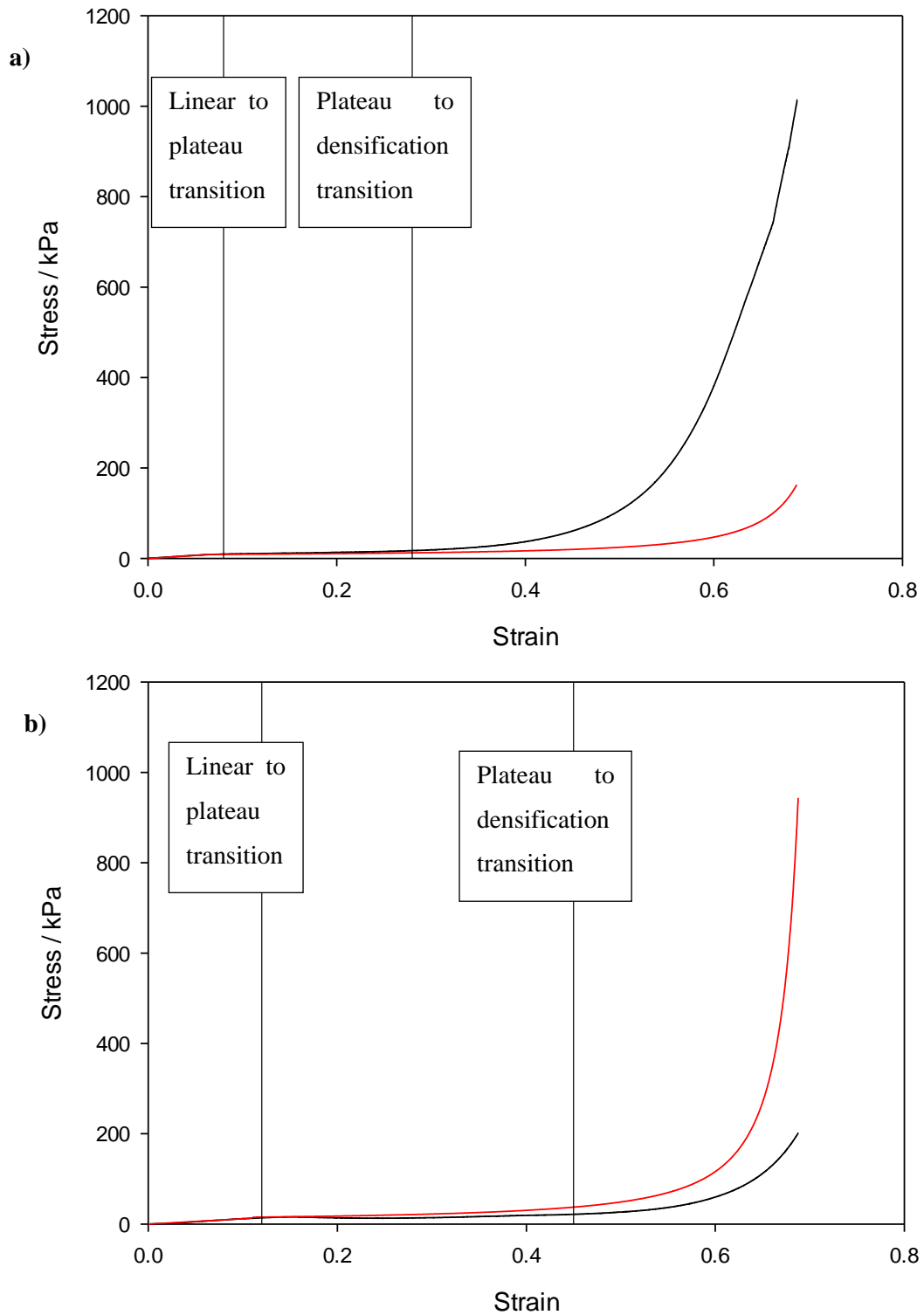
Figure 6.10: Experimental (━) and theoretical (━) compressive engineering stress-strain curves for **a)** auxetic and **b)** conventional systems, where boundary regions are given for experimental data.

In an attempt to converge the plateau and densification regions of the model to the experimental, the goal seeking algorithm within Microsoft Excel 2011 was used to vary the density and C_3 constant.
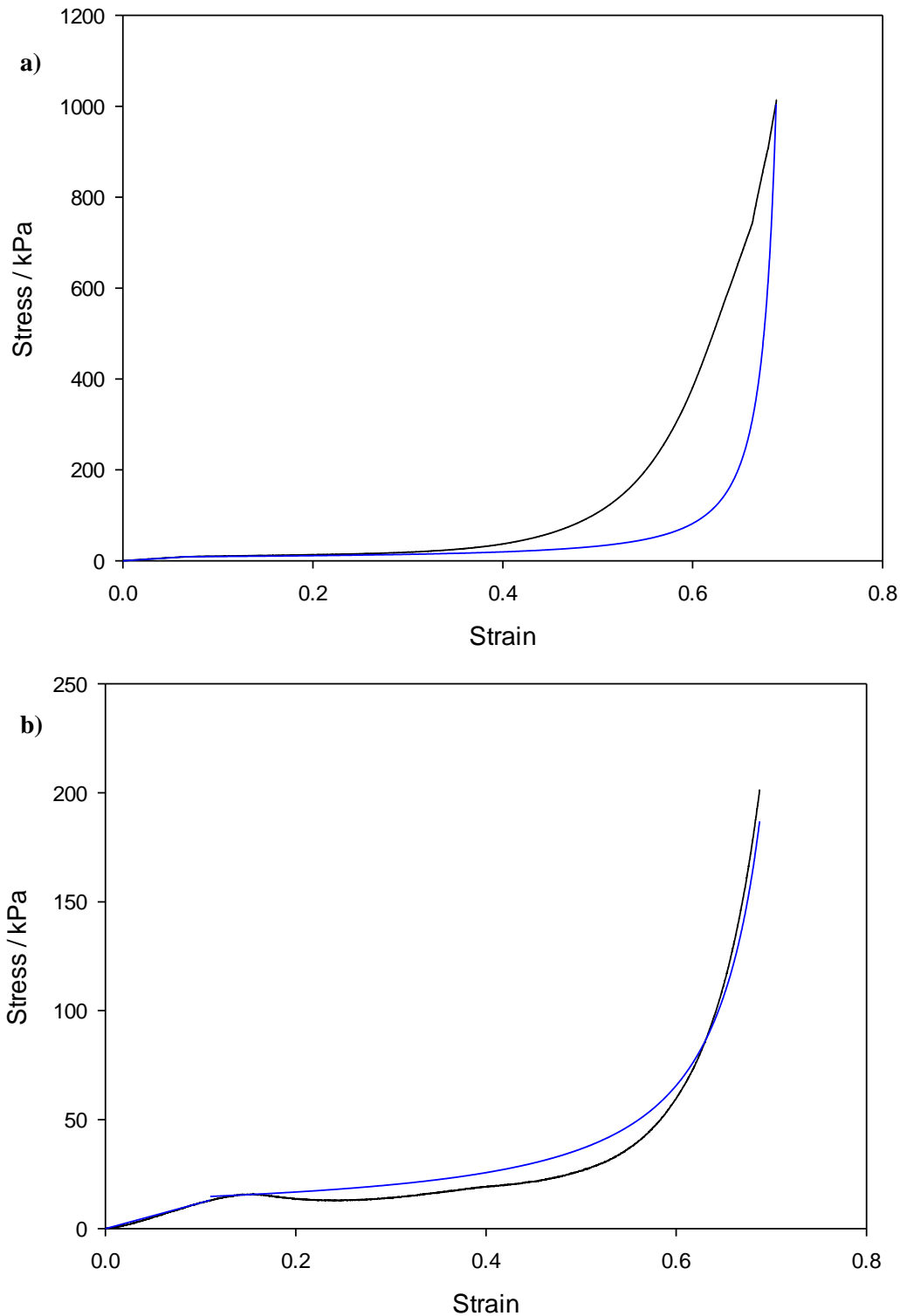
Figure 6.11: Experimental (—) and model based on goal seeking algorithm (—) compressive engineering stress-strain curves for: **a)** auxetic system and **b)** conventional system.

It was found that for the conventional systems, a reduction in density by 18% greatly increased the model's fit to the experimental data (Figure 6.11b), while the auxetic system required an increase in density of 18% to improve fit of the model (Figure 6.11a). However, even with this correction, the auxetic model still underestimated the initiation of densification but was shown to

converge to the same peak stress at maximum compressive strain. The underestimation of densification in auxetic system is likely to be caused by the assumption that these systems experience cell ribs bending, as opposed to buckling [131].

To ascertain if the equations and constants calculated for the mean of both conventional and auxetic systems can be used to predict the mechanical performance of different systems prior to manufacturing, theoretical stress-strain curves were constructed with the aim of replicating the individual auxetic and conventional utilised in generating the mean stress-strain curves shown in Figure 6.9.
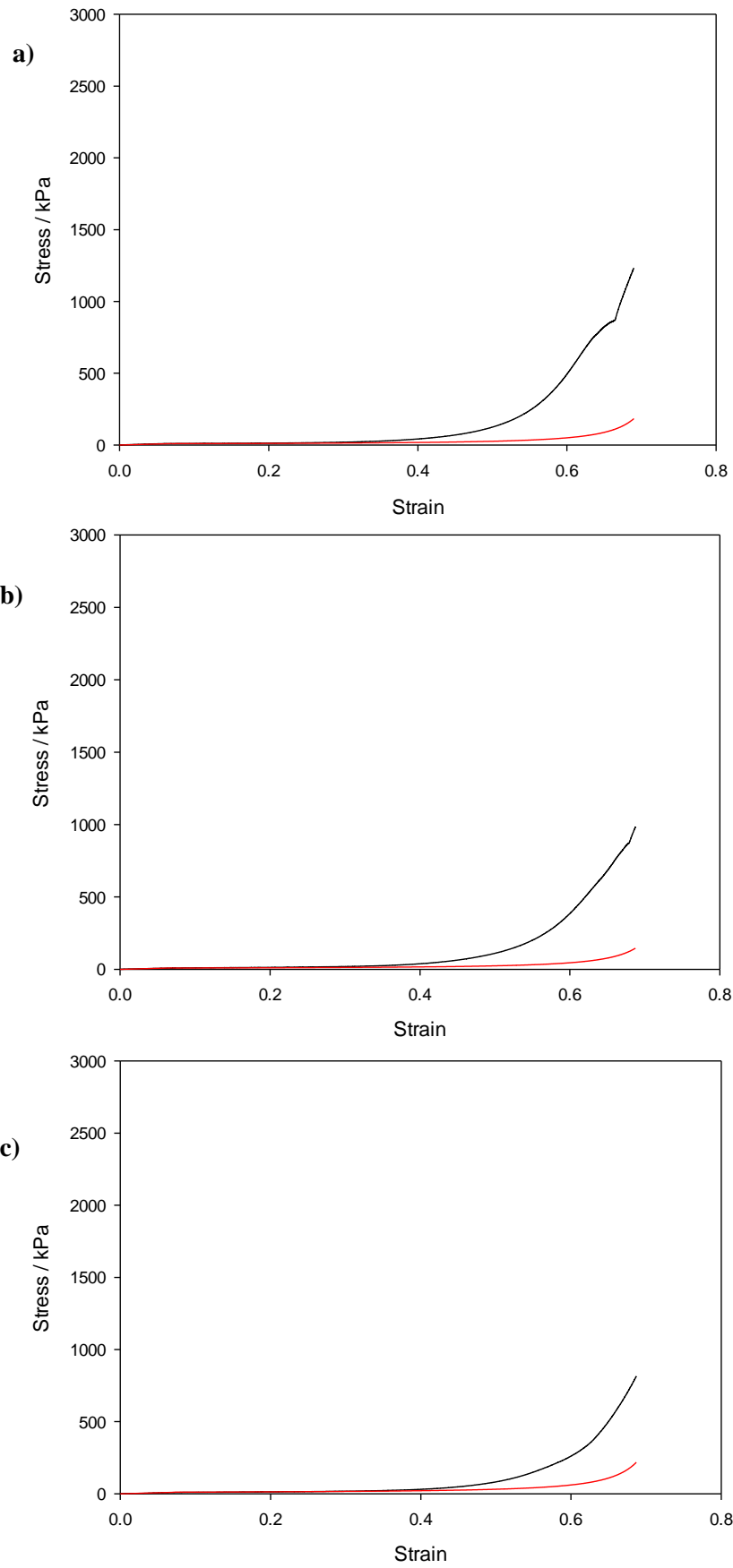
Figure 6.12: Auxetic theoretical stress-strain curves plotted against experimental data for: **a)** sample 1, **b)** sample 2 and **c)** sample 3.
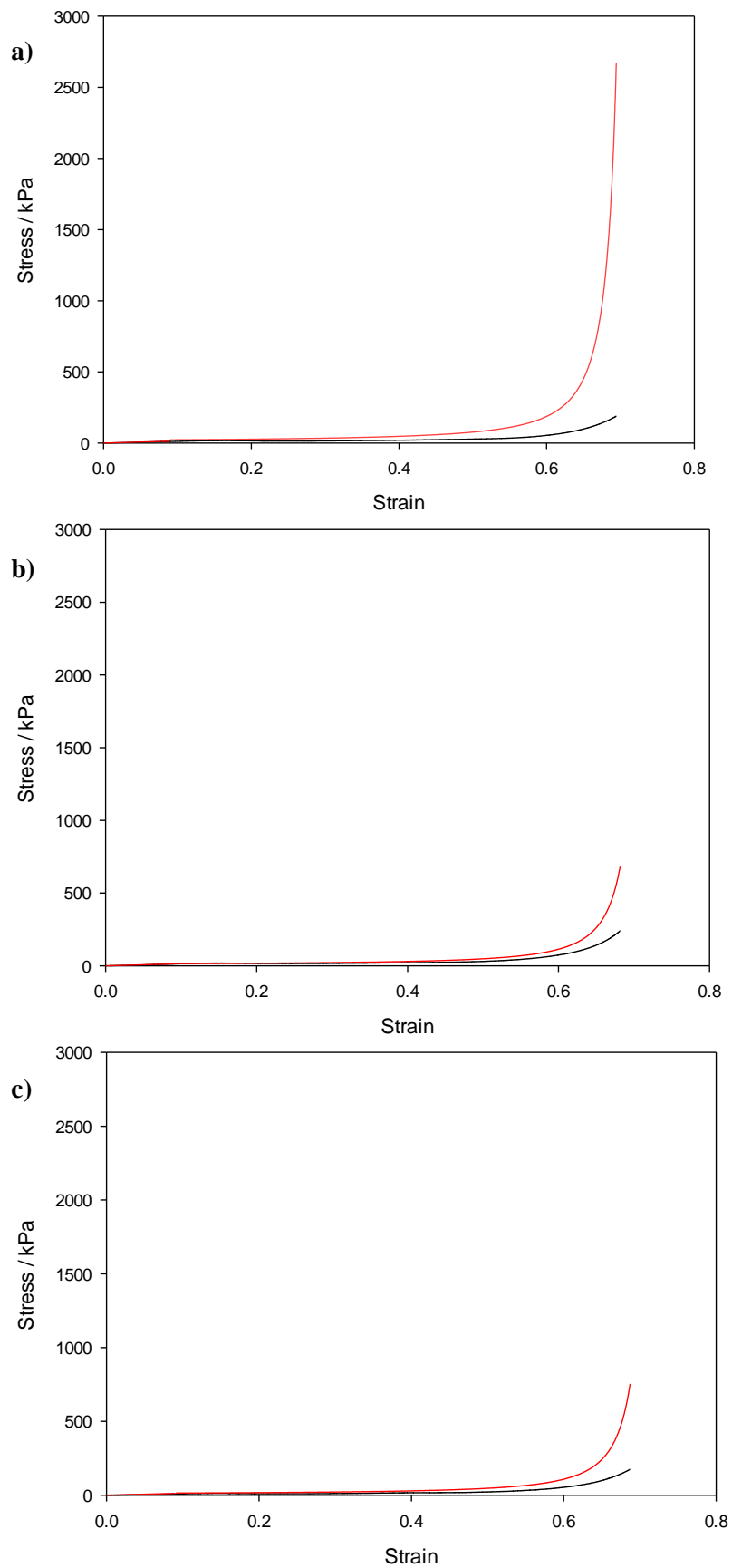
Figure 6.13: Conventional theoretical stress-strain curves plotted against experimental data for **a)** sample 1, **b)** sample 2 and **c)** sample 3.

Figure 6.12 and Figure 6.13 show the resulting theoretical stress-strain curves plotted against experimental data of auxetic and conventional systems. The theoretical model accurately replicated the experimental linear elastic region, however on transiting into the plateau region the model digressed from the experimental behaviour for both conventional and auxetic systems. When this behaviour was observed for the mean auxetic and conventional stress-strain curves, a goal seeking algorithm was required to vary the density and C_3 constants to increase the models fit. Although possible with empirical datasets to compare against, without this data, any data produced from the goal seeking algorithm cannot be validated.

Consequently, utilising constants drawn from similar systems is an unsuitable approach for predicting sample behaviour prior to fabrication, as each system has many variables such as cell size, internal cell angles, relative density, etc. Due to the complexity of many adjustable parameters, it is not possible to accurately predict stress-strain response using these analytical models without first performing experimental testing to obtain empirical constants. This makes it difficult in terms of material development for predicting mechanical behaviour prior to manufacture. FE models may however offer more accurate predictions of mechanical performance.

6.2.2.3 Digital Volume Correlation

While 3D printing of auxetic foams introduces a level of repeatability, it is currently unclear if the samples produced in this way behave similarly under impact conditions as those fabricated by the classic three stage fabrication method. To explore this behaviour digital volume correlation (DVC) was employed. First introduced in the late 1990s, DVC is the 3D equivalent of the better known digital image correlation (DIC) technique. Since its inception, DVC has developed in to a powerful computational tool for mapping and detailing full field deformations. Although originally conceived as a means to investigate the mechanics of skeletal tissues [250, 251], it soon became apparent that any material that exhibits texture or a traceable pattern is usable with DVC. To date, DVC has been used in a wide range of studies [250, 252], including auxetic foams [241, 253].

Using the methodology found in Section 3.3.3 two auxetic foam types (3D printed and classic) along with conventional 45 PPI and 10 PPI foams (Table 6.3) of dimensions 30 mm × 30 mm × 30 mm were studied with respect to displacement resolution error. To determine the resolution of the DVC software, a stationary, zero load study was first performed for each foam type, i.e., auxetic and conventional foams. These studies consisted of an initial scan (no deformation)

followed by a second scan, identical to the first. Should no unforeseen experimental difficulties occur, both scans will be alike, excluding reconstruction anomalies and the background noise introduced by the HMX X-Ray CT scanner [253].

Table 6.3: Samples utilised in digital volume correlation analysis

Name	Heating Time	Volumetric Compression Ratio
3D Printed	N/A	N/A
Classic Auxetic 45 PPI	60 Minutes	4.88
Classic Auxetic 10 PPI	60 Minutes	4.88
Conventional 45 PPI	N/A	N/A
Conventional 10 PPI	N/A	N/A

When processed by the DVC software, the algorithm using the user settings (user inputs are determined by trialling a selection of sub-volume dimensions that are large enough to incorporate structural features, but remaining small enough to maximise displacement data) shown in Table 6.4 converts both volumes into a test matrix, and correlates each sub-volume relative to the two volumes (Figure 3.11).

Table 6.4: Digital volume correlation sub volumes, where the values highlighted blue only apply to the 3D printed auxetic sample

Sub volume dimensions (Pixels)	Overlap between correlation search	Number of passes
160×160×160	50%	2
128×128×128	50%	2
96×96×96	50%	2
64×64×64	50%	2
48×48×48	50%	2
32×32×32	50%	2

As the only variation between both volumes is the systematic noise and reconstruction anomalies, the output values can be considered to be resulting from background noise, and thus indicating the deformation resolution. By determining the deformation resolution, the real strain data can be differentiated from systematic error, for all subsequent DVC analysis. The maximum systematic displacement error resolutions for each foam type and sub-volume are shown in Table 6.5, where the underlined values indicate the optimal sub-volume dimensions for all foams tested. For each foam, the optimal sub-volume size was chosen to be large enough to capture and correlate structural features of the foam microstructure, but remains small enough to maximise displacement data.

Table 6.5: Deformation error where underlining highlights the optimal sub-volume for all tested foam samples

Sub-volume dimensions (Pixels)	Auxetic 10 PPI /mm	Conventional 10 PPI /mm	Auxetic 45 PPI /mm	Conventional 45 PPI /mm	3D print / mm
160×160×160	N/A	N/A	N/A	N/A	0.07
128×128×128	0.13	0.19	0.64	0.13	<u>0.10</u>
96×96×96	<u>0.09</u>	<u>0.12</u>	0.48	0.14	0.23
64×64×64	0.11	0.08	<u>0.34</u>	<u>0.10</u>	0.26
48×48×48	0.10	0.07	0.25	0.12	0.27
32×32×32	0.08	0.08	0.16	0.13	0.21

Having determined the optimal sub-volume and its associated displacement resolution error for each foam type, the effect of quasi-static loading was then investigated. At maximum loading, it was found that all test foams experience a displacement direction opposite to the load direction at one end of the sample, while the other displaces in conjunction with the load, as indicated by the aqua blue vectors on the right hand side in Figure 6.14. This behaviour is the result of the ball load acting as a local pivot point causing the material adjacent the ball to experience a bending moment. This bending moment however only occurs on one side of the sample, as the volumes used in this study represent only a small volume of a larger foam sample.

a)
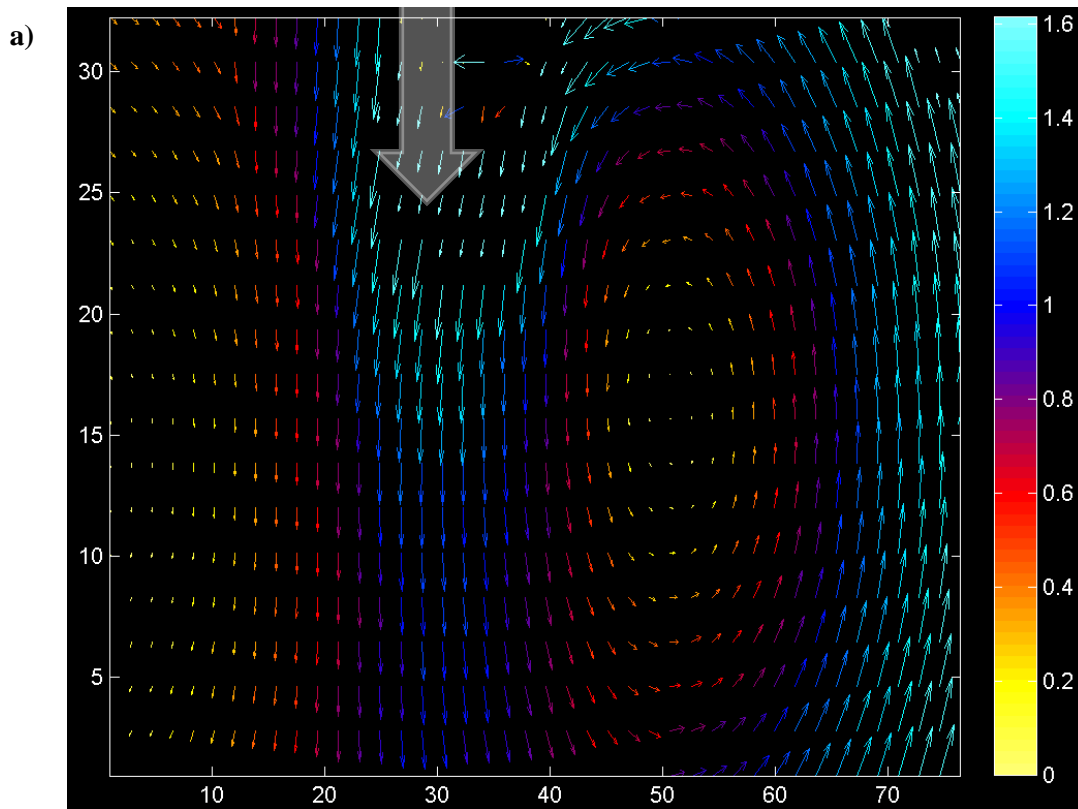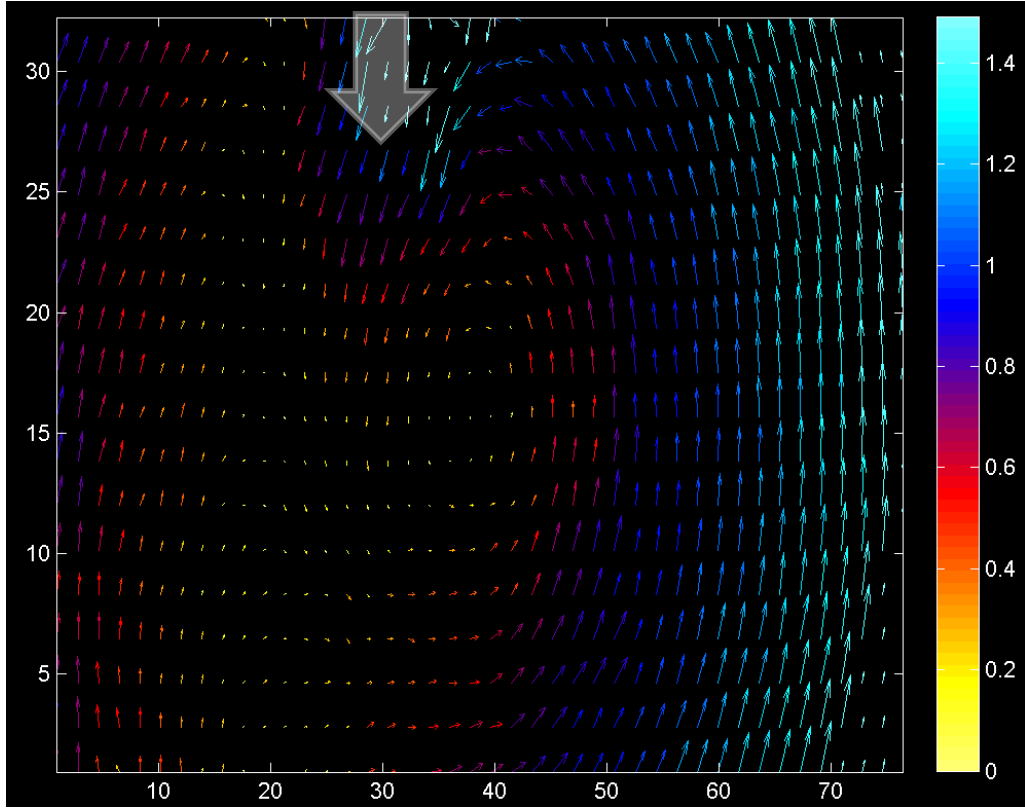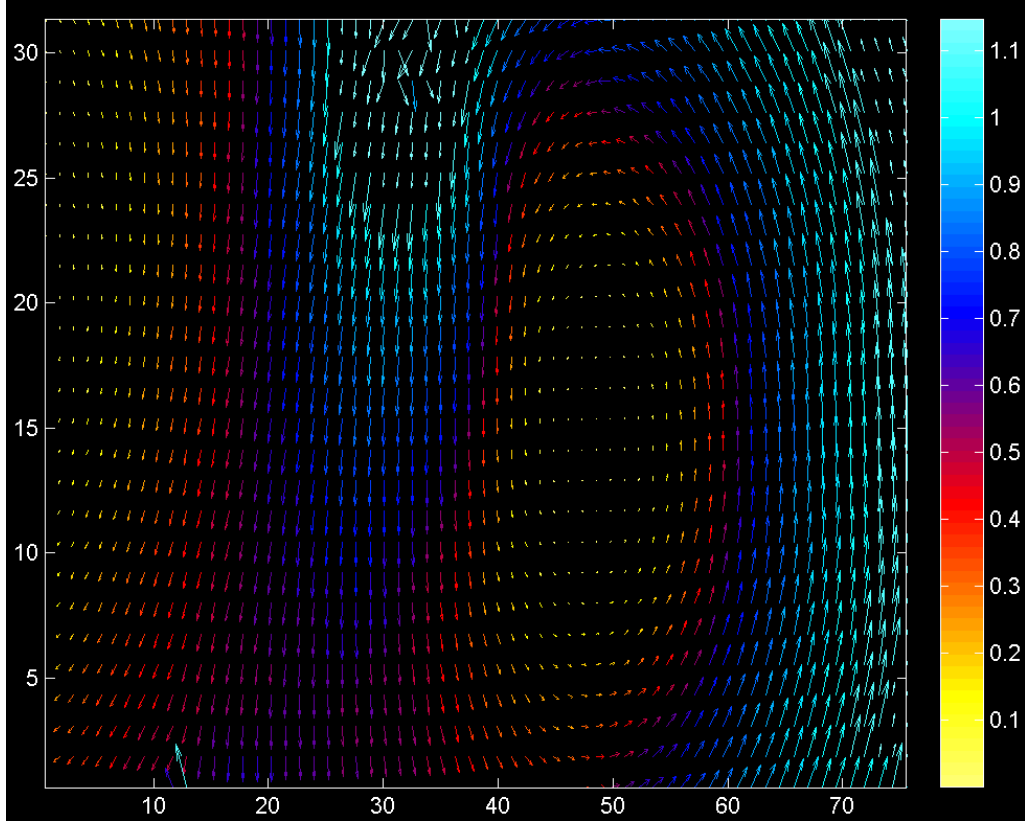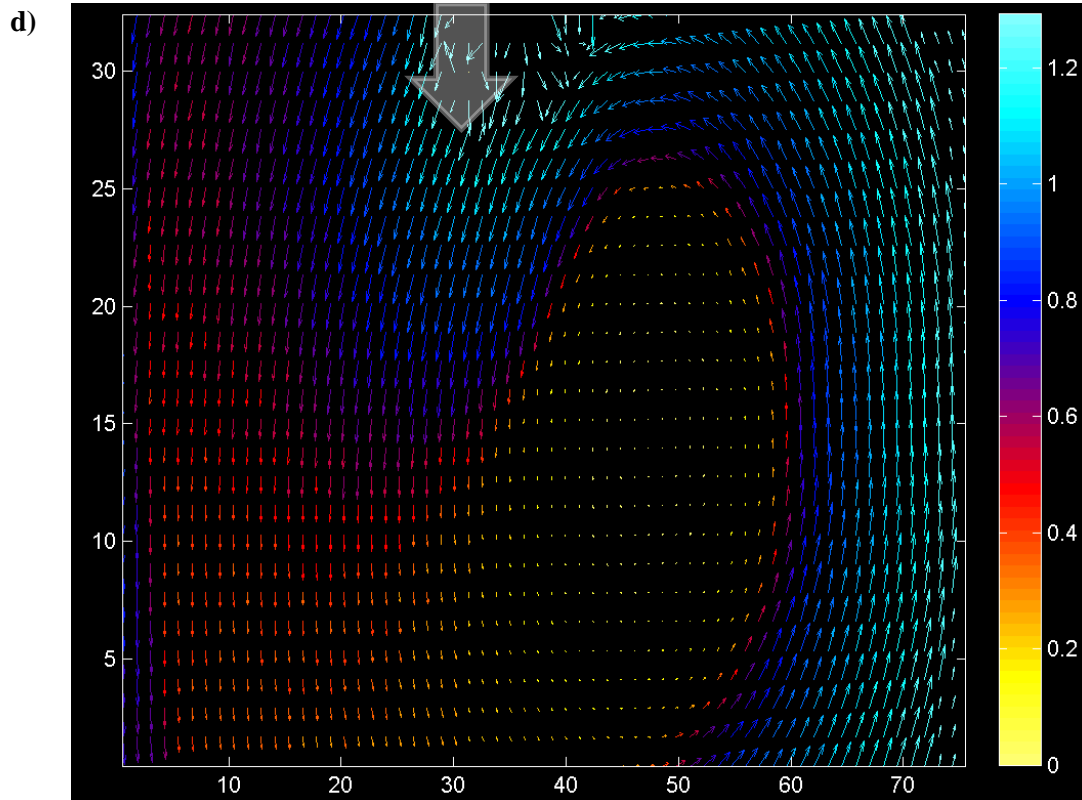
Figure 6.14: Displacement vector plots in the X-Z plane for: **a)** auxetic 10 PPI, **b)** conventional 10 PPI, **c)** auxetic 45 PPI and **d)** conventional 45 PPI, where the white arrow represents the loaded region**.**

In addition to the rotational moments, all foam samples were additionally found to experience large displacements of approximately 1 mm, or greater, directly beneath the loading region. These displacement magnitudes however were reduce as the distance from the loading increases which was further confirmed when the same region was considered about the X-Y plane (Figure 6.15).

The X-Y plane also suggests that both the classic and 3D printed auxetic foams resist loading by drawing material into the region, (as indicated by the white dashed regions in Figure 6.14) unlike the conventional foams where a load causes material within the region to either move in the direction of loading (compressing) or away from the load. This is significant as it indicates that the 3D printed foams exhibit not only the same behaviour as regular foams under loading but also exhibit the same increased resistance to indentation as classic auxetic foams, as demonstrated by the presence of a negative Poisson's ratio. Thus, the 3D printed foams are a suitable replacement for the current three stage manufacture of auxetic foams, when considered with respect to loading applications.

c)

d)

e)
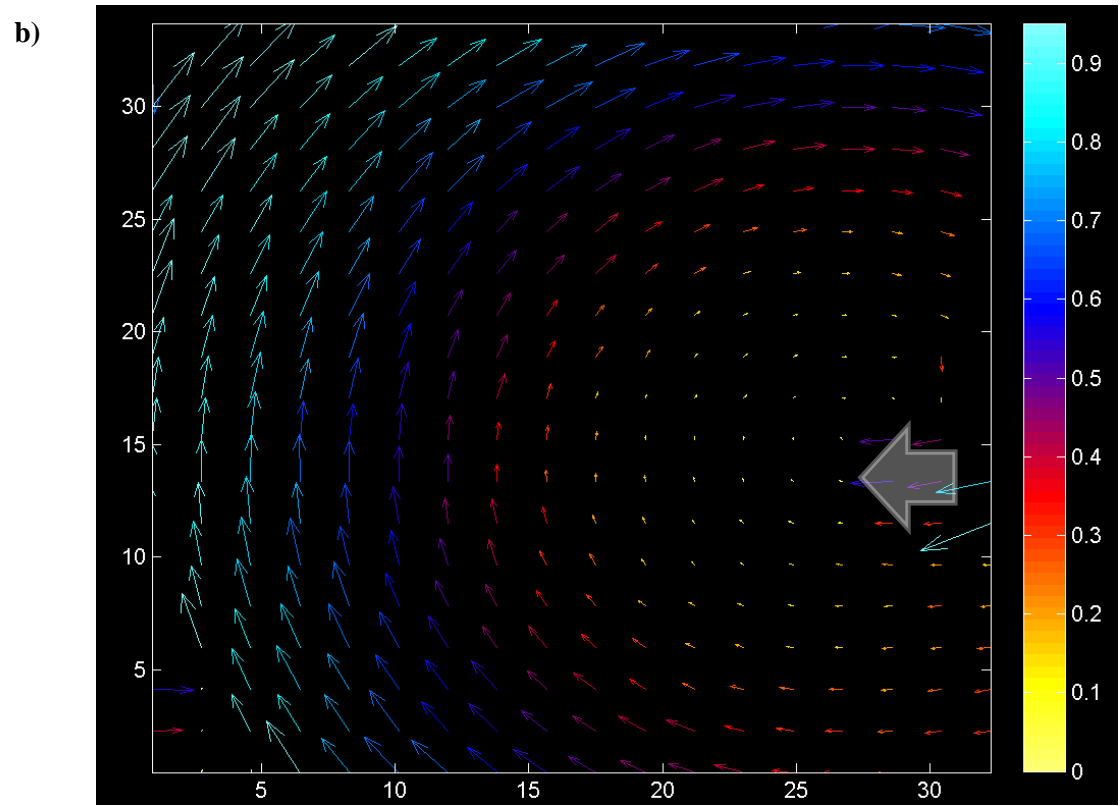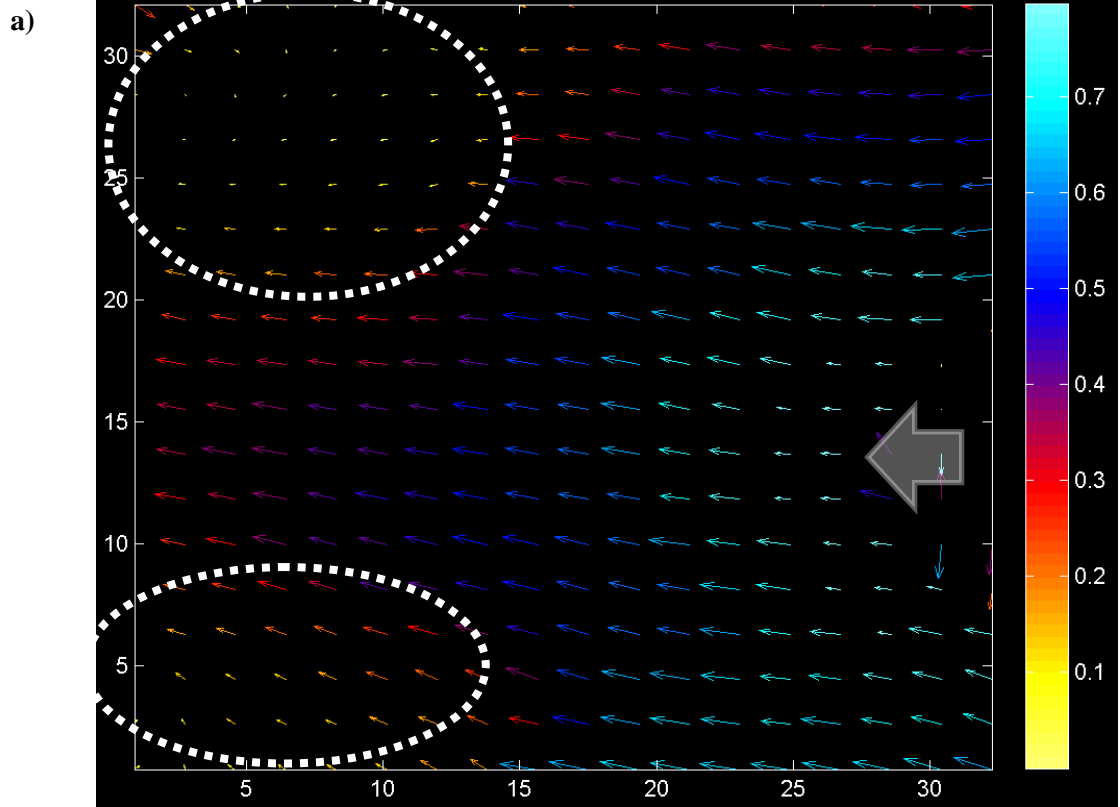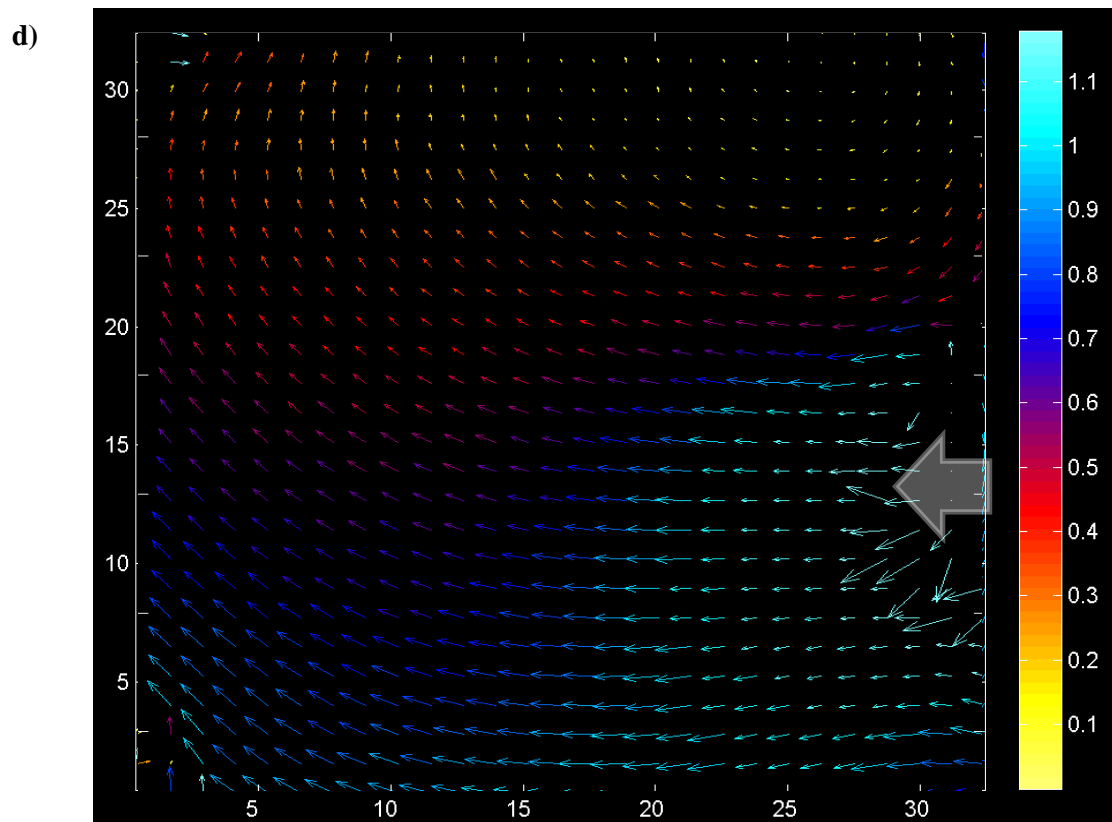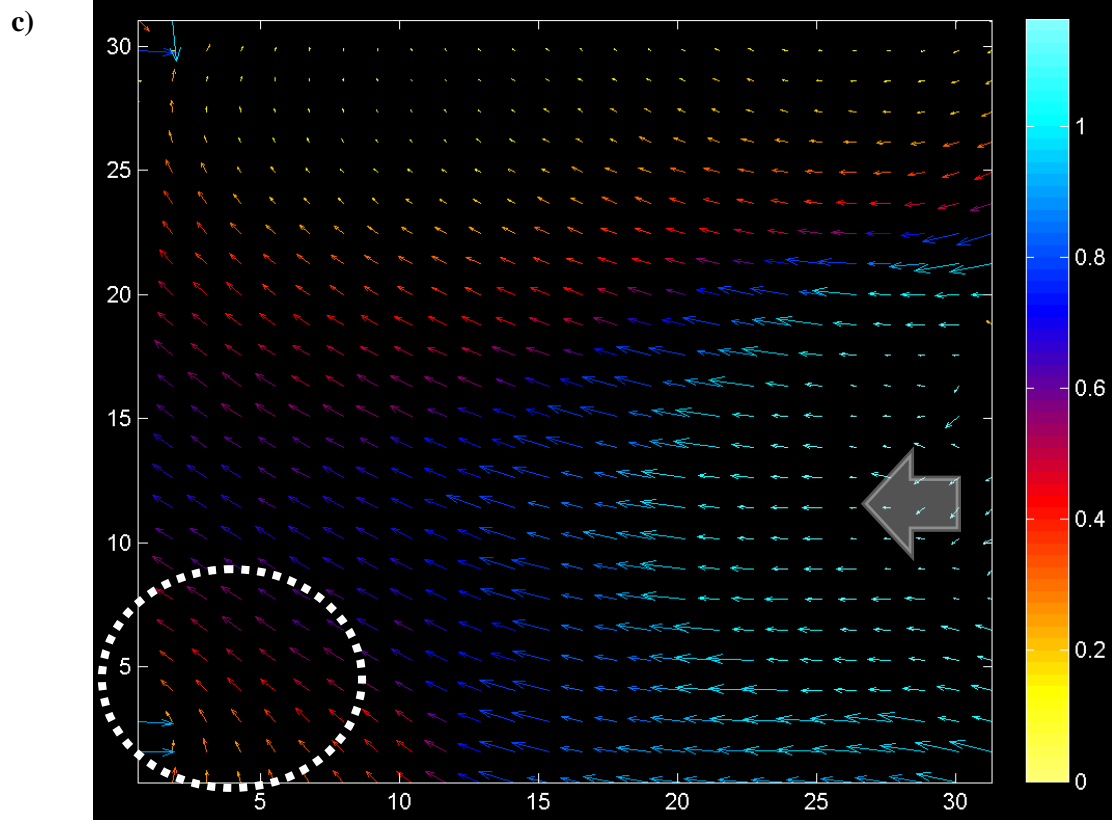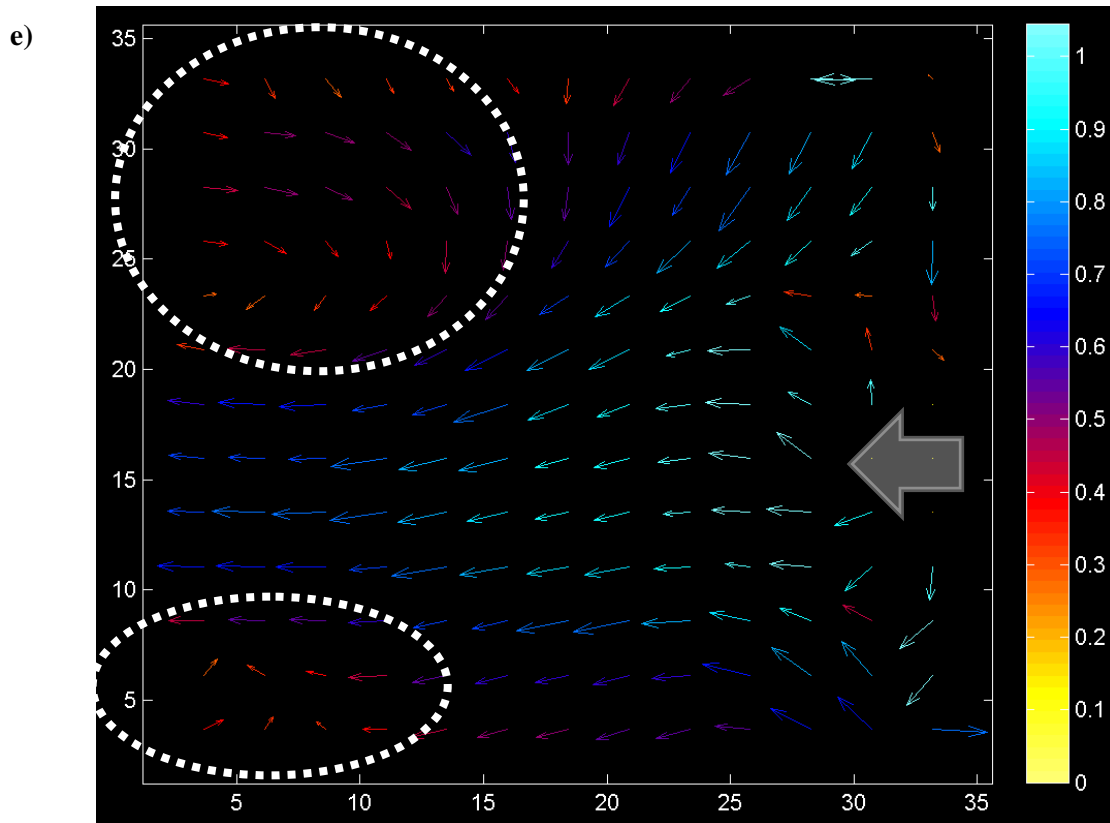
Figure 6.15: Displacement vector plots in the X-Y plane for: **a)** auxetic 10 PPI, **b)** conventional 10 PPI, **c)** auxetic 45 PPI, **d)** conventional 45 PPI and **e)** 3D printed, where the white arrow represents the loaded region.

6.2.2.4 Energy Absorption

To assess if the presence of an auxetic system with the same relative density as a conventional system enhances energy absorption (and thus reduce penetration depth) 3D printed auxetic and conventional samples were impacted by a free fall drop tower (high mass, low velocity) and a high strain projectile (low mass, high velocity) as detailed in Section 3.4. To keep the density effects to a minimum both sample types were designed to have matching dimensions and densities, as shown in Table 6.6.

For samples used in the high velocity, low mass impact tests both auxetic and conventional samples were bonded to a hard outer layer of 32 ply carbon fibre of dimensions 30 mm × 30 mm × 5 mm, supplied by Cytec, UK, following recommendation from the Joint Grant Scheme - EPSRC Impact and erosion resistant coatings (EP/G042195/1).

Table 6.6: 3D printed sample parameters

Sample type	Dimensions			Endplate	Designed Density / kg m^{-3}
	X / mm	Y / mm	Z / mm		
Auxetic – High mass, low velocity	30	30	30	N	300
Auxetic – Low mass, high velocity	30	30	15	Y	400
Conventional – High mass, low velocity	30	30	30	N	300
Conventional – Low mass, high velocity	30	30	15	Y	400
Solid block – Low mass, high velocity	30	30	15	N/A	1140

6.2.2.5 Energy Absorption - High mass, low velocity impact

Table 6.7 shows the high mass, low velocity impact data where the auxetic and conventional systems exhibited mean crater depths of 2.9 ± 0.3 mm and 3.0 ± 1.3 mm, and mean energy absorption of 5.38 ± 0.5 J and 5.47 ± 1 J, respectively (error provided by 95% confidence intervals). Some variability was noticeable between samples, such that samples with identical densities, exhibited different energy absorption and crater depths. This behaviour, however, can be attributed to disparities and damage within the samples, induced by the Objet printing system and the potassium hydroxide treatment, as previously described. Based on the stress-strain curves in Section 6.2.2.2, for a given density, auxetic systems were shown to experience densification earlier in comparison to the conventional systems, which would suggest that they should absorb more energy for a given displacement. However, Table 6.7 indicates that similar magnitudes of energy are absorbed for a given density. It is likely that a difference between sample behaviour is indistinguishable due to the clay's inability to detect small changes in energy absorption, however to confirm this, variation in tup mass, foam thickness and drop height should be explored. Additionally, should instrumentation be introduced, parameters such as stress-strain behaviour, temperature and strain rate effects can also be explored.

Table 6.7: Low velocity, high mass 3D printed sample parameters.

Sample	Imposed density / kg m^{-3}	Actual density / kg m^{-3}	Relative Density	Energy Absorbed / J	Crater Depth / mm
Auxetic 1	300	285	0.25	5.64	2.9
Auxetic 2	300	284	0.25	5.29	3.1
Auxetic 3	300	289	0.25	5.22	2.8
Conventional 1	300	300	0.26	4.9	3.7
Conventional 2	300	302	0.27	6.03	2.6
Conventional 3	300	300	0.26	5.48	2.6

6.2.2.6 Low mass, high velocity impact

Following the high mass, low velocity impact testing, samples with identical cellular structures to the auxetic and conventional foams, but with dimensions of 30 mm ×30 mm × 15 mm (Table 6.6), were impacted under high strain rate conditions. As previously observed, some variability was noticeable between samples, as highlighted in Table 6.8. Virgin 32 ply carbon fibre, and solid TangoBlack backings, were also considered in order to provide a benchmark for the printed samples.

Table 6.8: High velocity, low mass 3D printed sample parameters.

Sample	Imposed density / kg m^{-3}	Actual density / kg m^{-3}	Relative Density
Auxetic 1	400	387	0.34
Auxetic 2	400	383	0.34
Auxetic 3	400	391	0.34
Auxetic 4	400	363	0.32
Auxetic 5	400	354	0.31
Auxetic 6	400	359	0.31
Conventional 1	400	412	0.36
Conventional 2	400	414	0.36
Conventional 3	400	417	0.37
Solid Block 1	1140	1134	1.00
Solid Block 2	1140	1133	0.99
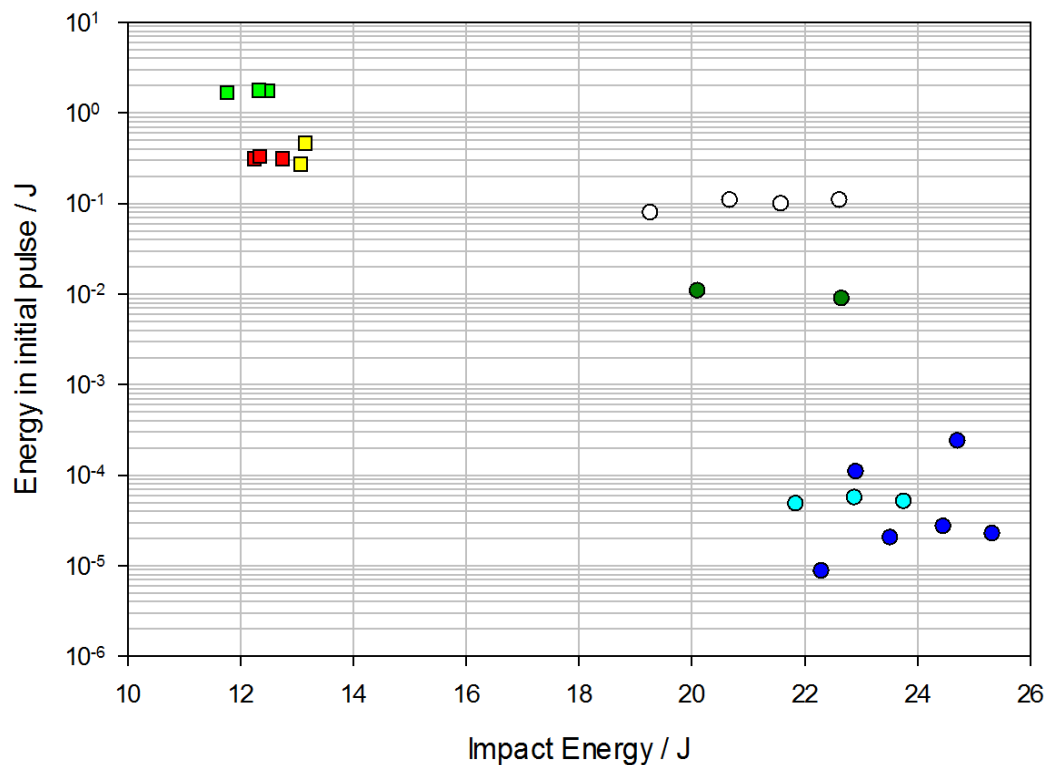
Figure 6.16: : Input energy of high strain rig verses measured energy from accelerometer for aluminium (■), Ti6Al4V alloy (■), copper (■), 32 ply virgin prepreg (o), 32 ply prepreg with auxetic printed backing (●), 32 ply prepreg with conventional honeycomb printed backing (●), and 32 ply prepreg with solid printed backing (●).

Figure 6.16 shows the energy absorbed measured at the initial pulse behind the samples (against energy absorbed. Three distinct groupings were shown to exist: (*i*) systems with no backing materials, (*ii*) solid backing material and (*iii*) foam backing material. Systems without backing materials were shown to transmit more energy to the accelerometer, even though these were tested at lower impact energies, in comparison to materials with backings. Where backing materials are considered, it is important that they absorb impact energy through cellular bending, buckling, yielding and crushing [159]. This is true when considering the solid backing against the porous backing, where two orders of magnitude are observed in attenuating energy transmission. Comparing auxetic to conventional foam backings, there are no discernible differences regarding energy absorption between the two systems. Factors that could contribute to the similarities in these results include but are not limited to: marginal changes in magnitude, high energy absorption by the outer plate and low deformation of the foams. To further explore this, higher impact velocity studies must be undertaken to see if there are any discernible differences regarding energy absorption between the two systems.

Although energy absorption is a key aspect in body armour systems, when designing to mitigate the effects of behind armour blunt trauma, it is paramount that the peak force acting on the body is kept to a minimum. Consequently, samples were considered with respect to their highest peak force (Table 6.9), as obtained by the accelerometers described in Section 3.5. Overall, the virgin 32 ply carbon fibre demonstrated the highest peak force of 1495 ± 27 kN, while the presence of backing materials reduced the mean peak force to 512 ± 72 kN, 86 ± 3 kN and 42 ± 26 kN for solid, conventional and auxetic samples respectively.

Table 6.9: Highest peak force for samples impacted by the high velocity, low mass regime.

Sample	Highest peak force / kN	Mean peak force / kN
Auxetic 1	38	
Auxetic 2	74	
Auxetic 3	75	42 ± 26
Auxetic 4	20	
Auxetic 5	21	
Auxetic 6	24	
Conventional 1	86	
Conventional 2	90	86 ± 3
Conventional 3	83	
Solid Block 1	461	512 ± 72
Solid Block 2	563	
32Ply 1	1521	
32Ply 2	1515	1495 ± 27
32Ply 3	1472	
32Ply 4	1472	

For any impact event, the peak force can only be mitigated by decelerating the load over a given distance. For the foam materials, deceleration occurs through elastic bending and buckling of the cell ribs, whereas in a solid material, these mechanisms are not present. When compared with the conventional systems, the auxetic foam samples exhibited a lower overall mean peak force by a factor of two. This raises the question as to what is important for reducing BABT regarding energy absorption and transmitted peak forces, as these two parameters may be a too simplistic metric. Whilst the auxetic system significantly reduced the transmitted peak force but maintained similar energy absorption when compared to the conventional system, it is difficult to say whether or not the auxetic system performed better than the conventional system. This is due to a current lack of understanding governing BABT due to the mechanical and biophysical interactions that take place [7, 34]. It is therefore important that more rigorous testing is undertaken to explore other effects including pressure wave propagation, ergonomics and replicating in-field conditions and the role of foams on these effects.

6.3   Summary

A 3D printing approach has been used to produce two types of repeatable pliable polymeric foam structures (re-entrant and honeycomb), where the majority of geometric features have a dimensional accuracy between 0.5% - 5.0% of the original computer-designed model.

Under tensile loading, as strain increases, the Poisson's ratio of the auxetic samples is shown to transition from a negative Poisson's ratio towards a positive Poisson's ratio almost linearly, as a result of the cellular geometry changing from a re-entrant to a honeycomb cell. The conventional samples were additionally shown to exhibit a Poisson's ratio change with respect to strain, however, an increase in strain caused a decrease in Poisson's ratio, until stabilising

When compared against a mathematical model, the predictions of Poisson's ratio showed a good fit to the experimental data for the conventional foams until 0.2 strain, while no fit was apparent for the auxetics. This poor fit between the experimental and modelled Poisson's ratios is likely due to the sample manufacturing, which led to distortions in the internal angles and the length of the cell walls in comparison to the original design specifications.

Alternatively, under compressive loading, samples displayed a high level of repeatability where the auxetic exhibited an almost linear transition from a negative Poisson's ratio towards a positive Poisson's ratio with respect to strain. Alternatively, the conventional samples exhibited an almost consistent Poisson's ratio of approximately 0.1 with respect to strain. Furthermore, from the stress-strain curves generated by the compressive test, the energy per unit volume represented by the area under the curve is greater in the auxetic case than the conventional system. As both systems have approximately the same relative density, it can be inferred that on a like-for-like weight, auxetic foams can absorb more energy for a given strain profile.

When evaluated using DVC, the 3D printed foams under quasi-static loading (representative of an impact) were shown to exhibit not only the same behaviour as commercial foams under loading but also exhibit the same increased resistance to indentation as classic auxetic foams (Figure 2.18), as demonstrated by the presence of a negative Poisson's ratio.

Under high mass, low velocity impacts, both auxetic and conventional sample types exhibited similar mean crater depths of 2.9 ± 0.3 mm and 3.0 ± 1.3 mm and mean energy absorption of 5.38 ± 0.45 J and 5.47 ± 1.10 J, respectively. Some variability in crater depth and energy absorption was apparent between samples, however, this was deemed to be the result of slight variation in relative density, cellular disparities and damage within the samples themselves.

Under low mass, high velocity impacts, three distinct groupings were shown to exist: (*i*) systems with no backing materials, (*ii*) solid backing material and (*iii*) foam backing material. Systems without backing materials were shown to transmit more energy, while the porous backings attenuated the of energy transmission by two orders of magnitudes greater. When comparing auxetic to conventional foam backings, no discernible differences regarding energy absorption

between the two systems was discernible. Alternatively, when considered with respect to peak force, the auxetic systems exhibited a lower overall mean peak force of a factor of two. Unfortunately due to the current limited understanding of the BABT formation process, it is difficult to ascertain if auxetics would be a suitable trauma attenuating backing, without first exploring the effects of pressure wave propagation, ergonomics and in-field conditions.

Chapter 7: Conclusions

The primary aim of this work was to investigate the feasibility of utilising auxetic foams as trauma-attenuating backings to reduce the most damaging effects of BABT. The influence of fabrication parameters on the classic three-step auxetic foam fabrication process have been explored, with a key focus on Poisson's ratio, energy absorption and crater depth. A total of 72+ combinations of porosity, volumetric compression ratio and heating time have been tested, where selection of fabrication parameter combinations was based on available published literature, coupled with a series of in-house experiments.

Auxetic foams have been produced from a number of fabrication parameter combinations, where heating time and volumetric compression ratio were identified to be co-dependent in determining whether a sample foam exhibited a negative Poisson's ratio. When a negative Poisson's ratio was present, a near-linear convergence towards a positive Poisson's ratio with respect to strain was observed. Once positive, the Poisson's ratio exhibited a plateau effect stabilising between values of 0.2 to 0.3 for the remaining intervals of strain, thus indicating a return to conventional foam behaviour. Where a negative Poisson's ratio was not obtained, samples only exhibited positive Poisson's ratios that initially fluctuated with increasing strain until stabilising between 0.1 and 0.3, due to the presence of both conventional and auxetic cells within the foam structures.

Although many of the fabrication parameters demonstrated improved energy absorption and reductions in crater depth, it was found that the presence of a negative Poisson's ratio had little effect upon the crater depth and energy absorption. Furthermore, through compressive testing there was evidence to suggest that auxetic foams do not exhibit greater energy absorption than their conventional counterparts due to their negative Poisson's ratio, but instead because of the increase in density that they obtain from the fabrication process. However, without comparison between auxetic and conventional foams of matching densities, it is not possible to deduce if auxetics are better at energy absorption due to their increase in density or because of their structure.

Instead, the improvements in energy dissipation were shown to stem from the increased density through the auxetic manufacturing process where heating time and volumetric compression ratio were also found to determine an auxetic foam's relative density. Both crater depth and energy absorption behaviour were identified as being directly influenced by relative density, since the density governs the energy absorption per unit volume of a porous material (linked to the deformation of a foam's structure through three distinct phases: elastic deformation, plastic

deformation, and densification). For foams with high relative densities, limited deflection occurs, leading to rapid deceleration and constrained energy absorption before densification due to their higher strength. In the case of low relative density foams, limited energy absorption occurs as only limited force is required to cause cellular deflection due to their low strength, causing the foam to bottom out with a sharp increase in force resulting in the remaining impact energy being transmitted to the backing material.

Unfortunately, due to the presence of defective and/or damaged cellular structures throughout some foam samples, coupled with the heterogeneous changes to the cellular geometry during the classic auxetic fabrication process, samples produced using the same fabrication parameters often had varying relative densities. Consequently, this caused highly erratic and unrepeatable auxetic behaviour, which in turn would make auxetic foams produced by the classic tri-axial method a poor material choice for the application of trauma-attenuating backing, as the wearer will have no confidence in the armour system, resulting in it not being worn.

In light of the limitations of the classic auxetic fabrication methodology, a 3D printing approach was developed to produce two types of repeatable pliable polymeric foam structures (re-entrant and honeycomb, auxetic and conventional, respectively), where the majority of geometric features had dimensional error between 0.5% - 5.0% of the original computer-designed model.

Under tensile loading, as strain increases, the Poisson's ratio of the auxetics were shown to transition from a negative Poisson's ratio towards a positive Poisson's ratio almost linearly, as a result of the cellular geometry changing from a re-entrant to a honeycomb cell. The conventional systems were additionally shown to exhibit a Poisson's ratio change with respect to strain, however, an increase in strain caused a decrease in Poisson's ratio, until stabilising.

When compared against a mathematical model, the predictions of Poisson's ratio showed a good fit to the experimental data for the conventional systems until 0.2 strain while no fit was apparent for the auxetics. This poor fit between the experimental and modelled Poisson's ratios was likely due to the sample manufacturing, which led to distortions in the internal angles and the length of the cell walls in comparison to the original design specifications.

Under compressive loading, samples displayed a high level of repeatability, where the auxetics exhibited an almost linear transition from a negative Poisson's ratio towards a positive Poisson's ratio with respect to strain. Alternatively, conventional samples exhibited an almost consistent Poisson's ratio of approximately 0.1 with respect to strain. Furthermore, from the stress-strain

curves generated by the compressive test, the energy per unit volume represented by the area under the curve was greater for the auxetics.

The 3D printed auxetic foams were compared to classic auxetic foams using digital volume correlation. Under quasi-static loading, 3D printed foams were found to exhibit not only the same behaviour as commercial foams but also demonstrated the same increased resistance to indentation as the classic auxetic foams, as demonstrated by the presence of a negative Poisson's ratio.

Under high mass, low velocity impacts, both printed auxetic and conventional foams exhibited similar mean crater depths of approximately 3 mm and mean energy absorption of approximately 5.4 J. Some variability in crater depth and energy absorption was present between samples, however, this was identified to be the result of a slight variation in either relative density, cellular disparities and / or damage within the samples themselves.

When the same cellular structures (but with reduced dimensions) were adhered to a 32-ply carbon fibre composite (with the composite as a top layer) and impacted under high velocity, low mass conditions, no discernible difference regarding energy absorption was shown between the auxetic and conventional systems. However, when considered with respect to the peak force, the auxetic systems exhibited a lower overall mean peak force by a factor of two. Whilst the auxetic system significantly reduced the transmitted peak force but maintained similar energy absorption when compared to the conventional system, it was difficult to surmise whether or not the auxetic system performed better than the conventional system. However, with respect to the quasi-static testing (where the auxetics exhibited a greater energy absorption per unit volume due to both systems having an approximately same relative density), for a like-for-like weight basis the auxetic foams absorb more energy than their conventional counterparts due to their structure and not just because of the increase in relative density that the classic auxetic fabrication process instils.

Therefore, it may be concluded that auxetics are potentially suitable for the application as a trauma attenuating backing material as they demonstrated that they satisfy the two key requirements that TAB materials must possess: the ability to absorb energy and reduce the transferable force. However, due to a current lack of understanding on the effects governing BABT, particularly in the area of mechanical and biophysical interactions that take place, it is important that more rigorous testing is undertaken to explore other effects, including pressure wave propagation, ergonomics and replicating in-field conditions before committing auxetic foams to a TAB application.

Chapter 8: Future work

While the scope of the work undertaken within this thesis has been centred on the feasibility of using auxetic foams to reduce the effects of behind armour blunt trauma, it is clear that there are many other potential applications. For instance, packaging, sandwich structures, biomedical components, smart filters and protective sports gear would all benefit from the capacity of additive manufacturing to tailor the construction of repeatable structures. Unfortunately, the 3D printing methodology utilised in this thesis has currently some systematic limitations associated with resolution / precision, support removal damage and limited material selection, and as such any further work should focus on reducing or if possible removing these limitations. One such way to rectify these limitations is through the employment of alternative additive manufacturing systems.

To date, there are various additive manufacturing systems available (extrusion, sintering, melting, curing and cutting), each with its own fabrication speeds, equipment charges, and cost and selection of compatible materials. While each application will have unique requirements (e.g. cost, materials, size, accuracy and precision), when producing foams it is imperative that the chosen system utilises an appropriate support material to allow the production of complex structures whilst also being more easily removable without causing damage. Structural damage is a serious issue for foams, as the loss of only 5% of the cells within a structure can reduce the Young's modulus or strength by over 30%, in turn reducing the overall energy absorption per unit volume. The chosen system should also have a high level of repeatability and resolution to ensure that not only can the computation foam structure be produced, but also limit structural variability between samples. A good range of compatible materials are also desirable, as they will not only allow for a greater range of mechanical properties to be available, but also enable the foam structures to be employed throughout various applications.

Furthermore, should the work retain a military focus the biophysical aspects of BABT should also be investigated, as the work here was considered with a primary focus on the mechanical and material engineering aspects of reducing the effects of BABT. To date, there have been a number of studies assessing the biophysical aspects of BABT utilising animals and cadavers, which suggest that the risk of injury from BABT is often dependent on the type and configuration of the armour, the projectile form, the energy and the physical characteristics of the person wearing the armour system.

Interestingly, aspects of the initial work has shown that the presence of trauma attenuated backing materials may provide some degree of protection by attenuating the pressure waves [6, 42], without determining what is a safe maximum allowable peak force, selection of TABs will be difficult. Defining a safe maximum allowable peak force with respect to biophysical aspects may be beyond the scope of this work, 3D printed foam samples of various topologies and materials should be further investigated to ascertain if the peak force can be reduced through methods other than relative density. Furthermore, while the initial work presented suggests that the presence of an auxetic structure provides greater energy absorption and a reduction in peak force, these materials still require testing under in-field conditions (e.g. deployment environments, full armour layup, high velocity rounds etc…) before committing auxetic foams to a TAB application.

Appendices

Appendix 4A: Calculating Poisson's ratio from raw data

Although Figures 4.1 to 4.4 present the mean Poisson's ratio per unit strain for each combination of the fabrication parameters (pore per inch, heating times, volume compression ratios and orientation), this is derived data that does not clearly indicate the variability that samples fabricated from the same parameters experience. Consequently, this appendix presents a worked example for the calculation of the Poisson's ratio from the raw data of the longitudinal 45 PPI 4.88 volumetric compression ratio, fabricated at a heating time of 60 minutes. The resulting data has then been plotted to indicate both the trends of the raw data and the error bars that arise when considered with respect to a 95% confidence. Raw data for Figures 4.1 to 4.4 are also included.

Calculating Poisson's ratio:

A Hounsfield tensile testing machine was employed to measure the Poisson's ratio, where samples were quasi-statically loaded along the longitudinal axis up to a strain of 1 at 0.1 intervals. For each interval of longitudinal strain (ε_{length}), the transverse strain (ε_{width}) was measured at the centre of the sample (as marked out prior to before placement into the testing equipment) to calculate the Poisson's ratio using Equation 4A.1.

$$\nu = -\frac{\varepsilon_{width}}{\varepsilon_{length}}$$

(Equation 4A.1)

Utilising this methodology, the resulting raw data for the longitudinal 45 PPI 4.88 volumetric compression ratio, fabricated at a heating time of 60 minutes is shown in Table 4A.1 and figure 4A.1.

From Figure 4A.1 it can be seen that between 0.1 to 0.4 strain, noticeable sample variation occurs. During this strain range, samples 1 and 2 increase in negative Poisson's ratios, while samples 3 and 4 demonstrate an almost linear convergence towards a positive Poisson's ratio per interval strain. It is only when the strain approaches 0.4 that all samples exhibit the same linear convergence towards a positive Poisson's ratio. This behaviour is further reflected when the same data is plotted as a mean with error bars provided by 95% confidence, as shown in Figure 4A.2. By considering the mean data with a 95% confidence, the extent of variability becomes further

shown, as the error bars predicts that a samples Poisson's ratio at its worse (0.1 strain) and it's best (0.3 strain) can be ±158% and ±45% of the mean, respectively.
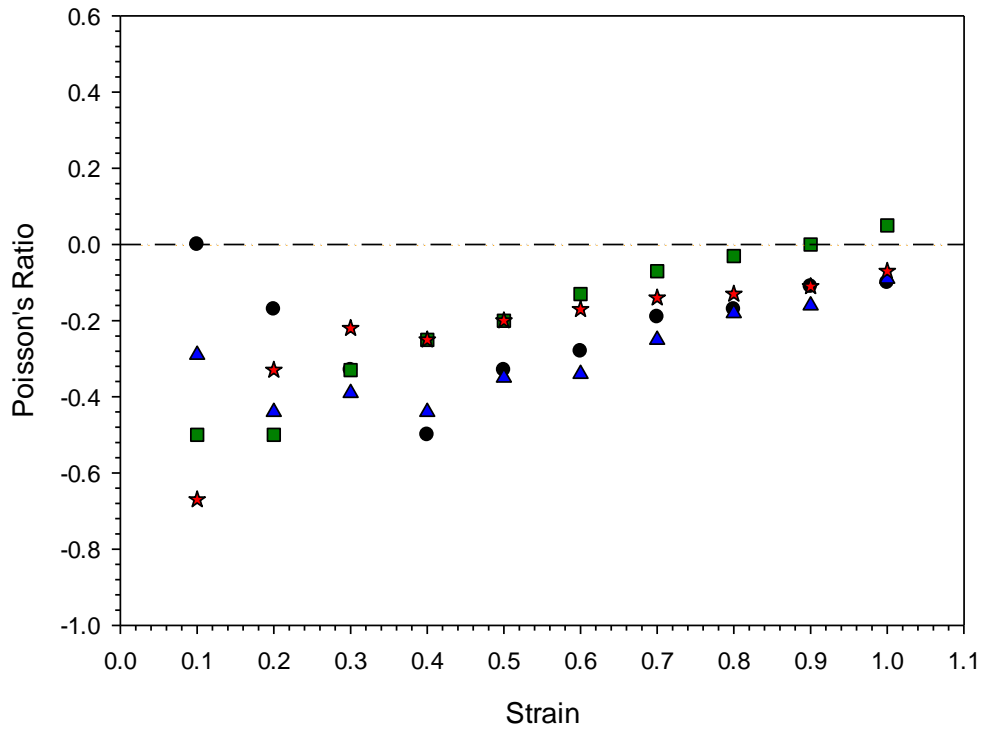
Figure 4A.1: Raw data for Poisson's ratio behaviour with respect to strain for the longitudinal 45 PPI 4.88 volumetric compression ratio, fabricated at a heating time of 60 minutes, for samples: 1(●), 2(▲), 3(■) and 4(★), where the dashed line denotes the negative and positive Poisson's ratio boundary.
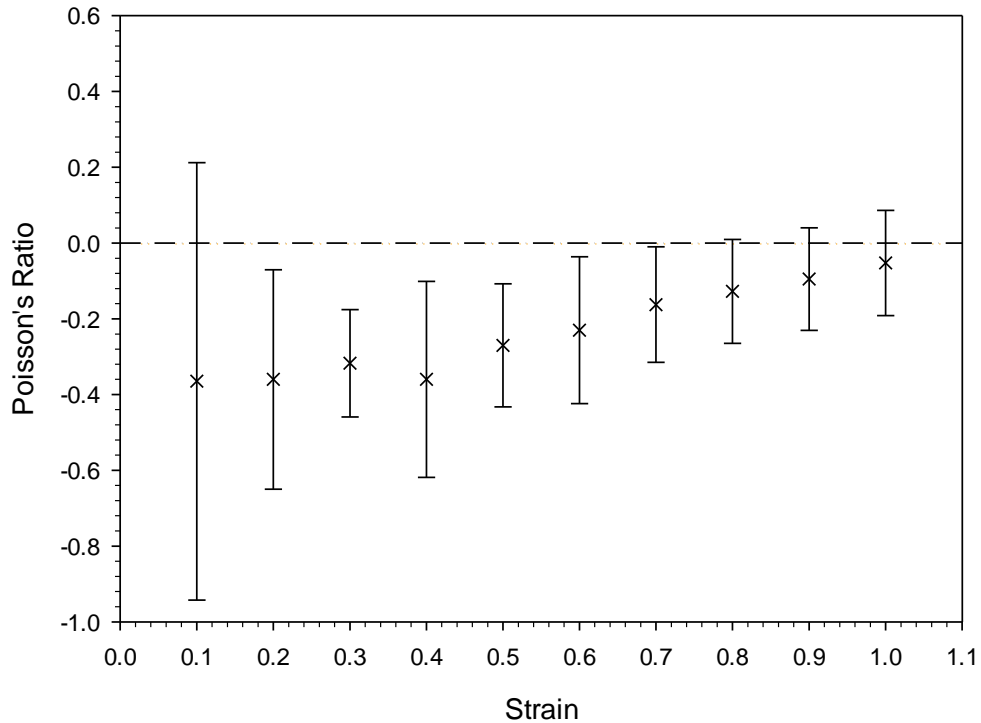
Figure 4A.2: Mean Poisson's ratio behaviour with respect to strain for the longitudinal 45 PPI 4.88 volumetric compression ratio, fabricated at a heating time of 60 minutes, where error bars are provided by a 95% confidence, where the dashed line denotes the negative and positive Poisson's ratio boundary.

Table 4A.1: Raw data for Poisson's ratio longitudinal 45 PPI 4.88 volumetric compression ratio

60 Minutes

Strain	Sample 1 Poisson's Ratio	Sample 2 Poisson's Ratio	Sample 3 Poisson's Ratio	Sample 4 Poisson's Ratio	Mean Poisson's Ratio
0	-	-	-	-	-
0.1	0.00	-0.29	-0.50	-0.67	-0.37
0.2	-0.17	-0.44	-0.50	-0.33	-0.36
0.3	-0.33	-0.39	-0.33	-0.22	-0.32
0.4	-0.50	-0.44	-0.25	-0.25	-0.36
0.5	-0.33	-0.35	-0.20	-0.20	-0.27
0.6	-0.28	-0.34	-0.13	-0.17	-0.23
0.7	-0.19	-0.25	-0.07	-0.14	-0.16
0.8	-0.17	-0.18	-0.03	-0.13	-0.13
0.9	-0.11	-0.16	0.00	-0.11	-0.10
1	-0.10	-0.09	0.05	-0.07	-0.05

55 Minutes

Strain	Sample 1 Poisson's Ratio	Sample 2 Poisson's Ratio	Sample 3 Poisson's Ratio	Sample 4 Poisson's Ratio	Mean Poisson's Ratio
0	-	-	-	-	-
0.1	-0.33	-0.57	-0.50	-0.65	-0.51
0.2	-0.24	-0.57	-0.38	-0.48	-0.42
0.3	-0.22	-0.48	-0.42	-0.54	-0.41
0.4	-0.28	-0.43	-0.31	-0.48	-0.38
0.5	-0.23	-0.46	-0.20	-0.39	-0.32
0.6	-0.22	-0.38	-0.13	-0.27	-0.25
0.7	-0.23	-0.33	-0.07	-0.18	-0.20
0.8	-0.20	-0.25	-0.03	-0.16	-0.16
0.9	-0.14	-0.16	0.00	-0.14	-0.11
1	-0.13	-0.11	0.03	-0.10	-0.08

50 Minutes

Strain	Sample 1 Poisson's Ratio	Sample 2 Poisson's Ratio	Sample 3 Poisson's Ratio	Sample 4 Poisson's Ratio	Mean Poisson's Ratio
0	-	-	-	-	-
0.1	-0.65	-0.57	-0.48	-0.32	-0.50
0.2	-0.32	-0.57	-0.60	-0.32	-0.45
0.3	-0.32	-0.38	-0.48	-0.32	-0.38
0.4	-0.32	-0.43	-0.30	-0.24	-0.32
0.5	-0.32	-0.46	-0.24	-0.19	-0.30
0.6	-0.38	-0.29	-0.12	-0.16	-0.24
0.7	-0.32	-0.24	-0.03	-0.18	-0.20
0.8	-0.28	-0.18	0.00	-0.16	-0.16
0.9	-0.18	-0.13	0.05	-0.11	-0.09
1	-	-0.09	0.10	-	0.00

45 Minutes

Strain	Sample 1 Poisson's Ratio	Sample 2 Poisson's Ratio	Sample 3 Poisson's Ratio	Sample 4 Poisson's Ratio	Mean Poisson's Ratio
0	-	-	-	-	-
0.1	-0.50	-0.50	-0.49	-0.29	-0.45
0.2	-0.50	-0.38	-0.49	-0.15	-0.38
0.3	-0.42	-0.42	-0.33	-0.29	-0.36
0.4	-0.31	-0.31	-0.24	-0.22	-0.27
0.5	-0.20	-0.20	-0.20	-0.18	-0.19
0.6	-0.17	-0.17	-0.08	-0.10	-0.13
0.7	-0.11	-0.11	0.00	-0.08	-0.07
0.8	-0.09	-0.03	0.03	-0.04	-0.03
0.9	-0.06	0.03	0.08	-0.03	0.01
1	0.00	0.12	0.14	0.00	0.06

40 Minutes

Strain	Sample 1 Poisson's Ratio	Sample 2 Poisson's Ratio	Sample 3 Poisson's Ratio	Sample 4 Poisson's Ratio	Mean Poisson's Ratio
0	-	-	-	-	-
0.1	-0.28	0.00	-0.21	-0.59	-0.27
0.2	-0.42	0.11	-0.21	-0.44	-0.24
0.3	-0.46	0.14	-0.07	-0.39	-0.20
0.4	-0.42	0.21	0.00	-0.29	-0.12
0.5	-0.33	0.30	0.04	-0.24	-0.06
0.6	-0.28	0.32	0.07	-0.29	-0.05
0.7	-0.20	0.30	0.12	-0.25	-0.01
0.8	-0.14	0.32	0.16	-0.15	0.05
0.9	-0.12	0.31	0.19	-0.13	0.06
1	-0.11	0.30	0.21	-0.09	0.08

35 Minutes

Strain	Sample 1 Poisson's Ratio	Sample 2 Poisson's Ratio	Sample 3 Poisson's Ratio	Sample 4 Poisson's Ratio	Mean Poisson's Ratio
0	-	-	-	-	-
0.1	-1.47	0.00	-0.23	-1.03	-0.68
0.2	-0.88	-0.11	-0.23	-0.88	-0.52
0.3	-0.98	0.00	-0.08	-0.59	-0.41
0.4	-0.74	0.11	-0.06	-0.66	-0.34
0.5	-0.71	0.21	0.05	-0.53	-0.24
0.6	-0.54	0.25	0.08	-0.39	-0.15
0.7	-0.46	0.24	0.10	-0.34	-0.11
0.8	-0.33	0.27	0.14	-0.22	-0.04
0.9	-0.20	0.26	0.18	-	0.08
1	-	0.26	0.16	-	0.21

30 Minutes

Strain	Sample 1 Poisson's Ratio	Sample 2 Poisson's Ratio	Sample 3 Poisson's Ratio	Sample 4 Poisson's Ratio	Mean Poisson's Ratio
0	-	-	-	-	-
0.1	-0.50	0.00	0.00	-0.54	-0.26
0.2	-0.38	0.10	-0.11	-0.41	-0.20
0.3	-0.33	0.14	0.07	-0.36	-0.12
0.4	-0.31	0.20	0.11	-0.34	-0.08
0.5	-0.25	0.24	0.13	-0.32	-0.05
0.6	-0.21	0.27	0.22	-0.23	0.01
0.7	-0.14	0.29	0.22	-0.15	0.05
0.8	-0.13	0.28	0.24	-	0.13
0.9	-0.08	0.25	0.22	-	0.13
1	-	-	-	-	-

20 Minutes

Strain	Sample 1 Poisson's Ratio	Sample 2 Poisson's Ratio	Sample 3 Poisson's Ratio	Sample 4 Poisson's Ratio	Mean Poisson's Ratio
0	-	-	-	-	-
0.1	-0.17	0.00	0.00	-0.32	-0.12
0.2	-0.10	0.00	0.10	-0.16	-0.04
0.3	-0.07	0.13	0.14	-0.32	-0.03
0.4	-0.05	0.20	0.21	-0.24	0.03
0.5	0.00	0.24	0.25	-0.19	0.07
0.6	0.04	0.27	0.31	-0.22	0.10
0.7	0.03	0.26	0.33	-0.18	0.11
0.8	-	0.28	0.31	-0.12	0.16
0.9	-	-	-	-	-
1	-	-	-	-	-

Table 4A.2: Raw data for Poisson's ratio longitudinal 45 PPI 3.91 volumetric compression ratio

60 Minutes

	Sample 1	Sample 2	Sample 3	Sample 4	Mean
Strain	Poisson's Ratio	Poisson's Ratio	Poisson's Ratio	Poisson's Ratio	Poisson's Ratio
0	-	-	-	-	-
0.1	0.00	-0.29	-0.50	-0.33	-0.28
0.2	0.00	-0.29	-0.50	-0.17	-0.24
0.3	0.00	-0.29	-0.25	-0.11	-0.16
0.4	0.00	-0.15	-0.13	-0.08	-0.09
0.5	0.00	-0.06	-0.05	-0.07	-0.04
0.6	0.06	0.00	0.04	-0.06	0.01
0.7	0.05	0.04	0.07	0.00	0.04
0.8	0.08	0.07	0.09	0.00	0.06
0.9	0.07	0.10	0.11	0.00	0.07
1	0.07	0.12	0.13	0.00	0.08

55 Minutes

	Sample 1	Sample 2	Sample 3	Sample 4	Mean
Strain	Poisson's Ratio	Poisson's Ratio	Poisson's Ratio	Poisson's Ratio	Poisson's Ratio
0	-	-	-	-	-
0.1	-0.32	-0.29	-0.27	0.00	-0.22
0.2	-0.32	-0.29	-0.27	-0.16	-0.26
0.3	-0.22	-0.19	-0.27	-0.21	-0.22
0.4	-0.24	-0.21	-0.20	-0.08	-0.18
0.5	-0.19	-0.11	-0.16	-0.06	-0.13
0.6	-0.16	-0.10	-0.05	-0.05	-0.09
0.7	-0.14	-0.04	0.00	-0.04	-0.06
0.8	-0.12	0.00	0.07	0.00	-0.01
0.9	-0.07	0.03	0.09	0.00	0.01
1	-	0.06	0.11	-	0.08

50 Minutes

	Sample 1	Sample 2	Sample 3	Sample 4	Mean
Strain	Poisson's Ratio	Poisson's Ratio	Poisson's Ratio	Poisson's Ratio	Poisson's Ratio
0	-	-	-	-	-
0.1	0.00	-0.53	-0.45	-0.32	-0.33
0.2	-0.16	-0.26	-0.23	-0.16	-0.20
0.3	-0.11	-0.09	-0.08	-0.11	-0.09
0.4	0.00	-0.07	0.06	-0.16	-0.04
0.5	0.06	0.00	0.14	-0.13	0.02
0.6	0.05	0.04	0.19	-0.11	0.04
0.7	0.05	0.11	0.23	-0.09	0.07
0.8	0.04	0.16	0.23	-0.08	0.09
0.9	0.04	0.18	0.23	-	0.15
1	0.03	0.20	0.26	-	0.16

45 Minutes

Strain	Sample 1 Poisson's Ratio	Sample 2 Poisson's Ratio	Sample 3 Poisson's Ratio	Sample 4 Poisson's Ratio	Mean Poisson's Ratio
0	-	-	-	-	-
0.1	-0.32	-0.28	-0.53	0.00	-0.28
0.2	0.00	-0.14	-0.39	-0.16	-0.17
0.3	0.00	0.00	-0.26	-0.11	-0.09
0.4	0.00	0.00	-0.13	-0.08	-0.05
0.5	0.06	0.06	-0.05	0.00	0.02
0.6	0.05	0.14	0.00	0.00	0.05
0.7	0.09	0.16	0.04	0.02	0.08
0.8	0.08	0.14	0.10	0.04	0.09
0.9	0.07	0.15	0.12	-	0.11
1	-	0.17	0.18	-	0.17

40 Minutes

Strain	Sample 1 Poisson's Ratio	Sample 2 Poisson's Ratio	Sample 3 Poisson's Ratio	Sample 4 Poisson's Ratio	Mean Poisson's Ratio
0	-	-	-	-	-
0.1	-0.30	0.22	-0.23	0.00	-0.08
0.2	-0.15	0.11	0.00	-0.15	-0.05
0.3	0.00	0.22	0.08	-0.10	0.05
0.4	0.00	0.28	0.17	-0.08	0.09
0.5	0.06	0.36	0.23	-0.06	0.15
0.6	0.05	0.33	0.30	0.00	0.17
0.7	0.04	0.35	0.32	0.00	0.18
0.8	0.04	0.33	0.31	0.00	0.17
0.9	0.03	0.32	0.30	0.00	0.16
1	0.03	0.29	0.30	0.00	0.15

35 Minutes

Strain	Sample 1 Poisson's Ratio	Sample 2 Poisson's Ratio	Sample 3 Poisson's Ratio	Sample 4 Poisson's Ratio	Mean Poisson's Ratio
0	-	-	-	-	-
0.1	-0.54	0.00	0.00	0.00	-0.14
0.2	-0.27	0.00	0.12	0.00	-0.04
0.3	-0.27	0.15	0.23	0.00	0.03
0.4	-0.20	0.17	0.23	0.20	0.10
0.5	-0.16	0.22	0.33	0.16	0.14
0.6	-0.05	0.30	0.39	0.18	0.20
0.7	0.00	0.32	0.37	0.15	0.21
0.8	0.00	0.31	0.35	0.13	0.20
0.9	0.00	0.30	0.31	0.15	0.19
1	-	0.29	0.30	-	0.30

30 Minutes

Strain	Sample 1 Poisson's Ratio	Sample 2 Poisson's Ratio	Sample 3 Poisson's Ratio	Sample 4 Poisson's Ratio	Mean Poisson's Ratio
0	-	-	-	-	-
0.1	-0.53	0.22	0.00	-0.28	-0.15
0.2	-0.26	0.22	0.11	-0.14	-0.02
0.3	-0.26	0.30	0.07	0.00	0.03
0.4	-0.26	0.33	0.17	0.00	0.06
0.5	-0.16	0.36	0.22	0.00	0.10
0.6	-0.13	0.37	0.30	0.05	0.15
0.7	-0.08	0.32	0.29	0.08	0.15
0.8	-0.07	0.33	0.28	0.03	0.15
0.9	-0.06	0.30	0.27	0.03	0.14
1	-0.03	0.29	0.27	-	0.18

25 Minutes

Strain	Sample 1 Poisson's Ratio	Sample 2 Poisson's Ratio	Sample 3 Poisson's Ratio	Sample 4 Poisson's Ratio	Mean Poisson's Ratio
0	-	-	-	-	-
0.1	0.00	0.21	0.00	0.00	0.05
0.2	0.00	0.21	0.11	0.00	0.08
0.3	0.08	0.35	0.14	0.09	0.17
0.4	0.06	0.37	0.21	0.07	0.18
0.5	0.15	0.38	0.30	0.11	0.23
0.6	0.13	0.35	0.28	0.09	0.21
0.7	0.11	0.33	0.27	0.08	0.20
0.8	0.09	0.32	0.27	0.10	0.20
0.9	0.10	0.31	0.26	0.09	0.19
1	0.09	0.30	0.26	0.08	0.18

Table 4A.3: Raw data for Poisson's ratio longitudinal 45 PPI 2.93 volumetric compression ratio

60 Minutes

Strain	Sample 1 Poisson's Ratio	Sample 2 Poisson's Ratio	Sample 3 Poisson's Ratio	Sample 4 Poisson's Ratio	Mean Poisson's Ratio
0	-	-	-	-	-
0.1	1.00	0.00	0.00	0.33	0.33
0.2	0.50	-0.16	0.14	0.33	0.20
0.3	0.44	0.00	0.28	0.22	0.24
0.4	0.33	0.08	0.35	0.25	0.25
0.5	0.27	0.06	0.33	0.20	0.22
0.6	0.28	0.11	0.28	0.17	0.21
0.7	0.24	0.14	-	0.14	0.17
0.8	-	-	-	-	-
0.9	-	-	-	-	-
1	-	-	-	-	-

55 Minutes

Strain	Sample 1 Poisson's Ratio	Sample 2 Poisson's Ratio	Sample 3 Poisson's Ratio	Sample 4 Poisson's Ratio	Mean Poisson's Ratio
0	-	-	-	-	-
0.1	0.00	0.32	0.28	0.33	0.23
0.2	0.33	0.32	0.42	0.17	0.31
0.3	0.33	0.32	0.37	0.22	0.31
0.4	0.25	0.32	0.35	0.17	0.27
0.5	0.20	0.39	0.33	0.20	0.28
0.6	0.17	0.38	0.32	0.17	0.26
0.7	0.14	0.32	0.28	0.10	0.21
0.8	-	-	-	-	#DIV/0!
0.9	-	-	-	-	-
1	-	-	-	-	-

50 Minutes

Strain	Sample 1 Poisson's Ratio	Sample 2 Poisson's Ratio	Sample 3 Poisson's Ratio	Sample 4 Poisson's Ratio	Mean Poisson's Ratio
0	-	-	-	-	-
0.1	-0.33	0.59	0.24	-0.32	0.04
0.2	0.00	0.59	0.24	-0.16	0.17
0.3	0.11	0.39	0.24	-0.11	0.16
0.4	0.17	0.37	0.37	0.00	0.23
0.5	0.20	0.35	0.39	0.06	0.25
0.6	0.17	0.34	0.41	0.05	0.24
0.7	-	0.34	0.38	-	0.36
0.8	-	-	-	-	-
0.9	-	-	-	-	-
1	-	-	-	-	-

45 Minutes

Strain	Sample 1 Poisson's Ratio	Sample 2 Poisson's Ratio	Sample 3 Poisson's Ratio	Sample 4 Poisson's Ratio	Mean Poisson's Ratio
0	-	-	-	-	-
0.1	0.32	0.29	0.27	-0.33	0.14
0.2	0.16	0.15	0.27	0.00	0.14
0.3	0.22	0.29	0.36	0.11	0.25
0.4	0.16	0.29	0.34	0.08	0.22
0.5	0.19	0.24	0.32	0.07	0.20
0.6	0.16	0.20	0.32	0.17	0.21
0.7	-	0.17	0.31	-	0.24
0.8	-	-	-	-	-
0.9	-	-	-	-	-
1	-	-	-	-	-

40 Minutes

Strain	Sample 1 Poisson's Ratio	Sample 2 Poisson's Ratio	Sample 3 Poisson's Ratio	Sample 4 Poisson's Ratio	Mean Poisson's Ratio
0	-	-	-	-	-
0.1	-0.31	0.49	0.00	-0.33	-0.04
0.2	-0.16	0.85	0.25	0.00	0.24
0.3	-0.10	0.81	0.33	0.00	0.26
0.4	-0.08	0.73	0.38	0.00	0.26
0.5	-0.06	0.59	0.35	0.00	0.22
0.6	-0.05	-	0.33	0.00	0.09
0.7	-	-	-	-	-
0.8	-	-	-	-	-
0.9	-	-	-	-	-
1	-	-	-	-	-

35 Minutes

Strain	Sample 1 Poisson's Ratio	Sample 2 Poisson's Ratio	Sample 3 Poisson's Ratio	Sample 4 Poisson's Ratio	Mean Poisson's Ratio
0	-	-	-	-	-
0.1	0.57	0.51	0.00	0.63	0.43
0.2	0.57	0.38	0.27	0.63	0.46
0.3	0.38	0.34	0.27	0.42	0.35
0.4	0.29	0.38	0.27	0.31	0.31
0.5	0.23	0.41	0.27	0.25	0.29
0.6	0.19	0.34	0.27	0.21	0.25
0.7	0.16	-	0.27	0.13	0.19
0.8	-	-	-	-	-
0.9	-	-	-	-	-
1	-	-	-	-	-

30 Minutes

Strain	Sample 1 Poisson's Ratio	Sample 2 Poisson's Ratio	Sample 3 Poisson's Ratio	Sample 4 Poisson's Ratio	Mean Poisson's Ratio
0	-	-	-	-	-
0.1	0.57	0.71	0.50	0.00	0.45
0.2	0.71	0.71	0.50	0.29	0.55
0.3	0.57	0.71	0.50	0.38	0.54
0.4	0.57	0.71	0.50	0.36	0.54
0.5	0.46	0.62	0.45	0.34	0.47
0.6	0.43	0.52	0.42	0.33	0.42
0.7	-	0.48	0.39	-	0.43
0.8	-	-	-	-	-
0.9	-	-	-	-	-
1	-	-	-	-	-

25 Minutes

Strain	Sample 1 Poisson's Ratio	Sample 2 Poisson's Ratio	Sample 3 Poisson's Ratio	Sample 4 Poisson's Ratio	Mean Poisson's Ratio
0	-	-	-	-	-
0.1	0.21	0.23	0.25	0.18	0.22
0.2	0.23	0.35	0.25	0.23	0.26
0.3	0.24	0.31	0.25	0.31	0.28
0.4	0.29	0.35	0.25	0.28	0.29
0.5	0.29	0.37	0.30	0.32	0.32
0.6	0.29	0.39	0.33	0.31	0.33
0.7	0.32	0.33	0.32	0.33	0.33
0.8	-	-	-	-	-
0.9	-	-	-	-	-
1	-	-	-	-	-

Table 4A.4: Raw data for Poisson's ratio longitudinal 10 PPI 4.88 volumetric compression ratio

60 Minutes

	Sample 1	Sample 2	Sample 3	Sample 4	Mean
Strain	Poisson's Ratio	Poisson's Ratio	Poisson's Ratio	Poisson's Ratio	Poisson's Ratio
0	-	-	-	-	-
0.1	-0.33	-0.57	-0.25	-0.65	-0.45
0.2	-0.33	-0.71	-0.38	-0.48	-0.48
0.3	-0.11	-0.38	-0.25	-0.32	-0.27
0.4	-0.08	-0.36	-0.25	-0.16	-0.21
0.5	0.00	-0.29	-0.15	-0.06	-0.13
0.6	0.06	-0.14	-0.08	-0.05	-0.06
0.7	0.05	-0.12	-0.07	0.05	-0.03
0.8	0.08	-0.04	0.00	0.08	0.03
0.9	0.11	-0.03	0.03	0.11	0.05
1	0.10	0.00	0.05	0.13	0.07

55 Minutes

	Sample 1	Sample 2	Sample 3	Sample 4	Mean
Strain	Poisson's Ratio	Poisson's Ratio	Poisson's Ratio	Poisson's Ratio	Poisson's Ratio
0	-	-	-	-	-
0.1	-0.50	-0.54	-0.48	-0.51	-0.51
0.2	-0.38	-0.41	-0.36	-0.35	-0.37
0.3	-0.25	-0.36	-0.24	-0.08	-0.23
0.4	-0.25	-0.27	-0.12	0.00	-0.16
0.5	-0.10	-0.27	0.00	0.09	-0.07
0.6	0.00	-0.18	0.04	0.12	-0.01
0.7	0.04	-0.12	0.07	0.13	0.03
0.8	0.06	-0.10	0.12	0.18	0.06
0.9	0.08	-0.06	0.16	0.18	0.09
1	0.10	-0.03	0.14	0.19	0.10

50 Minutes

	Sample 1	Sample 2	Sample 3	Sample 4	Mean
Strain	Poisson's Ratio	Poisson's Ratio	Poisson's Ratio	Poisson's Ratio	Poisson's Ratio
0	-	-	-	-	-
0.1	-0.29	-0.75	0.00	-0.44	-0.37
0.2	-0.43	-0.63	0.00	-0.11	-0.29
0.3	-0.38	-0.42	-0.07	-0.15	-0.25
0.4	-0.36	-0.31	-0.05	0.00	-0.18
0.5	-0.23	-0.25	0.00	0.00	-0.12
0.6	-0.19	-0.21	0.07	0.04	-0.07
0.7	-0.12	-0.14	0.12	0.06	-0.02
0.8	-0.11	-0.09	0.16	0.14	0.03
0.9	-0.06	-0.08	0.17	0.15	0.04
1	-0.03	0.00	0.13	0.16	0.06

45 Minutes

Strain	Sample 1 Poisson's Ratio	Sample 2 Poisson's Ratio	Sample 3 Poisson's Ratio	Sample 4 Poisson's Ratio	Mean Poisson's Ratio
0	-	-	-	-	-
0.1	-0.03	0.00	0.00	0.00	-0.01
0.2	-0.03	-0.11	0.10	0.26	0.06
0.3	-0.05	-0.07	0.13	0.18	0.05
0.4	-0.05	-0.06	0.20	0.20	0.07
0.5	-0.08	0.00	0.24	0.16	0.08
0.6	-0.03	0.00	0.23	0.14	0.09
0.7	-0.05	0.06	0.26	0.16	0.11
0.8	-0.08	0.08	0.25	0.18	0.11
0.9	-0.11	0.12	0.24	0.19	0.11
1	-0.18	0.16	0.22	0.03	0.06

40 Minutes

Strain	Sample 1 Poisson's Ratio	Sample 2 Poisson's Ratio	Sample 3 Poisson's Ratio	Sample 4 Poisson's Ratio	Mean Poisson's Ratio
0	-	-	-	-	-
0.1	0.00	0.00	-0.21	0.26	0.01
0.2	0.12	0.11	-0.21	0.26	0.07
0.3	0.16	0.14	-0.07	0.34	0.14
0.4	0.23	0.21	0.00	0.26	0.18
0.5	0.23	0.30	0.04	0.26	0.21
0.6	0.23	0.32	0.07	0.30	0.23
0.7	0.20	0.30	0.12	0.29	0.23
0.8	0.20	0.32	0.16	0.29	0.24
0.9	0.23	0.31	0.19	0.31	0.26
1	0.21	0.30	0.21	0.31	0.26

35 Minutes

Strain	Sample 1 Poisson's Ratio	Sample 2 Poisson's Ratio	Sample 3 Poisson's Ratio	Sample 4 Poisson's Ratio	Mean Poisson's Ratio
0	-	-	-	-	-
0.1	0.22	0.00	0.21	0.00	0.11
0.2	0.11	0.11	0.10	0.10	0.10
0.3	0.36	0.07	0.14	0.13	0.18
0.4	0.33	0.11	0.10	0.20	0.18
0.5	0.35	0.30	0.17	0.24	0.26
0.6	0.36	0.28	0.17	0.23	0.26
0.7	0.34	0.30	0.21	0.26	0.28
0.8	0.33	0.29	0.21	0.25	0.27
0.9	0.31	0.26	0.23	0.24	0.26
1	-	0.26	0.23	-	0.24

30 Minutes

Strain	Sample 1 Poisson's Ratio	Sample 2 Poisson's Ratio	Sample 3 Poisson's Ratio	Sample 4 Poisson's Ratio	Mean Poisson's Ratio
0	-	-	-	-	-
0.1	0.00	0.00	0.40	0.00	0.10
0.2	0.10	0.20	0.30	0.10	0.18
0.3	0.20	0.27	0.27	0.14	0.22
0.4	0.20	0.30	0.30	0.21	0.25
0.5	0.20	0.32	0.32	0.21	0.26
0.6	0.23	0.33	0.33	0.28	0.29
0.7	0.26	0.34	0.31	0.27	0.30
0.8	0.25	0.33	0.33	0.26	0.29
0.9	0.24	0.31	0.29	0.25	0.27
1	0.24	0.30	0.28	0.25	0.27

25 Minutes

Strain	Sample 1 Poisson's Ratio	Sample 2 Poisson's Ratio	Sample 3 Poisson's Ratio	Sample 4 Poisson's Ratio	Mean Poisson's Ratio
0	-	-	-	-	-
0.1	0.00	0.00	0.00	0.20	0.05
0.2	0.20	0.00	0.10	0.10	0.10
0.3	0.26	0.13	0.14	0.26	0.20
0.4	0.25	0.20	0.21	0.29	0.24
0.5	0.27	0.24	0.25	0.31	0.27
0.6	0.26	0.27	0.31	0.29	0.28
0.7	0.31	0.26	0.33	0.31	0.30
0.8	0.27	0.28	0.31	0.32	0.29
0.9	-	-	-	0.31	0.31
1	-	-	-	0.29	0.29

60 Minutes

	Sample 1	Sample 2	Sample 3	Sample 4	Mean
Strain	Poisson's Ratio	Poisson's Ratio	Poisson's Ratio	Poisson's Ratio	Poisson's Ratio
0	-	-	-	-	-
0.1	-0.29	0.00	0.00	0.00	-0.07
0.2	-0.44	-0.43	-0.15	0.00	-0.26
0.3	-0.49	-0.19	-0.30	0.00	-0.25
0.4	-0.37	-0.07	-0.15	0.06	-0.13
0.5	-0.24	-0.06	-0.12	0.10	-0.08
0.6	-0.20	-0.05	-0.05	0.09	-0.05
0.7	-0.13	0.04	-0.04	0.11	0.00
0.8	-0.11	0.07	0.00	0.13	0.02
0.9	-0.03	0.10	0.03	0.14	0.06
1	-0.03	0.14	0.09	0.15	0.09

55 Minutes

	Sample 1	Sample 2	Sample 3	Sample 4	Mean
Strain	Poisson's Ratio	Poisson's Ratio	Poisson's Ratio	Poisson's Ratio	Poisson's Ratio
0	-	-	-	-	-
0.1	-0.25	-0.57	-0.68	0.00	-0.38
0.2	-0.25	-0.29	-0.34	-0.23	-0.28
0.3	-0.17	-0.19	-0.23	-0.08	-0.17
0.4	0.00	0.00	-0.06	0.00	-0.01
0.5	0.15	0.00	-0.05	0.09	0.05
0.6	0.17	0.00	0.08	0.08	0.08
0.7	0.21	0.04	0.13	0.17	0.14
0.8	0.25	0.07	0.17	0.17	0.17
0.9	0.25	0.06	0.18	0.23	0.18
1	0.25	0.09	0.18	0.23	0.19

50 Minutes

	Sample 1	Sample 2	Sample 3	Sample 4	Mean
Strain	Poisson's Ratio	Poisson's Ratio	Poisson's Ratio	Poisson's Ratio	Poisson's Ratio
0	-	-	-	-	-
0.1	-1.14	-0.25	0.00	0.00	-0.35
0.2	-0.57	-0.38	-0.11	0.12	-0.23
0.3	-0.29	-0.17	0.00	0.08	-0.09
0.4	-0.21	-0.06	0.11	0.06	-0.03
0.5	0.00	0.00	0.17	0.14	0.08
0.6	0.00	0.04	0.21	0.16	0.10
0.7	0.08	0.11	0.21	0.20	0.15
0.8	0.14	0.13	0.21	0.20	0.17
0.9	0.13	0.14	0.19	0.21	0.17
1	0.14	0.13	-	0.19	0.15

45 Minutes

Strain	Sample 1 Poisson's Ratio	Sample 2 Poisson's Ratio	Sample 3 Poisson's Ratio	Sample 4 Poisson's Ratio	Mean Poisson's Ratio
0	-	-	-	-	-
0.1	0.32	0.00	0.00	0.00	0.08
0.2	0.16	0.21	0.21	0.00	0.15
0.3	0.22	0.28	0.28	0.16	0.24
0.4	0.24	0.37	0.32	0.18	0.28
0.5	0.26	0.34	0.34	0.29	0.31
0.6	0.32	0.35	0.35	0.28	0.33
0.7	0.32	0.33	0.33	0.28	0.32
0.8	0.28	0.32	0.29	0.27	0.29
0.9	0.32	0.28	0.28	0.30	0.30
1	0.32	-	-	0.29	0.31

40 Minutes

Strain	Sample 1 Poisson's Ratio	Sample 2 Poisson's Ratio	Sample 3 Poisson's Ratio	Sample 4 Poisson's Ratio	Mean Poisson's Ratio
0	-	-	-	-	-
0.1	0.48	0.40	0.00	0.00	0.22
0.2	0.36	0.40	0.00	0.26	0.25
0.3	0.32	0.33	0.15	0.26	0.26
0.4	0.24	0.25	0.22	0.32	0.26
0.5	0.24	0.40	0.22	0.36	0.30
0.6	0.20	0.37	0.30	0.30	0.29
0.7	0.24	0.37	0.32	0.26	0.30
0.8	0.27	0.35	0.28	0.29	0.30
0.9	0.29	0.33	0.27	0.28	0.30
1	0.29	0.30	0.27	0.28	0.28

35 Minutes

Strain	Sample 1 Poisson's Ratio	Sample 2 Poisson's Ratio	Sample 3 Poisson's Ratio	Sample 4 Poisson's Ratio	Mean Poisson's Ratio
0	-	-	-	-	-
0.1	0.00	0.00	0.00	0.00	0.00
0.2	0.31	0.30	0.21	0.35	0.29
0.3	0.27	0.33	0.14	0.39	0.28
0.4	0.36	0.35	0.27	0.35	0.33
0.5	0.37	0.40	0.30	0.33	0.35
0.6	0.41	0.37	0.32	0.31	0.35
0.7	0.35	0.37	0.33	0.27	0.33
0.8	0.33	0.38	0.29	0.26	0.32
0.9	0.29	0.33	0.28	0.23	0.29
1	0.29	0.34	0.26	0.23	0.28

30 Minutes

Strain	Sample 1 Poisson's Ratio	Sample 2 Poisson's Ratio	Sample 3 Poisson's Ratio	Sample 4 Poisson's Ratio	Mean Poisson's Ratio
0	-	-	-	-	-
0.1	0.40	0.20	0.00	0.00	0.15
0.2	0.40	0.30	0.10	0.20	0.25
0.3	0.40	0.33	0.20	0.27	0.30
0.4	0.40	0.30	0.25	0.26	0.30
0.5	0.40	0.36	0.28	0.24	0.32
0.6	0.43	0.33	0.30	0.27	0.33
0.7	0.40	0.29	0.29	0.29	0.32
0.8	0.40	0.28	0.25	0.28	0.30
0.9	0.36	0.24	-	0.27	0.29
1	0.34	-	-	0.27	0.30

25 Minutes

Strain	Sample 1 Poisson's Ratio	Sample 2 Poisson's Ratio	Sample 3 Poisson's Ratio	Sample 4 Poisson's Ratio	Mean Poisson's Ratio
0	-	-	-	-	-
0.1	0.00	0.20	0.42	0.21	0.21
0.2	0.12	0.50	0.31	0.32	0.31
0.3	0.32	0.47	0.42	0.28	0.37
0.4	0.36	0.50	0.42	0.27	0.38
0.5	0.33	0.44	0.42	0.21	0.35
0.6	0.32	0.43	0.42	0.28	0.36
0.7	0.31	0.37	0.39	0.33	0.35
0.8	0.30	0.38	0.34	0.32	0.33
0.9	0.34	0.33	0.32	0.33	0.33
1	0.33	-	-	0.34	0.34

60 Minutes

Strain	Sample 1 Poisson's Ratio	Sample 2 Poisson's Ratio	Sample 3 Poisson's Ratio	Sample 4 Poisson's Ratio	Mean Poisson's Ratio
0	-	-	-	-	-
0.1	0.00	0.00	0.29	0.00	0.07
0.2	0.32	0.16	0.15	0.14	0.19
0.3	0.22	0.11	0.20	0.19	0.18
0.4	0.24	0.24	0.29	0.21	0.25
0.5	0.26	0.26	0.24	0.17	0.23
0.6	0.32	0.27	0.29	0.19	0.27
0.7	0.28	0.28	0.29	0.24	0.27
0.8	0.24	-	-	-	0.24
0.9	-	-	-	-	-
1	-	-	-	-	-

55 Minutes

Strain	Sample 1 Poisson's Ratio	Sample 2 Poisson's Ratio	Sample 3 Poisson's Ratio	Sample 4 Poisson's Ratio	Mean Poisson's Ratio
0	-	-	-	-	-
0.1	0.00	0.00	0.00	0.70	0.17
0.2	0.16	0.00	0.13	0.35	0.16
0.3	0.21	0.10	0.25	0.23	0.20
0.4	0.23	0.08	0.31	0.35	0.24
0.5	0.31	0.18	0.35	0.42	0.32
0.6	0.31	0.20	0.33	0.35	0.30
0.7	0.27	0.17	0.36	0.37	0.29
0.8	0.27	0.23	0.31	-	0.27
0.9	0.24	0.20	-	-	-
1	0.22	-	-	-	-

50 Minutes

Strain	Sample 1 Poisson's Ratio	Sample 2 Poisson's Ratio	Sample 3 Poisson's Ratio	Sample 4 Poisson's Ratio	Mean Poisson's Ratio
0	-	-	-	-	-
0.1	0.00	0.00	0.00	0.25	0.06
0.2	0.00	0.13	0.25	0.50	0.22
0.3	0.19	0.17	0.25	0.33	0.24
0.4	0.14	0.25	0.31	0.31	0.25
0.5	0.17	0.30	0.35	0.40	0.31
0.6	0.24	0.29	0.33	0.38	0.31
0.7	0.20	0.32	0.32	0.36	0.30
0.8	0.21	-	-	0.34	-
0.9	-	-	-	-	-
1	-	-	-	-	-

45 Minutes

Strain	Sample 1 Poisson's Ratio	Sample 2 Poisson's Ratio	Sample 3 Poisson's Ratio	Sample 4 Poisson's Ratio	Mean Poisson's Ratio
0	-	-	-	-	-
0.1	0.31	0.22	0.43	0.28	0.31
0.2	0.16	0.33	0.43	0.42	0.33
0.3	0.21	0.43	0.43	0.37	0.36
0.4	0.23	0.49	0.43	0.35	0.38
0.5	0.25	0.52	0.43	0.33	0.38
0.6	0.26	0.51	0.40	0.28	0.36
0.7	0.36	0.43	0.37	0.32	0.37
0.8	0.43	0.43	0.35	0.31	0.38
0.9	-	-	-	-	-
1	-	-	-	-	-

40 Minutes

Strain	Sample 1 Poisson's Ratio	Sample 2 Poisson's Ratio	Sample 3 Poisson's Ratio	Sample 4 Poisson's Ratio	Mean Poisson's Ratio
0	-	-	-	-	-
0.1	0.24	1.49	0.25	0.56	0.63
0.2	0.36	1.06	0.38	0.42	0.55
0.3	0.24	0.85	0.42	0.37	0.47
0.4	0.18	0.74	0.63	0.28	0.46
0.5	0.24	0.72	0.50	0.33	0.45
0.6	0.28	0.60	0.46	0.32	0.42
0.7	0.34	0.52	0.39	0.36	0.40
0.8	0.36	-	-	0.35	0.35
0.9	-	-	-	0.34	0.34
1	-	-	-	-	-

35 Minutes

Strain	Sample 1 Poisson's Ratio	Sample 2 Poisson's Ratio	Sample 3 Poisson's Ratio	Sample 4 Poisson's Ratio	Mean Poisson's Ratio
0	-	-	-	-	-
0.1	0.45	0.22	0.44	0.43	0.39
0.2	0.57	0.22	0.44	0.43	0.41
0.3	0.53	0.29	0.37	0.50	0.42
0.4	0.57	0.33	0.50	0.48	0.47
0.5	0.50	0.39	0.44	0.47	0.45
0.6	0.53	0.40	0.44	0.39	0.44
0.7	0.45	0.40	0.41	0.43	0.42
0.8	-	0.35	0.36	-	0.36
0.9	-	-	-	-	-
1	-	-	-	-	-

30 Minutes

Strain	Sample 1 Poisson's Ratio	Sample 2 Poisson's Ratio	Sample 3 Poisson's Ratio	Sample 4 Poisson's Ratio	Mean Poisson's Ratio
0	-	-	-	-	-
0.1	0.44	0.22	0.22	0.47	0.34
0.2	0.44	0.33	0.33	0.35	0.36
0.3	0.59	0.43	0.43	0.47	0.48
0.4	0.56	0.43	0.38	0.47	0.46
0.5	0.53	0.43	0.43	0.47	0.47
0.6	0.44	0.40	0.43	0.47	0.44
0.7	0.44	0.34	0.37	0.43	0.40
0.8	0.42	-	-	0.41	-
0.9	-	-	-	-	-
1	-	-	-	-	-

25 Minutes

Strain	Sample 1 Poisson's Ratio	Sample 2 Poisson's Ratio	Sample 3 Poisson's Ratio	Sample 4 Poisson's Ratio	Mean Poisson's Ratio
0	-	-	-	-	-
0.1	0.26	0.20	0.42	0.32	0.30
0.2	0.26	0.40	0.42	0.16	0.31
0.3	0.34	0.33	0.49	0.43	0.40
0.4	0.32	0.40	0.47	0.40	0.40
0.5	0.36	0.40	0.46	0.45	0.42
0.6	0.38	0.43	0.38	0.38	0.39
0.7	0.40	0.40	0.39	0.32	0.38
0.8	0.38	0.38	-	0.32	-
0.9	-	-	-	-	-
1	-	-	-	-	-

Table 4A.7: Raw data for Poisson's ratio latitudinal 45 PPI 4.88 volumetric compression ratio

60 Minutes

Strain	Sample 1 Poisson's Ratio	Sample 2 Poisson's Ratio	Sample 3 Poisson's Ratio	Sample 4 Poisson's Ratio	Mean Poisson's Ratio
0	-	-	-	-	-
0.1	0.33	-0.32	-0.60	-0.32	-0.23
0.2	0.00	-0.32	-0.45	-0.32	-0.27
0.3	-0.11	-0.32	-0.30	-0.32	-0.26
0.4	-0.17	-0.32	-0.30	-0.32	-0.28
0.5	-0.20	-0.26	-0.24	-0.32	-0.26

50 Minutes

Strain	Sample 1 Poisson's Ratio	Sample 2 Poisson's Ratio	Sample 3 Poisson's Ratio	Sample 4 Poisson's Ratio	Mean Poisson's Ratio
0	-	-	-	-	-
0.1	0.00	-0.30	0.00	0.00	-0.08
0.2	-0.17	-0.30	0.00	-0.15	-0.16
0.3	-0.22	-0.30	0.11	-0.10	-0.13
0.4	-0.17	-0.30	0.08	-0.08	-0.12
0.5	-0.13	-0.24	0.13	-0.06	-0.08

40 Minutes

Strain	Sample 1 Poisson's Ratio	Sample 2 Poisson's Ratio	Sample 3 Poisson's Ratio	Sample 4 Poisson's Ratio	Mean Poisson's Ratio
0	-	-	-	-	-
0.1	-0.61	0.00	0.24	-0.28	-0.16
0.2	-0.45	0.12	0.24	-0.28	-0.09
0.3	-0.30	0.17	0.24	-0.09	0.00
0.4	-0.15	0.25	0.24	0.00	0.08
0.5	0.00	0.25	0.24	0.11	0.15

30 Minutes

Strain	Sample 1 Poisson's Ratio	Sample 2 Poisson's Ratio	Sample 3 Poisson's Ratio	Sample 4 Poisson's Ratio	Mean Poisson's Ratio
0	-	-	-	-	-
0.1	0.00	0.00	0.00	0.00	0.00
0.2	0.16	0.15	0.31	0.14	0.19
0.3	0.21	0.19	0.41	0.19	0.25
0.4	0.16	0.22	0.39	0.21	0.24
0.5	0.19	0.23	0.44	0.17	0.26

Table 4A.8: Raw data for Poisson's ratio latitudinal 45 PPI 3.91 volumetric compression ratio

60 Minutes

Strain	Sample 1 Poisson's Ratio	Sample 2 Poisson's Ratio	Sample 3 Poisson's Ratio	Sample 4 Poisson's Ratio	Mean Poisson's Ratio
0	-	-	-	-	-
0.1	-0.33	-0.32	-0.31	-0.33	-0.33
0.2	-0.17	-0.32	-0.31	-0.33	-0.28
0.3	-0.22	-0.21	-0.31	-0.22	-0.24
0.4	-0.17	-0.16	-0.24	-0.17	-0.18
0.5	-0.13	-0.06	-0.19	-0.20	-0.15

50 Minutes

Strain	Sample 1 Poisson's Ratio	Sample 2 Poisson's Ratio	Sample 3 Poisson's Ratio	Sample 4 Poisson's Ratio	Mean Poisson's Ratio
0	-	-	-	-	-
0.1	0.00	0.00	-0.30	-0.33	-0.16
0.2	0.00	0.00	-0.30	-0.16	-0.12
0.3	0.00	0.00	-0.30	-0.11	-0.10
0.4	0.00	0.08	-0.15	-0.16	-0.06
0.5	-0.06	0.13	-0.12	-0.07	-0.03

40 Minutes

Strain	Sample 1 Poisson's Ratio	Sample 2 Poisson's Ratio	Sample 3 Poisson's Ratio	Sample 4 Poisson's Ratio	Mean Poisson's Ratio
0	-	-	-	-	-
0.1	-0.36	0.33	0.33	-0.34	-0.01
0.2	-0.18	0.17	0.16	-0.17	-0.01
0.3	-0.12	0.22	0.22	-0.11	0.05
0.4	-0.09	0.17	0.16	0.00	0.06
0.5	0.00	0.20	0.20	0.07	0.12

30 Minutes

Strain	Sample 1 Poisson's Ratio	Sample 2 Poisson's Ratio	Sample 3 Poisson's Ratio	Sample 4 Poisson's Ratio	Mean Poisson's Ratio
0	-	-	-	-	-
0.1	0.00	0.33	0.00	0.34	0.17
0.2	0.14	0.33	0.16	0.34	0.24
0.3	0.19	0.33	0.21	0.34	0.27
0.4	0.14	0.33	0.23	0.42	0.28
0.5	0.23	0.33	0.25	0.47	0.32

60 Minutes

Strain	Sample 1 Poisson's Ratio	Sample 2 Poisson's Ratio	Sample 3 Poisson's Ratio	Sample 4 Poisson's Ratio	Mean Poisson's Ratio
0	-	-	-	-	-
0.1	0.33	0.31	0.00	0.00	0.16
0.2	0.17	0.15	0.16	0.17	0.16
0.3	0.22	0.10	0.10	0.11	0.14
0.4	0.25	0.08	0.16	0.17	0.16
0.5	0.20	0.12	0.19	0.13	0.16

50 Minutes

Strain	Sample 1 Poisson's Ratio	Sample 2 Poisson's Ratio	Sample 3 Poisson's Ratio	Sample 4 Poisson's Ratio	Mean Poisson's Ratio
0	-	-	-	-	-
0.1	-0.33	0.00	-0.59	0.31	-0.15
0.2	0.00	-0.15	-0.15	0.16	-0.04
0.3	0.00	-0.21	0.00	0.11	-0.02
0.4	0.08	-0.08	0.15	0.16	0.08
0.5	0.13	0.00	0.18	0.19	0.12

40 Minutes

Strain	Sample 1 Poisson's Ratio	Sample 2 Poisson's Ratio	Sample 3 Poisson's Ratio	Sample 4 Poisson's Ratio	Mean Poisson's Ratio
0	-	-	-	-	-
0.1	0.33	0.32	0.00	0.34	0.25
0.2	0.50	0.16	0.15	0.17	0.25
0.3	0.44	0.22	0.31	0.11	0.27
0.4	0.50	0.24	0.39	0.17	0.33
0.5	0.47	0.26	0.37	0.28	0.34

30 Minutes

Strain	Sample 1 Poisson's Ratio	Sample 2 Poisson's Ratio	Sample 3 Poisson's Ratio	Sample 4 Poisson's Ratio	Mean Poisson's Ratio
0	-	-	-	-	-
0.1	0.00	0.00	0.31	0.30	0.15
0.2	0.50	0.00	0.31	0.15	0.24
0.3	0.56	0.11	0.21	0.10	0.25
0.4	0.50	0.17	0.23	0.23	0.28
0.5	0.47	0.20	0.25	0.30	0.31

Table 4A.10: Raw data for Poisson's ratio latitudinal 10 PPI 4.88 volumetric compression ratio

60 Minutes

Strain	Sample 1 Poisson's Ratio	Sample 2 Poisson's Ratio	Sample 3 Poisson's Ratio	Sample 4 Poisson's Ratio	Mean Poisson's Ratio
0	-	-	-	-	-
0.1	-0.29	-0.32	-0.62	-0.33	-0.39
0.2	-0.29	-0.32	-0.47	-0.17	-0.31
0.3	0.00	-0.32	-0.42	-0.11	-0.21
0.4	0.00	-0.24	-0.39	-0.08	-0.18
0.5	0.00	-0.19	-0.37	-0.07	-0.16

50 Minutes

Strain	Sample 1 Poisson's Ratio	Sample 2 Poisson's Ratio	Sample 3 Poisson's Ratio	Sample 4 Poisson's Ratio	Mean Poisson's Ratio
0	-	-	-	-	-
0.1	-0.33	-0.30	-0.29	0.00	-0.23
0.2	-0.33	-0.30	-0.43	-0.16	-0.30
0.3	-0.33	-0.20	-0.19	-0.21	-0.23
0.4	-0.33	-0.15	-0.07	-0.24	-0.20
0.5	-0.20	-0.18	0.00	-0.06	-0.11

40 Minutes

Strain	Sample 1 Poisson's Ratio	Sample 2 Poisson's Ratio	Sample 3 Poisson's Ratio	Sample 4 Poisson's Ratio	Mean Poisson's Ratio
0	-	-	-	-	-
0.1	0.32	0.33	0.32	0.30	0.32
0.2	0.32	0.33	0.16	0.30	0.28
0.3	0.32	0.33	0.21	0.30	0.29
0.4	0.32	0.33	0.24	0.30	0.30
0.5	0.32	0.33	0.26	0.30	0.30

30 Minutes

Strain	Sample 1 Poisson's Ratio	Sample 2 Poisson's Ratio	Sample 3 Poisson's Ratio	Sample 4 Poisson's Ratio	Mean Poisson's Ratio
0	-	-	-	-	-
0.1	0.33	0.31	0.31	0.00	0.24
0.2	0.33	0.31	0.31	0.16	0.28
0.3	0.33	0.31	0.31	0.22	0.29
0.4	0.33	0.31	0.31	0.24	0.30
0.5	0.33	0.31	0.31	0.26	0.30

Table 4A.11: Raw data for Poisson's ratio latitudinal 10 PPI 3.91 volumetric compression ratio

60 Minutes

	Sample 1	Sample 2	Sample 3	Sample 4	Mean
Strain	Poisson's Ratio	Poisson's Ratio	Poisson's Ratio	Poisson's Ratio	Poisson's Ratio
0	-	-	-	-	-
0.1	-0.64	-0.31	-0.33	0.00	-0.32
0.2	-0.48	-0.31	-0.33	-0.17	-0.32
0.3	-0.43	-0.31	-0.22	-0.11	-0.27
0.4	-0.32	-0.23	-0.25	-0.08	-0.22
0.5	-0.26	-0.19	-0.13	0.00	-0.14

50 Minutes

	Sample 1	Sample 2	Sample 3	Sample 4	Mean
Strain	Poisson's Ratio	Poisson's Ratio	Poisson's Ratio	Poisson's Ratio	Poisson's Ratio
0	-	-	-	-	-
0.1	-0.34	0.00	0.00	0.00	-0.08
0.2	-0.34	-0.34	0.14	0.00	-0.13
0.3	-0.22	-0.34	0.19	0.00	-0.09
0.4	-0.17	-0.34	0.21	0.08	-0.05
0.5	-0.07	-0.21	0.23	0.13	0.02

40 Minutes

	Sample 1	Sample 2	Sample 3	Sample 4	Mean
Strain	Poisson's Ratio	Poisson's Ratio	Poisson's Ratio	Poisson's Ratio	Poisson's Ratio
0	-	-	-	-	-
0.1	0.30	0.32	0.00	0.33	0.24
0.2	0.30	0.32	0.17	0.33	0.28
0.3	0.30	0.22	0.22	0.33	0.27
0.4	0.30	0.24	0.25	0.33	0.28
0.5	0.30	0.26	0.27	0.33	0.29

30 Minutes

	Sample 1	Sample 2	Sample 3	Sample 4	Mean
Strain	Poisson's Ratio	Poisson's Ratio	Poisson's Ratio	Poisson's Ratio	Poisson's Ratio
0	-	-	-	-	-
0.1	0.00	0.00	0.33	0.34	0.17
0.2	0.16	0.30	0.17	0.34	0.24
0.3	0.21	0.30	0.22	0.34	0.27
0.4	0.24	0.30	0.25	0.34	0.28
0.5	0.25	0.30	0.33	0.27	0.29

Table 4A.12: Raw data for Poisson's ratio latitudinal 10 PPI 2.93 volumetric compression ratio

60 Minutes

	Sample 1	Sample 2	Sample 3	Sample 4	Mean
Strain	Poisson's Ratio	Poisson's Ratio	Poisson's Ratio	Poisson's Ratio	Poisson's Ratio
0	-	-	-	-	-
0.1	-0.32	0.00	0.00	0.31	0.00
0.2	-0.16	0.17	0.00	0.31	0.08
0.3	-0.11	0.11	0.11	0.21	0.08
0.4	0.00	0.17	0.17	0.16	0.12
0.5	0.00	0.13	0.20	0.19	0.13

50 Minutes

	Sample 1	Sample 2	Sample 3	Sample 4	Mean
Strain	Poisson's Ratio	Poisson's Ratio	Poisson's Ratio	Poisson's Ratio	Poisson's Ratio
0	-	-	-	-	-
0.1	0.32	0.32	0.32	-0.33	0.16
0.2	0.16	0.16	0.16	0.00	0.12
0.3	0.11	0.11	0.22	0.00	0.11
0.4	0.16	0.08	0.24	0.00	0.12
0.5	0.13	0.13	0.32	0.07	0.16

40 Minutes

	Sample 1	Sample 2	Sample 3	Sample 4	Mean
Strain	Poisson's Ratio	Poisson's Ratio	Poisson's Ratio	Poisson's Ratio	Poisson's Ratio
0	-	-	-	-	-
0.1	0.30	0.00	0.00	0.00	0.08
0.2	0.30	0.17	0.17	0.00	0.16
0.3	0.30	0.22	0.22	0.11	0.21
0.4	0.23	0.33	0.17	0.16	0.22
0.5	0.24	0.33	0.27	0.19	0.26

30 Minutes

	Sample 1	Sample 2	Sample 3	Sample 4	Mean
Strain	Poisson's Ratio	Poisson's Ratio	Poisson's Ratio	Poisson's Ratio	Poisson's Ratio
0	-	-	-	-	-
0.1	0.33	0.00	0.33	0.00	0.17
0.2	0.17	0.16	0.33	0.16	0.21
0.3	0.22	0.33	0.33	0.22	0.27
0.4	0.25	0.33	0.41	0.25	0.31
0.5	0.27	0.39	0.39	0.26	0.33

Appendix 4B: Thermocouple graphs

a)

b)
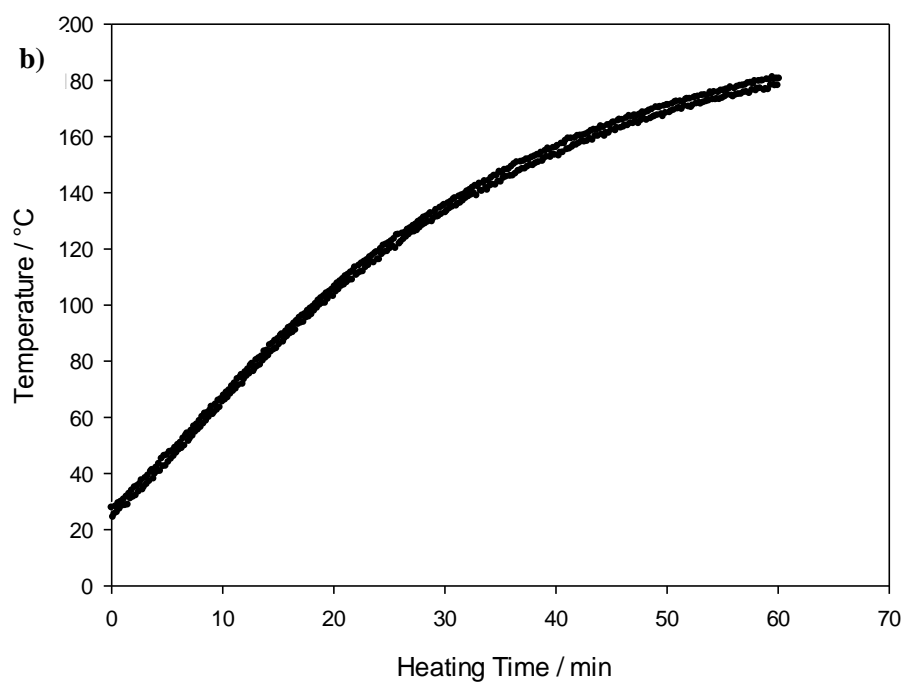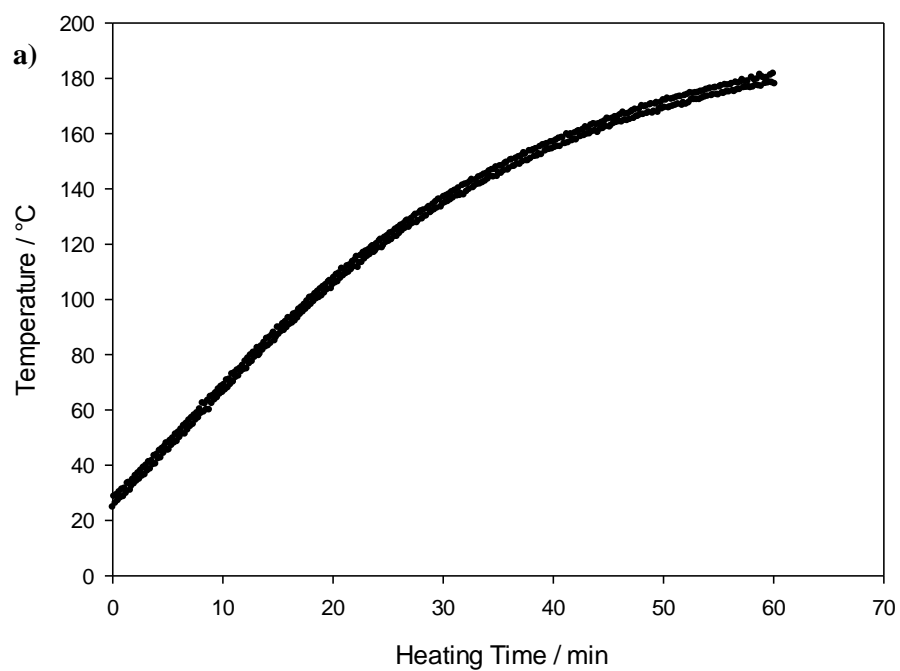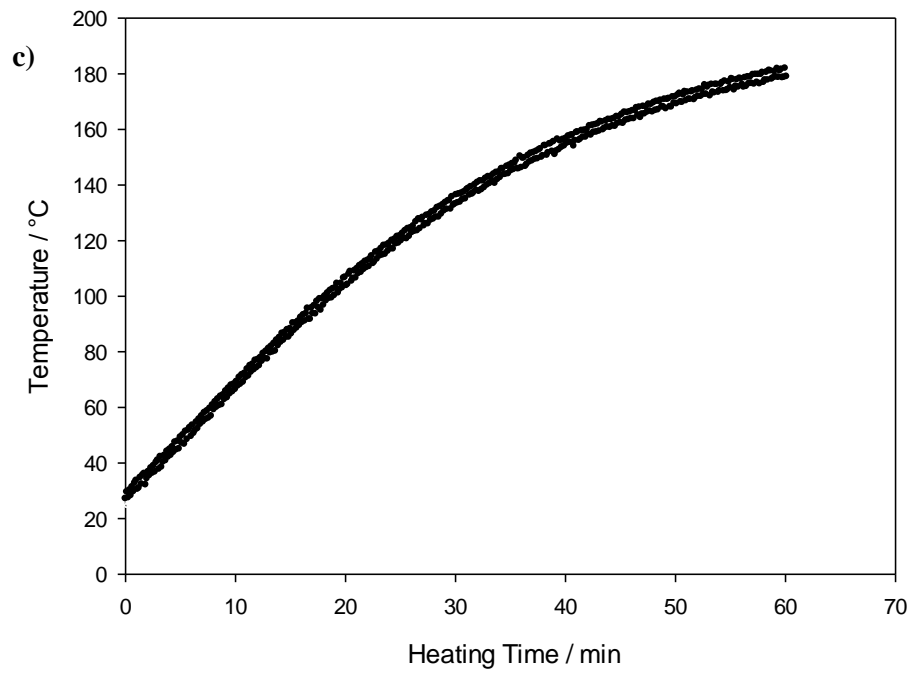
Figure 4B.1: Raw experimental thermocouple data for the 45 PPI foam compressed at a volumetric compression ratio of 4.88, where: **a)** sample 1, **b)** sample 2 and **c)** sample 3.

Appendix 5A: Calculating energy absorption from raw data

Although Figures 5.2 to 5.6 present the mean crater depths for each combination of the fabrication parameters (pore per inch, heating times, volume compression ratios and orientation), this is derived data. This appendix presents a worked example of calculating the crater depth and energy absorption from the raw data of the longitudinal 45 PPI 4.88 volumetric compression ratio, fabricated at a heating time of 60 minutes.

Measuring crater depth and energy absorption:

A Taicaan XYRIS 2000 surface profilometer was employed to measure the physical craters that resulted from impacting samples over a clay body. Unlike a physical surface profilometer, the Taicaan uses a triangulation laser sensor vertically aligned towards a surface at a standoff distance. To ensure that the maximum working range was utilised to capture the region of interest, a preliminary scan of the surface was undertaken at a Z height of 0. If the region of interest exceeded the working area, multiple scans were run then "stitched" together, where the starting position was set at initial values plus / minus the original Z height. After completing a scan, the specialist Taicaan software BODIES was then used to both measure the maximum and minimum height of the crater and calculate the volume of the crater.

Whilst measurement of the maximum and minimum height is easily obtained from the software (as shown in Figure 5A.1, where it can be see that the overall crate depth is 8.34, as given by the total overall range), the volume of the crater is calculated by normalizing the clay surface via a best fit plane.
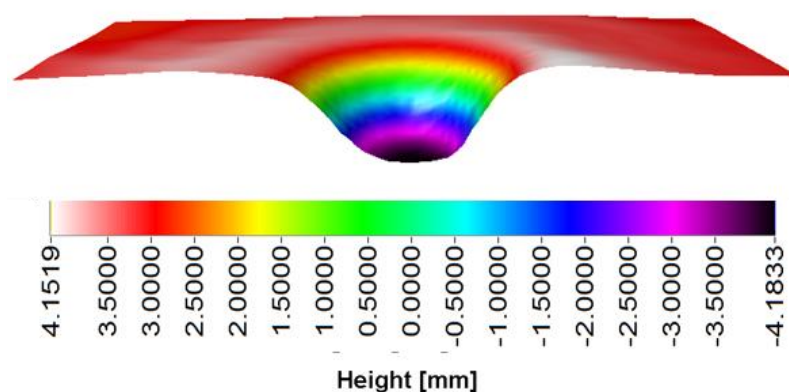
Figure 5A.1: Taicaan cross-sectional representation of Roma Plastilina No. 1 clay craters produced from the impact of an auxetic 45 PPI foam produced heated for 60 minutes at a volumetric compression ratio of 4.88.

In order to use the best fit plane with BODIES, three surface positions were required. To ensure that the effects of impact were kept to a minimum, these surface positions were taken from the far corners of the overall surface. Once applied, it is then possible for the software to calculate the volumes above and below the newly created normalised surface. As the clay is an incompressible material, it was imperative that both volume types are considered. Since the reference surface positions have the capacity to influence the normalised plane, four combinations of corner parameters were taken, and averaged to give an overall average surface volume. An example of the resulting datasets is as follows:

Table 5A.1: Table outlining normalised plane volume data

Volume Above				
Plane 1 / mm^3	Plane 2 / mm^3	Plane 3 / mm^3	Plane 4 / mm^3	Above Average / mm^3
2094.8	1978.1	1965.0	2094.2	2033.0
Volume Below				
Plane 1 / mm^3	Plane 2 / mm^3	Plane 3 / mm^3	Plane 4 / mm^3	Below Average / mm^3
2471.2	2502.9	2514.1	2502.6	2497.7
Volume Total				
Plane 1 / mm^3	Plane 2 / mm^3	Plane 3 / mm^3	Plane 4 / mm^3	Volume Average / mm^3
4566.0	4481.0	4479.2	4596.8	4530.8

Once the average volume had been calculated, this value was then multiplied by an energy constant that was obtained by dividing the average volume of a calibration impact by the potential energy of the drop tower. By multiplying the average volume by the energy constant, to total energy absorbed by the crater can be calculated. Finally to calculate the energy absorbed by the sample, the energy absorbed by the crater was subtracted from the potential energy to give the energy absorbed by the foam samples. An example of a complete dataset is shown below.

Table 5A.2: Table energy absorption

	Volume Average / mm^3	Energy Absorbed by Crater / J	Energy Absorbed by Foam / J
Sample 1	2755.2	4.5	2.9
Sample 2	3104.0	5.0	2.3
Sample 3	2720.9	4.8	2.5
Sample 4	3121.0	5.5	1.8

References

1.   British Army. *Combat Body Armour,* 2014 [cited 2015 21/01/2015]. Available from: http://www.army.mod.uk/equipment/23216.aspx.

2.   Dawson, D. *Army to Field Improved Body Armor.* 2007 [cited 2015 21/01/2015]. Available from: http://www.army.mil/article/2497/army-to-field-improved-body-armor/.

3.   Cannon, L. *Behind Armour Blunt Trauma-An Emerging Problem*, Journal of the Royal Army Medical Corps. 2001 2001;147(1):87-96.

4.   Cronin, D. S., Worswick, M. J., Ennis, A. V., Bourget, D., Williams, K. V., Pageau, G., editors. *Behind Armour Blunt Trauma for Ballistic Impacts on Rigid Body Armour*. 19th International Symposium of Ballistics. 2001. Switzerland: Vulnerability Modelling and Wound Ballistics.

5.   Shen, W., Niu, Y., Bykanova, L., Laurence, P., Link, N. *Characterizing The Interaction Among Bullet, Body Armor, And Human And Surrogate Targets*, Journal of biomechanical engineering. 2010 Dec;132(12):121001.

6.   Tan, V. B. C., Lim, C. T., Cheong, C. H. *Perforation Of High-Strength Fabric By Projectiles Of Different Geometry*, International Journal of Impact Engineering. 2003 Feb;28(2):207-22.

7.   US-Army. *Testing Of Body Armour Materials: Phase iii.* Washington DC, New York: US Army, Defence Do; 2012 ISBN: 978-0-309-25599-8.

8.   Mukasey, M. B., Sedgwick, J. L., Hagy, D. W. *Ballistic Resistance Of Body Armour NIJ Standard-0101.06*. National Institute of Justice, 2006 2008. Report No.

9.   Evans, K. E., Nkansah, M. A., Hutchinson, I. J., Rogers, S. C. *Molecular Network Design*, Nature. 1991;353(6340):124-.

10.   Choi, J. B., Lakes, R. S. *Design of a Fastener Based on Negative Poisson's Raio*, Cellular Polymers. 1991;10(3):205-12.

11.   Lakes, R. S. *Design Considerations for Materials with Negative Poisson's Ratios*, Journal of Mechanical Design. 1993 Dec;115(4):696-700.

12.   Evans, K. E., Alderson, A. *Auxetic Materials: Functional Materials and Structures from Lateral Thinking!*, Advanced Materials. 2000, 12(9):617-28.

13.   Chan, N., Evans, K. E. *Fabrication Methods for Auxetic Foams*, Journal of Material Science. 1997;32(22):5945-53.

14.   Lakes, R. *Deformation Mechanisms in Negative Poisson's Ratio Materials: Structural Aspects*, Journal of Material Science. 1991 May;26(9):2287-92.

15.   Scarpa, F., Tomlin, P. J. *On the Transverse Shear Modulus of Negative Poisson's Ratio Honeycomb Structures*, Fatigue & Fracture of Engineering Materials. 2000 Aug;23(8):717-20.

16.   Lakes, R. *New Materials - No Contractile Obligations*, Nature. 1992 Aug;358(6389):713-4.

17.   Friis, E. A., Lakes, R. S., Park, J. B. *Negative Poisson Ratio Polymeric and Metallic Foams* Journal of Material Science. 1988 Dec;23(12):4406-14.

18.   Scarpa, F., Yates, J. R., Ciffo, L. G., Patsias, S. *Dynamic Crushing of Auxetic Open-Cell Polyurethane Foam*, Proceedings of the Institution of Mechanical Engineers, Part C - Journal of Mechanical Engineering Science 2002;216(12):1153-6.

19.   Alderson, A. *A Triumph of Lateral Thought*, Chemistry and Industry. 1999 May(10):384 - 91.

20.   Lakes, R. S., Elms, K. *Indentability of Conventional and Negative Poisson's Ratio Foams*, Journal of Composite Materials. 1993;27(12):1193-202.

21.   Smith, C. W., Lehman, F., Wootton, R. J., Evans, K. E. *Strain Dependent Densification During Indentation in Auxetic Foams*, Cellular Polymers Journal. 1999;18(2):79-101.

22.   Bezazi, A., Scarpa, F. *Tensile Fatigue of Conventional and Negative Poisson's Ratio Open-Cell PU Foams*, International Journal of Fatigue. 2009 Mar;31(3):488-94.

23.   Bezazi, A., Scarpa, F. *Mechanical Behaviour of Conventional and Negative Poisson's Ratio Thermoplastic Polyurethane Foams Under Compressive Cyclic Loading*, International Journal of Fatigue. 2007 May;29(5):922-30.

24.   Scarpa, F., Pastorino, P., Garelli, A., Patsias, S., Ruzzene, A. *Auxetic Compliant Flexible PU Foams: Static and Dynamic Properties*, Phys Status Solidi B-Basic Solid State Phys. 2005 Mar;242(3):681-94.

25.   Scarpa, F., Bullough, W. A., Lumley, P. *Trends in Acoustic Properties of Iron Particle Seeded Auxetic Polyurethane Foam*, Proceedings of the Institution of Mechanical Engineers Part C - Journal of Mechanical Engineering Science. 2004 Feb;218(2):241-4.

26.   Scarpa, F., Smith, F. C. *Passive and MR Fluid-Coated Auxetic PU Foam - Mechanical, Acoustic, and Electromagnetic Properties*, Journal of Intelligent Material Systems and Structures. 2004 Dec;15(12):973-9.

27.   David, N. V., Gao, X. L., Zheng, J. Q. *Ballistic Resistant Body Armor: Contemporary and Prospective Materials and Related Protection Mechanisms*, Applied Mechanics Reviews. 2009 Sep;62(5).

28.   Starley, D. *Determining the technological origins of iron and steel*, Journal of Archaeological Science . 1999 Aug;26(8):1127-33.

29.   Merkle, A. C., Ward, E. E., O'Connor, J. V., Roberts, J. C. *Assessing behind armor blunt trauma (BABT) under NIJ Standard-0101.04 conditions using human torso models*, Journal of Trauma and Acute Care Surgery. 2008 Jun;64(6):1555-61.

30.   Mahoney, P. F., Ryan, J., Brooks, A. J., Schwab, C. W. *Ballistic Trauma: A Practical Guide.* Springer; 2005.

31.   Jacobs, M. J. N., Van Dingenen, J. L. J. *Ballistic Protection Mechanisms In Personal Armour*, Journal of Materials Science. 2001 Jul;36(13):3137-42.

32.   Kaufmann, C., Cronin, D., Worswick, M., Pageau, G., Beth, A. *Influence Of Material Properties On The Ballistic Performance Of Ceramics For Personal Body Armour*, Shock and Vibration. 2003;10(1):51-8.

33.   Sonden, A., Rocksen, D., Riddez, L., Davidsson, J., Persson, J. K., Gryth, D., Bursell, J., Arborelius, U. P. *Trauma Attenuating Backing Improves Protection Against Behind Armor Blunt Trauma*, Journal of Trauma and Acute Care Surgery. 2009 Dec;67(6):1191-9.

34.   Ouellet, S., Cronin, D. S., Doman, D., Bourget, D., Worswick, M. J., *Parametric Study Of An Anti-Trauma Layer To Reduce BABT*. Personal Armor Systems Symposium; 2004 September 6–10; The Hague, The Netherlands.

35.   Peleg, K., Rivkind, A., Aharonson-Damel, L., Israeli Trauma, G. *Does body armor protect from firearm injuries?*, Journal of the American College of Surgeons. 2006 Apr;202(4):643-8.

36.   Kosashvili, Y., Hiss, J., Davidovic, N., Lin, G., Kalmovic, B., Melamed, E., Levy, Y., Blumenfeld, A. *Influence of personal armor on distribution of entry wounds: Lessons learned from urban-setting warfare fatalities*, Journal of Trauma and Acute Care Surgery. 2005 Jun;58(6):1236-40.

37.   History-of-Armor. *History of Armour* 2011 [cited 2012 19/06/2012]. Available from: http://www.history-of-armor.com/.

38.   U.S. Department of Justice. *Selection and Application Guide to Personal Body Armour*. In: Defence Do, editor. https://www.ncjrs.gov/pdffiles1/nij/189633.pdf: The National Institute of Justice's National Law Enforcement and Corrections Technology Center; 2001.

39.   Gao, X. L., Mall, S. *A Two Dimensional Rule-Of-Mixtures Micromechanics Model For Woven Fabric Composites*, Journal of Composites Technology and Research. 2000 Apr;22(2):60-70.

40.   Tan, V. B. C., Tay, T. E., Teo, W. K. *Strengthening Fabric Armour With Silica Colloidal Suspensions*, International Journal of Solids and Structures. 2005 Mar;42(5-6):1561-76.

41.   Ulven, C., Vaidya, U. K., Hosur, M. V. *Effect Of Projectile Shape During Ballistic Perforation Of Vartm Carbon/Epoxy Composite Panels*, Composite Structures. 2003 Jul-Aug;61(1-2):143-50.

42.   Cheeseman, B. A., Bogetti, T. A. *Ballistic Impact Into Fabric And Compliant Composite Laminates*, Composite Structures. 2003 Jul-Aug;61(1-2):161-73.

43.   Barauskas, R., Abraitiene, A. *Computational Analysis of Impact of a Bullet Against the MultilayerFabrics in LS-DYNA*, International Journal of Impact Engineering. 2007 Jul;34(7):1286-305.

44.   Shim, V. P. W., Zeng, X. S., Tan, V. B. C. *Influence Of Boundary Conditions On The Ballistic Performance Of High-Strength Fabric Targets*, International Journal of Impact Engineering. 2005 Dec.;32(1-4):631-42.

45.   Nadler, B., Steigmann, D. J. *A Model For Frictional Slip In Woven Fabrics*, C R Mec. 2003 Dec;331(12):797-804.

46.   Duan, Y., Keefe, M., Bogetti, T. A., Cheeseman, B. A. *Modeling The Role Of Friction During Ballistic Impact Of A High-Strength Plain-Weave Fabric*, Composite Structures. 2005 May;68(3):331-7.

47.   Zeng, X. S., Tan, V. B. C., Shim, V. P. W. *Modelling Inter-Yarn Friction In Woven Fabric Armour*, International Journal for Numerical Methods in Engineering. 2006 May;66(8):1309-30.

48.   Lyons, J. *Impact Phenomena In Textiles*. MIT Press: MIT Press; 1962. p. 239.

49.   Shim, V. P. W., Tan, V. B. C., Tay, T. E. *Modeling Deformation And Damage Characteristics Of Woven Fabric Under Small Projectile Impact*, International Journal of Impact Engineering. 1995 Aug;16(4):585-605.

50.   Roylance, D. *Stress Wave-Propagation In Fibers - Effect Of Crossovers*, Fibre Science & Technology. 1980;13(5):385-95.

51.   Lee, B. L., Walsh, T. F., Won, S. T., Patts, H. M., Song, J. W., Mayer, A. H. *Penetration Failure Mechanisms Of Armor-Grade Fiber Composites Under Impact*, Journal of Composite Materials. 2001;35(18):1605-33.

52.   Cunniff, P. M. *An Analysis Of The System Effects In Woven Fabrics Under Ballistic Impact*, Textile Research Journal. 1992 Sep;62(9):495-509.

53.   Roylance, D., Wang, S. S. *Penetration Mechanics Of Textile Structures - Influence Of Nonlinear Viscoelastic Relaxation*, Polymer Engineering & Science. 1978;18(14):1068-72.

54.   Field, J. E., Sun, Q. *A High-Speed Photographic Study Of Impact On Fibers And Woven Fabrics*. Bellingham: Spie - International Society for Optical Engineering; 1991. 703-12 p.

55.   Prosser, R. A., Cohen, S. H., Segars, R. A. *Heat As A Factor In The Penetration Of Cloth Ballistic Panels By 0.22 Caliber Projectiles*, Textile Research Journal. 2000 Aug;70(8):709-22.

56.   Laible, R. C. *Ballistic Materials And Penetration Mechanics* .New York: Elsevier Scientific Publishing Company; 1980, 297.

57.   Roylance, D., Wilde, A., Tocci, G. *Ballistic Impact Of Textile Structures*, Textile Research Journal. 1973;43(1):34-41.

58.   Chitrangad, *Hybrid Ballistic Fabric*. United States patent US 5187003 A. 1993.

59.   Montgomery, T. G., Grady, P. L., Tomasino, C. *The Effects of Projectile Geometry on the Performance of Ballistic Fabrics*, Textile Research Journal. 1982 July 1, 1982;52(7):442-50.

60.   Kirkland, K. M., Tam, T. Y., Weedon, G. C. *New Third-Generation Protective Clothing From High-Performance Polyethylene Fiber From Knives To Bullets*. ACS Symposium Series.1991. p. 214-37.

61.   Lee, B. L., Song, J. W., Ward, J. E. *Failure Of Spectra(R) Polyethylene Fiber-Reinforced Composites Under Ballistic Impact Loading*, Journal of Composite Materials. 1994;28(13):1202-26.

62.   Walsh, T.F, Lee, B.L. Song, J.W, . *Penetration Failure Mechanisms Of Woven Textile Composites*. Proceedings of the American Society for Composites 11th Technical Conference; 7–9 October 1996; Atlanta, Georgia. p. 979–88.

63.   Firstdefence. Kevlar vs Spectra Shield [cited 2015 19/01/2015]. Available from: http://www.firstdefense.com/html/vest_kevlar_vs_spectra.htm.

64.   Saertex.com. ondulierte. [cited 2015 19/01/2015]. Available from: http://wwwsaertexcom/fileadmin/user_upload/Produkt_Technik/Produkte/ondulierte_egif.

65.   Freeston, W. D., Claus, W. D. *Strain-Wave Reflections During Ballistic Impact of Fabric Panels*, Textile Research Journal. 1973 June 1, 1973;43(6):348-51.

66.   Ting, C., Ting, J., Cunniff, P., Roylance, D. *Numerical Characterization Of The Effects Of Transverse Yarn Interaction On Textile Ballistic Response*. International Sampe Technical Conference Series. 30. Covina: Soc Advancement Material & Process Engineering; 1998. p. 57-67.

67.   Cunniff, P. M., *Decoupled Response Of Textile Body Armour*. 18th International Symposium on Ballistics; 15 - 19 November; San Antonio, Texas. Proceedings of the 18th International Symposium on Ballistics1999. p. 814–21.

68.   Larsson, F., Svensson, L. *Carbon, Polyethylene And PBO Hybrid Fibre Composites For Structural Lightweight Armour*, Composites Part A: Applied Science and Manufacturing . 2002;33(2):221-31.

69.   Iremonger, M. J., Went, A. C. *Ballistic Impact Of Fibre Composite Armours By Fragment-Simulating Projectiles*, Composites Part A: Applied Science and Manufacturing . 1996;27(7):575-81.

70.   Scott, B. R. *The Penetration Of Compliant Laminates By Compact Projectiles*. 18th International Symposium on Ballistics; 15–19 November 1999; San Antonio, Texas1999. p. 1184-91.

71.   Briscoe, B. J., Motamedi, F. *The Ballistic Impact Characteristics Of Aramid Fabrics - The Influence Of Interface Friction*, Wear. 1992 Oct;158(1-2):229-47.

72.   Bazhenov, S. *Dissipation Of Energy By Bulletproof Aramid Fabric*, Journal of Materials Science. 1997 Aug;32(15):4167-73.

73.   Lim, C. T., Tan, V. B. C., Cheong, C. H. *Perforation Of High-Strength Double-Ply Fabric System By Varying Shaped Projectiles*, International Journal of Impact Engineering. 2002 Jul;27(6):577-91.

74.   Martinez, M. A., Navarro, C., Cortes, R., Rodriguez, J., Sanchezgalvez, V. *Friction And Wear Behavior Of Kevlar Fabrics*, Journal of Materials Science. 1993 Mar;28(5):1305-11.

75.   Carr, D. J. *Failure Mechanisms Of Yarns Subjected To Ballistic Impact*, Journal of Materials Science. 1999 Apr;18(7):585-8.

76.   Mitchell, C. A., Carr, D. J. *Post Failure Examination Of A New Body Armour Textile By The Use Of An Environmental Scanning Electron Microscope*. Electron Microscopy and Analysis 1999. Institute of Physics Conference Series. Bristol: Iop Publishing Ltd; 1999. p. 103-6.

77.   Iremonger, M. J., *Polyethylene Composites For Protection Against High Velocity Small Arms Bullets*. 18th International Symposium on Ballistics; 15–19 November 1999; San Antonio, Texas. Proceedings of the 18th International Symposium on Ballistics1999. p. 946–53.

78.   Susich, G., Dogliotti, L. M., Wrigley, A. S. *Microscopical Study of a Multilayer Nylon Body Armor Panel After Impact*, Textile Research Journal. 1958 May 1, 1958;28(5):361-77.

79.   Prevorsek, D. C., Kwon, Y. D., Chin, H. B. *Analysis Of The Temperature Rise In The Projectile And Extended-Chain Polyethylene Fiber-Composite Armor During Ballistic Impact And Penetration*, Polymer Engineering & Science. 1994 Jan;34(2):141-52.

80.   Desper, C. R., Cohen, S. H., King, A. O. *Morphological Effects Of Ballistic Impact On Fabrics Of Highly Drawn Polyethylene Fibers*, Journal of Applied Polymer Science. 1993 Feb;47(7):1129-42.

81.   Lin, L. C., Bhatnagar, A., Lang, D. C., Chang, H. W., *Comparison Of Ballistic Performance Of Composites*. 33rd International SAMPE Symposium; 7–10 March 1988; Anaheim, California. Proceedings of the 33rd International SAMPE Symposium1988. p. 883–9.

82.   Zhang, X., Mai, Y.W. *Damage Wave Propagation in Elastic-brittle Materials*. In: Wang R, editor. IUTAM Symposium on Rheology of Bodies with Defects. Solid Mechanics and its Applications. 64: Springer Netherlands; 2002. p. 179-90.

83.   Riou, P., Denoual, C., Cottenot, C. E. *Visualization Of The Damage Evolution In Impacted Silicon Carbide Ceramics*, International Journal of Impact Engineering. 1998 Apr;21(4):225-35.

84.   Nemat-Nasser, S., Sarva, S., McGee, J., Isaacs, J. *The Effect Of Thin Membrane Restraint On The Ballistic Performance Of Armor Grade Ceramic Tiles*, International Journal of Impact Engineering. 2007 Feb.;34(2):277-302.

85.   LaSalvia, J. C., Horwath, E. J., Rapacki, E. J., James Shih, C., Meyers, M. A. *Microstructural and Micromechanical Aspects of Ceramic/Long-Rod Projectile Interactions: Dwell/Penetration Transitions*. Explomet 2000; Albuquerque, New Mexico, USA: Elsevier Science, New York; 2001. p. 437-46.

86.   Normandia, M. J. *Impact Response And Analysis Of Several Silicon Carbides*, International Journal of Applied Ceramic Technology. 2004;1(3):226-34.

87.   Doyoyo, M. *Experiments On The Penetration Of Thin Long-Rod Projectiles Into Thick Long-Cylindrical Borosilicate Targets Under Pressure-Free Polycarbonate, Aluminum And Steel Confinements*, International Journal of Solids and Structures. 2003 Oct;40(20):5455-75.

88.   LaSalvia, J. C., Normandia, M. J., Miller, H. T., Mackenzie, D. E. *Sphere Impact Induced Damage in Ceramics: I. Armor-grade SiC and TiB 2*, Ceramic Engineering and Science Proceedings. 2005 2005;26(7):171-81.

89.   Chen, M. W., McCauley, J. W., Hemker, K. J. *Shock-Induced Localized Amorphization In Boron Carbide*, Science. 2003 Mar;299(5612):1563-6.

90.   Woodward, R. L., Baxter, B. J. *Ballistic Evaluation Of Ceramics - Influence Of Test Conditions*, International Journal of Impact Engineering. 1994 Apr;15(2):119-24.

91.   den Reijer, P. C. *Impact on Ceramic Faced Armour*: PhD Thesis. Technische University Delft (Netherlands); 1991.

92.   Shockey, D. A., Marchand, A. H., Skaggs, S. R., Cort, G. E., Burkett, M. W., Parker, R. *Failure Phenomenology Of Confined Ceramic Targets And Impacting Rods*. Ceramic Armor Materials by Design. Ceramic Transactions. 134. Westerville: Amer Ceramic Soc; 2002. p. 385-402.

93.   Wilkins, M. L. *Mechanics Of Penetration And Perforation*, International Journal of Engineering Science. 1978;16(11):793-807.

94.   Sternberg, J. *Material Properties Determining The Resistance Of Ceramics To High-Velocity Penetration*, Journal of Applied Physics. 1989 May;65(9):3417-24.

95.   Rosenberg, Z., Bless, S. J., Brar, N. S. *On The Influence Of The Loss Of Shear-Strength On The Ballistic Performance Of Brittle Solids*, International Journal of Impact Engineering. 1990;9(1):45-9.

96.   Hanlon, E., Gillich, P. *Origin of the 44-mm Behind-Armor Blunt Trauma Standard*, Milit Med. 2012 Mar;177(3):333-9.

97.   Montanarelli, N., Hawkins, C., Goldfarb, M., Ciurej, T., *Protective Garments for Public Official*. US Army Land Warfare Laboratory, 1973 Contract No.: AD A089163.

98.   Shepard, G. H., Ferguson, J. L., Foster, J. H. *Pulmonary contusion*, The Annals of thoracic surgery. 1969 Feb;7(2):110-9.

99.   U.S. Congress,. *Police Body Armor Standards and Testing, Volume II: Appendices*. Washington, DC: U.S. Government Printing Office1992.

100.   Cooper, G. J., Taylor, D. E. *Biophysics Of Impact Injury To The Chest And Abdomen*, Journal of the Royal Army Medical Corps. 1989 1989;135(2):58-67.

101.   Langdon. M. G., *Requirements For Minimising Thoracic Injury In Side Impact Experiments*. International Research Committee on the Biokinetics of Impacts (IRCOBl); 1986; Zurich.

102.   Van Bree J.L.M.J., van der Heiden, N., *Behind Armour Pressure Profiles In Tissue Simulant*. Proceedings of the Personal Armour Systems Symposium; 1996 3-6 Sep 1996; Colchester, UK.

103.   Lakes, R. *Foam Structures with a Negative Poisson's Ratio*, Science. 1986 Feb;235(4792):1038-40.

104.   Love, A. E. H., *A Treatise on the Mathematical Theory of Elasticity*: Dover Publications; 1927.

105.   McClintock, F. A., Argon, A. S. *Mechanical Behaviour of Materials*: Addison-Wesley; 1966.

106.   Bianchi, M., Scarpa, F. L., Smith, C. W. *Stiffness and Energy Dissipation in Polyurethane Auxetic Foams*, Journal of Materials Science. 2008 Sep;43(17):5851-60.

107.   Bianchi, M., Scarpa, F., Smith, C. W. *Shape Memory Behaviour in Auxetic Foams: Mechanical Properties*, Acta Materialia. 2010 Feb;58(3):858-65.

108.   Evans, K. E. *Auxetic Polymers - A New Range of Materials*, Endeavour. 1991;15(4):170-4.

109.   Caddock, B. D., Evans, K. E. *Microporous Materials with Negative Poisson's ratios. I. Microstructure and Mechanical Properties*, Journal of Physics D: Applied Physics. 1989;22(12):1877.

110.   Yeganeh-Haeri, A., Weidner, D. J., Parise, J. B. *Elasticity of agr-Cristobalite: A Silicon Dioxide with a Negative Poisson's Ratio*, Science. 1992 Jul 31;257(5070):650-2.

111.   Veronda, D. R., Westmann, R. A. *Mechanical Characterization of Skin—Finite Deformations*, Journal of Biomechanics.3(1):123-4.

112.   Lees, C., Vincent, J. F., Hillerton, J. E. *Poisson's Ratio In Skin*, Bio-medical materials and engineering. 1991;1(1):19-23.

113.   Ravirala, N., Alderson, A., Alderson, K. L. *Interlocking Hexagons Model for Auxetic Behaviour*, Journal of Materials Science. 2007 Sep;42(17):7433-45.

114.   Yang, W., Li, Z. M., Shi, W., Xie, B. H., Yang, M. B. *On Auxetic Materials*, Journal of Materials Science. 2004 May;39(10):3269-79.

115.   Andersson, A., Lundmark, S., Magnusson, A., Maurer, F. H. J. *Shear Behavior of Flexible Polyurethane Foams Under Uniaxial Compression*, Journal of Applied Polymer Science. 2009;111(5):2290-8.

116.   Stott, P. J., Mitchell, R., Alderson, K. L., Alderson, A. *Auxetic Materials - Applications: Azom & Materials World*; 2000 [cited 2010 25/06/2010]. Available from: http://www.azom.com/details.asp?ArticleID=168.

117.   Evans, K. E., Alderson, K. L. *Auxetic Materials: The Positive Side of Being Negative*, Engineering Science and Education Journal. 2000;9(4):148-54.

118.   Stavroulakis, G. E. *Auxetic Behaviour: Appearance and Engineering Applications*, Phys Status Solidi B-Basic Solid State Phys. 2005 Mar;242(3):710-20.

119.   Liu, Q. *Literature Review: Materials with Negative Poisson's Ratios and Potential Applications to Aerospace and Defence*. Victoria, Australia: Defence Science and Technology Organisation, 2006 Contract No.: DSTO-GD-0472.

120.   Alderson, A., Alderson, K. L. *Auxetic Materials*, Proceedings of the Institution of Mechanical Engineers Part G: Journal of Aerospace Engineering. 2007 Aug;221(G4):565-75.

121.   Liu, Y. P., Hu, H. *A Review on Auxetic Structures and Polymeric Materials*, Scientific Research and Essays. 2010;5(10):1052-63.

122.   Prawoto, Y. *Seeing Auxetic Materials From The Mechanics Point Of View: A Structural Review On The Negative Poisson's Ratio*, Computational Materials Science. 2012 Jun;58:140-53.

123.   Greaves, G. N., Greer, A. L., Lakes, R. S., Rouxel, T. *Poisson's Ratio And Modern Materials*, Nat Mater. 2011;10(11):823-37.

124.   Elipe, J. C. A., Lantada, A.D. *Comparative Study Of Auxetic Geometries By Means Of Computer-Aided Design And Engineering*, Smart Materials and Structures. 2012;21.

125.   Alderson, A. *Auxetic Materials: Stretching the Imagination. Chemistry and Industry*. 2011:18-20.

126.   Kolpakov, A. G. *Determination Of The Average Characteristics Of Elastic Frameworks*, Applied Mathematics and Mechanics. 1985 1985;49(6):739-745745.

127.   Gaspar, N. *A Granular Material With A Negative Poisson's Ratio*, Mechanics of Materials. 2010;42(7):673-7.

128.   Smith, C. W., Grima, J. N., Evans, K. E. *A Novel Mechanism for Generating Auxetic Behaviour in Reticulated Foams: Missing Rib Foam Model*, Acta Materialia. 2000 Nov;48(17):4349-56.

129.   Scarpa, F., Ciffo, L. G., Yates, J. R. *Dynamic Properties of High Structural Integrity Auxetic Open Cell Foam*, Smart Mater Structures. 2003 Feb;13(1):49-56.

130.   Bianchi, M., Scarpa, F., Smith, C. W., Whittell, G. R. *Physical and Thermal Effects on the Shape Memory Behaviour of Auxetic Open Cell Foams*, Journal of Materials Science. 2010 Jan;45(2):341-7.

131.   Choi, J. B., Lakes, R. S. *Non-Linear Properties of Polymer Cellular Materials With a Negative Poisson's Ratio*, Journal of Materials Science. 1992 Sep;27(17):4678-84.

132.   McDonald, S. A., Ravirala, N., Withers, P. J., Alderson, A. *In-Situ Three-Dimensional X-ray Microtomography of an Auxetic Foam Under Tension*, Scripta Materialia. 2009 Feb;60(4):232-5.

133.   Cadamagnani, F., Frontoni, S., Bianchi, M., Scarpa, F. *Compressive Uniaxial Properties of Auxetic Open cell PU based foams*, Phys Status Solidi B-Basic Solid State Phys. 2009 Sep;246(9):2118-23.

134.   Wang, Y. C., Lakes, R., Butenhoff, A. *Influence of Cell Size on Re-Entrant Transformation of Negative Poisson's Ratio Reticulated Polyurethane Foams*, Cellular Polymers Journal. 2001;20(6):373-85.

135.   Alderson, K., Alderson, A., Ravirala, N., Simkins, V., Davies, P. *Manufacture And Characterisation Of Thin Flat And Curved Auxetic Foam Sheets*, physica status solidi (b). 2012;249(7):1315-21.

136.   Grima, J. N., Attard, D., Gatt, R., Cassar, R. N. *A Novel Process for the Manufacture of Auxetic Foams and for Their Re-Conversion to Conventional Form*, Advanced Engineering Materials. 2009 Jul;11(7):533-5.

137.   Lisiecki, J., Błażejewicz, T., Kłysz, S., Gmurczyk, G., Reymer, P., Mikułowski, G. *Tests Of Polyurethane Foams With Negative Poisson's Ratio*, physica status solidi (b). 2013;250(10):1988-95.

138.   Bianchi, M., Scarpa, F., Banse, M., Smith, C. W. *Novel Generation of Auxetic Open Cell Foams for Curved and Arbitrary Shapes*, Acta Materialia. 2011;59(2):686-91.

139.   Bianchi, M., Frontoni, S., Scarpa, F., Smith, C. W. *Density Change During the Manufacturing Process of PU-PE Open Cell Auxetic Foams*, physica status solidi (b). 2011;248(1):30-8.

140.   Gibson, I., Rosen, D. W., Stucker, B. *Additive Manufacturing Technologies: Rapid Prototyping to Direct Digital Manufacturing*. Springer New York: Springer; 2010 2010.

141.   Wong, K. V., Hernandez, A. *A Review of Additive Manufacturing*, ISRN Mechanical Engineering. 2012;2012:10.

142.   Schwerdtfeger, J., Schury, F., Stingl, M., Wein, F., Singer, R. F., Körner, C. *Mechanical Characterisation Of A Periodic Auxetic Structure Produced By SEBM*, physica status solidi (b). 2012;249(7):1347-52.

143.   Yang, L. *Structural Design, Optimization and Application of 3D Re-entrant Auxetic Structures*. PhD Thesis. North Carolina State University; 2011.

144.   Li, Y., Harrysson, O., West, H., Cormier, D. *Compressive Properties Of Ti-6Al-4V Auxetic Mesh Structures Made By Electron Beam Melting*, Acta Materialia. 2012 May;60(8):3370-33793379.

145.   Yang, L., Cormier, D., West, H., Harrysson, O., Knowlson, K. *Non-stochastic Ti–6Al–4V Foam Structures With Negative Poisson's Ratio*, Materials Science and Engineering: A. 2012 12/15/;558(0):579-85.

146.   Hu, H., Silberschmidt, V. *A Composite Material With Poisson's Ratio Tunable From Positive To Negative Values: An Experimental And Numerical Study*, Journal of Materials Science. 2013 2013/12/01;48(24):8493-500.

147.   Shen, J., Zhou, S., Huang, X., Xie, Y. M. *Simple Cubic Three-Dimensional Auxetic Metamaterials*, physica status solidi (b). 2014;251(8):1515-22.

148.   Fozdar, D. Y., Soman, P., Lee, J. W., Han, L.-H., Chen, S. *Three-Dimensional Polymer Constructs Exhibiting a Tunable Negative Poisson's Ratio*, Advanced Functional Materials. 2011;21(14):2712-20.

149.   Baker, C. E. *Auxetic spinal implants: Consideration of negative Poisson's ratio in the design of an artificial intervertebral disc*: Masters Disertation. University of Toledo; 2011.

150.   Abdul-Aziz, A., Limbert, G., Young, P. G., Beresford-West, T. *Using ABAQUS with 3D Imaging Techniques For Material Characterization.* 2007 ABAQUS Users' Conference; May 22-24 2007; Paris, France.2007. p. 12.

151.   Babaee, S., Shim, J., Weaver, J. C., Chen, E. R., Patel, N., Bertoldi, K. *3D Soft Metamaterials with Negative Poisson's Ratio*, Advanced Materials. 2013;25(36):5044-9.

152.   Xu, B., Arias, F., Brittain, S. T., Zhao, X. M., Grzybowski, B., Torquato, S., Whitesides, G. M. *Making Negative Poisson's Ratio Microstructures by Soft Lithography*, Advanced Materials. 1999;11(14):1186-9.

153.   Lee, T., Lakes, R. *Anisotropic Polyurethane Foam With Poisson's ratio Greater Than 1*, Journal of Materials Science. 1997;32(9):2397-401.

154.   Lisiecki, J., Kłysz, S., Błażejewicz, T., Gmurczyk, G., Reymer, P. *Tomographic Examination Of Auxetic Polyurethane Foam Structures*, physica status solidi (b). 2014;251(2):314-20.

155.   Chekkal, I., Bianchi, M., Remillat, C., Becot, F. X., Jaouen, L., Scarpa, F. *Vibro-Acoustic Properties of Auxetic Open Cell Foam: Model and Experimental Results*, Acta Acust United Acustica. 2010 Mar-Apr;96(2):266-74.

156.   Pierron, F., McDonald, S. A., Hollis, D., Fu, J., Withers, P. J., Alderson, A. *Comparison of the Mechanical Behaviour of Standard and Auxetic Foams by X-ray Computed Tomography and Digital Volume Correlation*, Strain. 2013;49(6):467-82.

157.   Sanami, M., Ravirala, N., Alderson, K., Alderson, A. *Auxetic Materials for Sports Applications*, Procedia Engineering. 2014 //;72(0):453-8.

158.   Chan, N., Evans, K. E. *Microscopic Examination of the Microstructure and Deformation of Conventional and Auxetic Foams*, Journal of Materials Science. 1997 Nov;32(21):5725-36.

159.   Gibson, L. J., Ashby, M. F. *Cellular Solids: Structure and Properties*. London: Cambridge University Press; 1988. 516 p.

160.   Mills, N. *Polymer Foams Handbook*: Elsevier Ltd; 2007. 535 p.

161.   Choi, J. B., Lakes, R. S. *Non-Linear Properties of Metallic Cellular Materials With a Negative Poisson's Ratio*, Journal of Materials Science. 1992 Oct;27(19):5375-81.

162.   Alderson, A., Rasburn, J., Evans, K. E. *Mass Transport Properties of Auxetic (Negative Poisson's Ratio) Foams*, Phys Status Solidi B-Basic Solid State Phys. 2007 Mar;244(3):817-27.

163.   Grima, J. N., Gatt, R., Ravirala, N., Alderson, A., Evans, K. E. *Negative Poisson's Ratios in Cellular Foam Materials*, Materials Science and Engineering: A - Structural Materials Properties Microstructure and Processing. 2006 May;423(1-2):214-8.

164.   Masters, I. G., Evans, K. E. *Models for the Elastic Deformation of Honeycombs*, Composite Structures. 1996 Aug;35(4):403-22.

165.   Wan, H., Ohtaki, H., Kotosaka, S., Hu, G. *A Study Of Negative Poisson's Ratios In Auxetic Honeycombs Based On A Large Deflection Model*, European Journal of Mechanics - A/Solids. 2004;23(1):95-106.

166.   Lim, T.-C. *Constitutive Relationship Of A Material With Unconventional Poisson's Ratio*, Journal of Materials Science Lett. 2003 2003/12/01;22(24):1783-6.

167.   Warren, T. L. *Negative Poisson's Ratio In A Transversely Isotropic Foam Structure*, Journal of Applied Physics. 1990;67(12):7591-4.

168.   Janus-Michalska, M. *Micromechanical Model Of Auxetic Cellular Materials*, Journal of Theoretical and Applied PhysicsMech. 2009 2009;4(47):737-50.

169.   Berthelot, J. M. *Relation Between Amplitudes and Rupture Mechanisms in Composite Materials*, Journal of Reinforced Plastics and Composites. 1988 May;7(3):284-99.

170.   Attard, D., Manicaro, E., Gatt, R., Grima, J. N. *On The Properties Of Auxetic Rotating Stretching Squares*, physica status solidi (b). 2009;246(9):2045-54.

171.   Grima, J. N., Zammit, V., Gatt, R., Attard, D., Caruana, C., Chircop Bray, T. G. *On The Role Of Rotating Tetrahedra For Generating Auxetic Behavior In Nat And Related Systems*, Journal of Non-Crystalline Solids. 2008;354(35–39):4214-20.

172.   Grima, J. N., Chetcuti, E., Manicaro, E., Attard, D., Camilleri, M., Gatt, R., Evans, K. E. *On The Auxetic Properties Of Generic Rotating Rigid Triangles*, Proceedings of the Royal Society A: Mathematical, Physical and Engineering Science. 2012 March 8, 2012;468(2139):810-30.

173. Grima, J. N., Farrugia, P. S., Gatt, R., Zammit, V. *Connected Triangles Exhibiting Negative Poisson's Ratios and Negative Thermal Expansion*, Journal of the Physical Society of Japan. 2007 1/2/2007;76(2):2.

174. Grima, J., Evans, K. *Auxetic Behavior From Rotating Triangles*, Journal of Materials Science. 2006;41(10):3193-6.

175. Attard, D., Grima, J. N. *A Three-Dimensional Rotating Rigid Units Network Exhibiting Negative Poisson's Ratios*, physica status solidi (b). 2012;249(7):1330-8.

176. Grima, J. N., Zammit, V., Gatt, R., Alderson, A., Evans, K. E. *Auxetic Behaviour From Rotating Semi-Rigid Units*, physica status solidi (b). 2007;244(3):866-82.

177. Grima, J. N., Manicaro, E., Attard, D. *Auxetic Behaviour From Connected Different-Sized Squares And Rectangles*, Proceedings of the Royal Society A: Mathematical, Physical and Engineering Science. 2010 August 4, 2010.

178. Grima, J. N., Evans, K. E. *Auxetic Behavior From Rotating Squares*, Journal of Materials Science Lett. 2000 2000/09/01;19(17):1563-5.

179. Grima, J. N., Gatt, R., Alderson, A., Evans, K. E. *On The Auxetic Properties Of 'Rotating Rectangles' With Different Connectivity*, Journal of the Physical Society of Japan. 2005 Oct;74(10):2866-7.

180. Attard, D., Manicaro, E., Grima, J. N. *On Rotating Rigid Parallelograms And Their Potential For Exhibiting Auxetic Behaviour*, Phys Status Solidi B-Basic Solid State Phys. 2009 Sep;246(9):2033-44.

181. Attard, D., Grima, J. N. *Auxetic Behaviour From Rotating Rhombi*, Phys Status Solidi B-Basic Solid State Phys. 2008 Nov;245(11):2395-404.

182. Grima, J. N., Gatt, R., Ellul, B., Chetcuti, E. *Auxetic Behaviour In Non-Crystalline Materials Having Star Or Triangular Shaped Perforations*, Journal of Non-Crystalline Solids. 2010;356(37–40):1980-7.

183. Gaspar, N., Smith, C. W., Evans, K. E. *Effect Of Heterogeneity On The Elastic Properties Of Auxetic Materials*, Journal of Applied Physics. 2003 Nov;94(9):6143-9.

184. Horrigan, E. J., Smith, C. W., Scarpa, F. L., Gaspar, N., Javadi, A. A., Berger, M. A., Evans, K. E. *Simulated Optimisation Of Disordered Structures With Negative Poisson's Ratios*, Mechanics of Materials. 2009;41(8):919-27.

185. Gaspar, N., Smith, C. W., Evans, K. E. *Auxetic Behaviour And Anisotropic Heterogeneity*, Acta Materialia. 2009 Feb;57(3):875-80.

186. Koenders, M. A., Gaspar, N. *The Auxetic Properties Of A Network Of Bending Beams*, physica status solidi (b). 2008;245(3):539-44.

187. Koenders, M. A. *Constitutive Properties Of Contacting Materials With A Finite-Sized Microstructure*, Molecular Simulation. 2005 2005/11/01;31(13):873-82.

188.   Blumenfeld, R., Edwards, S. F. *Theory of strains in auxetic materials*, Journal of Superconductivity and Novel Magnetism. 2012;25:7.

189.   Blumenfeld, R. *Auxetic Strains—Insight From Iso-Auxetic Materials*, Molecular Simulation. 2005 2005/11/01;31(13):867-71.

190.   Choi, J. B., Lakes, R. S. *Non-Linear Analysis of the Poisson Ratio of Negative Poisson's Ratio Foams*, Journal of Composite Materials. 1995;29(1):113-28.

191.   Choi, J. B., Lakes, R. S. *Analysis of Elastic-Modulus of Conventional Foam and of Re-entrant Foam Materials with a Negative Poisson's Ratio*, International Journal of Mechanical Sciences. 1995 Jan;37(1):51-9.

192.   Evans, K. E., Nkansah, M. A., Hutchinson, I. J. *Auxetic Foams - Modeling Negative Poisson's Ratios*, Acta Metallurgica Materialia. 1994 Apr;42(4):1289-94.

193.   Attenborough, F. R. *The Modelling Of Network Polymers*.PhD Thesis. Liverpool: University of Liverpool; 1997.

194.   Chen, C. P., Lakes, R. S. *Analysis of the Structure - Property Relations of Foam Materials*, Cellular Polymers Journal. 1995;14(3):186-202.

195.   Zhu, H. X., Knott, J. F., Mills, N. J. *Analysis of the Elastic Properties of Open-cell Foams with Tetrakaidecahedral Cells*, Journal of the Mechanics and Physics of Solids. 1997 Mar;45(3):319-25.

196.   Grima, J. N., Caruana-Gauci, R., Attard, D., Gatt, R. *Three-Dimensional Cellular Structures With Negative Poisson's Ratio And Negative Compressibility Properties*, Proceedings of the Royal Society A: Mathematical, Physical and Engineering Science. 2012 October 8, 2012;468(2146):3121-38.

197.   Lu, Z.-X., Liu, Q., Yang, Z.-Y. *Predictions of Young's modulus and negative Poisson's ratio of auxetic foams*, physica status solidi (b). 2011;248(1):167-74.

198.   Elliott, J. A., Windle, A. H., Hobdell, J. R., Eeckhaut, G., Oldman, R. J., Ludwig, W., Boller, E., Cloetens, P., Baruchel, J. *In-Situ Deformation Of An Open-Cell Flexible Polyurethane Foam Characterised By 3d Computed Microtomography*, Journal of Materials Science. 2002 Apr;37(8):1547-55.

199.   Gaspar, N., Smith, C. W., Miller, E. A., Seidler, G. T., Evans, K. E. *Quantitative Analysis of the Microscale of Auxetic Foams*, Phys Status Solidi B-Basic Solid State Phys. 2005 Mar;242(3):550-60.

200.   Timoshenko, S. P., Goodier, J. N. *Theory of Elasticity*. United States: McGraw-Hill, Inc.; 1970. 591 p.

201.   Mindlin, R. D. *Stress Functions for a Cosserat Continuum*, International Journal of Solids and Structures. 1965;1(3):265-71.

202.   Lakes, R. S. *Experimental Microelasticity of 2 Porous Solids*, International Journal of Solids and Structures. 1986;22(1):55-63.

203.   Burns, S. *Negative Poisson's Ratio Materials*, Science. 1987 Oct;238(4826):551-.

204.   Argatov, I. I., Guinovart-Díaz, R., Sabina, F. J. *On Local Indentation And Impact Compliance Of Isotropic Auxetic Materials From The Continuum Mechanics Viewpoint*, International Journal of Engineering Science. 2012 5//;54(0):42-57.

205.   Sneddon, I. N. *Fourier Transforms*. New York: McGraw-Hill, Inc.; 1951. 542 p.

206.   Bezazi, A. R., El Mahi, A., Berthelot, J. M., Bezzazi, B. *Flexural Fatigue Behavior of Cross-Ply Laminates: An Experimental Approach*, Strength of Materials. 2003;35(2):149-61.

207.   Askes, H., Nguyen, D., Tyas, A. *Increasing the Critical Time Step: Micro-Inertia, Inertia Penalties and Mass Scaling*, Computational Mechanics. 2011:1-11.

208.   Lim, T. C., Alderson, A., Alderson, K. L. *Experimental Studies On The Impact Properties Of Auxetic Materials*, physica status solidi (b). 2014;251(2):307-13.

209.   Qi, C., Yang, S., Wang, D., Yang, L.-J. *Ballistic Resistance of Honeycomb Sandwich Panels under In-Plane High-Velocity Impact*, The Scientific World Journal. 2013;2013:20.

210.   Hou, Y., Neville, R., Scarpa, F., Remillat, C., Gu, B., Ruzzene, M. *Graded Conventional-Auxetic Kirigami Sandwich Structures: Flatwise Compression And Edgewise Loading*, Composites Part B: Engineering. 2014 3//;59(0):33-42.

211.   Alderson, K. L., Coenen, V. L. *The Low Velocity Impact Response Of Auxetic Carbon Fibre Laminates*, physica status solidi (b). 2008;245(3):489-96.

212.   Schultz, J., Griese, D., Shankar, P., Summers, J. D., Ju, J., Thompson, L. *Optimization Of Honeycomb Cellular Meso-Structures For High Speed Impact Energy Absorption*. ASME 2011 International Design Engineering Technical Conferences and Computers and Information in Engineering Conference; 28-31 August 2011; Washington, DC, USA 2011. p. 955-65.

213.   Scarpa, F., Tomlinson, G. *Theoretical Characteristics of the Vibration of Sandwich Plates with In-Plane Negative Poisson's Ratio Values*, Journal of Sound and Vibration. 2000 Feb;230(1):45-67.

214.   Caddock, B. D., Evans, K. E. *Negative Poisson Ratios and Strain-Dependent Mechanical Properties in Arterial Prostheses*, Biomaterials. 1995 Sep;16(14):1109-15.

215.   Ruzzene, M., Scarpa, F. *Control of Wave Propagation in Sandwich Beams with Auxetic Core*, Journal of Intelligent Material Systems and Structures. 2003 Jul;14(7):443-53.

216.   Scarpa, F., Smith, F. C., Chambers, B., Burriesci, G. *Mechanical and Electromagnetic Behaviour of Auxetic Honeycomb Structures*, Aeronautical Journal. 2003 Mar;107(1069):175-83.

217.   Smith, F. C., Scarpa, F. *Design of Honeycomb-like Composites for Electromagnetic and Structural Applications*, EE Proceedings - Science, Measurement and Technologyl. 2004 Jan;151(1):9-15.

218.   Whitty, J. P. M., Alderson, A., Myler, P., Kandola, B. *Towards the Design of Sandwich Panel Composites with Enhanced Mechanical and Thermal Properties by Variation of the In-Plane Poisson's Ratios*, Composites Part A - Applied Science and Manufacturing. 2003;34(6):525-34.

219.   EnvironMolds. *Environmolds technical bulletin: Roma Plastilina No. 1 ballistic clay*: EnvironMolds; 2008 [cited 2008 13/11/2008]. 1]. Available from: http://www.artmolds.com/pdf/Roma%20Plastilina%20No%201%20Tech%20Bulletin.pdf.

220.   ObJet. *Objet Connex 350 Technical Specification 2013* [cited 2013 27/03/2013]. Available from: http://objet.com/sites/default/files/pdfs/Connex350_A4_stratasys_lowres.pdf.

221.   John, F. *Partial Differential Equations*. 4th Edition ed: Springer; 1991 1991.

222.   Limited, G. D. *CES EduPack 2010. 6.2.0.0 ed*. Cambridge: Granta Design Limited; 2010.

223.   US-Army. T*esting of Body Armor Materials for Use by the U.S. Army--Phase II:* Letter Report. Letter Report. Washington DC, New York: US Army, Defence Do; 2010 2010. Report No.: ISBN: 0-309-15222-4.

224.   Shearer, P. M. *Introduction to Seismology: The wave equation and body waves. University of California*, San Diego: Institute of Geophysics and Planetary Physics, University of California, San Diego, Oceanography Io; 2010 June 2010. Report No.

225.   van Putten, E., Akbulut, D., Bertolotti, J., Vos, W., Lagendijk, A., Mosk, A. *Scattering Lens Resolves Sub-100 nm Structures with Visible Light*, Physical Review Letters. 2011;106(19).

226.   Goodhew, P. J., Humphreys, J., Beanland, R. *Electron Microscopy and Analysis*. 3rd ed. New York: Taylor and Francis; 2001. 251 p.

227.   Grima, J. N., Alderson, A., Evans, K. E. *An Alternative Explanation for the Negative Poisson's Ratios in Auxetic Foams*, Journal of the Physical Society of Japan. 2005 Apr;74(4):1341-2.

228.   Martz, E. O., Lee, T., Lakes, R. S., Goel, V. K., Park, J. B. *Re-Entrant Transformation Methods In Closed Cell Foams*, Cellular Polymers Journal. 1996;15(4):229-49.

229.   Lisiecki, J., Blazejewicz, T., Klysz, S. *Flexible Auxetic Foams - Fabrication, Properties and Possible Application Areas* Research Works of Air Force Institute of Technology. 2010 14/09/2010;27(1):57-75.

230.   Uleth. *Operation of the Polaron E5100 Series II Sputter Coater*, 2001 [updated 2001; cited 2015 24/21/2015]. Available from: http://www.uleth.ca/emf/2001/equipment/Sputter_coater_inst.pdf.

231.   X-TekGroup. *X-Tek group X-Ray system range 2006* [cited 2012 16/05/2012]. Available from: http://www.xtekxray.com/products/systems.html#bt.

232.   Metris. *CT Pro User Manual*. http://www.southampton.ac.uk2009. p. 62.

233.   Reinhard, C., *Industrial Computer Tomography - A Universal Inspect Tool*. World Conference on Nondestructive Testing,; 2008 25-28 Oct 2008; Shanghai, China.

234.   Random.org. *Random.org 2015* [cited 2015 24/01/2015]. Available from: https://www.random.org/.

235.   Lee, T. C., Kashyap, R. L., Chu, C. N. *Building Skeleton Models via 3-D Medial Surface Axis Thinning Algorithms*, CVGIP: Graphical Models and Image Processing. 1994 11//;56(6):462-78.

236.   Berman, A. T., Salter, F. *Low-Velocity Gunshot Wounds In Police Officers*, Clinical Orthopaedics and Related Research. 1985 (192):113-9.

237.   Slaughter, W. S. *The Linearized Theory of Elasticity*: Birkhäuser Boston; 2002.

238.   Bauchau, O. A., Craig, J. I. *Structural Analysis with Applications to Aerospace Structures*: Springer; 2009.

239.   Flores-Johnson, E. A., Li, Q. M., Mines, R. A. W. *Degradation of Elastic Modulus of Progressively Crushable Foams in Uniaxial Compression*, ournal of Cellular Plastics. 2008 September 1, 2008;44(5):415-34.

240.   Ashby, M. F., Shercliff, H., Cebon, D., *Materials: Engineering Science, Processing and Design*. 3rd ed: Butterworth-Heinemann; 2013.

241.   Pierron, F. *Identification Of Poisson's Ratios Of Standard And Auxetic Low-Density Polymeric Foams From Full-Field Measurements*, The Journal of Strain Analysis for Engineering Design. 2010 May 1, 2010;45(4):233-53.

242.   Mills, N. J., Fitzgerald, C., Gilchrist, A., Verdejo, R. *Polymer Foams For Personal Protection: Cushions, Shoes And Helmets*, Composites Science and Technology. 2003;63(16):2389-400.

243.   Soman, P., Fozdar, D. Y., Lee, J. W., Phadke, A., Varghese, S., Chen, S. C. *A Three-Dimensional Polymer Scaffolding Material Exhibiting A Zero Poisson's Ratio*, Soft Matter. 2012;8(18):4946-51.

244.   Li, Y., Harrysson, O., West, H., Cormier, D. *Modeling Of Uniaxial Compression In A 3D Periodic Re-Entrant Lattice Structure*, Journal of Materials Science. 2013 Feb.;48(4):1413-14221422.

245.   ASM International., *Characterization and Failure Analysis of Plastics*. Lampman S, editor. ASM International: ASM International; 2003 2003. 482 p.

246.   Maiti, S. K., Gibson, L. J., Ashby, M. F. *Deformation And Energy Absorption Diagrams For Cellular Solids*, Acta Metallurgica. 1984 11//;32(11):1963-75.

247.   Gent, A. N., Thomas, A. G. *Mechanics of Foamed Elastic Materials*, Rubber Chemistry and Technology. 1963 1963/07/01;36(3):597-610.

248.   Rusch, K. C. *Load-Compression Behavior Of Brittle Foams*, Journal of Applied Polymer Science. 1970;14(5):1263-76.

249.   Ashby, M. F., Medalist, R. F. M. *The Mechanical Properties Of Cellular Solids*, MTA. 1983 1983/09/01;14(9):1755-69.

250.   Bay, B. K. *Methods and applications of digital volume correlation*, The Journal of Strain Analysis for Engineering Design. 2008 August 1, 2008;43(8):745-60.

251.   Bay, B. K., Smith, T. S., Fyhrie, D. P., Saad, M. *Digital volume correlation: Three-dimensional strain mapping using X-ray tomography*, Experimental Mechanics. 1999 1999/09/01;39(3):217-26.

252.   Gillard, F., Boardman, R., Mavrogordato, M., Hollis, D., Sinclair, I., Pierron, F., Browne, M. *The application of digital volume correlation (DVC) to study the microstructural behaviour of trabecular bone during compression*, Journal of the mechanical behavior of biomedical materials. 2014 Jan;29:480-99.

253.   Pierron, F., McDonald, S. A., Hollis, D., Withers, P. J., Alderson, A. *Assessment of the Deformation of Low Density Polymeric Auxetic Foams by X-Ray Tomography and Digital Volume Correlation*, Applied Mechanics and Materials. 2011;70:5.